Imperial College
London

Imperial College London
Department of Mechanical Engineering

Non-linear vibration transmission through rolling-element bearings in rotating machines

Alexander Haslam

Submitted in part fulfilment of the requirements for the degree of
Doctor of Philosophy
September 2020

Abstract

Modern aircraft engines are pushing established design methodologies to the limits, in order to satisfy current environmental and economic constraints. This calls existing assumptions into question, such as modelling rolling-element bearings (REB) with linear springs, which cannot accurately predict the transmission of vibrations from one rotor to another, known as "cross-shaft coupling". This is further complicated by the inherent non-linearities present in REBs. An improved understanding of the mechanisms governing this phenomenon is required, in order to be able to better diagnose such vibration problems and develop mitigating strategies.

An in-depth numerical study was first carried out, analysing the nonlinear dynamic response of a Jeffcott rotor supported by an REB. A physical bearing model was developed based on the existing literature, which could capture the effect of a wide range of parameters, and the response was computed using a novel application of the Harmonic Balance Method. A strongly nonlinear response was observed due to the bearing, with large shifts in the resonance frequency with excitation amplitude. An extensive parameter study was then carried out, with a particular emphasis on providing physical explantations for the observed behaviour.

These results were then investigated using an existing rotordynamic rig. A well-correlated model of the rig was first developed and parameterised with extensive component-level testing. A separate bearing test rig was designed and built, which was used to validate the bearing model and to identify some key parameters. The focus then moved onto the unbalance response of the rotor rig. The bearing model was found to accurately predict both the vibration transmission to ground, as well as some of the non-linear behaviour, thereby validating the modelling approach in a rotordynamic setting.

The main outcome of this thesis was a fully validated bearing model, which is capable of accurately predicting the vibration transmission, as well as the associated simulation methods. These tools can now be applied in industry, in order to better predict cross-shaft coupling in the future.

Statement of Originality

I declare that the contents of this thesis are entirely my own work, and that any additional sources of information have been duly cited.

Copyright Declaration

The copyright of this thesis rests with the author and is made available under a Creative Commons Attribution Non-Commercial No-Derivatives 4.0 international licence (CC BY-NC-ND 4.0). Researchers are free to copy, distribute or transmit the thesis on the condition that they attribute it, that they do not use it for commercial purposes and that they do not alter, transform or build upon it. For any reuse or redistribution, researchers must make clear to others the licence terms of this work.

Acknowledgements

I would like to thank my supervisor Dr Christoph Schwingshackl for giving me the opportunity to study and work at Imperial College, and for his advice and direction along the way. I would also like to thank Dr Andrew I J Rix from Rolls-Royce plc for sharing his expertise in rotordynamics and useful comments.

I am grateful for Dr Luke Muscutt and Dr Michał Szydłowski's efforts in setting up and commissioning the ARES rig. My experimental research wouldn't have been possible without your mechanical and electronic wizardry. Thank you very much for your advice and encouragement when things didn't go according to plan. Mr Peter Higgs also deserves a special mention for being an admin ninja behind the scenes, which allowed me to focus on the research.

Now I wish to thank my colleagues at the VUTC, who have been a brilliant group of people to work with. Thank you for the technical advice, coffee break chats, and of course, the after-work beers at Eastside! In particular, I would like to thank my good friends and fellow rotordynamicists Dr Daniel Heller and Dr Ali Tatar.

Finally, I would like to thank my family for their support and unwavering belief in me. My girlfriend Dominique deserves special credit for her immense patience, and sustaining me through the highs and lows of this journey.

Table of Contents

List of Figures **xi**

List of Tables **xxi**

Nomenclature **xxiii**

1 Introduction **1**

1.1 Overview 1

1.2 Objectives 2

1.3 Outline of thesis 3

2 Literature review **5**

2.1 Rotordynamics 5

2.2 Rolling-element bearings 12

2.3 Rotor-bearing test rigs 24

2.4 Simulation methods 26

2.5 Summary 27

3 Background theory **29**

3.1 Finite-element rotor model 29

3.2 Quasi-static bearing model 48

3.3 Harmonic balance method 61
3.4 Summary 70

4 Parametric study of a Jeffcott rotor supported by a DGBB 72

4.1 Deep-groove ball-bearing model 73
4.2 Jeffcott rotor 82
4.3 Application of GHBM 85
4.4 Baseline system 87
4.5 Parameter study 95
4.6 Discussion 114
4.7 Conclusions 116

5 The ARES test rig and model development 118

5.1 Overview of the ARES test rig 118
5.2 Stiffness of the fixed bearing 128
5.3 Rotor 139
5.4 Bearing support structure 151
5.5 Ancillary components 175
5.6 Summary 182

6 Forced response of the ARES test rig 183

6.1 Complete rig model using ROLADYN 183
6.2 Setup optimisation 187
6.3 Prediction of frequency response using HBM 200
6.4 Hammer tests 204
6.5 Rotating tests 211
6.6 Summary 235

7 Conclusions **237**

7.1 Summary of the thesis 237

7.2 Main contributions 242

7.3 Future work 243

Appendix A HarmLAB: derivation of analytical derivatives **247**

A.1 Alternating Frequency-Time 247

A.2 Analytical Jacobians 250

Appendix B ARES hammer tests **252**

B.1 Rotor 252

B.2 Bearing support structure 253

B.3 Complete rig 258

Appendix C ARES unbalance responses **262**

Appendix D ARES support model **266**

D.1 Equations of motion 266

D.2 Interface plate stiffness 267

D.3 FE Analysis of L-shape 268

Appendix E BELOS Technical drawings **270**

References **275**

List of Figures

2.1 Rotor co-ordinate system 6

2.2 An example of a Campbell diagram for a rigid rotor 8

2.3 Rotor FRFs for synchronous and asynchronous excitation 9

2.4 Example of 1D and 3D FE meshes of a dual-rotor system 10

2.5 Application of Craig-Bampton method to a plate structure 12

2.6 Schematic of the 2 classes of rolling element bearing 13

2.7 Schematic of single and double row angular contact bearings 13

2.8 Depiction of element loads for an applied radial load 14

2.9 Contact angle before and after the shaft tilts by an angle θ 14

2.10 Roller slicing technique for predicting out-of-plane stiffness 16

2.11 Size of the loaded zone for different levels of clearance 16

2.12 Dynamic loads and velocities of a ball element 17

2.13 Compliant ring deformation under radial load on bearing 19

2.14 Depiction of the variable compliance in REBs 20

2.15 Schematics of existing single-rotor test rigs 25

2.16 Schematics of existing dual-rotor test rigs 25

3.1 Example of a 1D mesh of a rotor 30

3.2 Lateral DOF at each node 31
3.3 1D beam element 32
3.4 Application of CMS to a simple rotor 40
3.5 Validation of ROLADYN 48
3.6 Definition of REB dimensions 49
3.7 Angular position of elements 50
3.8 Free-body force diagram of ball at low-speeds 52
3.9 Bearing contact geometry at low-speeds 53
3.10 Deformed contact geometry at high-speeds 55
3.11 Free-body force diagram of ball at high-speeds 56
3.12 Definition of ball velocities 56
3.13 Comparison of continuous load distributions and discrete element loads . 61
3.14 Depiction of hyper-time for quasi-periodic orbits 63
3.15 Set of harmonics included in GHBM $\left(M_1^H = 5, M_2^H = 3\right)$ 64
3.16 Validation of HarmLAB 70

4.1 Bearing dimensions 73
4.2 Contact forces and deflections 75
4.3 Ring compliance model 77
4.4 Variation of bearing stiffness with cage position 81
4.5 Jeffcott rotor mounted on a REB 82
4.6 Depiction of hyper-time for the Jeffcott rotor 86
4.7 Comparison of the orbits obtained from integrating the ODE and GHBM 88
4.8 Variation of the average bearing stiffness with rotor position for the baseline system 89

4.9 Variation of the stiffness with cage angle for the baseline system 91

4.10 Frequency response of the baseline system 92

4.11 Unbalance transmissibility of the baseline system at resonance 94

4.12 VC forcing of the baseline system at resonance 94

4.13 Variation of the average bearing stiffness with rotor position for different clearance levels 97

4.14 Variation of elemental stiffness distribution in equilibrium position for different clearance levels 97

4.15 Variation of the bearing stiffness with cage angle for different clearance levels 98

4.16 Variation of number of loaded elements with cage angle for different clearance levels 98

4.17 Variation of unbalance transmissibility at resonance with clearance 99

4.18 Variation of VC forcing at resonance with clearance 100

4.19 Variation of the average bearing stiffness with rotor position for different levels of ring compliance 102

4.20 Elemental stiffness distribution in equilibrium position for different levels of ring compliance 102

4.21 Variation of the bearing stiffness with cage angle for different levels of ring compliance 103

4.22 Variation of number of loaded elements with cage angle for different levels of ring compliance 103

4.23 Variation of unbalance transmissibility at resonance with ring compliance 104

4.24 Variation of VC forcing at resonance with ring compliance 105

4.25 Variation of the average bearing stiffness with rotor position at $\Omega = 600\,\mathrm{Hz}$ for different levels of centrifugal loading 107

4.26 Elemental stiffness distribution in equilibrium position at $\Omega = 600\,\text{Hz}$ for different levels of centrifugal loading 107

4.27 Variation of the bearing stiffness with cage angle at $\Omega = 600\,\text{Hz}$ for different levels of centrifugal loading 108

4.28 Variation of number of loaded elements with cage angle at $\Omega = 600\,\text{Hz}$ for different levels of centrifugal loading 108

4.29 Variation of unbalance transmissibility at resonance with centrifugal loading 109

4.30 Variation of VC forcing at resonance with centrifugal loading 110

4.31 Variation of mean vertical rotor position with centrifugal loading for different speeds with $\epsilon = 1 \times 10^{-8}\,\text{m}$ 110

4.32 Variation of the average bearing stiffness with rotor position for different levels of stator compliance 111

4.33 Variation of the bearing stiffness with cage angle for different levels of stator compliance 112

4.34 Variation of unbalance transmissibility at resonance with stator compliance 113

4.35 Variation of VC forcing at resonance with stator compliance 113

5.1 CAD model of the ARES rig 119

5.2 Photos of the ARES test rig 120

5.3 ARES shaft 120

5.4 ARES balancing disc 121

5.5 Floating ARES bearing 122

5.6 Structure supporting the fixed ARES bearing (flexible configuration) . . 123

5.7 Structure supporting the fixed ARES bearing (rigid configuration) 124

5.8 PEA excitation system attached to the ARES bearing support structure 125

5.9 PEA voltage orbits 126

5.10 BKH/60/93/30/35 coupling used to drive the ARES rotor 127

5.11 EPC Model 776 encoder used to measure the angle of the ARES rotor . . 127

5.12 BELOS bearing housing 129

5.13 BELOS test rig in the vertical loading configuration 130

5.14 BELOS test rig in the horizontal loading configuration 132

5.15 BELOS shaft compliance model 133

5.16 Predicted variation of vertical bearing displacement y with cage angle ψ_c for a load $f_y = 1.25\,\mathrm{kN}$ 135

5.17 Results from vertical loading tests on BELOS 136

5.18 Results from horizontal loading tests on BELOS 137

5.19 Schematic of FE model of ARES rotor 141

5.20 ARES rotor hammer test setup 142

5.21 Comparison of the natural frequencies of the ARES rotor from experiments and the numerical model 144

5.22 Comparison of the damping ratios of the ARES rotor from experiments and the numerical model 145

5.23 Comparison of experimental and numerical mode shapes of the ARES rotor with two discs 146

5.24 Simplified model of the bearing support structure (horizontal plane) . . . 152

5.25 Experimental setup to measure the interface plate stiffness 156

5.26 Experimental results from interface plate stiffness test 156

5.27 PEA voltage-displacement relation from quasi-static loading test 157

5.28 Variation of PEA voltage-displacement gain from quasi-static loading test with amplitude of PEA voltage 158

5.29 Schematic of L-shape hammer tests 159

5.30 Schematic of interface plate hammer tests 160

5.31 Experimental setup for hammer tests on interface plate 161

5.32 Schematic of bearing housing hammer tests 161

5.33 Experimental setup for hammer tests on rigid bearing housing 162

5.34 Experimental setup for hammer tests on flexible bearing housing 162

5.35 Mode shapes of the L-shape 166

5.36 Modal properties of the L-Shape and interface plate supports (PEAs disconnected) 168

5.37 Mode shapes of the interface plate (PEAs disconnected) 169

5.38 Modal properties of the rigid and flexible bearing configurations (PEAs disconnected) 170

5.39 Mode shapes of the rigid bearing configuration (PEAs disconnected) . . . 171

5.40 Mode shapes of the flexible bearing configuration (PEAs disconnected) . 171

5.41 Mode shapes of the rigid bearing configuration (PEAs connected) 172

5.42 Modal properties of the rigid and flexible bearing configurations (PEAs connected) 173

5.43 Mode shapes of the flexible bearing configuration (PEAs connected) . . . 174

5.44 Coupling test setup 176

5.45 Coupling deflections and loads during test 176

5.46 Coupling load-displacement relation for different loading positions 177

5.47 Variation of coupling compliance with loading position 178

5.48 Coupling inertia 180

5.49 Encoder inertia 181

6.1 Schematic ROLADYN model of ARES rig 184

6.2 Application of CMS to ARES rig 186

6.3 Comparison of natural frequencies with and without the rigid bearing approximation 188

6.4 Potential ARES configurations 189

6.5 Degrees of freedom and geometric constraints in bDBD configuration . . 191

6.6 Non-linear geometric constraints due to chamber stiffeners 192

6.7 Bearing load ratios for different rig configurations 198

6.8 Mode shapes for different rig configurations (V denotes vertical mode) . . 198

6.9 Performance metric for different rig configurations 199

6.10 Response of the ARES rig for $m_{\mathrm{UB}} = 2.1\,\mathrm{g}$ at resonance ($\Omega = 27.25\,\mathrm{Hz}$) . 201

6.11 Backbone curve for different floating bearing models 203

6.12 Experimental setup for hammer tests on fully assembled ARES test rig . 205

6.13 ARES test rig configured in optimised bDBD setup 205

6.14 Comparison of the experimental and numerical natural frequencies of the assembled ARES rig 207

6.15 Comparison of the experimental and numerical modal properties of the ARES rig 207

6.16 Comparison of the experimental and numerical damping ratios of the assembled ARES rig 208

6.17 ARES test rig instrumentation 212

6.18 Numerical and experimental front disc response in the nominally "balanced" case 214

6.19 Predicted variation of ARES fixed bearing stiffness with rotor speed . . . 217

6.20 Predicted Campbell diagram of the ARES rig 218

6.21 Predicted mode shapes of the ARES rig at $\Omega = 50\,\mathrm{Hz}$ 219

6.22 Response of the ARES rig to PEA excitation 220

6.23 Predicted variation of ARES fixed bearing stiffness with cage position . . 222

6.24 Spectrum of ARES response during ramp-up 224

6.25 Predicted variation of ARES fixed bearing stiffness with displacement . . 226

6.26 Frequency response of the front disc due to front disc unbalance 228

6.27 Disc orbits at resonance with a 2.1 g front disc unbalance 229

6.28 Frequency response of the reacted interface plate force due to front disc unbalance 230

6.29 Backbone curve for different floating bearing models 232

B.1 Comparison of the experimental and numerical mode shapes of the ARES rotor for different numbers of discs 253

B.2 Modal properties of the bearing supports (PEAs disconnected) 254

B.3 Mode shapes of the rigid bearing configuration (PEAs disconnected) . . . 255

B.4 Mode shapes of the flexible bearing configuration (PEAs disconnected) . 256

B.5 Modal properties of the bearing supports (PEAs connected) 257

B.6 Mode shapes of the rigid bearing configuration (PEAs connected) 257

B.7 Comparison of the experimental and numerical modal properties of the ARES rig with and without the PEAs connected 258

B.8 Comparison of the experimental and numerical mode shapes of the ARES rig with and without the PEAs connected 259

B.9 Comparison of the experimental and numerical modal properties of the ARES rig with different ancillary components connected 260

B.10 Comparison of the experimental and numerical modal properties of the ARES rig with different numbers of discs 261

C.1 Frequency response of the rear disc due to front disc unbalance 263

C.2 Frequency response of the interface plate due to front disc unbalance . . 264

C.3 Frequency response of the bearing housing due to front disc unbalance . . 265

D.1 Static response of the L-shape due to moments from the interface plate support rods 269

E.1 Bearing housing 271

E.2 Solid loading shaft 272

E.3 Base plate for mounting to test bed 273

E.4 Bracket for Keyence laser displacement sensors 274

List of Tables

4.1 SKF 6002 dimensions 73

4.2 SKF 6002 contact parameters 74

4.3 Baseline Jeffcott rotor parameters 83

4.4 Harmonic balance parameters for the Jeffcott rotor 88

4.5 Configurations for each section of the parameter study 95

5.1 ARES bearing dimensions 122

5.2 PEA excitation types 126

5.3 BELOS rig parameters 129

5.4 BELOS shaft compliance parameters 134

5.5 Estimated values of unknown bearing parameters 135

5.6 Identified bearing parameters 138

5.7 Measured rotor component weights 141

5.8 Identified inertial and elastic rotor parameters 148

5.9 Identified rotor damping parameters 149

5.10 Measured rotor component weights 149

5.11 MAC for the mode shapes of the rotor 151

5.12 Support rod dimensions 153

5.13 Inertia of different support components 154

5.14 Identified L-shape parameters 163

5.15 Interface plate support rod parameters 164

5.16 Identified bearing housing rod parameters 164

5.17 Identified PEA parameters 165

5.18 Comparison of effective interface plate stiffness from the quasi-static loading test and equivalent numerical model 166

5.19 Comparison of L-shape inertia from hammer test and equivalent numerical model 167

5.20 Identified coupling stiffnesses 179

5.21 Estimated coupling inertia 181

5.22 Estimated encoder inertia 181

6.1 Component separation distances in linear geometric constraints 192

6.2 Chamber stiffener geometric constraint parameters 193

6.3 Maximum allowable misalignments for BKH/60/93/30/35 coupling . . . 194

6.4 Position of components in chosen rig configuration 199

6.5 ARES ball pass frequencies 200

6.6 Harmonic balance parameters for the ARES rig 202

6.7 Identified rig damping parameters 210

6.8 MAC for mode shapes of the assembled ARES rig 211

6.9 List of ARES sensors 213

6.10 Identified rotor runout and residual unbalance parameters 215

Nomenclature

Abbreviations

1X Synchronous component

ARES Asynchronous Rotor Excitation System (Test rig)

BELOS BEaring LOading System (Test rig)

BPF Ball Pass Frequency

BW Backward Whirl

CoG Centre of Gravity

CMS Component Mode Synthesis

DC 0 Hz component

DOF Degree of Freedom

DGBB Deep-Groove Ball Bearing

FE Finite Element

FFT Fast Fourier Transform

FRF Frequency Response Function

FW Forward Whirl

GA Genetic Algorithm

HarmLAB Implementation of HBM (MATLAB toolbox)

GHBM Generalised Harmonic Balance Method

HBM Harmonic Balance Method

MAC Modal Assurance Criterion

PEA Piezo-Electric Actuator

REB Rolling-Element Bearing

ROLADYN ROtating LAteral DYNamics (MATLAB toolbox)

SABB Self-aligning Ball Bearing

VC Variable Compliance

Bearing model

A Distance between bearing race centres of curvature

B Bearing width

β Ball speed angle

C_e Hertzian contact coefficient

c_r Radial bearing clearance

D Ball diameter

d_e Diameter of the race at the contact

δ_e Bearing contact deflection

d_m Diameter between ball centres

e Can be replaced with i or o to refer to each ring

F_e Frictional load at the contact

F_c Centrifugal load on an element

γ Ball diameter ratio given by $\gamma = \frac{D}{d_m}$

I_e Second moment of area of bearing rings

i, o Subscript referring to inner/outer ring

j Bearing element index

K_e Elemental contact stiffness

M_g Gyroscopic moment on an element

n Hertzian contact exponent

N_e Radial ring load

ν_m Cage speed ratio

ν_s Ball spin ratio

ω_b Velocity of ball about its own CoG

ω_s Spin velocity of ball

ψ_c Angular position of bearing cage

$\dot{\psi}_b$ Orbital velocity of element

Q_e Normal load at contact

$r(\psi), z(\psi)$ Relative radial/axial displacement between rings

$\boldsymbol{R}(\alpha)$ Rotation matrix converting normal and tangential forces at each contact to radial and axial forces

r_b, z_b Radial/axial deflection of each element

r_e Radius of curvature of the races

R_e, z_e Radial/axial position of centre of curvature of bearing races

$\boldsymbol{T}(\psi)$ Transformation matrix converting radial and axial forces at each element to horizontal and vertical forces

v_e Radial ring deflection

X Distance between element CoG and centre of outer race curvature

Z Number of bearing elements

Rotor FE model

ϵ Eccentricity of rotor GoG

α, β Rayleigh damping coefficients

c Viscous damping constant

δ_x, δ_y Horizontal and vertical deflections

E Young's Modulus

f Force

$\boldsymbol{f}_e$ Excitation forces

$\boldsymbol{f}_g$ Force due to gravity

$\boldsymbol{f}_{nl}$ Forces from non-linear joints in the machine

$\boldsymbol{G}$ Gyroscopic matrix

g Gravitational constant

I Diametral moment of inertia

J Polar moment of inertia

k Stiffness

$\boldsymbol{M}, \boldsymbol{C}, \boldsymbol{K}$ Mass, damping and stiffness matrices

m Component mass

ν Poisson's ratio

Ω, Θ Rotor speed, angle

$\boldsymbol{R}$ Matrix rotating element into nodal co-ordinates

ρ Density

r, s, b Subscripts referring to rotor/stator/joint element

$\boldsymbol{S}$ Matrix mapping global to local co-ordinates

τ Moment

θ_x, θ_y Rotation about the horizontal and vertical axes

$\boldsymbol{x}$ Displacement vector

Harmonic balance

$\boldsymbol{A}, \boldsymbol{B}$ Hill's method matrices due to linear terms

$\boldsymbol{F}_{k_1,k_2}$ Phasor representation of non-linear force vector $\boldsymbol{f}_{nl}$

k_1, k_2 Index of each harmonic in HBM

$\boldsymbol{L}$ HBM matrix due to linear terms

λ Floquet exponents

M^H Number of harmonics included in HBM

M^T Number of FFT points used in HBM

μ Continuation parameter which scales the base frequencies

$\boldsymbol{\nu}$ Vector relating base frequencies in $\boldsymbol{\omega}$ to continuation parameter μ

$\boldsymbol{\omega}$ Vector of base frequencies

p, q Numerator, denominator of rational approximation of ratio between base frequencies for adjusted HBM

$\boldsymbol{r}$ Complex vector of all HBM residuals

$\boldsymbol{U}_{k_1,k_2}$ Phasor representation of excitation force vector $\boldsymbol{f}$

$\boldsymbol{X}_{k_1,k_2}$ Phasor representation of state vector $\boldsymbol{x}$

$\boldsymbol{z}, \boldsymbol{g}, \boldsymbol{h}$ Vector containing all frequency components within $\boldsymbol{X}, \boldsymbol{U}, \boldsymbol{F}$

ARES test rig

$\alpha_{\mathrm{S}}, \beta_{\mathrm{S}}$ Shaft proportional damping coefficients

β_{C} Coupling proportional damping coefficient

c_{B}^{θ} Bearing tilt damping constant

$c_{\mathrm{E}}^{\delta}, c_{\mathrm{E}}^{\theta}$ Encoder damping constants

Δ Minimum separation distance between components

$\delta_{\mathrm{C}}, \theta_{\mathrm{C}}$ Coupling deflections

E_{S} Shaft Young's modulus

$f_{\mathrm{IP}}^{x}, f_{\mathrm{IP}}^{y}$ Horizontal/vertical force reacted at the interface plate

f_{UB} Unbalance force

G_{PEA} Voltage-displacement gain of the piezo-electric actuators

$m_{\mathrm{C}}, I_{\mathrm{C}}, J_{\mathrm{C}}$ Coupling inertia terms

$m_{\mathrm{E}}, I_{\mathrm{E}}$ Encoder inertia terms

$I_{\mathrm{L}}^{x}, I_{\mathrm{L}}^{y}$ Effective L-shape moment of inertia

$k_{\mathrm{BH}}, k_{\mathrm{IP}}$ Stiffness of bearing housing/interface plate support rods

$k_{\mathrm{C}}^{\delta,\delta}, k_{\mathrm{C}}^{\theta,\delta}, k_{\mathrm{C}}^{\theta,\theta}$ Coupling stiffness terms

$k_{\mathrm{D}}^{\theta}, c_{\mathrm{D}}^{\theta}$ Disc root stiffness and viscous damping constant

$k_{\mathrm{L}}^{x}, k_{\mathrm{L}}^{y}$ Effective L-shape stiffness

$k_{\mathrm{PEA}}^{\delta}, k_{\mathrm{PEA}}^{\theta}$ Effective stiffness of the piezo-electric actuators

k_{IP}^{test} Effective interface plate stiffness measured during quasi-static loading test

$l_{\mathrm{BH}}, l_{\mathrm{IP}}$ Length of bearing housing/interface plate support rods

l_{S} Shaft length

$m_{\mathrm{BH}}, m_{\mathrm{IP}}$ Effective mass of bearing housing/interface plate

m_{UB} Unbalance mass

$\Omega_{i,H}^{\mathrm{crit}}, \Omega_{i,V}^{\mathrm{crit}}$ Critical speeds where the ith mode pair is excited

$\omega_{i,H}^{\mathrm{crit}}, \omega_{i,V}^{\mathrm{crit}}$ Natural frequencies of the ith mode pair

θ_{L} L-shape rotation

r_{B} Floating-to-fixed bearing load ratio

$\rho_{\mathrm{S}}, \rho_{\mathrm{D}}$ Shaft/disc density

σ_{S} Shaft stress

V_{PEA} Voltage applied to the piezo-electric actuators

$x_{\mathrm{D}}^{f}, y_{\mathrm{D}}^{f}$ Horizontal/vertical front disc displacement

$x_{\mathrm{D}}^{r}, y_{\mathrm{D}}^{r}$ Horizontal/vertical rear disc displacement

$\ddot{x}_{\mathrm{BH}}, \ddot{y}_{\mathrm{BH}}$ Horizontal/vertical bearing housing acceleration

$\ddot{x}_{\mathrm{IP}}, \ddot{y}_{\mathrm{IP}}$ Horizontal/vertical interface plate acceleration

$z_{\mathrm{B}}^{f}, z_{\mathrm{B}}^{r}$ Axial location of front/rear bearing

$z_{\mathrm{D}}^{f}, z_{\mathrm{D}}^{r}$ Axial location of front/rear disc

$z_{\mathrm{BH}}, z_{\mathrm{IP}}, z_{\mathrm{L}}$ Axial location of bearing housing/interface plate/L-shape

Mathematical operations

bold Matrices and vectors

$\Re, \Im$ Real/imaginary part

$.^{T}$ Transpose

Chapter 1

Introduction

1.1 Overview

Jet engines consist of an axial compressor and turbine which are connected together by a shaft. In between the two, combustion occurs thereby energising the air. Some of this energy is taken from the air as it passes through the turbine, which in turn drives the compressor to draw more air into the engine. In most modern aircraft, the turbine also drives a fan on the front of the engine to create what is known as a turbofan arrangement. The remainder of the energy is eventually converted into kinetic energy as the air passes through the nozzle at the rear of the engine, thus producing thrust. It is more efficient to allow the high pressure sections of the compressor to rotate faster, so most engines now have multiple concentric shafts, each connecting a different turbine to a different compressor stage. This allows for a more compact design for the same thrust, as compared to an engine with a single shaft [1]. The shafts are supported by bearings, which are typically rolling-element bearings (REB) due to the high loads which they must react. The rotor can either be connected to the casing via a flexible supporting structure, or if space considerations do not allow this, the rotor may be supported by another rotor via an inter-shaft bearing.

One of the key phenomena which must be considered in the mechanical design of a jet engine is lateral vibration of the rotors. The different shafts rotate at speeds from 3000 rpm to 12 000 rpm for large civil engines and up to 50 000 rpm for small engines such as those used in helicopters. Since the rotors spin at such high speeds, any small imperfections on a rotor can lead to large excitation forces due to the eccentricity of the centre of gravity from the axis of rotation. This can cause the shafts to vibrate, which in turn requires the bearings to react significant loads. This is generally a well understood problem, and is encompassed within the field of rotordynamics. The bearings are typically modelled using linear springs and dampers, which allows the response of the system to

be computed analytically. This allows any unacceptable levels of vibration to be dealt with at the design stage.

However, it has been observed from testing on real engines that vibrations can be transferred from rotor to another rotor, both directly through inter-shaft bearings or indirectly via the casing. As one rotor resonates due to an unbalance or some other excitation source, this will lead to a forcing which may pass through the bearings to another rotor, which is known as "cross-shaft coupling". Current design techniques under-predict this phenomenon, so that such vibration problems can only be mitigated with a more conservative design. For example, the natural frequencies of a rotor could be moved such that they are no longer excited by the forcing from the other rotor, or extra dissipative components can be added, such as fluid dampers, which reduce the maximum response of the rotor. Since the bearings are the main transmission path of loads between the rotors, it is believed that this phenomenon is highlighting a limitation of the simplified approach used to model them.

Rolling-element bearings are known to display significant non-linear characteristics, but this makes prediction of the response significantly more difficult. For a linear system, the response of the system to any arbitrary input can be computed very efficiently, which is why it is desirable to approximate components such as REBs with linear elements. Although this is often a valid assumption for low excitation levels, the non-linearities in the system can start to become significant at larger excitation levels. In this non-linear regime, the response can become much more complex, with the introduction of extra harmonics or even chaos in the extreme case. The influence of the non-linearities on the transmission of vibrations through the bearing has not been investigated in detail and is poorly understood.

This project aims to develop methods to accurately predict the transmission of vibrations through rolling-element bearings within rotating machinery, in order to provide insight into the cross-shaft coupling phenomenon in aero-engines. This includes both the development of new approaches for modelling the bearings, which incorporate the most significant non-linearities which are otherwise often neglected, as well as any associated numerical methods required to simulate such systems. It is crucial that an improved understanding of the physical mechanisms governing these phenomena is also developed, in order to be able to diagnose problematic vibrations and develop mitigating strategies.

1.2 Objectives

Cross-shaft coupling is a complicated phenomenon, which spans rotordynamics, tribology as well as non-linear dynamics. Therefore, this thesis will reduce the scope to focus on

the transmission of synchronous vibrations in single rotor systems, which allows better insight into the mechanisms at play. Only systems with ball bearings will be analysed, since they are more widely used in practice. In spite of these simplifications, much of the improved understanding will extend to multi-shaft systems, and rotors supported by roller bearings. This project aims to achieve the following three objectives:

1. *Develop a simplified REB model for rotordynamic applications and any associated numerical methods:* In order to predict the transmission of vibrations through the bearing, a high-fidelity low-order bearing model is required. This must capture the relevant physics, including any significant non-linear effects, whilst remaining light-weight to evaluate, so that it is suitable for integration into models of complete rotating machines. Due to the non-linear nature of REBs, it is expected that this may require the novel application of advanced numerical methods, in order to reduce the simulation time.

2. *Provide physics-based explanations for the influence of REB non-linearities in rotating machines:* Although the influence of rolling-element bearings on the nonlinear dynamic response of simple rotor-bearing systems has been studied in great detail, little attention has been paid to the transmissibility or the influence of the different physical mechanisms. A systematic study is therefore required, where the influence of many different bearing parameters can be investigated on a single rotor-bearing system, which is representative of industrial rotating machines. In addition, attention should be paid to providing physics-based interpretations for any observed non-linear behaviour.

3. *Experimentally validate the REB modelling approach using a rotordynamic test rig:* In order to develop confidence in the level of vibration transmission through the bearings predicted by the model, there is a real need to experimentally validate the approach using a representative rotordynamic test rig. It is crucial that a well-correlated model of the system is developed in tandem to the experimental work, so that quantitative comparisons can be made with the experimental data, unlike in many existing studies. This will allow the contribution of any observed non-linear behaviour from the bearings to be assessed.

1.3 Outline of thesis

This project aims to develop an improved understanding of the influence of non-linearities on the transmission of vibrations through rolling-element bearings, and the dynamics of rotating machines. An approach for modelling REBs and simulating rotor-bearing

systems will be developed, which will then be validated against experiments. Based on the results, recommendations will be made for the design of future rotating machines. This thesis is structured as follows:

1. The state of the art relating to the response of rotor-bearing systems containing rolling-element bearings will be presented in Chapter 2. The fundamentals of rotordynamics will be introduced, before moving onto bearing modelling. The use of experimental test rigs will be reviewed, as well as the relevant numerical techniques.

2. In Chapter 3, the necessary background theory for modelling and simulating compliant rotors supported by rolling-element bearings will be introduced. A 1D finite-element rotor model will be presented, which can capture the lateral dynamics of flexible rotors. The quasi-static approach for modelling ball bearings will be introduced. Finally, the Generalised Harmonic Balance will be summarised, which will later be used to simulate the response of rotor-bearing systems containing REBs in an efficient manner.

3. An in-depth numerical study will be performed in Chapter 4, considering the non-linear unbalance response of a Jeffcott rotor supported by a deep-groove ball bearing. The transmissibility of loads through the bearing will be investigated. A parameter study will be performed to quantify the significance of the different mechanisms within the bearing, with a particular emphasis on providing physical explanations for the observed behaviour. Both the non-linear bearing stiffness and transmission of unbalance loads will be considered.

4. The ARES test rig will be introduced in Chapter 5. This rotordynamic rig is representative of an aircraft engine, and will be used in later chapters to validate the modelling approach. Over the course of this chapter, high-fidelity models of the different subsystems will be developed, and then parameterised using results from component-level testing. Particular effort will be put into identifying the unknown bearing parameters using a separate test rig known as BELOS.

5. In Chapter 6, the attention will move onto the forced response of the ARES test rig. The model will be used to optimise the setup in order to maximise the influence of the bearing non-linearity. The forced response will then be investigated experimentally, with a particular focus on the vibration transmission through the instrumented bearing. The results will be compared to the predictions from the model, thereby validating the approach in a dynamic setting. The significance of the bearing non-linearities will also be quantified.

6. The main conclusions will be summarised in Chapter 7. Areas for further research will also be recommended.

Chapter 2

Literature review

A thorough review of the existing literature was carried out, with a focus on 3 main areas. The first section presents a brief summary of the field of rotordynamics, with a particular emphasis on the lateral dynamics. The next section introduces the physical phenomena within rolling-element bearings which contribute to their stiffness and damping, as well as existing modelling techniques. In the last two sections, the attention moves onto existing experimental and numerical techniques for investigating the behaviour of systems involving rolling-element bearings.

2.1 Rotordynamics

Rotordynamics is the study of dynamic behaviour of rotating machinery, including both the motion of the different components, and the loads passing through them. All rotating machinery consists of [2]:

- A rotor which spins at relatively high speeds, such that the rotation has an effect on the dynamics.
- Bearings which support the rotor, while allowing it to rotate freely.
- A non-rotating stator which connects the rotor to ground via bearings.

In many rotating machines, there can be multiple rotors which are supported by many sets of bearings. In addition, the rotors can be of varying complexity. In the simplest case, the rotor may be quite stocky and can be approximated as rigid, which is known as a Jeffcott rotor [3]. At the other extreme, a rotor may have many rows of bladed discs, which introduce their own dynamics.

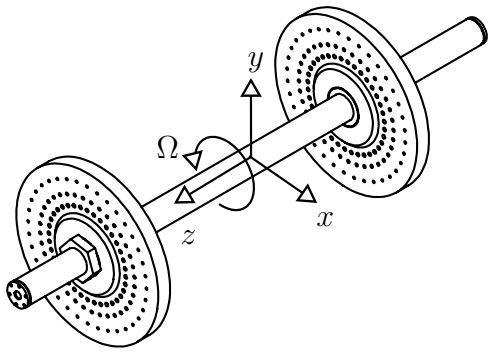


Figure 2.1: Rotor co-ordinate system

2.1.1 Frames of reference

In the field of rotordynamics, the system is usually analysed in one of 2 different frames of reference:

- *Inertial frame:* This is useful for axisymmetric rotors as the rotor inertia tensor is independent of the rotation angle. Anisoptropic stators can be easily modelled in this frame, but any asymmetry in the rotor appears as a time-varying parameter.
- *Rotating body-fixed frame:* The rotating frame fixed to the rotor is useful when the rotor is asymmetric; for example, for bladed discs. Any anisotropy in the stator appears as a time-varying parameter.

For this thesis, the focus is on the characteristics of the bearings and rotor supports, which may include anisotropic effects. Therefore, it is more natural to work in the inertial frame. As a consequence, it is necessary to restrict the analysis to axisymmetric rotors, so that the rotor has constant parameters in the inertial frame, thereby allowing a linear treatment.

Multiple coordinate systems were found to be used in the literature, but this thesis will use the one from [2], which is depicted in Fig. 2.1. The z axis is aligned with the axis of rotation, and then the x and y axes are set to run horizontally and vertically respectively.

2.1.2 Lateral, torsional and axial vibration

The analysis of such rotating machinery is often split into different categories depending on the nature of motion. Torsional vibration involves rotation around the z axis, which is of particular interest in geared machinery. Axial vibration involves translational motion along the z axis, but the stiffness is normally high in this direction so these modes are normally less of a concern. Lateral vibration includes both flexural and translational motion in the x-z and y-z planes, and are often the lowest frequency modes [4]. These

modes are most heavily influenced by the support structure characteristics [2]. In the general case, these different types of motion can be coupled together such as through helical gears [2,4]. However, it is often valid to assume that they are decoupled from each other.

2.1.3 Centrifugal loading

The rotational speed of the rotor introduces centrifugal loading. This means that any small asymmetry on the rotor leads to a net centrifugal load, which can excite the rotor [5]. Centrifugal loading can also lead to a stiffening effect in flexible discs so the stiffness matrix will be speed dependent [2]. The net centrifugal load is known as an *unbalance* (or *out-of-balance*) which is the most common form of lateral excitation experienced by a rotor [4]. It can be thought of as an harmonic excitation at the rotation frequency. The forcing will rotate with the rotor, so that there will be components with the same magnitude in the x and y-directions, with a 90° phase difference between them [2].

2.1.4 Gyroscopic moments & whirl

As the rotor deflects about the x or y axes, it will experience gyroscopic moments. These have a tendency to couple pairs of the lateral modes. If there are 2 orthogonal modes when the rotor is stationary, with one horizontal mode involving motion in the x-z plane and another vertical mode in the y-z plane, then these modes will combine into a pair of elliptical modes as the rotation speed is increased; one mode in which the rotor *whirls* in the same direction as its own spin, and another in the opposite direction. These are termed *forwards whirl* (FW) and *backwards whirl* (BW) modes [4]. The natural frequencies of these modes also become speed dependent; the FW modes tend to increase in frequency with speed and the BW ones tend to decrease. Purely translational modes involving no rotation about the x or y axis will feel no gyroscopic moment, so will not display these effects [2]. It is often useful to plot the natural frequencies against rotation speed to create a *Campbell diagram*. An example is plotted in Fig. 2.2. In this case, modes 1 & 2 are purely translational modes with no whirl, whereas modes 3 & 4 are a pair of FW and BW whirl modes.

Gyroscopic effects can be incorporated into the equation of motion for the rotating machine by the addition of a speed dependent term proportional to the rotation speed Ω:

$$\boldsymbol{M}\ddot{\boldsymbol{x}} + (\boldsymbol{C} + \Omega\boldsymbol{G})\,\dot{\boldsymbol{x}} + \boldsymbol{K}\boldsymbol{x} = \boldsymbol{f}_e \tag{2.1}$$

where $\boldsymbol{M}$, $\boldsymbol{C}$ and $\boldsymbol{K}$ are the conventional mass, damping and stiffness matrices respectively. The matrix $\boldsymbol{G}$ in Eq. (2.1) is the *gyroscopic matrix*. The non-zero elements of the

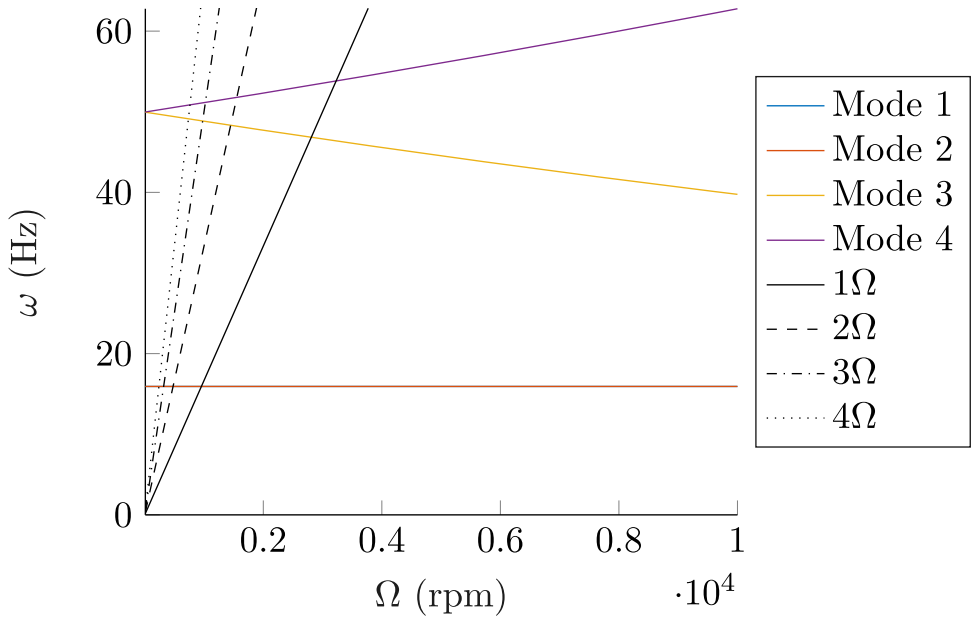


Figure 2.2: An example of a Campbell diagram for a rigid rotor

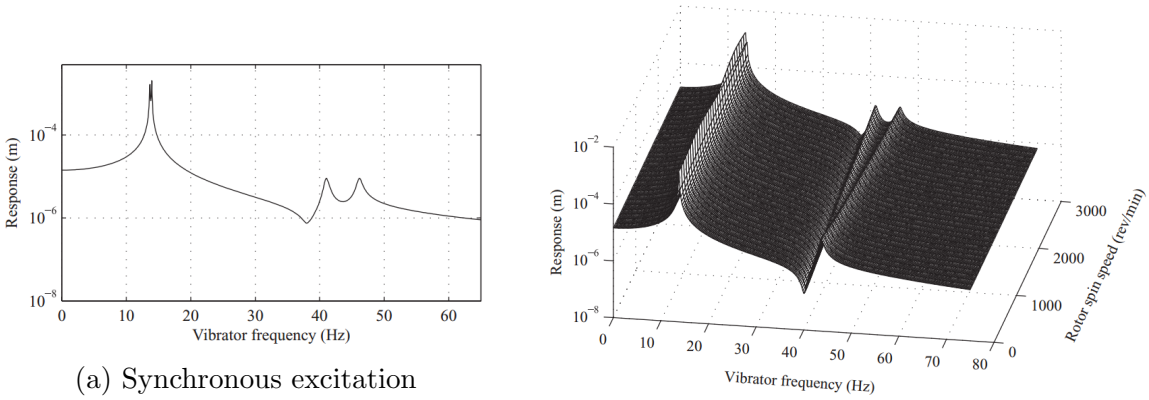
gyroscopic matrix are associated with the polar moment of inertia of the rotor. It can be shown that this matrix will always be skew-symmetric [2], which is due to the fact that cross-products are involved in the derivation of the gyroscopic terms. This means that the left and right eigenvectors are not equal, so both must be computed when performing modal analysis [6].

If a multi-rotor system operates with fixed speed ratios between the shafts, this can be accounted for by scaling the relevant terms in the gyroscopic matrix by the speed ratio of the respective rotor [7, 8].

2.1.5 Synchronous and Asynchronous excitation

As described in Section 2.1.3, an out-of-balance leads to an harmonic excitation at the rotation frequency. It is also possible to have excitations at multiples or fractions of the rotation frequency. This can arise for example when there is an out-of-balance on another rotor coupled to the rotor of interest, rotating at a fixed speed ratio [9, 10]. Another example is when there is a defect in the raceway of a rolling-element bearing [11, 12]. These are collectively known as *synchronous* excitations, because the frequency scales with the rotation speed. The constant of proportionality is known as the *engine order*. These excitations can also be plotted as lines on a Campbell diagram. For example, the first four engine orders are plotted in black in Fig. 2.2. When an engine order line crosses a natural frequency, this can lead to resonance and is known as a *critical speed*. The response to such excitations can be encapsulated in an FRF plotted against rotation speed, as shown in Fig. 2.3a.

It is also possible for a rotor to experience excitations at a frequency unrelated to the current rotor speed. This could come from a variety of sources, such as fluctuating aerodynamic forces [4] or excitation through the supports from another structure [2]. These are known as *asynchronous* excitations. It is more complex to analyse the response to such excitations, because it is a function of both the excitation frequency and rotation speed. The FRF can then be plotted in 3D to create a *waterfall* plot as shown in Fig. 2.3b. Asynchronous excitations can be a useful way to experimentally extract Campbell diagrams, as they allow the resonance frequencies at each speed to be found [13].



(a) Synchronous excitation

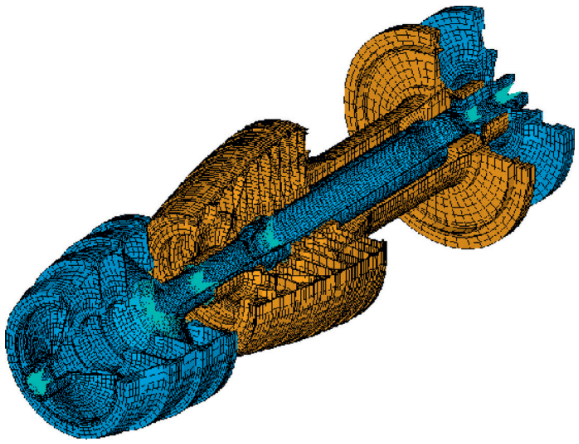
(b) Asynchronous excitation

Figure 2.3: Rotor FRFs for synchronous and asynchronous excitation [2]

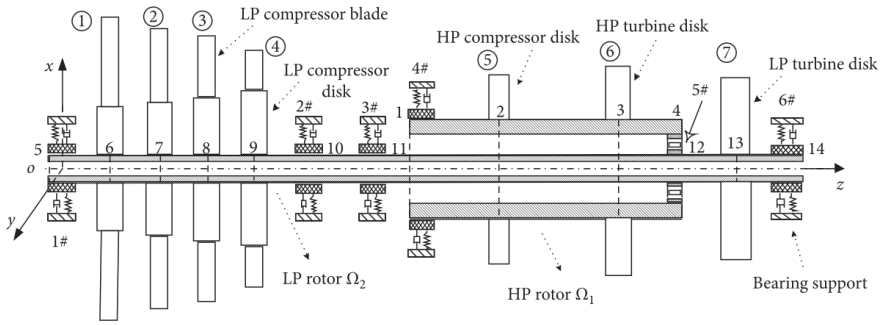
2.1.6 Finite-element models

It has been established that the equation of motion for a rotating machine with no centrifugal softening or stiffening effects and rotating at a constant speed Ω, can be written in the form in Eq. (2.1). For simple rigid rotors, it is possible to specify the mass matrix, stiffness matrix and so on analytically. However, industrial rotors, such as those in modern turbomachinery, typically have very complex geometries for improved aerodynamic or hydrodynamic efficiency. In addition, with a drive to reduce inertia and material costs, the rotors are typically becoming ever more lightweight, and therefore can not simply be modelled as rigid. Numerical techniques are therefore required to compute these four matrices for such rotors. The most commonly used approach is the Finite Element (FE) method, in which the components are discretised into many nodes, which are coupled together with elastic elements.

To capture all of the dynamics of a rotating machine, a dense 3D FE model of the rotor and stator can be created. An example of such a 3D mesh is shown in Fig. 2.4. Such an FE model is able to incorporate localised effects such as out-of-plane bending of the rotor, or deformation at the joint between the discs and shafts. This approach can also capture coupling between different modes of vibration; for example, bladed



(a) 3D FE model



(b) 1D FE model

Figure 2.4: Example of 1D and 3D FE meshes of a dual-rotor system [18]

disks can couple torsional and lateral vibrations [14, 15]. Meshing and simulating such complex geometries requires the use of commercial finite element software [16]. Abaqus, ANSYS, NX NASTRAN and SAMCEF have all been found to be able to simulate rotating machinery accurately [17]. However, such models will have many thousand degrees of freedom (DOF) so are computationally expensive to analyse.

For simpler rotors, approximations can be made to significantly reduce the number of DOF whilst maintaining sufficient accuracy. It can often be assumed the discs are sufficiently stiff so that their bending frequencies are well outside the range of interest, so that they can be modelled as rigid bodies. Localised effects on the shaft can be neglected, so that it can be modelled as a beam. The stator can be modelled as a separate mass-spring system, and the bearings can also often be further simplified; for example, a self-aligning bearing will provide little constraint against any tilting motion of the shaft, leading to zero terms in its stiffness matrix [19]. Additionally, if it can be assumed that the lateral, torsional and axial motion are uncoupled, then only the relevant DOFs need to be retained. For example, to investigate the lateral dynamics, this requires only 4 DOF per disc.

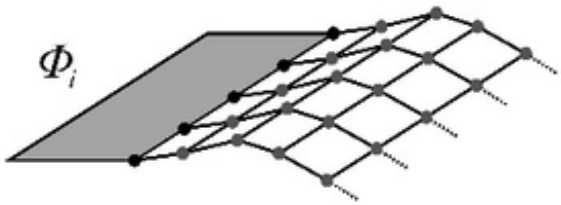
The shaft is a continuous component so must be somehow discretised for use in numerical

models. In the past, this was often achieved using the Transfer Matrix method [20–22], but with the increase in computing resources, the FE Method has become the most common approach. Both approaches approximate the shaft with a finite number of *nodes*, each with the same number of DOF as one lumped disc element. The FE method was first applied to rotordynamics by Ruhl [23], and then extended by Nelson et al. to include the effects of gyroscopic moments, rotary inertia and axial loads [24]. Timoshenko beam elements are most appropriate for shafts in turbomachinery [2] which are often stocky, so shear deformations can be significant [25]. Specialised versions of these elements can be derived for tapered shafts [2]. An example of the equivalent 1D line model is shown in Fig. 2.4.

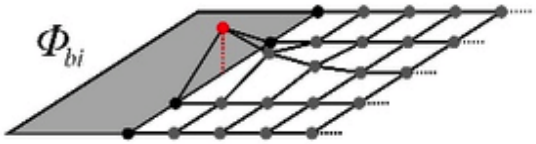
2.1.7 Component mode synthesis

The Finite-Element model of the rotor or stator may have many DOF, but it is possible to reduce the number of DOF whilst maintaining a sufficient level of accuracy by applying model reduction techniques. One of the most commonly used approaches in the field of rotordynamics is Component Mode Synthesis (CMS) [26]. The structure is partitioned into boundary nodes at the interfaces, with the remaining nodes known as interior nodes. The response is then assumed to be made up of a sum of "normal modes", and a set of "constraint modes" associated with the interfaces. The normal modes are the modes of the structure with all of the boundary DOF either held fixed, known as the Craig-Bampton method [27], or free [28–30]. The Craig-Bampton method is more widely used, in part because it is more accurate for the same number of normal modes [29, 31]. The free interface method is more attractive when the normal modes are to be determined experimentally, since the results from free hammer tests can be used [31]. It is also possible to use a hybrid approach [32], where a subset of the boundary nodes are held fixed, whilst the remainder are kept free. An example of the application of CMS to a plate is shown in Fig. 2.5.

In the Craig-Bampton method, the constraint modes can be computed by performing a Guyan reduction on the interior DOF [33,34]; ie. compute the static response of the structure by perturbing each boundary DOF in turn. For the free-interface method, constraint modes are not a requirement, because the normal modes have non-zero displacements at the boundaries. Nevertheless, constraint modes can be included to produce solutions closer in accuracy to the fixed-interface method [31]. However, the method of computing the constraint modes is more involved than with the Craig-Bampton method [29, 32]. All of the methods discussed so far assume that the system is proportionally damped, but Craig and Chang presented a complex form of CMS for non-proportionally damped systems [35].



(a) Example of a normal mode, with all boundary DOF held fixed



(b) Example of a constraint mode, where a single boundary DOF has been perturbed

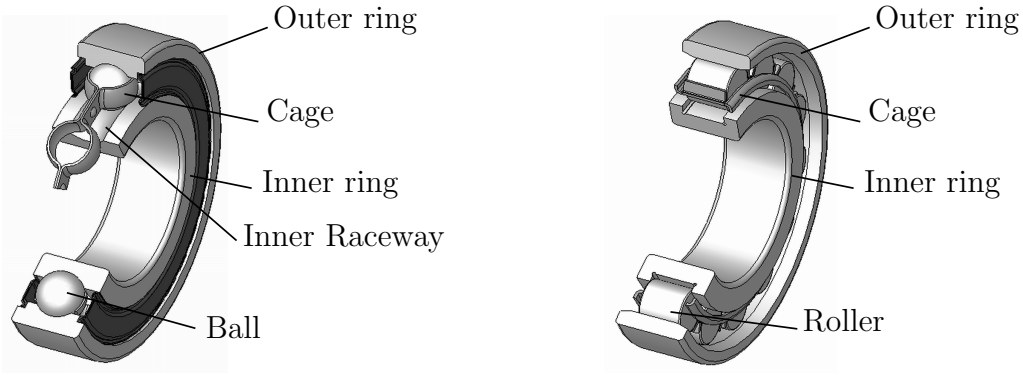
Figure 2.5: Application of Craig-Bampton method to a plate structure [36]

Application of CMS to rotor-bearing systems is well established, and is most often applied to the rotor as this is often the most complex component. Glasgow and Nelson applied the fixed-boundary method to analyse the whirl instability of a two-rotor system [37]. It was found that the error in the natural frequencies was less than 6 % when only a third of the normal modes were retained. Wang and Kirkhope applied a modified free-interface method to the same dual-rotor system, incorporating extra terms for dissipative effects [31]. It was found that the accuracy was improved compared to the fixed-boundary approach. Li and Gunter analysed a more complex twin-spool aircraft engine as a benchmark, and developed rules of thumb for how many normal modes must be retained for sufficient prediction of the natural frequencies and damping ratios [38]; it was found that modes with frequencies up to 5× the maximum rotor speed must be included for accurate determination of critical speeds. Wang and Kirkhope applied the complex form of CMS from [35] the same dual-rotor system, but found that conventional CMS was sufficiently accurate as long as the damping ratio does not exceed 70 % [39].

2.2 Rolling-element bearings

Bearings are a critical component of a rotating machine, since they support the rotor and allow it to rotate. Rolling-element bearings (REB) are widely used in heavy machinery, and are chosen for their high load capacity and low friction [19]. Although hydrodynamic bearings also possess these properties so are often used in turbo-generators, they are unable to resist axial, out-of-plane or static radial loads so are not suitable for jet engines. Therefore the focus of this review will be on REBs. Every REB consists of 3 main components: multiple rolling elements, a cage which keeps the elements circumferentially

separated, and finally 2 races (or rings) on which the elements rotate. If the rolling-elements are spherical, the bearing is known as a "ball bearing", and if they are cylindrical, then the bearing is known as a"roller bearing". These are depicted in Fig. 2.6. Rolling-element bearings usually have a single row of elements, it is also possible to have a double-row arrangement as depicted in Fig. 2.7, in order to increase the load capacity of the bearing.



(a) Ball Bearing [40] (b) Roller Bearing [41]

Figure 2.6: Schematic of the 2 classes of rolling element bearing



(a) Single row [42] (b) Double row [43]

Figure 2.7: Schematic of single and double row angular contact bearings

2.2.1 Load distribution

The overwhelming majority of rolling-element bearing models from the literature build upon the work of Jones and Harris [44, 45]. This quasi-static approach models each element explicitly, and assumes that they are always in static-equilibrium; ie. the dynamics of the elements are assumed fast so are ignored. The contributions from each element can then be summed to yield the total bearing load and stiffness; for example, the discrete element loads are depicted in Fig. 2.8 for the case of an applied radial load. In the case of roller bearings each element can deflect in one direction, but in ball bearings, the elements can move in both the radial and axial directions. Ball bearings have the added

complexity that as the balls move, the contact angle between the ball and the race can change due to the curvature of the raceways [45], as depicted in Fig. 2.9.

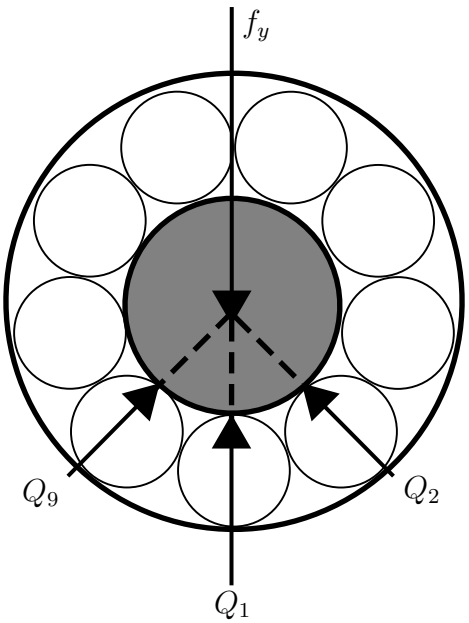
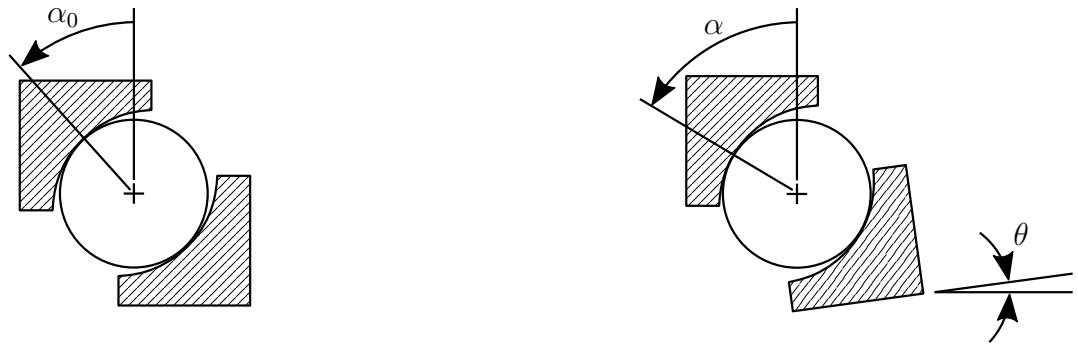


Figure 2.8: Depiction of element loads for an applied radial load

Considering each element like this allows the full stiffness matrix to be accurately captured [46], which is important for capturing the transmission of flexural shaft vibrations to the stator [47]. An approach has been presented to yield analytical expressions for the bearing stiffness matrix [48], although the derivation is involved.



(a) Initial configuration with contact angle α_0

(b) Final configuration with contact angle $\alpha > \alpha_0$

Figure 2.9: Contact angle before and after the shaft tilts by an angle θ

If the bearing can be assumed to operate at sufficiently low speeds such that inertial loads on the elements can be ignored, a concise analytical solution for the deflected position of the elements can be found [46]. Some authors have proposed a further simplification for analysing ball bearings, which is to assume the contact angle remains constant [49, 50], which can be justified if the load variation on the balls is not too high [51].

Sjovall introduced an alternative approach where the elements are “smoothed out” over

a continuous domain around the cage; examples of such a continuous load distribution are depicted in Fig. 2.11. This means that the total bearing loads must be computed by integrating the element load distribution [52]. In certain cases, this allows an analytical expression for the bearing stiffness to be found [52]. Houpert extended this approach to deal with out-of-plane deflections [49]. However, this analysis neglected dynamic effects, and is unable to capture "variable compliance" effects discussed later.

2.2.2 Contact stiffness

The most significant source of compliance in a REB is from the contacts, which are often assumed to be Hertzian. The contact force Q is related to the deflection δ by a power law:

$$Q = C\delta^n \tag{2.2}$$

where the exponent n is $\frac{10}{9}$ for roller bearings with line contacts, and $\frac{3}{2}$ for ball bearings with point contacts [19]. The coefficient C will depend upon the elastic properties and radii of the elements and races. This is simple to compute when the contact surfaces are flat (which is the case for most roller bearings), but when the raceways are curved (which is the case for ball bearings) a more complex formula involving elliptical integrals must be used [19]. Houpert developed a more accurate way to tabulate these values [53]. For roller bearings, there will be an additional stiffness term as the roller rotates into the contact. The most rigorous approach is to employ FE analysis, but a simplified method involves splitting the roller into multiple slices and applying the standard results for line and point contacts to each [45, 54]. This is shown in Fig. 2.10.

2.2.3 Internal clearance

One of the biggest non-linearities in REBs is clearance between the elements and the races [56–59]. The region of the bearing where the elements are loaded is referred as the "loaded zone", which is depicted in Fig. 2.11. When the clearance is large, some of the elements are unloaded, so the size of the loaded zone is reduced [60], as shown in Fig. 2.11b. However, the bearings can be preloaded in some way to counteract this, which increases the size of the loaded zone, as shown in Fig. 2.11c. In the case of an angular contact ball-bearing or tapered roller-bearing, this can be done by applying a constant axial load. For purely radial bearings, this can be achieved with an interference fit. However, in many machines such as jet engines, clearance may be necessary to accommodate thermal expansion. It has been demonstrated that clearance can reduce the number of loaded elements, which reduces the bearing stiffness [60].

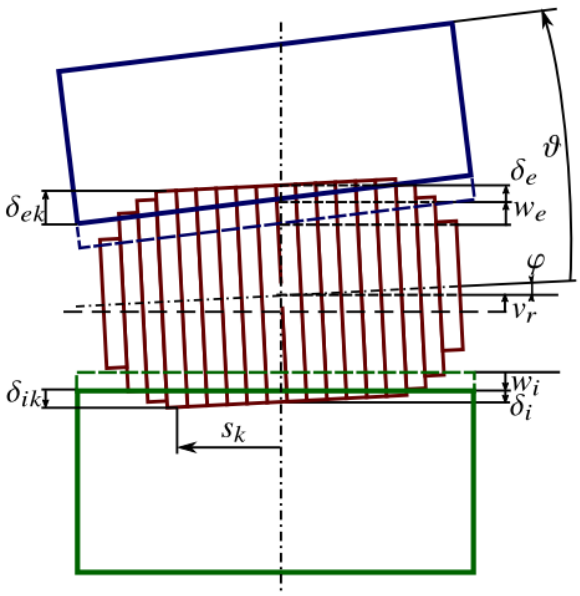
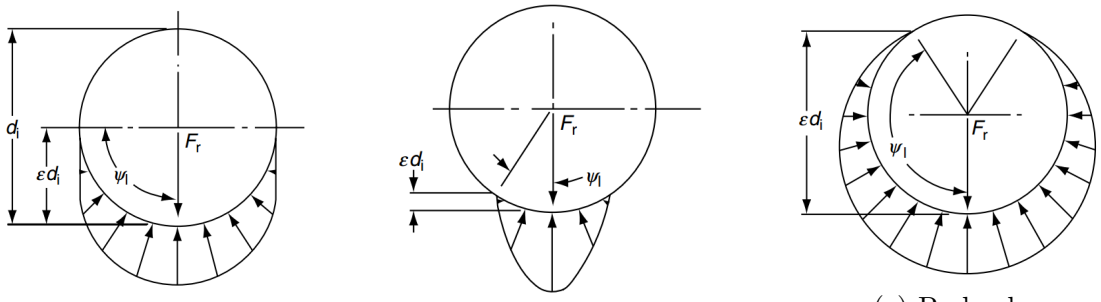


Figure 2.10: Roller slicing technique for predicting out-of-plane stiffness [55]



(a) No clearance or preload (b) Clearance (c) Preload

Figure 2.11: Size of the loaded zone for different levels of clearance [19]

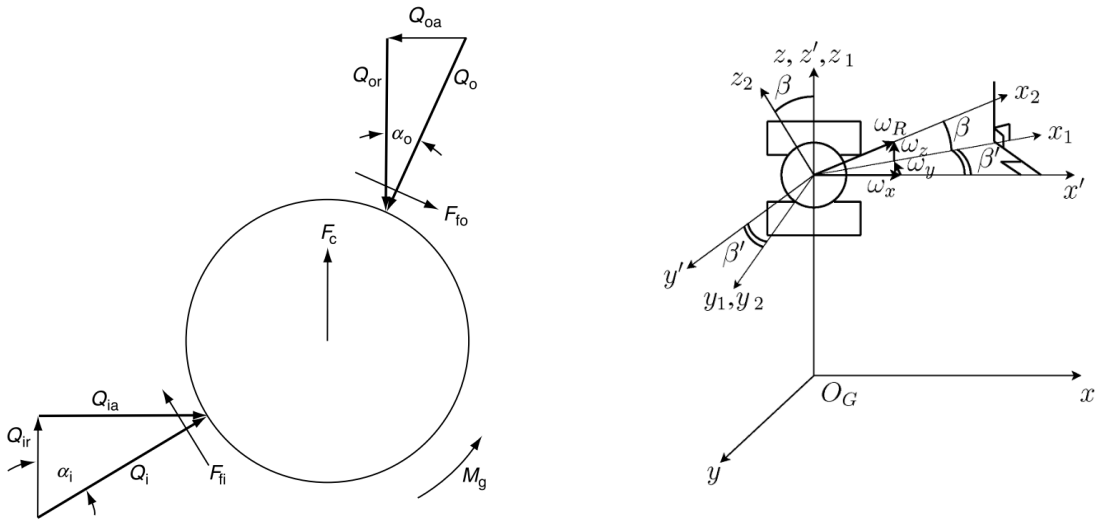
Harris [45], Lim and Singh [46] and Houpert [49] all demonstrated how to extend their respective approaches to include radial clearance by including an offset when computing the contact deformations. Such models have been used to analyse the effect of the clearance on the linearised bearing stiffness. Lim and Singh showed that the bearing can be locally unstable when the clearance is large [47]. Royston and Bosdogan showed that for self-aligning ball bearings, the radial/axial coupling is amplified by any clearance [61], since the balls become more heavily loaded on one row than the other.

Many studies have also focused on the non-linear effects of bearing clearance on the dynamics of simple rotating machines. Saito simulated a model of a flexible rotor mounted on bearings to investigate the effect of radial clearance. A simplified bearing model was used which had a power law to model the Hertzian stiffening and a deadband to model the clearance. This analysis showed that the clearance introduces changes in the resonance frequencies as well as jump phenomena [62]. In the extreme case, chaotic responses can be observed [63, 64], which are heavily dependent on the applied preload

[65]. Ehrich used a piece-wise linear bearing model to show that clearance is a possible cause of supercritical sub-harmonic [56] and sub-critical super-harmonic [57] responses, with chaotic regimes at frequencies between these regions [66]. The numerical model displayed qualitatively similar behaviour to experimental vibration data from industrial turbomachinery. Although the impact of the bearing clearance on the rotor response is well recorded in the literature, there is only a limited understanding of the underlying physical mechanisms that drive these phenomena.

2.2.4 Dynamic loads on the elements

As the bearing cage rotates, the elements will experience an outward centrifugal load. In the case of ball bearings, the elements can also experience a gyroscopic moment, but these typically have less influence than the centrifugal loads [45]. These loads are depicted for the case of a ball bearing in Fig. 2.12a. The dynamic loads can significantly alter the bearing stiffness [45], since they alter the load distribution between the inner and outer contacts as well as the contact angle in ball bearings.



(a) Dynamic loads on a ball [45]

(b) Ball velocities [67]

Figure 2.12: Dynamic loads and velocities of a ball element

The most rigorous approach to incorporate the effect of these dynamic loads into the model is to introduce extra internal states for the position of the element (1 for rollers, 2 for bearings) [44]. These internal states can then be solved for by solving for radial and axial equilibrium of each element, using an iterative procedure like Newton-Raphson. Once the equilibrium position of each element is found, the contact loads can be computed using the elastic law. In the case of a ball bearing, if the loads are not too high, it is possible to assume the contact angle remains constant and that frictional loads will laterally restrain the balls, so that it can be analysed in the same way as a roller bearing.

If it is further assumed that the centrifugal loads do not change the load distribution between the inner and outer contacts, an approximate analytical solution can be found [51].

Computation of the dynamic loads requires knowledge of the velocities of the elements, which are depicted in Fig. 2.12b. The orbital speed is the speed of the ball CoG around the bearing axis, denoted by ω_x. The spin speed is the speed of the ball about the radial axis, denoted by ω_z. The most rigorous approach for computing these velocities is to incorporate them as additional internal states in the model, and explicitly model the frictional loads at the contacts [45]. However, such a frictional model is normally not available, so another approach is to apply a hypothesis so that these speeds can be computed purely from kinematics. In the case of ball bearings, the most common approach is the "Control Theory" hypothesis from Jones [44], which states that there is either no slip at the inner or the outer contact. This choice is not always valid and should be verified experimentally before it is used [68], but it is often a good approximation [45]. Other alternative relations have been proposed, such as assuming the same spin-to-roll ratio at each contact [68] or by using d'Alembert's principle [69]. This hypothesis can also be used to distribute the frictional loads due to the gyroscopic moment on ball bearings between the inner and outer contacts [45, 68].

It has been demonstrated that these loads can lead to a reduction in the radial bearing stiffness with increasing speed [68, 70, 71] and an increase in the effective clearance [72]. However, Noel showed that the different kinematic hypotheses used to calculate the element speeds and ultimately dynamic loads, can lead to differences in the bearing stiffness by up to 10% [68]. Fang et al. demonstrated that the reduction in stiffness with speed cannot be counteracted by axially preloading the bearing [71]. A few studies have included such dynamic loads when investigating the nonlinear dynamics of a rotor system [73–76], but no comparison was made between the behaviour with and without them. Therefore there is little understanding of the specific influence of these dynamic loads on the dynamics of rotating machines.

2.2.5 Ring compliance

The inner and outer rings of the bearing are normally assumed rigid, which is often a valid assumption if the bearing is supported by a rigid housing. However, in some machines such as jet engines, the support structures and casings around the bearings are quite soft in order to minimise weight, so the compliance of the housing may be significant. The compliance of the rings can also be exacerbated by radial clearance between the rings of the bearing and the housing. An example of the ring deflection in the case of an applied radial load is shown in Fig. 2.13. It has been shown that ring compliance can significantly

change the load distribution between the rolling elements [77], leading to a reduction in the peak ball load [55, 78].

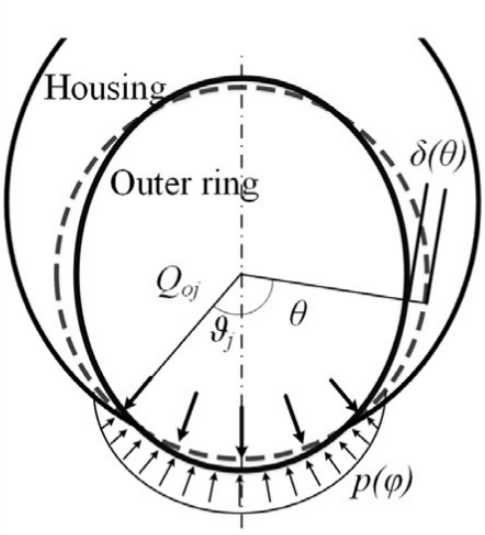
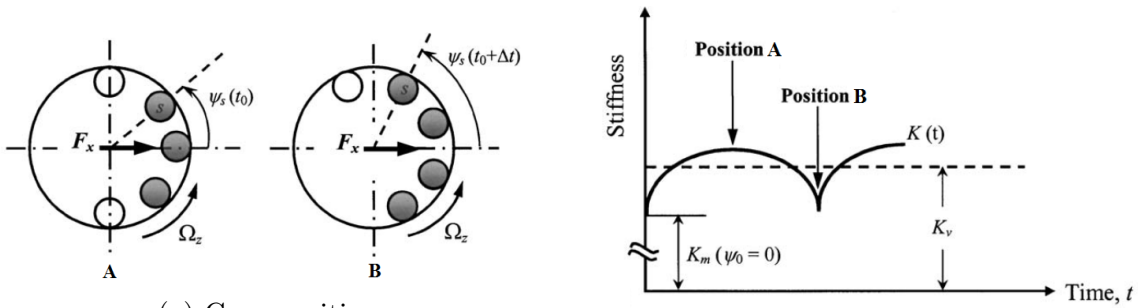


Figure 2.13: Compliant ring deformation under radial load on bearing [79]

The ring compliance will couple the equations for equilibrium of all the elements making the problem harder to solve, but characterising the ring compliance is also difficult. One approach is to approximate the ring deformation to a point load from one of the balls with a Fourier basis, but only include a few harmonics [78]. Wensing presented a more sophisticated approach based on CMS which included the inertia of the outer ring [80]. Another approach is to use a FE model with a coarse mesh, so it is no longer necessary to use model reduction techniques [81]. This analysis was entirely quasi-static, but the effect of clearance between the outer race and housing was also considered. Leontiev showed that if it can be assumed that the bending strains are negligible, ring compliance can be modelled as a spring in series with each element, so the equations for each element remain decoupled [55]. Whilst it is understood that ring compliance alters the load distribution in the bearing, little is known about the influence in rotor-bearing systems. It has been shown that ring flexibility can attenuate the higher harmonics in the response [82], but the ring compliance is otherwise usually neglected.

2.2.6 Variable compliance

The global bearing stiffness is determined by the contribution from each element, and this will be constant in a frame rotating with the cage. However, the compliance in the inertial frame will vary due to the motion of the cage and elements, which is known as "variable compliance" (VC). For example, the vertical stiffness is typically largest when there is an element directly under the shaft, but is at its lowest value when there are elements either side. This is depicted in Fig. 2.14. The compliance will vary at the Ball



(a) Cage position

(b) Time history

Figure 2.14: Depiction of the variable compliance in REBs [94]

Pass Frequency (BPF) [83, 84], which is related to the cage speed and the number of elements in the bearing.

Many studies have analysed the radial dynamics of a rotor supported by a REB under constant radial load, and it has been shown that harmonics of the BPF can appear in the rotor response [11, 75, 85, 86], and sometimes even chaotic behaviour can arise [75, 87, 88]. Mevel et al. demonstrated that chaos can arise due to an interaction of the 2nd harmonic of the shaft speed and the BPF [87]. However, While [60] demonstrated that if a sufficiently static radial load is applied, the variation in stiffness can be less than 0.5 % so this effect becomes negligible. It is then possible to use a Sjovall integral-based formulation to compute the stiffness [49, 52, 89]. However, this is no longer the case when there is large dynamic loading from a rotor unbalance [90].

It has been shown that in rotor-bearing systems, the variable compliance leads to a resonance where the BPF crosses the natural frequency of the rotor. Increasing the number of elements has been found to increase the natural frequency of the rotor due to an increase in overall bearing stiffness [91, 92]. However, the frequency of BPF excitation also increases, so that the resonance associated with VC occurs at a lower frequency [92]. Tomović demonstrated using a purely analytical approach with a simplified bearing model that the magnitude of the variable compliance increases with the clearance, and decreases with the number of loaded elements [93]. In addition, it was found that increasing the radial preload reduces the effect of the variable compliance excitation, which was also found by Aktürk using a more conventional quasi-static bearing model [92]. However, no studies were found to consider the influence of other parameters, such as dynamic loads on the elements or ring compliance, on the significance of the self-excitation from variable compliance.

2.2.7 Damping

Rolling-element bearings are typically quite lightly damped components [5], but nonetheless they can still be a source of energy dissipation in a rotating machine [95]. It has been observed that roller-bearings typically have larger levels of damping than ball-bearings, which is attributed to the line contacts [96]. It has also been shown that the damping increases with the number of elements [97,98]. However, the damping within REBs is much less well-understood than the stiffness, so many studies either estimate an equivalent linear damping term based on the literature [65,86,99,100], or simply neglect it [92,101,102].

One of the major sources of damping in a bearing is the lubricant film around the elements, which can introduce viscous losses [98]. The contacts then operate in what is known as the "elasto-hydrodynamic" (EHD) regime [99]. As an approximation, the fluid film can be assumed stiff, so its primary effect is to reduce the effective clearance between the ball and the races [45,99]. The most common way to compute the film thickness is to use the non-dimensionalised relations from Hamrock and Dowson [103].

To include the damping effect from the fluid film, the most common approach is to fit a linearised damping constant to detailed simulations on a single lubricated contact [104, 105], although load dependent models have also been proposed [75, 106]. Another approach is to incorporate the EHD physics into the bearing model [91, 107]. Nonato et al. showed that the EHD film has a tendency to reduce the rotor deflection to a constant radial load, but also attenuates some higher harmonics [105]. This approach has been used to model the bearing damping in an experimental test rig, and it was found that the size of the orbit was accurately predicted [108]. The lubricant also leads to drag forces and churning moments on the elements although this is mostly relevant when computing power losses [83], and controlling cage instabilities [109–111].

In experiments, it has been found that the damping from the lubricant can reduce with rotation speed [97,112]. However, it has also been shown that there is a strong dependence on the bearing temperature [113]. Some studies have found that a radial preload reduces the damping [97, 112], while others found that it was insensitive to preload [98]. In general, it can be said while it is trivial to incorporate the damping from EHD into the model, the effect of the lubricant appears to be complex and it remains very hard to accurately predict the overall contribution to the bearing damping [96].

Another major source of damping are the joints between the bearing and its housing and the shaft passing through it [96]. Walford and Stone demonstrated that a bearing model with damping from *only* from the lubricant significantly under-predicts the damping measured from experiments [114]. It was later demonstrated experimentally using a test rig, in which the bearings could be replaced with rigid blocks, that the joints around the bearing can provide up to 10× the damping from the bearing itself [115]. It has been

proposed that the other possible damping mechanism is material damping due to the deformation at the Hertzian contacts [98, 99]. However, this is believed to have a much less significant contribution than the lubricant and joints [98, 114].

2.2.8 Experimental investigations

There is large body of research into developing approaches for experimentally determining the bearing stiffness and damping. There are broadly three main approaches, which will now be explained in more detail.

2.2.8.1 Impact tests

A common approach to indirectly detect the bearing stiffness and damping is to carry out a hammer test on the rotor it supports. Kraus used modal analysis on a stocky rotor to determine the axial and radial bearing stiffness and damping by trying to match the natural frequencies and damping ratios [116]. The effect of speed and axial preload were considered. It was found that the dynamic stiffness was very similar to the static stiffness. Zeilinger used a similar approach to quantify the sources of damping in a bearing [115]. It was found that some damping arises from the Hertzian contacts and can be modelled with a loss factor, whilst much more damping is due to the housing interface which increases with preload and is more complex to model. Knaapen extracted FRFs using hammer tests on a short shaft mounted on a single bearing for different levels of axial preload [117]. The diagonal stiffness and damping terms were found by fitting a model to the FRFs. It was also found that the damping increased with preload. Gunduz et al. considered the axial dynamics of a rigid rotor and examined the effect of the axial preload on the FRF from hammer tests [118]. The limitation of this approach is that only linearised bearing parameters can be extracted.

2.2.8.2 Harmonic excitation

Another approach is to harmonically excite the bearing. Walford applied a harmonic force using a shaker to a shaft-bearing system with 2 bearings and measured the radial stiffness and damping for a range of rotation speeds and forcing amplitudes [95]. Luo measured bearing stiffness dynamically using a stocky rotor and applying an unbalance mass [119]. This was carried out for different preloads and rotation speeds, and there was found to be good correlation with a quasi-static bearing model. Jacobs et al. measured the radial stiffness of a DGBB using shakers [113], considering the influence of cage angular position, rotation speed and fluid film thickness. It was found that the damping varies by up to 24 % with speed. Royston extended this approach by applying both axial and

radial excitation to a self-aligning REB using shakers, and considered the effect of both axial and radial preload on the dynamics [61]. As with the experiments using impact excitation, all of these studies identified only the local linearised bearing properties.

2.2.8.3 Static loading

Although the nonlinear bearing stiffness characteristic can be identified indirectly by finding the variation of the linearised bearing stiffness with preload, the non-linear bearing stiffness can be measured directly with static loading. Lacroix et al. investigated the axial stiffness of a 4-point bearing using a compression test machine and found good correlation with an FEA model of the housing coupled with Hertzian elements [120]. De Mul measured the nonlinear radial stiffness of a cylindrical roller bearing by statically loading the bearing [121]. Jin et al. applied a static radial load to a bearing on a rigid rotor, as shown in Fig. 2.15b, to measure the non-linear load-displacement relation [122]. However, none of these studies measured the radial or axial clearance, since the bearing was only loaded in one direction, so the clearance was taken up.

2.2.9 Summary

From the literature review, it can be seen that there is a well-established approach for modelling the elastic behaviour of rolling-element bearings. The primary source of compliance in REBs is from the contacts, which have an inherently non-linear Hertzian characteristic. Clearance is another significant non-linearity, and can lead to large changes in the number of elements contributing to the stiffness. In addition, the compliance from the bearing elements varies as the cage rotates, which can lead to self-excitation, which is believed to be more significant when the preload is low.

There are a wide variety of other phenomena which can alter the bearing stiffness. Dynamic loads of the contacts alter the load distribution between the inner and outer contacts, and reduce the bearing stiffness at high speeds. The rings are normally assumed rigid, but this is not always a valid assumption. In this case, ring compliance can significantly reduce the peak loads on the elements. However, the influence of these effects in a rotordynamics context is unknown.

The damping within the bearing itself is usually low, but the damping from the joints between the housing and bearing is believed to be significant. There are no well established approaches for predicting the damping from rolling-element bearings.

2.3 Rotor-bearing test rigs

Many rotor-bearing test rigs have been developed in order to investigate the influence of rolling-element bearings on rotordynamic systems. These studies can be split into three categories; some studies consider the influence of the bearings only in the linear regime, by analysing the natural frequencies of the system. Others consider the case with larger excitation levels where the rig operates in the non-linear regime. The remainder of the studies have used experimental data from the test rig to identify unknown bearing parameters.

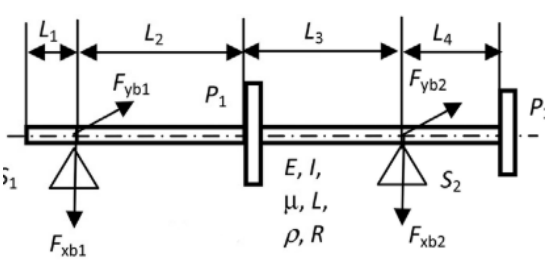
2.3.0.1 Linearised investigations

Sinou et al. experimentally tested a rotor-bearing test rig and measured the Campbell diagram [123]. This was extended to include a flexible support and the Campbell diagram was measured experimentally using asynchronous excitation with a shaker [13]. Very good correlation with the FE model was obtained. However, there was no way to measure the forces passing through the bearings. The same setup was then used to investigate the effect of bearing temperature [124] and damping from rubber pads [125]. Guskov et al. extended the same test rig to consider the case of a dual-shaft configuration [7] where the rotors were co-rotating. The rotors were concentric but axially offset from one another (see Fig. 2.16b) which has the advantage that the shaft deflections can be measured along the whole length.

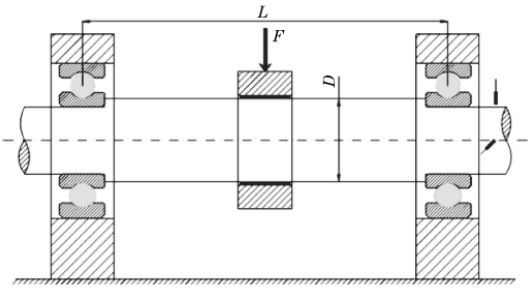
Gupta et al. looked at the unbalance response of a similar dual-shaft test rig [21] where the rotors were counter-rotating as shown in Fig. 2.16a. The results were compared to a numerical model using the Transfer Matrix method and a linear bearing model. Quasi-periodic responses were observed in some regions due to the cross-excitation.

2.3.0.2 Non-linear investigations

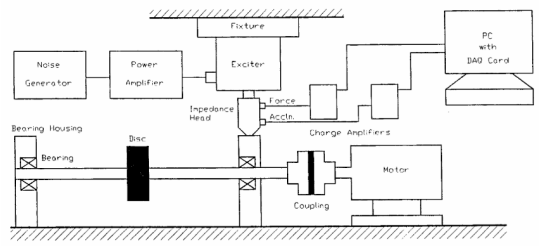
The response of rotor-bearing systems in the lightly non-linear regime has also been considered. Bai et al. investigated the non-linear dynamics of a rotor-bearing system with a single disc shown in Fig. 2.15d. Sub-harmonic excitation was observed leading to a resonance above the critical speed, which matched the predictions from a non-linear model well [128]. This was investigated in more detail in [129]. Jin used the same test rig as earlier static bearing experiments from Fig. 2.15b to investigate the unbalance response. The model demonstrated a qualitatively similar non-linear response to experiments, with similar spectra and jump phenomena [130]. A sub-critical resonance due to forcing at the BPF was observed, and this was investigated in more detail in [131] using the same rig.



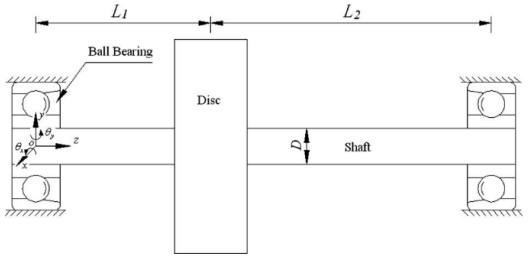
(a) Chen et al. [126]



(b) Jin et al. [122]

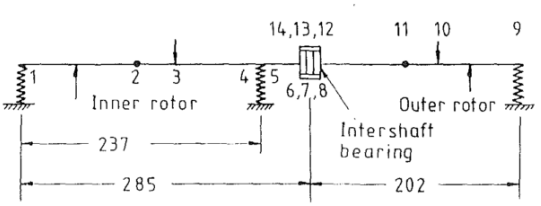


(c) Kahn et al. [127]

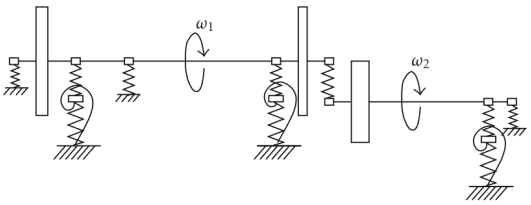


(d) Bai et al. [128]

Figure 2.15: Schematics of existing single-rotor test rigs



(a) Gupta et al. [21]



(b) Guskov et al. [7]

Figure 2.16: Schematics of existing dual-rotor test rigs

Other studies have considered the behaviour in the extremely non-linear regime, by introducing very strong non-linearities into the supports. Chen considered a simple 2-disk rotor-bearing system as shown in Fig. 2.15a. This was first used to validate a rotor model [126]. The model was then used to investigate the effect of a large clearance between the bearing and housing on the response, and this was compared to the experimental data [132]. It was found that the response of the test rig contained super-synchronous content at the same frequencies predicted by the simulations. Mevel et al. investigated the routes to chaos in rotors supported by very loose REBs on an experimental test rig [84]. It was found that the rig response contained components at the same sub-harmonics of the BPF and displayed a similar transition to chaos as the simulations from [87].

It can be said that although many experimental studies have been carried on non-linear rotor-bearing systems containing REBs, very few quantitative comparisons have been made with numerical models. In some studies, it appears limited effort has been put into parameterising the model first, even in the linear regime. In other studies, the behaviour

is analysed in a regime where the response is extremely non-linear and chaotic, so that the behaviour is very sensitive to the parameters. This makes correlation very difficult, and is not representative of most industrial rotating machines.

2.3.0.3 Model updating

Since the bearing properties are often difficult to estimate a priori, much attention has been paid to methods to update the bearing parameters to match experimental data. Edwards et al. identified the linear bearing parameters from a run down on a different test rig [133], which was later used by Tiwari to identify the linear speed-dependent bearing parameters [134]. Čermelj tuned the bearing stiffness to match an FRF obtained from an impact in least-squares sense [135]. Chouksey updated the bearing stiffness and rotor parameters using impact hammer tests [136]. Sinou and Guskov tuned the bearing tilting stiffness in an FE model of a machine, in order to minimise the least-squares error in the natural frequencies [7, 13].

It has also been shown to be possible to identify nonlinear bearing stiffness from experimental data using simplified bearing models. Tiwari et al. used random excitation of a single disk system to identify the unknown bearing stiffness [137], assuming the bearing force has linear and cubic terms. This was then extended to the case where there is additional unbalance forcing [138], and to include the effect of the shaft compliance [139]. Kahn [127] and Chatterjee [140] used the same experimental setup, shown in Fig. 2.15c to extract the non-linear bearing stiffness using Volterra series. However, no studies were found to identify the parameters of a physical bearing model.

2.4 Simulation methods

Once an accurate model of a rotor-bearing system has been developed, the most obvious use is to predict the forced response of the system. If the system is linear, the frequency response can be computed analytically from the matrices governing the equations of motion. However, it was shown in Section 2.2 that REBs are inherently non-linear components, so alternative techniques are required to compute the forced response numerically.

2.4.1 Time-integration

Time-integration remains the most common technique for analysing non-linear rotor-bearing systems [11, 65, 72, 75, 82, 86–88]. This approach allows all forms of non-linear dynamic responses to be captured, including periodic, quasi-periodic and chaotic rotor responses since no assumptions are made about the nature of the response. In addition,

it is simple to incorporate models which display time-dependence, which is the case with rolling-element bearings due to their variable compliance. The most widely used methods were found to be the Runge-Kutta [59, 72, 85, 92, 141, 142], and Newmark-Beta [75, 101, 106, 143–145] algorithms. The time step is the only parameter which must be selected, although care must be taken to ensure the method is stable. However, time-integration comes at a high computational cost, especially for stiff systems where a small time-step is required.

2.4.2 Harmonic-balance method

An alternative, more efficient approach was consequently developed, known as the Harmonic Balance Method (HBM) [146]. This is a Galerkin method, whereby the response is assumed to be the sum of a set of basis functions. In the case of HBM, a Fourier basis is chosen, which thereby allows the steady-state periodic response to be found directly. However, care must be taken to include a sufficient number of harmonics. This has been used to simulate rotors with a wide variety of types of non-linearity including bearings with clearance [59, 62], squeeze-film dampers [147–149] and rolling-element bearings [64, 102, 150].

Conventional HBM cannot capture quasi-periodic responses, which are common in rotor-bearing systems due to the variable compliance of the rolling-element bearing, or excitation from another rotor. The Generalised HBM (GHBM) overcomes this limitation and is able to additionally capture quasi-periodic responses very efficiently [151], by introducing a second base frequency, but this increases the computational complexity. So far, this technique has been applied primarily to rotor systems with simplified non-linear bearing models [152, 153], or systems with multi-harmonic excitation [154, 155]. More recently the GHBM has been applied to a dual-shaft system with a physical REB model, where the two base frequencies were the speeds of the two rotors [156].

2.5 Summary

The lateral dynamics of rotors are well understood. Centrifugal forces can lead to synchronous harmonic excitation, but rotors can also experience asynchronous vibration to which the response can be speed dependent. Gyroscopic forces cause the frequencies of the modes to bifurcate with speed. There are many techniques for modelling rotors with compliant shafts, although the finite element method is most common, and component mode synthesis can be applied to reduce the number of DOF.

Modelling of REBs has been the subject of much research because of their wide usage, and most models are now based upon the same quasi-static framework. Bearings are non-

linear in nature, primarily due to their clearance and Hertzian contacts. It has been shown that rotor-bearing systems containing REBs can display highly non-linear responses, including jump phenomena or even chaos. There are many additional phenomena within the bearing which influence the bearing stiffness, such as dynamic loads on the elements and ring compliance. However, there is a very limited physical understanding of how the different bearing parameters influence the non-linear response of rotor-bearing systems.

There have been a few experimental studies into the dynamics of rotor-bearing systems. However, most existing studies have focused on linear analysis. Very few of those that have investigated the response in the non-linear regime have made any quantitative comparisons to numerical models. Therefore, there is a need to investigate the influence of the bearing non-linearities experimentally using a more scientific approach.

The application of the harmonic balance method to rotor-bearing systems is now well established. This can be used to simulate the frequency response of non-linear systems in an efficient manner. However, the more complex Generalised HBM which can capture quasi-periodic response is only starting to be applied within the field of rotordynamics.

Chapter 3

Background theory

This thesis aims to investigate the influence of rolling-element bearings on rotating machines, and therefore models of both rotors and the bearings which support them are required. In Section 3.1, a rotor model based on the well-established Finite Element method will be presented. A high-fidelity bearing model will then be presented in Section 3.2, which is based on the widely-used quasi-static approach.

These models will require efficient numerical methods to be able to compute the forced response of such systems in an efficient manner. The Generalised Harmonic Balance Method (GHBM) will be introduced in Section 3.3, which is able to solve directly for periodic and quasi-periodic responses.

3.1 Finite-element rotor model

This thesis will focus on the influence of bearing non-linearities on the lateral-dynamics of rotating machines, rather than the dynamics of the rotor itself. Therefore, in both the numerical and experimental studies, only simple rotors will be considered. Therefore, a 1D FE modelling approach was sufficient, which will now be briefly summarised.

3.1.1 1D Mesh

The first stage in the creation of the FE model is to specify the location of the nodes, and the elements connecting them. Rotor, stator and joint elements will now be introduced.

3.1.1.1 Rotor elements

In this thesis, a rotor consists of zero or more compliant shaft sections, along which discs may be mounted. Multiple nodes should be placed along each shaft, with nodes at

the disc roots. Compliant shaft elements span each adjacent pair of nodes. A sufficient number of nodes should be placed along each shaft section, in order to accurately capture the influence of the shaft compliance and inertia. Suitable nodal locations are depicted in Fig. 3.1.

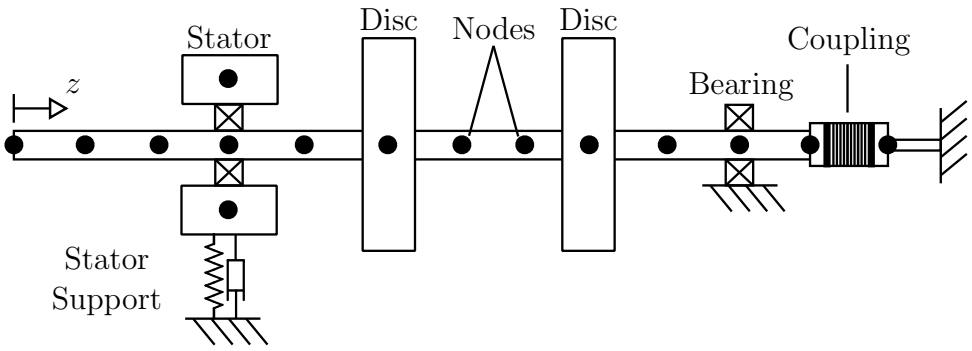


Figure 3.1: Example of a 1D mesh of a rotor

3.1.1.2 Stator elements

Stator elements can be used to model the non-rotating components supporting the rotor. In general, the stator can be a flexible structure with its own dynamics. However, it was assumed here that their natural frequency was significantly higher than the running range of the machine, so that they could be modelled as lumped masses. An example of a stator is shown on the left within Fig. 3.1. Typically the stator node will be chosen to align with the CoG of the stator, but this is not mandatory.

3.1.1.3 Joint elements

Joints make up the last type of element within the FE model. Within the FE model, a joint is defined as an elastic connection between one rotor or stator to another rotor or stator node, or to ground. This general definition means that a joint encompasses a wide variety of components including:

- Couplings between two shafts
- Compliant structures supporting a stator element
- Rolling-element bearings

These are all depicted in Fig. 3.1. Nodes must be placed on the rotor and stator at the points connected by each joint.

3.1.1.4 Nodal displacements

In the most general case, each node along the shaft will have 6 DOF; there will be 2 lateral DOF in the vertical plane, a further 2 lateral DOF in the horizontal plane, and 1 axial and 1 torsional DOF. In some rotating machines, the lateral, torsional and axial dynamics can be inherently coupled together. For example, the lateral dynamics can couple with the torsional dynamics if the system is driven by helical gears [157, 158]. However, for the cases considered in this thesis, the lateral dynamics will be decoupled from the torsional and axial dynamics. Therefore it is only necessary to include 4 lateral DOF per node, as depicted in Fig. 3.2.

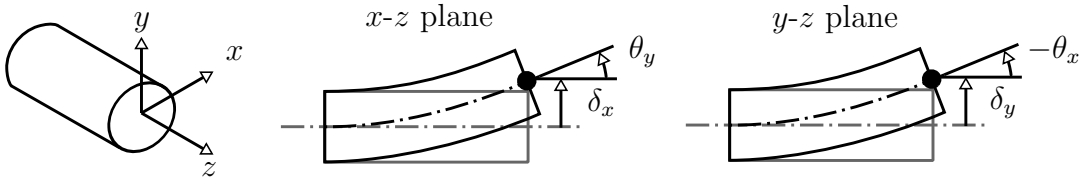


Figure 3.2: Lateral DOF at each node

The translations in the horizontal and vertical directions are denoted by δ_x and δ_y respectively, and θ_x and θ_y are the rotations around each of these axes. It will be convenient to introduce the following vector of nodal displacements:

$$\boldsymbol{x}_{\text{nodal}} = \begin{bmatrix} \delta_x & \delta_y & \theta_x & \theta_y \end{bmatrix}^T \tag{3.1}$$

Note that these coordinates have been specified in the inertial frame, and therefore the coordinates do not rotate with the rotor. Any anisotropic joints will have constant properties within this frame of reference, which simplifies the analysis and ultimately makes linear analysis possible [2]. For example, rolling-element bearings are typically stiffer in the vertical direction than the horizontal direction [5]. However, this choice of reference frame does restrict the analysis to systems with axisymmetric rotors, since asymmetric rotors will have time varying properties in the inertial frame. Now that the nodal DOF have been defined, attention can move onto defining the matrices of the rotor, stator and joint elements.

3.1.2 Rotors

In this thesis, rotors were modelled with a combination of compliant shaft elements, and rigid disc elements. Shafts are continuous entities, and therefore the process of determining their mass and stiffness matrices is more complex, whereas the matrices for solid discs can be specified analytically. This will now be discussed in more detail.

3.1.2.1 Shafts

Shafts can be modelled with beam elements, each of which spans between two nodes. There are three types of commonly used beam element, of varying complexity [159]:

- Euler-bernoulli elements which neglect shear deformations and rotational inertia
- Rayleigh elements which neglect shear deformations, but include rotational inertia
- Timoshenko elements which include both shear deformations and rotational inertia

For slender shafts, the shear deformations are small so Euler-Bernoulli and Rayleigh elements will give very similar results to the more complex Timoshenko elements. However, the shafts in rotating-machinery are often relatively stocky so that the shear deformations can become significant, so that it is recommended that Timoshenko elements are used [2]. Although the derivation of the matrices for the Timoshenko elements is more complex, there is no additional computational cost when calling the resulting model. For these reasons, Timoshenko beam elements were used to model the shaft.

Shaft coordinates Since this thesis will only consider axisymmetric shafts, it is convenient to analyse the flexure in the $x-z$ and $y-z$ planes separately, since they will be elastically decoupled. For example, the 1D beam element in Fig. 3.3 shows the flexure in a single plane.

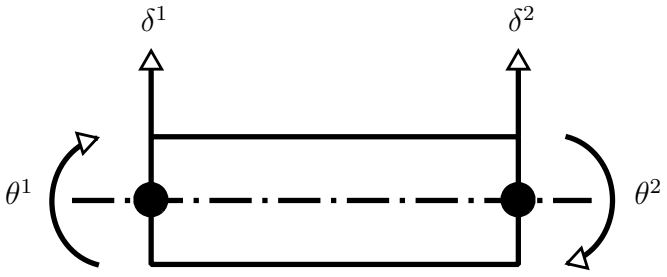


Figure 3.3: 1D beam element

Since it is necessary to use quadratic element for flexural problems, there are 2DOF at each node. The displacement vector is then defined as:

$$\boldsymbol{u} = \begin{bmatrix} \delta^1 & \theta^1 & \delta^2 & \theta^2 \end{bmatrix}^T \tag{3.2}$$

The displacement vectors in each plane can then be stacked together, to yield the displacement for the complete shaft element:

$$\{\boldsymbol{x}_s\}_{\text{elem}} = \begin{bmatrix} \boldsymbol{u}_x \\ \boldsymbol{u}_y \end{bmatrix} \tag{3.3}$$

The stiffness, mass, damping and gyroscopic matrices will now be presented.

Stiffness matrix The stiffness matrix of the Timoshenko element can be found by performing an integral of the potential energy over the element using quadratic basis functions. The derivation will not be reproduced here, but the final stiffness matrix has the following form:

$$\{\boldsymbol{K}_s\}_{\text{elem}} = \begin{bmatrix} \boldsymbol{K} & \boldsymbol{0} \\ \boldsymbol{0} & \boldsymbol{K} \end{bmatrix} \tag{3.4}$$

which can be observed to be block-diagonal, since the elastic forces do not couple the two planes. The submatrix $\boldsymbol{K}$ is the stiffness matrix of the 1D beam element in a single plane, shown in Fig. 3.3, which is given by [2, 24]:

$$\boldsymbol{K} = \frac{EI}{(1+\phi_e)l_e^3} \begin{bmatrix} 12 & 6l_e & -12 & -6l_e \\ 6l_e & (4+\phi_e)l_e^2 & -6l_e & -(4+\phi_e)l_e^2 \\ -12 & -6l_e & 12 & 6l_e \\ -6l_e & -(4+\phi_e)l_e^2 & 6l_e & (4+\phi_e)l_e^2 \end{bmatrix} \tag{3.5}$$

where E is the Young's modulus of the shaft, I is the second moment of area of the section and l_e is the length of the element. The non-dimensional constant ϕ_e accounts for the shear deformations and is given by [2, 25, 160]:

$$\phi_e = \frac{12EI}{\kappa G A l_e^2} \tag{3.6}$$

where G is the shear modulus, given by $G = \frac{E}{2(1+\nu)}$ where ν is the Poisson's ratio of the shaft. The non-dimensional constant κ depends on the cross section of the shaft. Only cylindrical shafts will be considered in this thesis, for which κ is given by [161]:

$$\kappa = \frac{6(1+\nu)\left(1+\mu^2\right)^2}{(7+6\nu)\left(1+\mu^2\right)^2 + (20+12\nu)\mu^2} \tag{3.7}$$

where $\mu = \frac{r_o}{r_i}$. If the effect of shear deformations is to be neglected, the parameter ϕ_e can simply be set to 0, which reduces the Timoshenko element to an Euler-Bernoulli element.

Mass matrix The mass matrix of the element can be calculated by performing another integral over the element, this time on the kinetic energy. The resulting mass matrix has the following block diagonal form, since the inertial forces, like the elastic forces, do not couple the two planes:

$$\{\boldsymbol{M}_s\}_{\text{elem}} = \begin{bmatrix} \boldsymbol{M} & \boldsymbol{0} \\ \boldsymbol{0} & \boldsymbol{M} \end{bmatrix} \tag{3.8}$$

where the submatrix $\boldsymbol{M}$ is given by:

$$\boldsymbol{M} = \boldsymbol{M}_{trans} + \boldsymbol{M}_{rot} \tag{3.9}$$

where the first term is due to the translation of the element, and the second term is due to the rotation of the element. This second term is neglected in Euler-Bernoulli theory, but included in Rayleigh and Timoshenko beam theory [159]. These matrices have the following form:

$$\boldsymbol{M}_{trans} = \frac{\rho A l_e}{840(1+\phi_e)^2} \begin{bmatrix} m_1 & m_2 & m_3 & m_4 \\ m_2 & m_5 & -m_4 & m_6 \\ m_3 & -m_4 & m_1 & -m_2 \\ m_4 & m_6 & -m_2 & m_5 \end{bmatrix} \tag{3.10}$$

$$\boldsymbol{M}_{rot} = \frac{\rho I}{30(1+\phi_e)^2 l_e} \begin{bmatrix} m_7 & m_8 & -m_7 & m_8 \\ m_8 & m_9 & -m_8 & m_{10} \\ -m_7 & -m_8 & m_7 & -m_8 \\ m_8 & m_{10} & -m_8 & m_9 \end{bmatrix} \tag{3.11}$$

where the terms m_1 to m_9 depend on ϕ_e. They have not been reproduced here for brevity, but can be found in [2].

Gyroscopic matrix Since the shaft is rotating, there is an additional speed dependent term in the equation of motion, due to the gyroscopic forces on the rotor. Unlike the mass and stiffness matrices, gyroscopic forces directly couple the two planes so they must be analysed in tandem. Upon performing another integral over the element, the resulting gyroscopic matrix has the following form:

$$\boldsymbol{G}_s = \begin{bmatrix} \boldsymbol{0} & \boldsymbol{G} \\ -\boldsymbol{G} & \boldsymbol{0} \end{bmatrix} \tag{3.12}$$

which is skew-symmetric, since the gyroscopic forces couple the two planes. The submatrix $\boldsymbol{G}$ has a dense form like the mass matrices:

$$\boldsymbol{G} = \frac{\rho A I}{15(1+\phi_e)^2 l_e}\begin{bmatrix} g_1 & g_2 & -g_1 & g_2 \\ g_2 & g_3 & -g_2 & g_4 \\ -g_1 & -g_2 & g_1 & -g_2 \\ g_2 & g_4 & -g_2 & g_3 \end{bmatrix}$$

where the terms g_1 to g_4 also depend on ϕ_e, and can be found in [2].

Damping matrix Since no physical shaft damping model was available, a simple proportional damping model was used, so that:

$$\boldsymbol{C}_s = \alpha \boldsymbol{M}_s + \beta \boldsymbol{K}_s \tag{3.13}$$

This model was found to be sufficient for this thesis, since the shaft behaviour was not the focus of the analysis, and other sources of damping tended to dominate.

Gravitational load The load due to the self-weight of the shaft can be computed by multiplying the mass matrix by an appropriate acceleration vector:

$$\left\{\boldsymbol{f}_{s,g}\right\}_{\text{elem}} = \left\{\boldsymbol{M}_s\right\}_{\text{elem}} \begin{bmatrix} \boldsymbol{0} \\ \boldsymbol{g} \end{bmatrix} \tag{3.14}$$

where the acceleration vector $\boldsymbol{g}$ is given by

$$\boldsymbol{g} = \begin{bmatrix} g & 0 & g & 0 \end{bmatrix}^T \tag{3.15}$$

and g is the acceleration due to gravity.

Transformation to nodal co-ordinates The mass, stiffness, damping and gyroscopic matrices have now been defined for the shaft element. The last step is to convert from the element co-ordinates $\boldsymbol{x}_{\text{elem}}$ defined in Fig. 3.3 into nodal co-ordinates $\boldsymbol{x}_{\text{nodal}}$ which are defined as:

$$\left\{\boldsymbol{x}_s\right\}_{\text{nodal}} = \begin{bmatrix} \boldsymbol{x}_1^T & \boldsymbol{x}_2^T \end{bmatrix} = \begin{bmatrix} \delta_x^1 & \delta_y^1 & \theta_x^1 & \theta_y^1 & \delta_x^2 & \delta_y^2 & \theta_x^2 & \theta_y^2 \end{bmatrix}^T \tag{3.16}$$

The two co-ordinates are related by the following matrix transformation:

$$\left\{\boldsymbol{x}_s\right\}_{\text{elem}} = \boldsymbol{R}_s \left\{\boldsymbol{x}_s\right\}_{\text{nodal}} \tag{3.17}$$

where $\boldsymbol{R}_s$ is a transformation matrix which reorders the DOF, and is given by:

$$\boldsymbol{R}_s = \begin{bmatrix} 1 & 0 & 0 & 0 & 0 & 0 & 0 & 0 \\ 0 & 0 & 0 & 1 & 0 & 0 & 0 & 0 \\ 0 & 0 & 0 & 0 & 1 & 0 & 0 & 0 \\ 0 & 0 & 0 & 0 & 0 & 0 & 0 & 1 \\ 0 & 1 & 0 & 0 & 0 & 0 & 0 & 0 \\ 0 & 0 & -1 & 0 & 0 & 0 & 0 & 0 \\ 0 & 0 & 0 & 0 & 0 & 1 & 0 & 0 \\ 0 & 0 & 0 & 0 & 0 & 0 & -1 & 0 \end{bmatrix}$$

This transformation matrix can also be used to transform the mass, stiffness, damping and gyroscopic matrices of the shaft element into nodal co-ordinates. For example, the stiffness matrix in nodal co-ordinates is given by:

$$\{\boldsymbol{K}_s\}_{\text{nodal}} = \boldsymbol{R}_s^T \{\boldsymbol{K}_s\}_{\text{elem}} \boldsymbol{R}_s \tag{3.18}$$

and similarly the gravitational force on the element is given by:

$$\left\{\boldsymbol{f}_{s,g}\right\}_{\text{nodal}} = \boldsymbol{R}_s^T \left\{\boldsymbol{f}_{s,g}\right\}_{\text{elem}} \tag{3.19}$$

This completes the definition of the Timoshenko shaft element.

3.1.2.2 Discs

Discs can be mounted along each shaft at one of the nodes. To incorporate the effect of the compliance of the disc, it is possible to discretise it using an FE approach with annular [162] or triangular [163] elements. This is necessary to analyse systems where the discs are very thin [164–167]. However, for this thesis, only systems with thick discs were analysed, for which it is sufficient to model the discs as rigid bodies. On the other hand, the connection between the disc and shaft, known as the disc root, was assumed to have some compliance. The equation of motion for the disc can therefore be written as (in nodal co-ordinates):

$$\begin{bmatrix} \boldsymbol{M}_d & 0 \\ 0 & 0 \end{bmatrix} \begin{bmatrix} \boldsymbol{x}_d \\ \boldsymbol{x}_s \end{bmatrix} + \left(\Omega \begin{bmatrix} \boldsymbol{G}_d & 0 \\ 0 & 0 \end{bmatrix} + \begin{bmatrix} \boldsymbol{C}_d & -\boldsymbol{C}_d \\ -\boldsymbol{C}_d & \boldsymbol{C}_d \end{bmatrix} \right) \begin{bmatrix} \boldsymbol{x}_d \\ \boldsymbol{x}_s \end{bmatrix} + \begin{bmatrix} \boldsymbol{K}_d & -\boldsymbol{K}_d \\ -\boldsymbol{K}_d & \boldsymbol{K}_d \end{bmatrix} \begin{bmatrix} \boldsymbol{x}_d \\ \boldsymbol{x}_s \end{bmatrix} = \begin{bmatrix} \boldsymbol{f}_{d,e} + \boldsymbol{f}_{d,g} \\ 0 \end{bmatrix} \tag{3.20}$$

where $\boldsymbol{x}_d$ is the disc CoG displacement, and $\boldsymbol{x}_s$ is the displacement of the shaft node where the disc is mounted. The disc excitation forces are denoted by $\boldsymbol{f}_{d,e}$, and the gravitational load by $\boldsymbol{f}_{d,g}$. Since this equation of motion has already been written in nodal co-ordinates, it will not be necessary to later transform the elemental matrices.

Mass and gyroscopic matrices Since only axisymmetric discs were considered in this thesis, the mass and gyroscopic matrices $\boldsymbol{M}_d$ and $\boldsymbol{G}_d$ have a simple form. The mass matrix $\boldsymbol{M}_d$ can be written as [24]:

$$\boldsymbol{M}_d = \begin{bmatrix} m_d & 0 & 0 & 0 \\ 0 & m_d & 0 & 0 \\ 0 & 0 & I_d & 0 \\ 0 & 0 & 0 & I_d \end{bmatrix} \tag{3.21}$$

where m_d is the mass of the disc, and I_d is the diametral moment of inertia. The gyroscopic matrix $\boldsymbol{G}_d$ is given by:

$$\boldsymbol{G}_d = \begin{bmatrix} 0 & 0 & 0 & 0 \\ 0 & 0 & 0 & 0 \\ 0 & 0 & 0 & J_d \\ 0 & 0 & -J_d & 0 \end{bmatrix} \tag{3.22}$$

where J_d is the polar moment of inertia of the disc.

Stiffness and damping matrices Assuming the disc root is also axisymmetric, the root stiffness will also have the following diagonal form:

$$\boldsymbol{K}_d = \begin{bmatrix} k_\delta & 0 & 0 & 0 \\ 0 & k_\delta & 0 & 0 \\ 0 & 0 & k_\theta & 0 \\ 0 & 0 & 0 & k_\theta \end{bmatrix} \tag{3.23}$$

It was assumed the damping would have the same diagonal form.

Unbalance forces It will be assumed that any unbalances in the rotor are located at one of the discs. Denoting the unbalance mass by m_{ub}, which is placed at an angle ϕ_{ub} and radius r_{ub}, the forcing from an unbalance on the disc can be written as:

$$\boldsymbol{f}_{d,e} = \Omega^2 m_{ub} r_{ub} \Re \left(\begin{bmatrix} 1 \\ -j \\ 0 \\ 0 \end{bmatrix} e^{j(\Omega t + \phi_{ub})} \right) \tag{3.24}$$

where it has been assumed that the rotor spins about the positive z axis. The unbalance can also expressed in terms of an eccentricity of the disc CoG, denoted by ϵ. This is related to the unbalance balance mass by:

$$\epsilon = \frac{m_{ub} r_{ub}}{m_d}$$

Gravitational load As with the shaft element, the load due to the self-weight of the disc can found by multiplying the disc mass matrix

$$\boldsymbol{f}_{d,g} = \boldsymbol{M}_d \boldsymbol{g} \tag{3.25}$$

where the vector $\boldsymbol{g}$ is from Eq. (3.15). The solid disc element incorporating root compliance and unbalance excitation has now been fully defined.

3.1.2.3 Assembly

Once the stiffness, damping, mass and gyroscopic matrices of each shaft and disc element have been computed, it is then possible to assemble the matrices for the complete rotor. The elemental displacements are related to the rotor displacement vector by the transformation matrix $\boldsymbol{S}$:

$$\{\boldsymbol{x}\}_{\text{nodal}} = \boldsymbol{S} \{\boldsymbol{x}_r\}_{\text{nodal}} \tag{3.26}$$

which essentially selects the nodes for the given element from the complete set of rotor nodes. The rotor matrices can then be found by summing the contribution of each element, whilst transforming from nodal to rotor co-ordinates. For example, the rotor stiffness matrix is given by:

$$\{\boldsymbol{K}_r\}_{\text{nodal}} = \sum_j \boldsymbol{S}_j^T \{\boldsymbol{K}_j\}_{\text{nodal}} \boldsymbol{S}_j \tag{3.27}$$

where the sum is carried out over all shaft and disc elements. The total rotor excitation and gravitational forces can be found in a similar way. For example, the total gravitational load is given by:

$$\left\{\boldsymbol{f}_{r,g}\right\}_{\text{nodal}} = \sum_j \boldsymbol{S}_j^T \left\{\boldsymbol{f}_{j,g}\right\}_{\text{nodal}} \tag{3.28}$$

The equation of motion of the rotor can now be written in the following form:

$$\boldsymbol{M}_r\ddot{\boldsymbol{x}} + (\boldsymbol{C}_r + \Omega\boldsymbol{G}_r)\,\dot{\boldsymbol{x}} + \boldsymbol{K}_r\boldsymbol{x} = \boldsymbol{f}_{r,e}(t) + \boldsymbol{f}_{r,g} \tag{3.29}$$

This completes the assembly of the rotor FE model.

3.1.2.4 Model reduction

Although the line-model of the rotor will have relatively few DOF, it is possible to maintain a sufficient level of accuracy whilst further reducing the number of DOF using model reduction techniques. One of the most common methods known as Component Mode Synthesis (CMS) was applied to each rotor, which will now be outlined. It was assumed that the damping and gyroscopic forces have negligible effect on the mode shapes of the rotor, so that they can be found from the following simplified equation of motion:

$$\boldsymbol{M}_r\ddot{\boldsymbol{x}} + \boldsymbol{K}_r\boldsymbol{x} = \boldsymbol{f}_r \tag{3.30}$$

where $\boldsymbol{f}_r$ is a vector of generic external forces. The structure is partitioned into boundary DOF at the interfaces, leaving the remainder as free DOF. In this thesis, the boundary DOF were selected to be those connected by joints. The equation of motion can then be written in the following partitioned form:

$$\begin{bmatrix}\boldsymbol{M}_{bb} & \boldsymbol{M}_{bi}\\ \boldsymbol{M}_{ib} & \boldsymbol{M}_{ii}\end{bmatrix}\begin{bmatrix}\ddot{\boldsymbol{x}}_b\\ \ddot{\boldsymbol{x}}_i\end{bmatrix} + \begin{bmatrix}\boldsymbol{K}_{bb} & \boldsymbol{K}_{bi}\\ \boldsymbol{K}_{ib} & \boldsymbol{K}_{ii}\end{bmatrix}\begin{bmatrix}\boldsymbol{x}_b\\ \boldsymbol{x}_i\end{bmatrix} = \begin{bmatrix}\boldsymbol{f}_b\\ \boldsymbol{f}_i\end{bmatrix} \tag{3.31}$$

where $\boldsymbol{x}_b$ are the boundary DOF, and $\boldsymbol{x}_i$ are the interior DOFs. The number of boundary DOF will be denoted by where N_b, whilst the number of interior DOF will be denoted by N_i. The response is assumed to be made up of a sum of constraint modes and normal modes. These will now be discussed in more detail.

Constraint modes The constraint modes can be found by perturbing each interface DOF in the vector $\boldsymbol{x}_b$, and solving for the static response. An example is shown in Fig. 3.4 for a simple rotor. The constraint mode is found by perturbing the node on the RHS, where the flexible bearing is attached. To solve for the constraint modes numerically, it can be noted that forces on the interior DOF $\boldsymbol{f}_i$ must be zero:

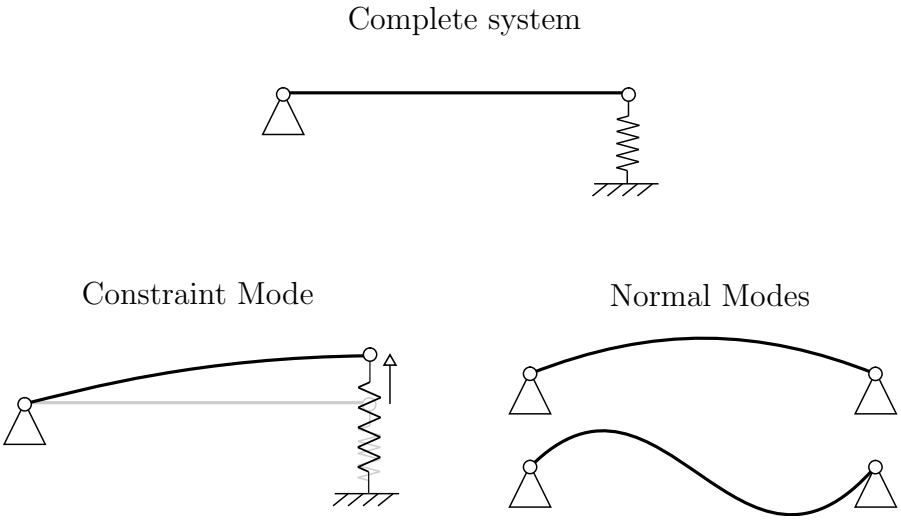


Figure 3.4: Application of CMS to a simple rotor

$$\begin{bmatrix} \boldsymbol{K}_{bb} & \boldsymbol{K}_{bi} \\ \boldsymbol{K}_{ib} & \boldsymbol{K}_{ii} \end{bmatrix} \begin{bmatrix} \boldsymbol{x}_b \\ \boldsymbol{x}_i \end{bmatrix} = \begin{bmatrix} \boldsymbol{f}_b \\ 0 \end{bmatrix}$$

which can be rearranged to solve for the interior DOF in terms of the boundary DOF:

$$\boldsymbol{x}_i = -\boldsymbol{K}_{ii}^{-1} \boldsymbol{K}_{ib} \boldsymbol{x}_b = \Psi_{i,b} \boldsymbol{x}_b \tag{3.32}$$

where $\Psi_{i,b}$ is a vector of interior DOF displacements for each constraint mode.

Normal modes The normal modes are defined as the modes of the structure with all of the boundary DOF either held fixed (so that $\boldsymbol{x}_b = 0$) or allowed to float so that ($\boldsymbol{f}_b = 0$). It is also possible to use a hybrid approach where some boundary DOF are held fixed, while others are allowed to float [32]. In this thesis, the most common method will be used, which is known as the Craig-Bampton method [27], in which the boundary DOF are held fixed. This is both simpler to implement and more accurate than the other approaches [29].

To compute the normal modes numerically, the boundary DOF can be eliminated since they are held fixed. This means the normal modes can be computed from the following eigenvalue problem involving only the interior DOF:

$$\left[\boldsymbol{K}_{ii} - \omega^2 \boldsymbol{M}_{ii}\right] \boldsymbol{x}_i = 0 \tag{3.33}$$

which yields a the matrix of eigenvectors denoted by Φ_i. The first two normal modes are depicted in Fig. 3.4. Note that there is no motion at the node on the RHS.

Reduced equation of motion The final stage is to assume that the response vector $\boldsymbol{x}$ of the complete rotor can now be approximated by a linear superposition of the constraint and normal modes, which can be written mathematically as:

$$\boldsymbol{x} \approx \begin{bmatrix} \boldsymbol{x}_b \\ \boldsymbol{x}_i \end{bmatrix} = \begin{bmatrix} \boldsymbol{I} & \boldsymbol{0} \\ \Psi_{i,b} & \hat{\Phi}_i \end{bmatrix} \begin{bmatrix} \boldsymbol{x}_b \\ \hat{\boldsymbol{x}}_i \end{bmatrix} = \boldsymbol{T}\boldsymbol{y} \tag{3.34}$$

where $\hat{\Phi}_i$ contains a truncated set of n normal modes, and $\hat{\boldsymbol{x}}_i$ contains the corresponding amplitudes of each mode. The vector $\boldsymbol{y}$ is the reduced set of rotor DOF. Since rotating machines typically only operate within a certain speed range, the response is typically dominated by only a few normal modes, and therefore $n << N_i$. However, the accuracy can be improved by including more higher order modes. The transformation matrix $\boldsymbol{T}$ can be substituted in to the equation of motion in Eq. (3.30), to yield the reduced equation of motion:

$$\begin{aligned} \boldsymbol{M}_r\ddot{\boldsymbol{x}} + \boldsymbol{K}_r\boldsymbol{x} &= \boldsymbol{f}_r \\ \boldsymbol{T}^T\boldsymbol{M}_r\boldsymbol{T}\ddot{\boldsymbol{y}} + \boldsymbol{T}^T\boldsymbol{K}_r\boldsymbol{T}\boldsymbol{y} &= \boldsymbol{T}^T\boldsymbol{f}_r \\ \tilde{\boldsymbol{M}}_r\ddot{\boldsymbol{y}} + \tilde{\boldsymbol{K}}_r\boldsymbol{y} &= \tilde{\boldsymbol{f}}_r \end{aligned} \tag{3.35}$$

where $\tilde{\boldsymbol{M}}_r$ and $\tilde{\boldsymbol{K}}_r$ are the mass and stiffness matrices of the reduced-order system. The number of DOF has been reduced from $N_b + N_i$ to $N_b + n$. Assuming that there are relatively few interface nodes and only a few normal modes need to be included, this can lead to a significant reduction in the size of the system.

3.1.3 Stators

The shaft and discs in a rotating machine are typically supported by stationary components. In general, the stators can have their own dynamics, but for this thesis, it was assumed that their natural frequency was significantly higher than the running range of the machine, so that they could be assumed rigid. This means that, like the discs, the stators only add inertia to the system. However, since they are non-rotating, they have no contribution to the gyroscopic matrix. Assuming the stator CoG coincides with the location of its node, the mass matrix will have a diagonal form:

$$\{\boldsymbol{M}_s\}_{\text{nodal}} = \begin{bmatrix} m_x & 0 & 0 & 0 \\ 0 & m_y & 0 & 0 \\ 0 & 0 & I_x & 0 \\ 0 & 0 & 0 & I_y \end{bmatrix} \tag{3.36}$$

which is very similar to the disc mass matrix, except that it is no longer assumed that the stator is axisymmetric, since m_x may not equal m_y and similarly for the moments of inertia. This mass matrix is already defined in nodal co-ordinates so no transformation is required. Like the disc elements, the self-weight of the stator can be computed using the mass matrix:

$$\boldsymbol{f}_{s,g} = \boldsymbol{M}_s \boldsymbol{g} \tag{3.37}$$

where $\boldsymbol{g}$ is from Eq. (3.15). The stator element has now been fully defined. Note that if the stator is supported by a flexible structure, this compliance can be modelled with joint elements, which will be introduced in the next section.

3.1.4 Joints

The final pieces of the FE model are the joint elements which connect the rotor and stator elements. The joint forces will depend on the relative displacement between the two components connected by the joint, as well as its derivatives. As with the shafts, it is convenient to partition the joint displacement vector, in order to separate the deflections within the horizontal and vertical planes. The joint displacement vector is therefore defined as:

$$\begin{aligned} \{\boldsymbol{x}_b\}_{\text{joint}} &= \begin{bmatrix} \delta_x^1 & \theta_y^1 & \delta_y^1 & -\theta_x^1 \end{bmatrix}^T - \begin{bmatrix} \delta_x^2 & \theta_y^2 & \delta_y^2 & -\theta_x^2 \end{bmatrix}^T \\ &= \{\boldsymbol{x}_1\}_{\text{joint}} - \{\boldsymbol{x}_2\}_{\text{joint}} \end{aligned} \tag{3.38}$$

where $\{\boldsymbol{x}_1\}_{\text{joint}}$ and $\{\boldsymbol{x}_2\}_{\text{joint}}$ are the deflections of the two components connected by the joint, specified in joint co-ordinates. It was assumed that the joints were the only possible source of non-linearity in the system. This means different approaches must be taken to include them in the FE model, depending on whether a joint is non-linear or linear.

3.1.4.1 Non-linear joints

Many types of joint, including rolling-element bearings, are inherently non-linear in nature, due to phenomena such as clearance or hysteresis. It will be assumed that there are no inertial effects within the joints, so that the force purely depends on the relative displacement and velocity, so that the non-linear joint force can be written as:

$$\{\boldsymbol{f}_b\}_{\text{joint}} = \boldsymbol{f}\left(\boldsymbol{x}_b, \dot{\boldsymbol{x}}_b\right) \tag{3.39}$$

where the function $\boldsymbol{f}(\cdot)$ comes from the joint model, such as the rolling-element bearing model which will be presented in Section 3.2.

3.1.4.2 Linearised joints

If a rotating machine is lightly excited, even non-linear joints may remain in the regime where they can be approximated as linear. This means the joint can be linearised about its equilibrium point:

$$\begin{aligned}\boldsymbol{f}_b\left(\boldsymbol{x}^b, \dot{\boldsymbol{x}}_b\right) &\approx \boldsymbol{f}\left(\boldsymbol{x}_b^0\right) + \boldsymbol{K}_b\left(\boldsymbol{x}_b - \boldsymbol{x}_b^0\right) + \boldsymbol{C}_b\dot{\boldsymbol{x}}_b \\ &= \left(\boldsymbol{f}\left(\boldsymbol{x}_b^0\right) - \boldsymbol{K}_b\boldsymbol{x}_b^0\right) + \boldsymbol{K}_b\boldsymbol{x}_b + \boldsymbol{C}_b\dot{\boldsymbol{x}}_b \\ &= \boldsymbol{f}_b^0 + \boldsymbol{K}_b\boldsymbol{x}_b + \boldsymbol{C}_b\dot{\boldsymbol{x}}_b \end{aligned} \tag{3.40}$$

where $\boldsymbol{f}_b^0$ is a zero offset term and $\boldsymbol{K}_b$ and $\boldsymbol{C}_b$ are the joint stiffness and damping matrices respectively. It should be noted that the additional zero offset force term $\boldsymbol{f}_b^0$ was not present with any of the rotor or stator elements. Each of the three terms in Eq. (3.40) can be written in a partitioned form. For example, the stiffness matrix can be written as:

$$\{\boldsymbol{K}_b\}_{\text{nodal}} = \begin{bmatrix}\boldsymbol{K}_{xx} & \boldsymbol{K}_{xy} \\ \boldsymbol{K}_{yx} & \boldsymbol{K}_{yy}\end{bmatrix} \tag{3.41}$$

where, for the special case of an isotropic joint, $\boldsymbol{K}_{xx} = \boldsymbol{K}_{yy}$ and $\boldsymbol{K}_{xy} = \boldsymbol{K}_{yx} = \boldsymbol{0}$. Each submatrix within Eq. (3.41) has the form:

$$\boldsymbol{K}_{xx} = \begin{bmatrix}k_{\delta\delta} & k_{\delta\theta} \\ k_{\theta\delta} & k_{\theta\theta}\end{bmatrix}$$

The radial stiffness is given by $k_{\delta\delta}$, and the tilt stiffness by $k_{\theta\theta}$. The cross-stiffness $k_{\delta\theta} = k_{\theta\delta}$ determines the cross-coupling between joint rotation and translation. For the special case of a joint with zero tilt stiffness, such as a self-aligning bearing, all of the tilt terms are near-zero, so each submatrix has the simpler form:

$$\boldsymbol{K}_{xx} = \begin{bmatrix}k_{\delta\delta} & 0 \\ 0 & 0\end{bmatrix} \tag{3.42}$$

Now that the joint forces have been defined, it is now necessary to transform them from joint to nodal coordinates.

3.1.4.3 Transformation to nodal coordinates

Now that the joint stiffness and damping model has been defined, it is necessary to convert it into nodal co-ordinates. Using the definition of nodal co-ordinates from Eq. (3.16), the transformation to joint co-ordinates is given by:

$$\begin{aligned}\{\boldsymbol{x}_b\}_{\text{joint}} &= \begin{bmatrix}\boldsymbol{R}_b & -\boldsymbol{R}_b\end{bmatrix} \left\{ \begin{bmatrix}\boldsymbol{x}_1 \\ \boldsymbol{x}_2\end{bmatrix} \right\}_{\text{nodal}} \\ &= \begin{bmatrix}\boldsymbol{R}_b & -\boldsymbol{R}_b\end{bmatrix} \{\boldsymbol{x}_b\}_{\text{nodal}}\end{aligned} \tag{3.43}$$

where the matrix $\boldsymbol{R}_b$ rearranges the nodal coordinates into joint co-ordinates and is given by:

$$\boldsymbol{R}_b = \begin{bmatrix}1 & 0 & 0 & 0 \\ 0 & 0 & 0 & 1 \\ 0 & 1 & 0 & 0 \\ 0 & 0 & -1 & 0\end{bmatrix}$$

For linear joints, the stiffness and damping matrices of the joint can simply be multiplied by this transformation to yield the joint properties in nodal co-ordinates. For example, the stiffness matrix in global co-ordinates is given by:

$$\{\boldsymbol{K}_b\}_{\text{nodal}} = \begin{bmatrix}\boldsymbol{R}_b^T \\ -\boldsymbol{R}_b^T\end{bmatrix} \{\boldsymbol{K}_b\}_{\text{joint}} \begin{bmatrix}\boldsymbol{R}_b & -\boldsymbol{R}_b\end{bmatrix} \tag{3.44}$$

In addition, the zero-offset force from the joint must be transformed to nodal coordinates

$$\left\{\boldsymbol{f}_b^0\right\}_{\text{nodal}} = \begin{bmatrix}\boldsymbol{R}_b^T \\ -\boldsymbol{R}_b^T\end{bmatrix} \left\{\boldsymbol{f}_b^0\right\}_{\text{joint}} \tag{3.45}$$

If the joints are non-linear, then the joint model must still be evaluated. However, the transformation matrices can be introduced to allow it to be evaluated in nodal coordinates:

$$\{\boldsymbol{f}_b\}_{\text{nodal}} = \begin{bmatrix}\boldsymbol{R}_b^T \\ -\boldsymbol{R}_b^T\end{bmatrix} \left\{ \boldsymbol{f}\left(\begin{bmatrix}\boldsymbol{R}_b & -\boldsymbol{R}_b\end{bmatrix} \{\boldsymbol{x}_b\}_{\text{nodal}} \right) \right\}_{\text{joint}} \tag{3.46}$$

The joint forces have now been fully defined in nodal coordinates, for both linear and non-linear joints.

3.1.5 Complete system

The rotor, stator and joint elements have now been defined, so that it is now possible to assemble the matrices for the complete system. The assembly process is very similar to that applied to the rotor in Section 3.1.2.3. The first step is to introduce a transformation matrix $\boldsymbol{S}$, which relates the elemental displacements to the global displacement vector:

$$\{\boldsymbol{x}\}_{\text{nodal}} = \boldsymbol{S}\,\{\boldsymbol{x}\}_{\text{global}} \tag{3.47}$$

The contributions of the linear components can be found by simply multiplying by this transformation. For example, the global mass matrix is given by:

$$\{\boldsymbol{M}\}_{\text{global}} = \sum_j \boldsymbol{S}_j^T\,\{\boldsymbol{M}_j\}_{\text{nodal}}\,\boldsymbol{S}_j \tag{3.48}$$

where the sum is carried out over all the rotor, stator and joint elements. The same procedure can be applied for the other matrices and forces to yield the following equation of motion of the complete rotating machine:

$$\boldsymbol{M}\ddot{\boldsymbol{x}} + (\Omega\boldsymbol{G} + \boldsymbol{C})\,\dot{\boldsymbol{x}} + \boldsymbol{K}\boldsymbol{x} + \boldsymbol{f}_{nl}\,(\boldsymbol{x}, \dot{\boldsymbol{x}}) = \boldsymbol{f}_e(t) + \boldsymbol{f}_g \tag{3.49}$$

where $\boldsymbol{M}$, $\boldsymbol{C}$, $\boldsymbol{K}$, and $\boldsymbol{G}$ are the mass, damping, stiffness and gyroscopic matrices of the whole system. The vectors $\boldsymbol{f}_e$ and $\boldsymbol{f}_g$ contain the excitation forces and gravitational loads of the complete system. The vector $\boldsymbol{f}_{nl}$ contains the forces from the non-linear joints.

3.1.6 Modal analysis

In order to perform modal analysis, all of the joints must be linearised, so that the non-linear term in Eq. (3.49) disappears. This allows the equation of motion in Eq. (3.49) to be rewritten in the following linearised state-space form [6]:

$$\boldsymbol{A}\dot{\boldsymbol{z}} + \boldsymbol{B}\boldsymbol{z} = \boldsymbol{u} \tag{3.50}$$

where $\boldsymbol{z} = [\dot{\boldsymbol{x}}, \boldsymbol{x}]^T$, and $\boldsymbol{u} = \left[\boldsymbol{f}_e + \boldsymbol{f}_g, \boldsymbol{0}\right]^T$. The matrices $\boldsymbol{A}$ and $\boldsymbol{B}$ are given by:

$$\boldsymbol{A} = \begin{bmatrix} \boldsymbol{M} & \Omega\boldsymbol{G} \\ \boldsymbol{0} & \boldsymbol{I} \end{bmatrix} \tag{3.51}$$

$$\boldsymbol{B} = \begin{bmatrix} \boldsymbol{C} & \boldsymbol{K} \\ -\boldsymbol{I} & \boldsymbol{0} \end{bmatrix} \tag{3.52}$$

This state-space representation has reduced Eq. (3.49) to a first-order ODE, which allows standard eigenvalue analysis tools to be used to compute the natural frequencies and critical speeds. This will now be discussed further.

3.1.6.1 Natural frequencies

The natural frequencies can be found by first making the system autonomous, by setting $\boldsymbol{u}$ to zero. Assuming an exponential solution of the form $\boldsymbol{z} = \boldsymbol{z}_0 e^{st}$, this can be substituted into Eq. (3.50) to yield:

$$(s\boldsymbol{S} + \boldsymbol{R})\,\boldsymbol{z}_0 = \boldsymbol{0} \tag{3.53}$$

This is a generalised eigenvalue problem and can be solved using the `eig` command in MATLAB. In this undamped case, the eigenvalues will come in pairs of the form $s = -\zeta\omega_n \pm j\omega_d$, and the corresponding eigenvectors $\boldsymbol{z}_0$ will also come in complex conjugate pairs. Each pair corresponds to a different mode. In order to compute the Campbell diagram, this equation can be solved for multiple rotor speeds, updating the $\boldsymbol{A}$ and $\boldsymbol{B}$ matrices each time, in order to ascertain how the modal properties vary. However, a continuation algorithm must be used to correctly match the modes from one speed to the next; this can be achieved in MATLAB using the function `eigenshuffle` [168].

The direction of rotor whirl at a given node can be determined by looking at the relative phase between the horizontal and vertical deflections. For a rotor spinning around the positive z axis, there is FW whirl if the y component lags the x component, and BW whirl if it leads the x component. If the rotor spins in the opposite direction, these rules are reversed.

3.1.6.2 Critical speeds

An unbalance on one of the rotors will lead to an excitation of the form $\boldsymbol{f}_s = \boldsymbol{f}_0 e^{jn\Omega t}$, where $n = 1$ which is the "engine order". Other forms of synchronous excitation can occur at different engine orders, for which $n \neq 1$. If the damping of the system is small, a harmonic response of the form $\boldsymbol{x} = \boldsymbol{x}_0 e^{jn\Omega t}$ can be assumed. Substituting this into Eq. (3.49) equating coefficients of $e^{jn\Omega t}$ yields:

$$\left(-n^2\Omega^2\left[\boldsymbol{M} - \frac{j}{n}\boldsymbol{G}\right] + jn\Omega\boldsymbol{C} + \boldsymbol{K}\right)\boldsymbol{x_0} = \boldsymbol{f}_0 \tag{3.54}$$

This can again be expressed in state-space form by making the substitutions $\boldsymbol{z}_0 = [j\Omega\boldsymbol{x}_0, \boldsymbol{x}_0]^T$ and $\boldsymbol{u}_0 = [\boldsymbol{f}_0, \boldsymbol{0}]^T$:

$$\left(j\Omega\begin{bmatrix} n^2\boldsymbol{M} - jn\boldsymbol{G} & 0 \\ \boldsymbol{0} & \boldsymbol{I} \end{bmatrix} + \begin{bmatrix} n\boldsymbol{C} & \boldsymbol{K} \\ -\boldsymbol{I} & \boldsymbol{0} \end{bmatrix}\right)\boldsymbol{z}_0 = \boldsymbol{u}_0 \tag{3.55}$$

At resonance, the matrix on the left must be near singular [2]. This leads to another generalised eigenvalue problem, where the eigenvalues directly yield the critical speeds

and the eigenvectors are the shape of the response. For an axisymmetric system on isotropic supports, it can be shown that the FW excitation pattern from the unbalance is orthogonal to the BW modes, so that only FW modes can be excited and only these critical speeds need to be retained. However, in the more general case of anisotropic supports, this orthogonality is lost, and it is then possible for unbalances to also excite BW modes so all critical speeds have to be considered.

3.1.7 MATLAB implementation

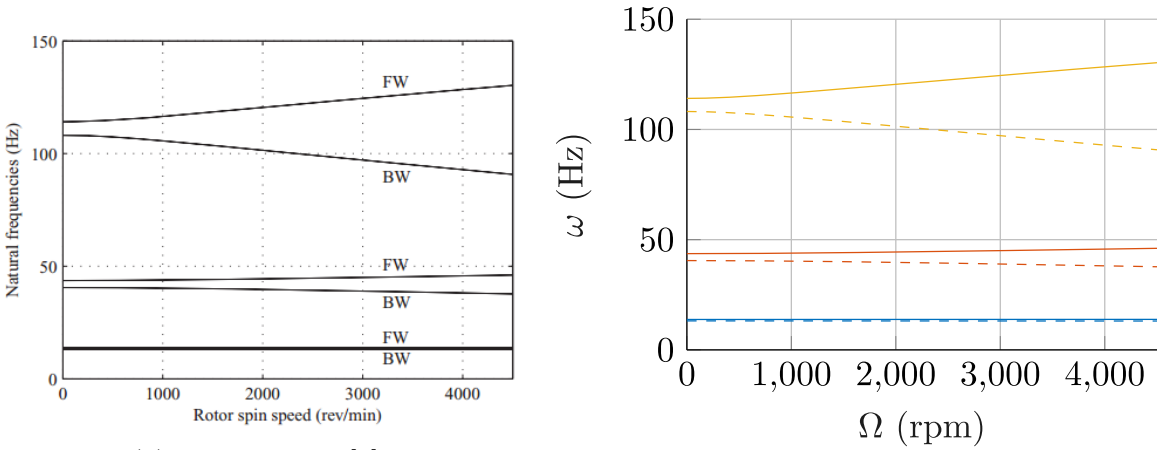
The presented Finite Element model was implemented in MATLAB as a general rotordynamic toolbox known as ROLADYN (ROtating LAteral DYNamics) [169]. In contrast to commercial FE packages which can handle highly complex rotor models, ROLADYN is tailored to lateral shaft dynamics. Since it is written in MATLAB, it is easy to automate tasks using scripts and integrate with other numerical tools.

ROLADYN supports systems with zero or more rotors, which are connected to zero or more rigid stators. The rotors and stators are connected to each other or to ground by joints, which can be linear or non-linear. The setup is entirely configurable by the user. ROLADYN first solves for the position where the system is in equilibrium with the self-weight, and then linearises the model about this point. There are routines to compute the natural frequencies, mode shapes and critical speeds of the system, as well as the synchronous and asynchronous frequency response.

ROLADYN can also be integrated with non-linear tools, such as time-marching solvers (incl. `ode45`) or more advanced techniques such as Harmonic Balance which will be presented in Section 3.3. In this case, ROLADYN no longer linearises the non-linear joints, but evaluates their forces using the non-linear joint model.

3.1.7.1 Validation

The toolbox was validated against results from the literature; for example, shown in Fig. 3.5 is the Campbell diagram for a flexible 2-disc rotor mounted on anisotropic bearings from [2]. It can be observed that ROLADYN matches the published results well.



(a) Results from [2]

(b) Results from ROLADYN

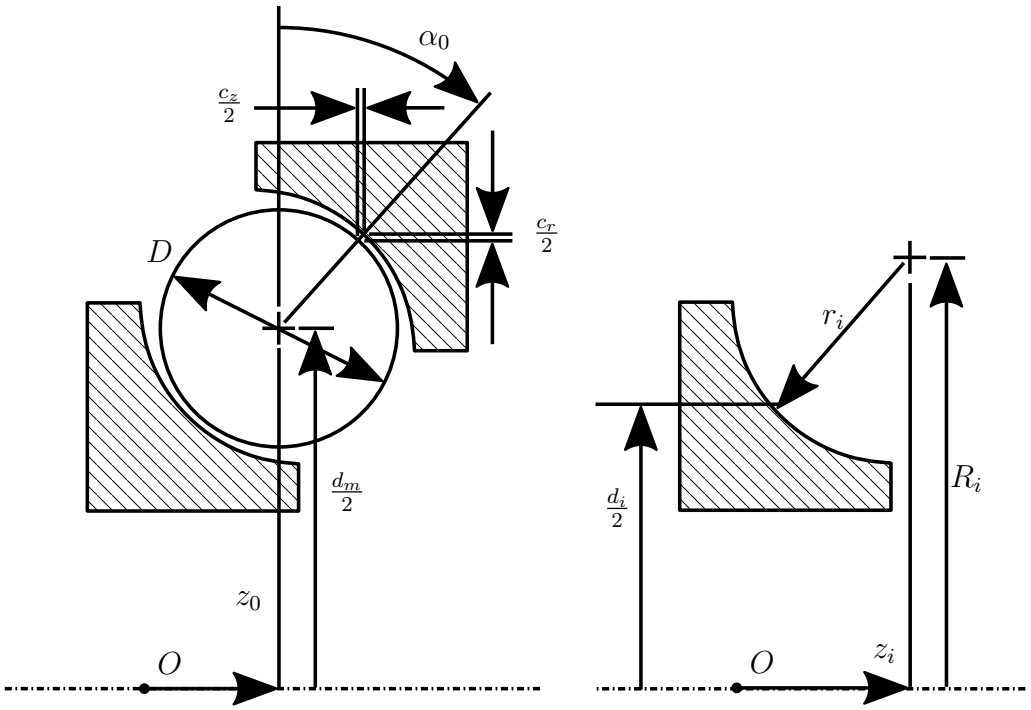
Figure 3.5: Validation of ROLADYN

3.2 Quasi-static bearing model

To accurately predict the response of a rotating machine supported by rolling element bearings, a detailed bearing model is required that can capture its non-linear stiffness, as well as the influence of features such as clearance and dynamic loading on the elements, whilst remaining fast to evaluate. The presented bearing model is based on the well-established quasi-static approach first introduced by Jones [44], and later developed by Harris [45]. The bearing model will only be presented for the case of ball-bearings, since these are more commonly used than roller bearings and only ball bearings will be analysed experimentally in this thesis. The quasi-static approach assumes that the ball dynamics are very fast, so that interactions between the cage and balls can be ignored, and the ball is in equilibrium with the rings. This significantly reduces the computational complexity, and removes unnecessary internal states [170].

Ball bearings typically consist of one or two rows of spherical elements held in place by a cage. These bearings are primarily used to resist radial loads, but can also be configured to have a significant axial load capacity. The balls can be arranged so that the contacts are in plane, or rotated by some angle α_0 which is known as the contact angle, as shown in Fig. 3.6a. If the bearing has multiple rows, the elements will be offset from the central plane of the bearing by z_0. The number of bearing elements will be denoted by Z.

The elements rotate along two curved raceways within the inner and outer rings. It is typically assumed that this curvature is constant, so that the geometry can be defined by specifying a radius of curvature r_e, and the axial and radial location of the centre of curvature, denoted by z_e and R_e. The subscript e is to be replaced with i for the inner ring, and o for the outer ring. This is depicted in Fig. 3.6b.



(a) Ball geometry (b) Race geometry

Figure 3.6: Definition of REB dimensions

3.2.1 Cage rotation

It is first necessary to define the angular location of each element. It will be assumed that the elements are adequately constrained by the cage, so that they remain evenly distributed around the circumference [44]. With reference to Fig. 3.7, the angular position of each ball ψ_j is given by [86, 102]:

$$\psi_j = (j-1)\Delta\psi + \psi_c \tag{3.56}$$

where ψ_c is the angle through which the cage has rotated from its initial position. This is defined to be zero when the first element is directly under the bearing centre. The angle between each adjacent pair of elements is denoted by $\Delta\psi = \frac{2\pi}{Z}$. Note that the subscripts j will be dropped in the following sections for brevity, but the equations should be applied to each element.

3.2.2 Ring deflections

The bearing deflections δ_x^b, δ_y^b, θ_x^b and δ_y^b are shown in Fig. 3.7. These deflections are defined as the inner ring *relative* to the outer ring, so that the outer ring can be considered fixed for the remainder of the derivation of the bearing properties [45, 46]. However, this

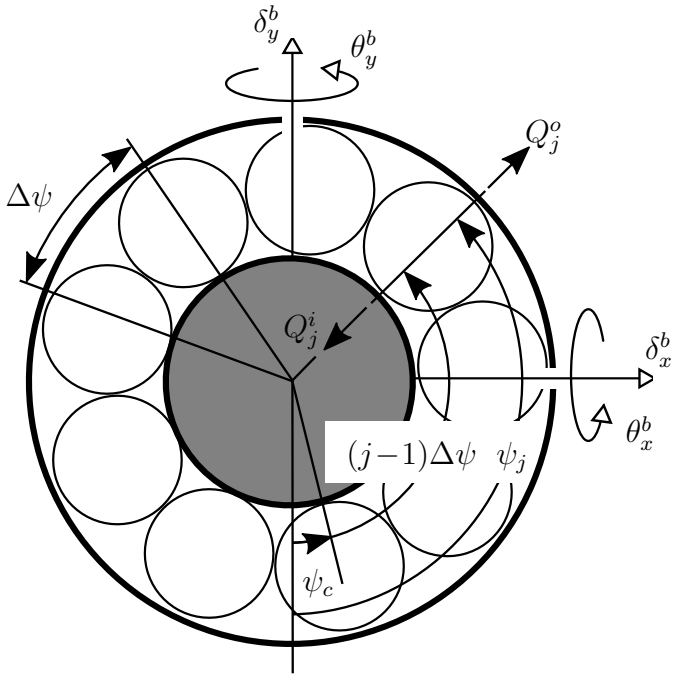


Figure 3.7: Angular position of elements

is without loss of generality, since the values of these deflections are equally sensitive to movements of either ring.

In order to determine the contact deflections at the jth element, it is necessary to first compute the radial and axial ring deflections, $r(\psi)$ and $x(\psi)$, around the bearing. Assuming the ring deflections are small, this is given by [46]:

$$\begin{bmatrix} r(\psi) \\ z(\psi) \end{bmatrix} = \boldsymbol{T}(\psi)\boldsymbol{x}_b - \begin{bmatrix} c_r \\ c_z \end{bmatrix} \tag{3.57}$$

where $\boldsymbol{x}_b$ is the following bearing displacement vector in nodal co-ordinates:

$$\boldsymbol{x}_b = \begin{bmatrix} \delta_x^b & \delta_y^b & \theta_x^b & \theta_y^b \end{bmatrix}^T \tag{3.58}$$

and the transformation matrix $\boldsymbol{T}$ is given by [171]:

$$\boldsymbol{T}(\psi) = \begin{bmatrix} \cos\psi & \sin\psi & -z_i\sin\psi & z_i\cos\psi \\ 0 & 0 & R_i\sin\psi & -R_i\cos\psi \end{bmatrix} \tag{3.59}$$

where the dimensions R_i and z_i are the radial and axial location of the centre of curvature of the inner race shown in Fig. 3.6b. The terms c_r and c_z are the radial and axial clearances respectively. These can have positive or negative values, corresponding to a loose or tight bearing respectively.

3.2.3 Contact forces

The contacts are assumed Hertzian, so that the inner and outer contacts can be computed from the following power law:

$$Q^e = C_e \left[\delta^e\right]_+^n \tag{3.60}$$

where the constant C_e is the Hertzian stiffness coefficient of the relevant contact, and $[\cdot]_+$ denotes saturation to positive values to ensure that there are no attractive contact forces. The exponent $n = 1.5$ for the point contacts present within ball bearings. The deflection at the contact is denoted by δ_e, but this has not yet been derived. The local stiffness of each Hertzian contact can be found by differentiating Eq. (3.60):

$$\frac{\partial Q_j^e}{\partial \delta^e} = C_e n \left[\delta_j^e\right]_+^{n-1} \tag{3.61}$$

The Hertzian stiffness coefficient C_e depends on both the material properties of the elements, as well as the curvatures of the elements and races. Assuming the races and elements are made of the same material, this coefficient has the form:

$$C_e = \frac{E}{1-\nu^2} F\left(r_e, d_e, D\right) \tag{3.62}$$

where E and ν are the Young's modulus and Poisson's ratio of the components, and $F\left(r_e, d_e, D\right)$ is a geometric factor involving elliptical integrals [19, 53]. This depends on the diameter of the elements D, as well as the diameter d_e and radius of curvature r_e of the races.

Attention must now turn to the computation of the unknown ball deflections δ_e, so that it is then possible to express the contact forces as a function of the ring deflections:

$$Q^e\left(\psi\right) = h_e\left(r\left(\psi\right), z\left(\psi\right)\right) \tag{3.63}$$

where the function $h_e(\cdot)$ will be termed a "contact model". Two different approaches will be introduced in the following sections, which apply for different operating conditions.

3.2.4 Low-speed contact model

The simplest case to analyse is where the bearing operates at low speeds, so that the dynamic loads can be neglected. The free body diagram under these conditions is shown in Fig. 3.8. It can be observed that the contact loads are the only loads on the balls. This

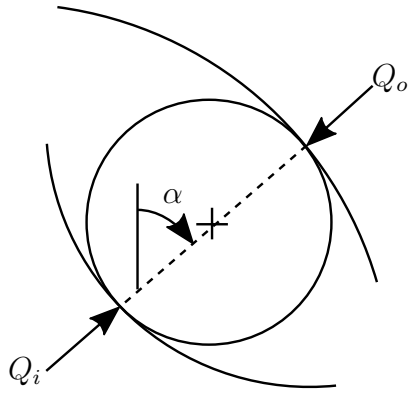


Figure 3.8: Free-body force diagram of ball at low-speeds

means that both the inner and outer contact loads *and* contact angles must be equal, in order to maintain both radial and axial equilibrium of the balls. This simplifies the analysis considerably.

3.2.4.1 Contact geometry

The geometry in both the deformed and undeformed cases is depicted in Fig. 3.9. It can be observed that the ball centre and centres of race curvature are co-linear both before and after the ring deflects. The initial contact geometry is depicted in Fig. 3.9a. The distance between the two centres of curvature, denoted by A_0, is given by [45]:

$$A_0 = \left(r_o - \frac{D}{2}\right) + \left(r_i - \frac{D}{2}\right) = r_o + r_i - D \tag{3.64}$$

After the rings deflect, the distance between curvature centres changes to a new value A, which has radial and axial components given by [46]:

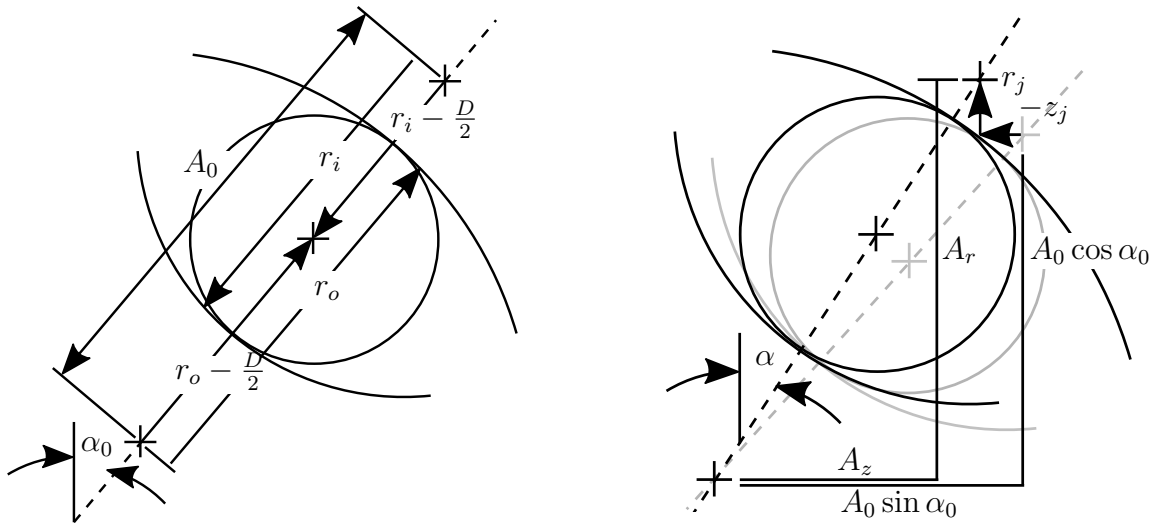
$$A_r(\psi) = A_0 \cos\alpha_0 + r(\psi) \tag{3.65}$$

$$A_z(\psi) = A_0 \sin\alpha_0 + z(\psi) \tag{3.66}$$

from which A can be computed from Pythagoras:

$$A(\psi) = \sqrt{A_z(\psi)^2 + A_r(\psi)^2} \tag{3.67}$$

With reference Fig. 3.9b, the contact angle can be computed directly from the radial and axial components of A [46]:



(a) Initial configuration

(b) Deformed bearing configuration

Figure 3.9: Bearing contact geometry at low-speeds

$$\tan \alpha = \frac{A_z(\psi)}{A_r(\psi)} \tag{3.68}$$

3.2.4.2 Contact forces

Since the loads at the inner and outer contacts must be equal, the two contacts can be combined and treated as a single Hertzian contact. The total contact deflection δ is given by:

$$\delta = A - A0 \tag{3.69}$$

which can then be substituted into the Hertzian contact law to yield the contact forces:

$$Q = Q^i = Q^o = C \left[\delta\right]_+^n \tag{3.70}$$

where the parameter C is the combined Hertzian coefficient of the inner and outer race contacts. This can be calculated from the contact coefficient of each individual contact [19]:

$$C = \left(C_i^{-\frac{1}{n}} + C_o^{-\frac{1}{n}}\right)^{-\frac{1}{n}} \tag{3.71}$$

The combined contact stiffness can be found by differentiating Eq. (3.70):

$$K = \frac{\partial Q}{\partial \delta} = Cn \left[\delta\right]_+^{n-1} \tag{3.72}$$

Now that the contact forces have been computed, the low-speed contact model is complete.

3.2.5 High-speed operation

If the bearing operates at high speed, the dynamic loads on the bearing cannot be neglected. In this case, it can no longer be assumed that the contact loads and contact angles are equal, and a more complex analysis is therefore required.

3.2.5.1 Contact geometry

The deflected configuration for the case with dynamic loads is depicted in Fig. 3.10. It can be observed that the points of contact and the centre of the ball are no longer colinear. In addition, the contact angles at the inner and outer contacts are now different. It is assumed that each element moves radially by r_b, and axially by z_b. The distance between the ball centre and the centre of curvature of the outer raceway will be denoted by X. With reference to Fig. 3.10, this has axial and radial components given by:

$$X_r = \left(r_o - \frac{D}{2}\right)\cos\alpha_0 + r_b \tag{3.73}$$

$$X_z = \left(r_o - \frac{D}{2}\right)\sin\alpha_0 + z_b \tag{3.74}$$

The contact deflections at both the inner and outer contacts can then be expressed in terms of A and X:

$$\delta_i = \sqrt{\left(A_z(\psi) - X_z\right)^2 + \left(A_r(\psi) - X_r\right)^2} - \left(r_i - \frac{D}{2}\right) \tag{3.75}$$

$$\delta_o = \sqrt{X_z^2 + X_r^2} - \left(r_o - \frac{D}{2}\right) \tag{3.76}$$

where the radial and axial components of the distance between race curvatures A_r and A_z can be computed from Eqs. (3.65) and (3.66) respectively. The contact angles in the deformed configuration at each contact can also be computed using X and A:

$$\tan\alpha_i = \frac{A_z(\psi) - X_z}{A_r(\psi) - X_r} \tag{3.77}$$

$$\tan\alpha_o = \frac{X_z}{X_r} \tag{3.78}$$

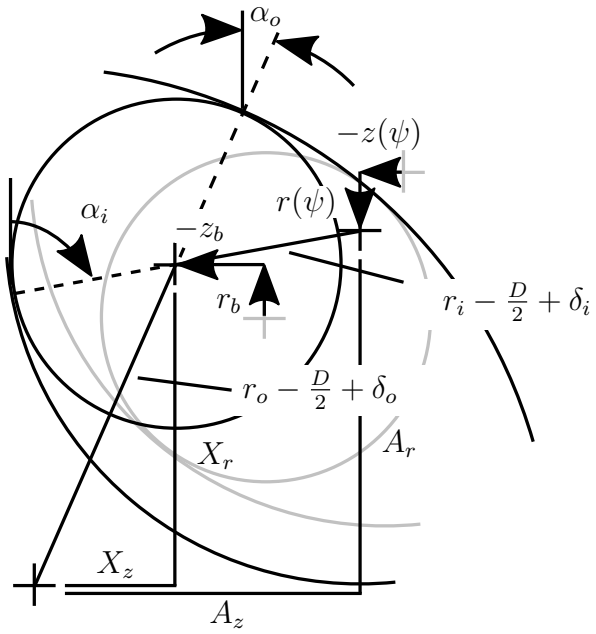


Figure 3.10: Deformed contact geometry at high-speeds

Now that the contact deflections have been defined, the contact loads can be computed from Eq. (3.60). Unlike in the low-speed model, the inner and outer contacts can no longer be combined, and must be treated as separate Hertzian contacts.

3.2.5.2 Equilibrium of the elements

In order to eventually solve for the values of the unknown ball deflections r_b and z_b, it is necessary to introduce another set of equations. This can be achieved by enforcing radial, axial and pivotal equilibrium on each ball:

$$Q_i \cos\alpha_i + F_i \sin\alpha_i - Q_o \cos\alpha_o - F_o \sin\alpha_o = -F_c \tag{3.79}$$

$$Q_i \sin\alpha_i - F_i \cos\alpha_i - Q_o \sin\alpha_o + F_o \cos\alpha_o = 0 \tag{3.80}$$

$$F_i + F_o = \frac{2M_g}{D} \tag{3.81}$$

where Q^e are the normal loads and F^e are the frictional loads at each contact. The dynamic loads F^c and M_g are the centrifugal load and gyroscopic moment on each element as shown in Fig. 3.11, which will be derived over the next sections.

3.2.5.3 Ball velocities

In order to compute the dynamic loads, it is first necessary to specify the velocities of the balls using a kinematic analysis. Each ball orbits around the z axis of the bearing

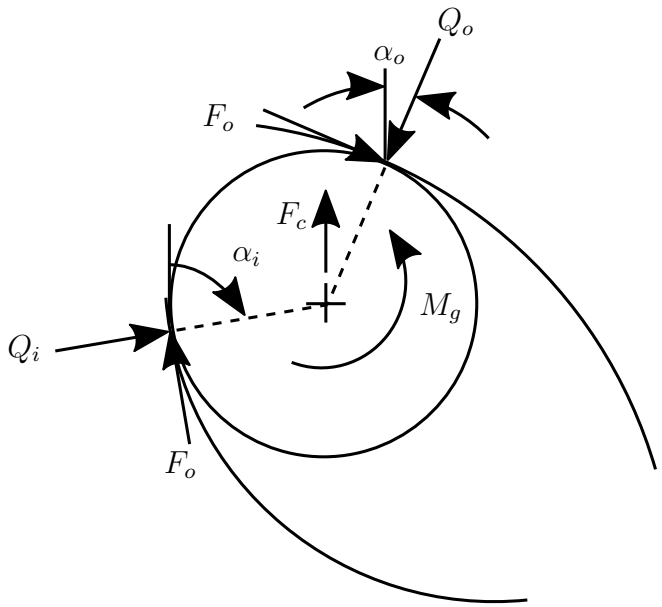


Figure 3.11: Free-body force diagram of ball at high-speeds

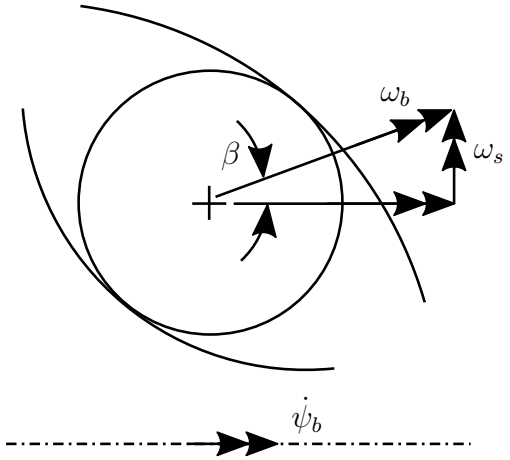


Figure 3.12: Definition of ball velocities

with a speed $\dot{\psi}_b$. In addition, each elements is able to roll and spin around its own axis, with a velocity ω_b. This has a component orthogonal to the axis of rotation z, which is known as the spin speed and is denoted by ω_s, as depicted in Fig. 3.12. Although the ball may also have some angular velocity about an axis through the page, which is termed gyroscopic motion, this can usually be assumed negligible compared to the rolling and spin velocities [45]. The element orbital speed linearly depends on the rotation speed of the inner and outer rings, denoted by Ω_i and Ω_o.

$$\dot{\psi}_b = (1 - \nu_m)\Omega_o + \nu_m\Omega_i \tag{3.82}$$

where the speed ratio ν_m can be found from kinematics [44, 45]:

$$\nu_m = \frac{1}{1 + \frac{1+\gamma\cos\alpha_o}{1-\gamma\cos\alpha_i}\frac{\cos\alpha_i+\tan\beta\sin\alpha_i}{\cos\alpha_o+\tan\beta\sin\alpha_o}} \tag{3.83}$$

where the ratio $\gamma \coloneqq \frac{D}{d_m}$. The resultant ball speed ω_b is also linearly proportional to the ring speeds. In this case, it scales with the difference in ring speeds:

$$\omega_b = \nu_s \left(\Omega_o - \Omega_o\right) \tag{3.84}$$

where the speed ratio ν_s can again be computed from kinematics [44, 45]:

$$\nu_s = \frac{1}{\left(\frac{\cos\alpha_o+\tan\beta\sin\alpha_o}{1+\gamma\cos\alpha_o} + \frac{\cos\alpha_i+\tan\beta\sin\alpha_i}{1-\gamma\cos\alpha_i}\right)\gamma\cos\beta} \tag{3.85}$$

Unfortunately this does not yet allow the orbital velocity $\dot{\psi}_b$ and rotational velocity ω_b to be computed, since the angle β is unknown. One approach is to add additional states for the velocity of each element, and to incorporate models for the rolling-resistance and cage interactions [172,173]. However, since the dynamics of these DOF are normally very fast, a very small time step would be required to accurately simulate this.

An alternative approach is to add a kinematic constraint, so that it is possible to instead solve for the angle β. The most common approach is the "Control Theory" hypothesis from [44]. This assumes that there are only frictional loads at either the inner or outer case, which is termed the race in "control". It is also assumed that there is no slip at the contact in control. In the case of outer race control, the angle β is given by:

$$\tan\beta = \frac{\sin\alpha_o}{\cos\alpha_o + \gamma} \tag{3.86}$$

and for inner race control:

$$\tan\beta = \frac{\sin\alpha_i}{\cos\alpha_i - \gamma} \tag{3.87}$$

Now that both $\dot{\psi}_b$ and ω_b are known, it is possible to compute the ball spin speed from:

$$\omega_s = \omega_b \sin\beta \tag{3.88}$$

After application of the control theory hypothesis, it should be verified that the rolling moment is larger on the race which is in "control" [44]. This may also not be the same for every ball. The conditions for inner and outer-race control depend on the loads Q_e and

some geometric parameters, and are given in [44]. One important special case is where the bearing contact angle is 0. In this case, the speed ratio ν_m reduces to:

$$\nu_m = \frac{1}{2}(1-\gamma)$$

and the balls do not spin so that $\nu_s = 0$.

3.2.5.4 Dynamic ball loads

Now that the ball velocities have been defined, the dynamic loads on the balls can be computed. The outward centrifugal load F_c on each ball is given by [45]:

$$F_c = \frac{1}{2} m_b d_m \dot{\psi}_b^2 \tag{3.89}$$

where m_b is the ball mass, and $\dot{\psi}_b$ is the ball orbital speed, given by Eq. (3.82). The gyroscopic moment is given by:

$$M_g = J_b \dot{\psi}_b \omega_s \tag{3.90}$$

where J_b is the ball moment of inertia, and ω_s is the spin velocity. The frictional loads can then be found directly by solving Eq. (3.81), and applying the race-control hypothesis. For outer raceway control, all the load will be resisted at the outer contact, and vice versa, so that the frictional forces can be written as:

$$F_i = \lambda_i \frac{2}{D} M_g \tag{3.91}$$

$$F_o = \lambda_o \frac{2}{D} M_g \tag{3.92}$$

where $\lambda_i = 1$ and $\lambda_o = 0$ for inner raceway control, and $\lambda_i = 0$ and $\lambda_o = 1$ for outer raceway control.

3.2.5.5 Solution for ball deflections

In order to solve for the unknown ball deflections r_b, z_b, the contact loads from Eq. (3.60) and dynamic loads from Eqs. (3.89) and (3.90) can be substituted into the equilibrium relations in Eqs. (3.79) and (3.80) to yield an algebraic problem in the elemental deflections r_b, z_b. In order to solve this problem numerically, it is convenient to introduce the following radial and axial forces residuals as:

$$\Delta F_r = Q_{i,j}\cos\alpha_{i,j} + F_{i,j}\sin\alpha_{i,j} - Q_{o,j}\cos\alpha_{o,j} - F_{o,j}\sin\alpha_{o,j} + F_{c,j}$$
$$\Delta F_z = Q_{i,j}\sin\alpha_{i,j} - F_{i,j}\cos\alpha_{i,j} - Q_{o,j}\sin\alpha_{o,j} + F_{o,j}\cos\alpha_{o,j}$$

which then allow the ball deflections to be found from a Newton-Raphson approach:

$$\begin{bmatrix} r_b \\ z_b \end{bmatrix}_{k+1} = \begin{bmatrix} r_b \\ z_b \end{bmatrix}_{k} - \begin{bmatrix} \frac{\partial}{\partial r_b}(\Delta F_r) & \frac{\partial}{\partial r_b}(\Delta F_r) \\ \frac{\partial}{\partial z_b}(\Delta F_z) & \frac{\partial}{\partial z_b}(\Delta F_z) \end{bmatrix}_{k}^{-1} \begin{bmatrix} \Delta F_r \\ \Delta F_z \end{bmatrix}_{k} \tag{3.93}$$

where the derivatives in the Jacobian are to be computed numerically. This relation is iterated until the equilibrium relations in Eq. (3.79) are satisfied to a tolerance of $1 \times 10^{-8}\,\mathrm{N}$. Once the ball deflections have been found, the ball deflections can be computed from Eqs. (3.75) and (3.76). These deflections can then be substituted into the Hertzian contact law in Eq. (3.60) to compute the contact loads. This completes the derivation of the high-speed contact model.

3.2.6 Total ring loads

Once the contact and frictional Q_j^e and F_j^e have been found using the relevant contact model from either Section 3.2.4 or Section 3.2.5, the total loads on the inner ring, $\boldsymbol{f}_b^i$, and outer ring, $\boldsymbol{f}_b^o$ can be computed. The contributions from each element can be summed up, taking their angular position into account (see Fig. 3.7):

$$\boldsymbol{f}_b^e(\boldsymbol{x}_b, \psi_c, \Omega_e) = \begin{bmatrix} f_x^e \\ f_y^e \\ \tau_x^e \\ \tau_y^e \end{bmatrix} = \sum_{j=1}^{Z} \boldsymbol{T}(\psi_j)^T \boldsymbol{R}(\alpha_j^e) \begin{bmatrix} Q_j^e \\ F_j^e \end{bmatrix} \tag{3.94}$$

where $\boldsymbol{T}$ is the transformation matrix from Eq. (3.59). The matrix $\boldsymbol{R}$ rotates the normal and tangential forces at the contact into radial and axial components and is given by:

$$\boldsymbol{R}(\alpha) = \begin{bmatrix} \cos\alpha & \sin\alpha \\ \sin\alpha & -\cos\alpha \end{bmatrix} \tag{3.95}$$

It should be noted that the total ring load, $\boldsymbol{f}_b^e$, depends on cage position ψ_c due to variable compliance, and ring speeds Ω_e due to dynamic loading on the elements. The bearing stiffness matrix $\boldsymbol{K}_b$ could be found by summing up the contributions from each element. However, this requires differentiation of the contact forces and contact angles w.r.t the

bearing displacements. If certain approximations are made, it is possible to derive very complex analytical expressions for the stiffness matrix [48]. In this thesis, the stiffness will instead be computed by numerically differentiating the bearing forces.

3.2.6.1 Ball pass frequency

Due to the cyclic-symmetry of the cage, an element will pass a particular location at a frequency known as the "Ball Pass Frequency" (BPF). This is also the frequency at which the bearing load and stiffness will oscillate due to "variable compliance", which can lead to a harmonic forcing on the structures connected via the bearings, even without any external excitation. The BPF is given by:

$$\omega_{BPF} = Z\dot{\psi}_c \tag{3.96}$$

where $\dot{\psi}_c$ is the rotation speed of the cage. Since the cage will rotate with the elements, this should be the same as the instantaneous orbital speed of the elements $\dot{\psi}_b$ from Eq. (3.82). However, the orbital speed of each element will fluctuate slightly due to changes in the contact angle, so that this approach would yield Z different values for the cage speed. To avoid this, the cage speed ratio was evaluated using Eq. (3.83) with the elements in the setup position where $\alpha_i = \alpha_o = \alpha_0$, which will yield a single "average" value for the cage speed.

3.2.7 Sjovall integral formulation

Although the effect of VC can be significant, the compliance oscillations are often ignored in the first instance, by computing the *average* load and stiffness in each direction. This decouples the influence of the bearing displacement $\boldsymbol{x}_b$, from the influence of the cage angle ψ_c, on the bearing load and stiffness [49, 89]. The average properties can be computed by considering the case of an infinite number of elements where the discrete ball locations ψ_j are replaced with a continuous domain ψ. The load per unit angle around the bearing can then be computed from the contact model:

$$\bar{Q}^e(\psi) = \frac{Z}{2\pi} h_e\left(r(\psi), z(\psi)\right) \tag{3.97}$$

where $h_e(r, z)$ is the appropriate contact model from Section 3.2.4 or Section 3.2.5. A comparison of this continuous load distribution and the discrete element loads for the same applied load is plotted in Fig. 3.13. It can be observed that the load is more unevenly distributed when there are discrete elements, with those at the bottom of the

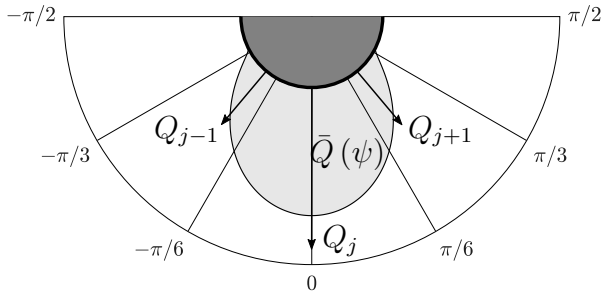


Figure 3.13: Comparison of continuous load distributions and discrete element loads

bearing being most highly loaded in this particular example. Rather than summing up the loads, the average ring load $\bar{\boldsymbol{f}}_b^e$ can be computed using an integral formulation [52]:

$$\bar{\boldsymbol{f}}_b^e(\boldsymbol{x}_b, \Omega_e) = \begin{bmatrix} \bar{f}_x^e \\ \bar{f}_y^e \\ \bar{\tau}_x^e \\ \bar{\tau}_y^e \end{bmatrix} = \int_0^{2\pi} \boldsymbol{T}(\psi)^T \boldsymbol{R}(\alpha(\psi)) \begin{bmatrix} \bar{Q}^e(\psi) \\ \bar{F}^e(\psi) \end{bmatrix} d\psi \tag{3.98}$$

where the transformation matrix $\boldsymbol{T}$ is from Eq. (3.59) and the rotation matrix $\boldsymbol{R}$ is from Eq. (3.95). This average load smooths out any fluctuations due to cage position, and is independent of the cage rotation angle ψ_c. However, it may still depend on the ring speeds Ω_e due to dynamic loads on the balls.

3.2.8 Summary

A general quasi-static model of a ball bearing has been presented which is able to capture the influence of internal bearing clearance and dynamic loading on the elements. Two different approaches have been presented for calculating the bearing load and stiffness; one which is time-varying and captures the variable compliance of the bearing, and another integral-based formulation which yields the average stiffness and is independent of cage angle. This model can now be integrated in a model of a rotating-machine.

3.3 Harmonic balance method

The rolling-element bearing model presented in Section 3.2 was shown to be fundamentally non-linear in nature. This means that once it is incorporated into the model of a rotating machine from Section 3.1, the equations of motion will also be non-linear, so that standard linear techniques are no longer applicable for a rigorous dynamic analysis. Such models could be simulated in the time domain, but they can be analysed more efficiently

in the frequency domain using the Harmonic Balance Method (HBM). A brief summary of this approach will now be introduced.

3.3.1 Equation of motion

To begin, the non-linear equation of motion for a general rotating machine from Eq. (3.49) will be re-written in the following form:

$$\boldsymbol{M}\ddot{\boldsymbol{x}} + \boldsymbol{C}\dot{\boldsymbol{x}} + \boldsymbol{K}\boldsymbol{x} + \boldsymbol{f}_{nl}\left(\boldsymbol{x}, \dot{\boldsymbol{x}}\right) = \boldsymbol{f}(t) \tag{3.99}$$

where the non-linear forces now include both the non-linear bearing forces and the gyroscopic forces (which are non-linear due to the dependence on rotation speed Ω):

$$\boldsymbol{f}_{nl}\left(\boldsymbol{x}, \dot{\boldsymbol{x}}, t\right) = \boldsymbol{f}_{b}\left(\boldsymbol{x}, \dot{\boldsymbol{x}}\right) + \Omega \boldsymbol{G}\dot{\boldsymbol{x}} \tag{3.100}$$

and the excitation force $\boldsymbol{f}(t)$ contains both the gravitational load as well as any harmonic forces, such as those from unbalances on the rotor:

$$\boldsymbol{f}(t) = \boldsymbol{f}_{e}(t) + \boldsymbol{f}_{g} \tag{3.101}$$

The equation of motion for the rotating machine has now been expressed in a form to which harmonic balance can now be applied.

3.3.2 Hyper-time representation

Conventional HBM assumes the system is excited at a single frequency denoted by ω, so that the response is periodic. Under these assumptions, the response can be written as a sum of harmonics of the excitation frequency [174]:

$$\boldsymbol{x}(t) = \Re\left(\sum_{0}^{M_{tot}^{H}} \boldsymbol{X}_{k_1,k_2} e^{ik\omega t}\right)$$

where each frequency component can be written as $\omega_k = k\omega_0$. The number of harmonics included is denoted by M_{tot}^{H}. Typically more harmonics can be included to improve the accuracy of the solution.

If a system is excited at two frequencies ω_1 and ω_2, the system will no longer respond periodically, unless the ratio between the frequencies happens to be rational. In the general case that the frequencies are not commensurate, the system is said to respond

quasi-periodically; this term emphasises how the response is still harmonic but no longer periodic. Harmonic balance can be extended to deal with such cases, which is known as the Generalised Harmonic Balance Method (GHBM). The response can have more frequency components than with a single base frequency. This is because the system can respond with both harmonics of the two frequencies, as well as various cross-terms. Mathematically, each frequency component can be expressed as follows [152, 154]:

$$\omega_{k_1,k_2} = k_1\omega_1 + k_2\omega_2 \tag{3.102}$$

The response of the system can then be written in the following form:

$$\boldsymbol{x}(t_1,t_2) = \Re\left(\sum_{k_1,k_2\in P} \boldsymbol{X}_{k_1,k_2} e^{i(k_1\omega_1 t_1 + k_2\omega_2 t_2)}\right) \tag{3.103}$$

where $\boldsymbol{X}_{k_1,k_2}$ is a complex phasor representing the amplitude and phase of the component at the frequency ω_{k_1,k_2}. A multi-dimensional time domain (also called hypertime) has been introduced, within which the true time domain is merely one line within hypertime; the line corresponding to $t_1 = t_2 = t$, as depicted visually in Fig. 3.14.

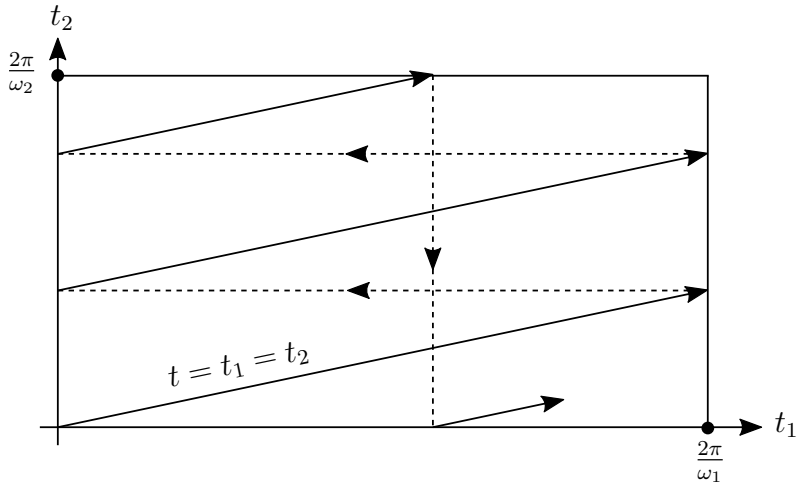


Figure 3.14: Depiction of hyper-time for quasi-periodic orbits

The set of integers P must be somehow truncated, but there are several strategies for achieving this [151]. One possible set is given by [59]:

$$P = \left\{k_1, k_2 \in \mathbb{Z} : -M_1^H \leq k_1 \leq M_1^H, -M_2^H \leq k_2 \leq M_2^H, k_1\omega_1 + k_2\omega_2 \geq 0\right\} \tag{3.104}$$

where M_1^H and M_2^H are constants. This set is depicted in Fig. 3.15 for the case of $M_1^H = 5, M_2^H = 3$. This leads to a total of M_{tot}^H included harmonics, given by [151]:

$$M_{tot}^H = \frac{(2M_1^H + 1)(2M_2^H + 1) + 1}{2}$$

Typically the larger the values of M_1^H, M_2^H, the greater the accuracy, at the expense of computational cost.

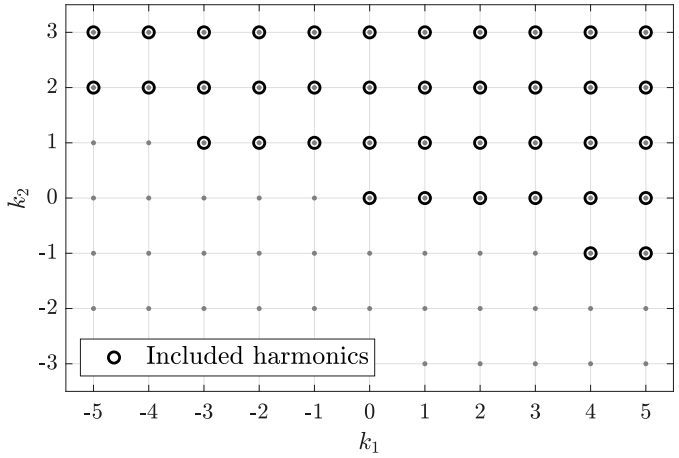


Figure 3.15: Set of harmonics included in GHBM $\left(M_1^H = 5, M_2^H = 3\right)$

In order to compute the time derivative whilst using this multi-dimensional time domain, it should be noted that:

$$\dot{\boldsymbol{x}} = \frac{\partial \boldsymbol{x}}{\partial t} = \sum_i \frac{\partial \boldsymbol{x}}{\partial t_i}\frac{\partial t_i}{\partial t} = \sum_i \frac{\partial \boldsymbol{x}}{\partial t_i}$$

since $\frac{\partial t_i}{\partial t} = 1$ for all i. Upon application of these relations to the expression for the displacement $\boldsymbol{x}$, the following expression for the velocity $\dot{\boldsymbol{x}}$ can be derived:

$$\dot{\boldsymbol{x}}(t_1, t_2) = \Re\left(\sum_{k_1,k_2 \in P} i\omega_{k_1,k_2} \boldsymbol{X}_{k_1,k_2} e^{i(k_1\omega_1 t_1 + k_2\omega_2 t_2)}\right) \tag{3.105}$$

where it can be observed that the complex phasor $\boldsymbol{X}_{k_1,k_2}$ has been pre-multiplied by $i\omega_{k_1,k_2}$. This corresponds to differentiation in the frequency domain.

3.3.3 Imposing harmonic balance

The expressions for the displacement $\boldsymbol{x}$ and velocity $\dot{\boldsymbol{x}}$ can again be substituted into the equations of motion in Eq. (3.99). The components at each frequency can be equated to yield M_{tot}^H equations of the form:

$$\left[-\omega_{k_1,k_2}^2 \boldsymbol{M} + i\omega_{k_1,k_2}\boldsymbol{C} + \boldsymbol{K}\right] \boldsymbol{X}_{k_1,k_2} + \boldsymbol{F}_{k_1,k_2} = \boldsymbol{U}_{k_1,k_2} \tag{3.106}$$

where $\boldsymbol{U}_{k_1,k_2}$ is the complex phasor of the excitation forces which can typically be specified directly. However, the complex phasor of the non-linear forces, denoted by $\boldsymbol{F}_{k_1,k_2}$, is unknown and must be computed. These M_{tot}^H equations can be combined into one equation by combining the phasors $\boldsymbol{X}_{k_1,k_2}$ into the vector $\boldsymbol{z}$:

$$\begin{aligned}\boldsymbol{z} = [\tilde{\boldsymbol{x}}_{0,0}^T \quad \Re(\tilde{\boldsymbol{x}}_{1,0})^T \quad \Im(\tilde{\boldsymbol{x}}_{1,0})^T \quad \Re(\tilde{\boldsymbol{x}}_{2,0})^T \quad \Im(\tilde{\boldsymbol{x}}_{2,0})^T \\ \ldots \quad \Re(\tilde{\boldsymbol{x}}_{0,1})^T \quad \Im(\tilde{\boldsymbol{x}}_{0,1})^T \ldots \quad \Re\left(\tilde{\boldsymbol{x}}_{M_1^H,M_2^H}\right)^T \quad \Im\left(\tilde{\boldsymbol{x}}_{M_1^H,M_2^H}\right)^T]^T\end{aligned} \tag{3.107}$$

similarly for $\boldsymbol{F}$ and $\boldsymbol{U}$. The algebraic problem in Eq. (3.106) can then be rewritten in the following form [151]:

$$\boldsymbol{r}(\boldsymbol{z},\boldsymbol{\omega}) = \boldsymbol{L}(\boldsymbol{\omega})\boldsymbol{z} + \boldsymbol{h}\left(\boldsymbol{\omega},\boldsymbol{z}\right) + \boldsymbol{g}\left(\boldsymbol{\omega}\right) \tag{3.108}$$

where $\boldsymbol{r}(\boldsymbol{z},\boldsymbol{\omega})$ denotes the residual to be minimised, and the frequency vector $\boldsymbol{\omega}$ contains the two excitation frequencies:

$$\boldsymbol{\omega} = \begin{bmatrix}\omega_1 & \omega_2\end{bmatrix}^T \tag{3.109}$$

The vector $\boldsymbol{h}\left(\boldsymbol{\omega},\boldsymbol{z}\right)$ in Eq. (3.108) contains the non-linear terms in $\boldsymbol{F}_{k_1,k_2}$, and the vector $\boldsymbol{g}\left(\boldsymbol{\omega}\right)$ contains the excitation terms in $\boldsymbol{U}_k$. The term involving the matrix $\boldsymbol{L}(\boldsymbol{\omega})$ is due to the linear parts of the model and has the form [151, 154, 174]:

$$\boldsymbol{L} = \begin{bmatrix} \boldsymbol{L}_{0,0} & \boldsymbol{0} & \ldots & \ldots & \ldots & \boldsymbol{0} \\ \boldsymbol{0} & \boldsymbol{L}_{1,0} & \ldots & \ldots & \ldots & \boldsymbol{0} \\ \vdots & \vdots & \ddots & \ldots & \ldots & \vdots \\ \vdots & \vdots & \vdots & \boldsymbol{L}_{0,1} & \ldots & \vdots \\ \vdots & \vdots & \vdots & \vdots & \ddots & \vdots \\ \boldsymbol{0} & \ldots & \vdots & \ldots & \ldots & \boldsymbol{L}_{M_1^H,M_2^H} \end{bmatrix} \tag{3.110}$$

with $\boldsymbol{L}_{0,0} = \boldsymbol{K}$, but for all other k_1 and k_2 $\boldsymbol{L}_{k_1,k_2}$ is given by:

$$\boldsymbol{L}_{k_1,k_2} = \begin{bmatrix} \boldsymbol{K} - \omega_{k_1,k_2}^2\boldsymbol{M} & -\omega_{k_1,k_2}\boldsymbol{C} \\ \omega_{k_1,k_2}\boldsymbol{C} & \boldsymbol{K} - \omega_{k_1,k_2}^2\boldsymbol{M} \end{bmatrix}$$

The final stage of GHBM is to compute the non-linear terms $\boldsymbol{F}_{k_1,k_2}$, which will now be presented.

3.3.4 Alternating Frequency-Time

These non-linear phasors $\boldsymbol{F}_{k_1,k_2}$ can be computed using an Alternating Frequency Time (AFT) approach [175]. The general idea is to convert the complex phasors representation $\boldsymbol{X}_{k_1,k_2}$ from the frequency domain into the time-domain, where the non-linear forces can be evaluated explicitly using Eq. (3.100). The forces can then be converted from the frequency domain back into the time domain to yield $\boldsymbol{F}_{k_1,k_2}$. The AFT approach can be extended to the general case with two base frequencies, by evaluating the non-linear forces in the hyper-time domain. The whole AFT process can be summarised as [154]:

$$\boldsymbol{X}_{k_1,k_2} \xrightarrow{\text{IFFT}} \boldsymbol{x}(t_1,t_2) \rightarrow \boldsymbol{f}_{nl}(\boldsymbol{x}(t_1,t_2),\dot{\boldsymbol{x}}(t_1,t_2)) \xrightarrow{\text{FFT}} \boldsymbol{F}_{k_1,k_2}$$

where the Inverse Fast Fourier Transform (IFFT) operation can be implemented using the harmonic series in Eq. (3.103). The Fast Fourier Transform (FFT) operation can be implemented using a multi-dimensional Fourier series approach:

$$\boldsymbol{F}_{k_1,k_2} = \begin{cases} \frac{1}{T_1 T_2}\int_0^{T_2}\int_0^{T_1} \boldsymbol{f}_{nl}(t_1,t_2)dt_1dt_2 & \text{for } k_1 = k_2 = 0 \\ \frac{2}{T_1 T_2}\int_0^{T_2}\int_0^{T_1} \boldsymbol{f}_{nl}(t_1,t_2)e^{i(k_1\omega_1 t_1 + k_2\omega_2 t_2)}dt_1dt_2 & \text{otherwise} \end{cases} \tag{3.111}$$

When implementing the AFT process numerically, the time domain will be discretised with M_1^T and M_2^T points over each axis of hypertime. A sufficient number of points must be selected to avoid aliasing of the higher harmonics present in the non-linear forces [175]. It is possible to compute the non-linear term $\boldsymbol{h}(\boldsymbol{\omega},\boldsymbol{z})$ directly from the vector $\boldsymbol{z}$, which is discussed in more detail in Appendix A. The complete AFT process has now been presented, and all terms within the equation for harmonic balance in Eq. (3.108) have now been defined. The harmonic balance equation in Eq. (3.108) can now be solved for a given set of base frequencies in $\boldsymbol{\omega}$ to find the quasi-periodic response of the system.

3.3.5 Stability

In nonlinear systems, some of the periodic solutions found from HBM will actually become unstable, and the system will diverge from the solution over time. The stability can be assessed with Hill's method [174], which yields approximate values of the Floquet exponents λ using a standard HBM formulation. If these are in the right half-plane, then the solution is unstable, and vice versa. It was demonstrated in [174] that, under the

assumption that the perturbation varies slowly with time, the Floquet exponents for a periodic response can be computed from the following quadratic eigenvalue problem:

$$\boldsymbol{A}\lambda^2 + \boldsymbol{B}\lambda + \frac{\partial \boldsymbol{r}}{\partial \boldsymbol{z}} = 0 \tag{3.112}$$

The terms involving $\boldsymbol{A}$ and $\boldsymbol{B}$ arise from the linear parts of the model, whilst the Jacobian $\frac{\partial \boldsymbol{r}}{\partial \boldsymbol{z}}$ contains additional contributions from the non-linearities. The matrix $\boldsymbol{A}$ is block-diagonal and given by $\boldsymbol{A} = \boldsymbol{I}_{M_{tot}^H} \otimes 2\boldsymbol{M}$ [174]. The matrix $\boldsymbol{B}$ is of a very similar form to the matrix $\boldsymbol{L}$ in Eq. (3.110) [174]:

$$\boldsymbol{B} = \begin{bmatrix} \boldsymbol{B}_0 & \boldsymbol{0} & \dots & \dots & \boldsymbol{0} \\ \boldsymbol{0} & \boldsymbol{B}_1 & \dots & \dots & \boldsymbol{0} \\ \vdots & \vdots & \boldsymbol{B}_2 & \dots & \vdots \\ \vdots & \vdots & \vdots & \ddots & \vdots \\ \boldsymbol{0} & \dots & \dots & \dots & \boldsymbol{B}_{M_H} \end{bmatrix}$$

where $\boldsymbol{B}_0 = \boldsymbol{C}$ but for all other k:

$$\boldsymbol{B}_k = \begin{bmatrix} \boldsymbol{C} & -2\omega_k \boldsymbol{M} \\ 2\omega_k \boldsymbol{M} & \boldsymbol{C} \end{bmatrix} \tag{3.113}$$

where ω_k denotes the kth frequency component included in the HBM problem, and M_H is the number of harmonics included.

Hill's method is only valid for periodic responses, and there is no equivalent when the response is quasi-periodic, so it is not possible to directly apply Hill's method to the solution found from GBHM in Section 3.3.2. However, it is possible to make the "adjusted HBM" approximation [151], where the two base frequencies are adjusted to be commensurate so that the response becomes periodic. To begin, the ratio of the two base frequencies $\frac{\omega_1}{\omega_2}$ can be approximated as the ratio of two integers p and q (to a specified tolerance):

$$\frac{\omega_1}{\omega_2} \approx \frac{p}{q} \tag{3.114}$$

which then means that the two base frequencies are no longer incommensurate. Using this approximation, each frequency component from GHBM in Eq. (3.102) can be rewritten as:

$$\begin{aligned}\omega_{k_1,k_2} &= k_1\omega_1 + k_2\omega_2 \\ &\approx (k_1 + k_2\frac{p}{q})\omega_1 \\ &\approx (k_1 q + k_2 p)\frac{\omega_1}{q}\end{aligned}$$

It can be observed that the base frequency of adjusted HBM is given by $\omega_0 = \frac{\omega_1}{q}$, and each approximated frequency component ω_k can therefore be written as:

$$\omega_k = (k_1 q + k_2 p)\omega_0 \tag{3.115}$$

The approximate frequencies ω_k from Eq. (3.115) can then be substituted into Section 3.3.5 to compute the value of the matrix $\boldsymbol{B}$. They can then also be used to compute the adjusted HBM Jacobian $\frac{\partial \boldsymbol{r}}{\partial \boldsymbol{z}}$ using the approach in Section 3.3.2; the second base frequency can be removed by setting $M_2^H = 0$, thereby reducing GHBM to standard HBM. This Jacobian can then be substituted into Eq. (3.112) to solve for the approximate Floquet exponents.

3.3.6 Frequency response

The frequency response function (FRF) characterises how the system responds to excitations at each frequency. For linear-systems, this fully characterises the system, but for non-linear systems, this function must be computed for a given amplitude. The FRF can become multi-valued at certain frequencies for non-linear systems as will be shown later, which leads to different responses to upward and downward frequency sweeps. Although it is possible to solve Eq. (3.108) sequentially for each frequency [176], this can miss sections of the response curve. Instead, a solution tangential to the previous solution needs to be found at each step, which is known as continuation.

It is first necessary to describe how the two base frequencies are to vary. In this thesis, the two base frequencies were assumed to be proportional to each other, so could be written as:

$$\boldsymbol{\omega} = \boldsymbol{\nu}\mu$$

where μ is the variable which scales the excitation frequencies, and can now be used as the continuation parameter. This can then be substituted into Eq. (3.108) to yield:

$$\boldsymbol{r}(\boldsymbol{z}, \boldsymbol{\nu}\mu) = \mathbf{0}$$

which is to be solved for a range of values for μ. A variety of algorithms can be found in [177] to solve problems like this. For this work, a pseudo-arc length predictor-corrector method was used, where the tangent at the current point is used to predict the next solution, and then the problem is linearised in the corrector stage to find an exact solution [178, 179]. This approach will now be briefly summarised.

3.3.6.1 Predictor

The phasor vector $\boldsymbol{z}$ and frequency scale μ can first be combined into one vector $\tilde{\boldsymbol{z}}$:

$$\tilde{\boldsymbol{z}} = \begin{bmatrix} \boldsymbol{z}^T & \mu \end{bmatrix}^T \tag{3.116}$$

In the predictor stage, an approximate solution is found using the tangent $\boldsymbol{t}_i$ at the previous solution:

$$\tilde{\boldsymbol{z}}_{i+1} = \tilde{\boldsymbol{z}}_i + \triangle s \cdot \boldsymbol{t}_i \tag{3.117}$$

where $\triangle s$ is the desired step size and $\boldsymbol{t}_i$ is a tangent vector. This can be computed by first computing the Jacobian w.r.t $\tilde{\boldsymbol{z}}$:

$$\frac{\partial \boldsymbol{r}}{\partial \tilde{\boldsymbol{z}}} = \begin{bmatrix} \frac{\partial \boldsymbol{r}}{\partial \boldsymbol{z}} & \frac{\partial \boldsymbol{r}}{\partial \mu} \end{bmatrix} \tag{3.118}$$

where the derivative w.r.t the frequency scale μ is given by:

$$\frac{\partial \boldsymbol{r}}{\partial \mu} = \boldsymbol{\nu}^T \frac{\partial \boldsymbol{r}}{\partial \boldsymbol{\omega}} \tag{3.119}$$

The tangent vector $\boldsymbol{t}_i$ can then be found from the null-space of this Jacobian in Eq. (3.118):

$$\boldsymbol{t}_i = \text{null}\left(\left[\frac{\partial \boldsymbol{r}}{\partial \tilde{\boldsymbol{z}}} \right]_i \right) \tag{3.120}$$

where $\boldsymbol{t}_i$ is normalised so that $|\boldsymbol{t}|_2 = 1$. It is shown how to compute the two terms $\frac{\partial \boldsymbol{r}}{\partial \boldsymbol{z}}$ and $\frac{\partial \boldsymbol{r}}{\partial \boldsymbol{\omega}}$ analytically in Appendix A. This completes the derivation of the predictor.

3.3.6.2 Corrector

This solution from the predictor will not be exact, so a corrector stage is necessary. Pseudo-inverse corrections must be applied iteratively, until Eq. (3.116) is solved to the

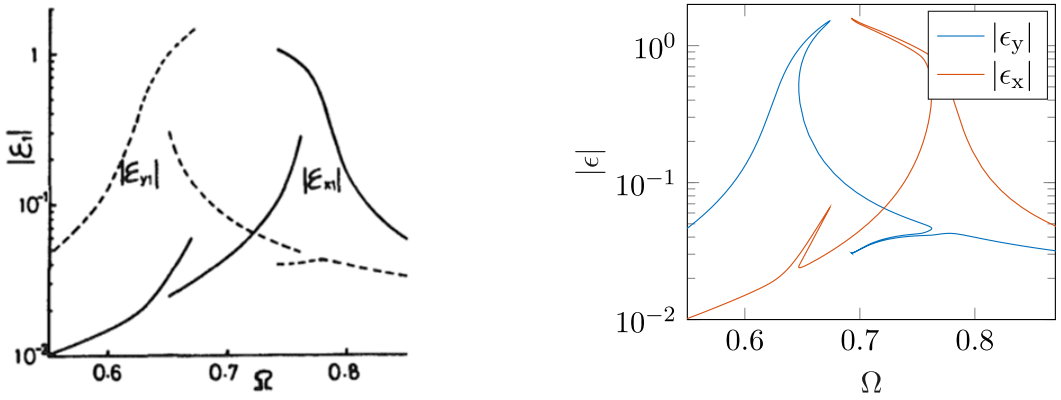
required degree of accuracy as shown below [179]:

$$\tilde{\boldsymbol{z}}_{i+1} = \tilde{\boldsymbol{z}}_i - \left[\frac{\partial \boldsymbol{r}}{\partial \tilde{\boldsymbol{z}}}\right]_i^+ \boldsymbol{r}(\tilde{\boldsymbol{z}}_i) \tag{3.121}$$

The final stage is to adjust the step size $\triangle s$ in order to speed up computation, using some heuristics. Typically the step size is increased when the corrector converges in very few iterations. Similarly, the step size is decreased when the corrector takes many iterations to converge or fails to converge at all. The computation is to be terminated if the corrector fails to converge even after reducing the step size a certain number of times.

3.3.7 MATLAB implementation

The HBM presented here was implemented in a MATLAB toolbox, called HarmLAB [180]. The open-source optimiser IP-OPT [181] was used to solve for a single quasi-periodic response. The pseudo arc-length continuation algorithm from Section 3.3.6 was implemented in order to allow non-linear FRFs to be computed. The toolbox was validated by computing the response of simple mass-spring-damper systems with non-linear stiffness and damping, using both HarmLAB and time integration, and verifying that the results from the two approaches agree. Additionally, some results from the literature were reproduced. For example, the non-linear frequency response of a rotor mounted on a loose bearing from [62] is shown in Fig. 3.16.



(a) Results from Saito [62]

(b) Results from HarmLAB

Figure 3.16: Validation of HarmLAB

3.4 Summary

A complete approach for modelling rotor-bearing systems with flexible shafts and rigid discs has been presented in Section 3.1, which has been implemented in the ROLADYN

toolbox. A high-fidelity non-linear bearing model was presented in Section 3.2, which captures the key physics in the bearing, whilst remaining quite fast to evaluate, so is ideal for integrating into the ROLADYN model of the rotating machine.

Linearised analysis, including computing natural frequencies and mode shapes, can be carried out using the ROLADYN model. However, for a fully non-linear treatment, the GHBM presented in Section 3.3 can be used, which is able to directly solve for quasi-periodic rotor responses, thereby avoiding computationally expensive time-integration. A continuation algorithm was presented allowing non-linear FRFs to be computed.

Chapter 4

Parametric study of a Jeffcott rotor supported by a deep-groove ball bearing

Rolling-element bearings are a potential source of non-linearity within rotating machinery, and hence there is a strong need to accurately predict their influence on the response of such systems. Although the effect of rolling-element bearings on the nonlinear dynamic response of rotor systems has been studied in great detail, little attention has been paid to the influence of the different physical mechanisms. Previous studies have also been limited by the available numerical techniques, and often only individual effects were investigated.

In this chapter, an in-depth study on a simplified rotor-bearing system will be carried out, which was initially published in [182]. The high fidelity rolling-element bearing model from Section 3.2 will be applied to the case of an unbalanced Jeffcott rotor supported by a deep-groove ball bearing (DGBB), to study the non-linear vibration transmission through the bearing. The Generalised Harmonic Balance Method (GHBM) from Section 3.3 will be applied in a novel way in order to also capture the quasi-periodicity in the rotor response due to variable compliance, which is otherwise often ignored.

An extensive parameter study will then be performed using this approach, in order to quantify the influence of the different physical effects in the bearing. Particular attention will be paid to providing physical explanations for the observed non-linear behaviour of the system. The parameter study will include internal radial clearance, compliance of the outer ring, centrifugal loading on the elements, and finally compliance in the stator supporting the bearing.

4.1 Deep-groove ball-bearing model

The bearing was chosen to be a SKF6002 deep-groove ball bearing (DGBB), which has already been examined in the literature by multiple authors [64, 73, 86, 144]. These bearings typically consist of a single row of spherical elements held in place by a cage, and are designed to resist primarily radial load. This bearing arrangement is depicted in Fig. 4.1. Note that the contact angle α_0 is zero.

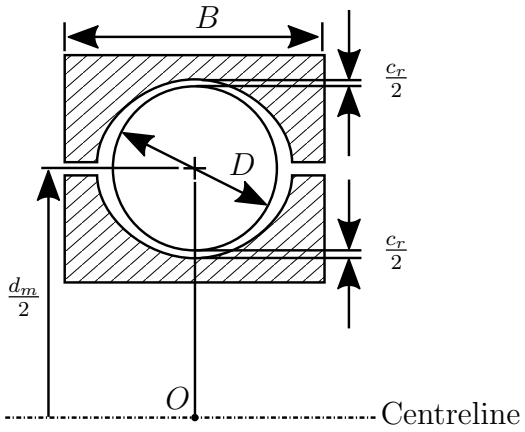


Figure 4.1: Bearing dimensions

4.1.1 Parameters

This bearing has known parameters which are listed in Table 4.1. The radial clearance is denoted by c_r, but this can vary depending on the bearing. Small clearance corresponds to the SKF designation C2, whereas large clearance corresponds to C5.

Table 4.1: SKF 6002 dimensions [144]

Symbol	Description	Value	Units
Z	Number of balls	9	-
B	Outer ring width	9	mm
D	Ball diameter	4.76	mm
d_m	Diameter between ball centres	23.5	mm
c_r	Radial clearance	2.5 (C2) 20 (C5)	µm

The values of the inner and outer race contact stiffness parameters for the SKF6002 bearing considered in this paper were obtained from [144] and are shown in Table 4.2.

Table 4.2: SKF 6002 contact parameters [144]

Symbol	Description	Value	Units
C_i	Stiffness constant of inner contact	1.939×10^{10}	$\mathrm{N\,m^{-3/2}}$
C_o	Stiffness constant of outer contact	2.055×10^{10}	$\mathrm{N\,m^{-3/2}}$

4.1.2 Simplified Model

The bearing model from Section 3.2 is able to accurately predict the behaviour of any type of ball bearing, including the DGBB used in this study. However, it is possible to make some simplifications for this type of bearing, in order to speed up the computation. The 2 DOF bearing deflection vector will be defined as:

$$\boldsymbol{x}_b = \begin{bmatrix} \delta_x^b & \delta_y^b \end{bmatrix}^T \tag{4.1}$$

4.1.2.1 Kinematics

If the bearing is only loaded radially, it can be assumed without loss of accuracy that both the rings and elements only move in plane, as shown in Fig. 4.2. The radial ring deflection $r(\psi)$ around the bearing can now be written simply as [46]:

$$r(\psi) = \delta_x^b \sin\psi - \delta_y^b \cos\psi - c_r \tag{4.2}$$

where δ_x^b and δ_y^b are the relative horizontal and vertical bearing deflections. As in the bearing model in Section 3.2, the ball is assumed to deflect radially, which is denoted by $r_{b,j}$. However, unlike in Section 3.2, the inner and outer rings of the bearing are no longer assumed rigid, so that the elastic ring deflections v_j^i and v_j^o have been introduced.

With reference to Fig. 4.2, the deflections at the inner, δ_j^i, and outer, δ_j^o, contacts can then be expressed as:

$$\delta_j^i = r(\psi_j) - v_j^i - r_{b,j} \tag{4.3}$$

$$\delta_j^o = -v_j^o + r_{b,j} \tag{4.4}$$

With all the contact deflections defined, attention can move to equilibrium of the elements.

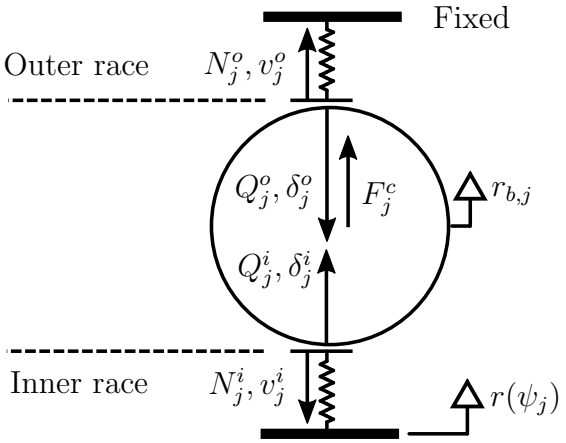


Figure 4.2: Contact forces and deflections

4.1.2.2 Equilibrium

Since the contact angle is zero, the elements will not spin, so there is no gyroscopic moment on the balls. This also means that there are no frictional loads at the contacts. However, the centrifugal load will remain, so the equation enforcing radial equilibrium of the jth ball can be reduced to:

$$Q_j^i - Q_j^o + F_j^c = 0 \tag{4.5}$$

where Q_j^e are the contact loads, and F_j^c are the centrifugal loads on each element as shown in Fig. 4.2. Similarly, the equations for radial equilibrium of the rings is given by:

$$Q_j^e - N_j^e = 0 \tag{4.6}$$

where N_j^e is the radial force reacted by the rings. Now that the contact loads and stiffnesses have been defined, attention can move onto determining the load and stiffness at each element.

4.1.3 Contact model

In Section 3.2.4 and Section 3.2.5, it was shown to be possible to express loads at the contacts as a function of the ring deflections only, once the unknown ball deflections have been solved for. However, for this simplified case with only planar motion, this can be further simplified, since the bearing only deflects radially and there are no frictional loads at the contacts. The contact load can now be expressed as a function of *only* the ring deflection $r(\psi_j)$:

$$Q^e = h_e\left(r(\psi)\right)$$

where the subscript j has been neglected for brevity. This notation will be maintained for the remainder of this section. The function $h_e(r)$ defines what will be referred to as the "contact model" which is consistent with Section 3.2. This expression can be substituted into the equilibrium relation Eq. (4.5), and differentiated with respect to r to give:

$$K = h_i'\left(r(\psi)\right) = h_o'\left(r(\psi)\right)$$

which is the total stiffness of the inner contact, outer contact, and rings in series with each other. It can be observed that this property is the same at either ring. Unlike with the general case where the contact angle can vary, this completely defines the contribution of the given element to the total bearing stiffness, since the contact angle is always zero. In the following sections, different types of contact model will be derived, based upon different assumptions about the speed of the rotor and ring flexibility.

4.1.3.1 Low-speed operation with compliant rings

The simplest case which will be considered is where the bearing operates at low-speed, so that the centrifugal loads can be neglected and $F^c = 0$. As in the general case in Section 3.2.4, the contacts can be combined into a single Hertzian contact, with a combined deflection given by:

$$\delta = \delta^i + \delta^o = r(\psi) - \left(v^i + v^o\right) \tag{4.7}$$

and the contact loads and stiffnesses can be evaluated from the combined contact law in Eqs. (3.70) and (3.72) respectively.

If the compliance arising from the elastic deflection of the rings is to be included in the model, the value of the ring deflections v^e in Eq. (4.7) are unknowns to be found. A simplified ring compliance model based on the recently presented work by Leontiev et al. [55] will be used here, where each ring is divided into Z segments of angle $\Delta\psi$, one for each element in the bearing. Each segment is then allowed to deflect radially by a uniform amount v^e, which leads to a deformation pattern similar to the one shown in Fig. 4.3. Under this assumption, the radial load N^e can then be computed [55]:

$$N^e = \left[\frac{EA_e v^e}{d_e/2} + \frac{EI_e v^e}{\left(d_e/2 \mp v^e\right)^3}\right]\Delta\psi \tag{4.8}$$

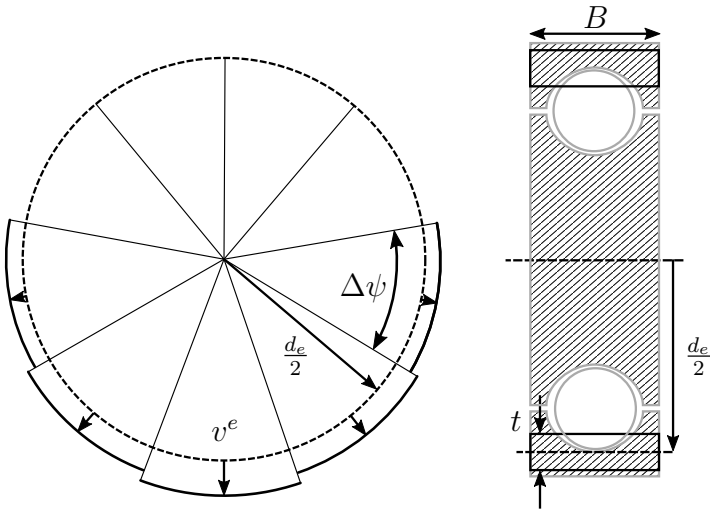


Figure 4.3: Ring compliance model from [55]

where E is the Young's Modulus, A is the area and I is the second moment of area of the outer ring. The first term in Eq. (4.8) is due to circumferential compression of the ring, and the second is due to the change in the curvature; note that the negative sign applies for the case of the inner ring ($e = i$), and the positive sign applies for the case of the outer ring ($e = o$). For the DGBB considered here, the race radius d_e can be calculated from $d_e = d_m \mp (D + c_r)$.

Differentiating Eq. (4.8) with regards to the radial displacement v^e leads to an expression for the ring stiffness for the segment:

$$\frac{\partial N^e}{\partial v^e} = \left[\frac{EA_e}{d_e/2} + \frac{EI_e}{(d_e/2 \mp v^e)^3}\left(1 \mp \frac{3v^e}{d_e/2 \mp v^e}\right)\right]\Delta\psi \tag{4.9}$$

Since the effect of inner and outer ring compliance will be qualitatively very similar, it will be assumed that only the outer ring is compliant in this work, and consequently the inner ring deflections v^i will be set to zero but the outer ring deflections v^o must be computed. The outer ring cross-section will be approximated as rectangular with width B, and an effective thickness t, as shown in Fig. 4.3, which will be varied during the analysis. It will be assumed to be made of steel with Young's modulus $E_{steel} = 200\,\text{GPa}$.

In order to solve for the values of v^e, the equations for the contact forces in Eq. (3.70) and the ring load in Eq. (4.8) describing the contact and ring forces respectively can be substituted into Eq. (4.6) to enforce ring equilibrium. This leads to a non-linear algebraic equation in v^o which can be solved numerically using the Newton-Raphson method:

$$[v^o]_{k+1} = [v^o]_k + \left[\frac{Q - N^o}{\frac{\partial Q}{\partial \delta} + \frac{\partial N^o}{\partial v^o}}\right]_k. \tag{4.10}$$

where the terms in the denominator can be found from Eqs. (3.72) and (4.9) respectively.

Starting from an initial guess $[v^o]_0 = 0$ only a few iterations were needed until the equilibrium equation in Eq. (4.6) was satisfied to a tolerance of 1×10^{-8} N.

Once the ring deflections and contact loads have been found, the elemental stiffness can be computed from:

$$K = \left(\left[\frac{\partial Q}{\partial \delta} \right]^{-1} + \left[\frac{\partial N^o}{\partial v^o} \right]^{-1} \right)^{-1} \tag{4.11}$$

where there is one contribution from contacts, and another from the outer ring compliance. If ring compliance is to be neglected, then the outer ring can simply be set to $v^o = 0$, and the contact loads can then be evaluated directly. The elemental stiffness then reduces to just that of the contacts:

$$K = \frac{\partial Q}{\partial \delta} \tag{4.12}$$

The expressions in Eq. (4.11) and Eq. (4.12) yield an accurate estimate of the contact stiffness when there are no dynamic loads on the balls. However, this model may give inaccurate results if the ring compliance or centrifugal loading become significant, in which case a more complex solution process is required. This will be introduced in the following section.

4.1.3.2 High-speed operation with rigid rings

The rotation of the cage during operation generates an outward centrifugal load F^c on each element, given by Eq. (3.89). In this investigation it will be assumed that the balls are made of steel with $\rho = \rho_{steel} = 7800\,\mathrm{kg\,m^{-3}}$. The influence of centrifugal loads will only be considered for the case with rigid rings for which $v^e = 0$, so that the influence of the centrifugal loads can be studied in isolation. This has the additional benefit that it simplifies the analysis. However, it is possible that in real applications both effects could be significant.

In order to find the contact loads, the inner and outer contacts can no longer be combined as the contact loads will be unequal. Instead, each contact load must be found separately from Eq. (3.60), where the contact deflections δ^e come from Eqs. (4.3) and (4.4), noting that $v^i = v^o = 0$ since the rings are assumed rigid.

In order to solve for the unknown ball deflection r_b, the centrifugal load from Eq. (3.89) and contact loads from Eq. (3.60) can be substituted into the equilibrium relation in Eq. (4.5) to yield an algebraic problem in the ball deflection r_b. As in Section 3.2.5.5, this can be solved using a Newton-Raphson approach, except that for this simpler planar bearing, analytical derivatives are now available:

$$[r_b]_{k+1} = [r_b]_k + \left[\frac{Q^i + F^c - Q^o}{\frac{\partial Q^i}{\partial \delta^i} + \frac{\partial Q^o}{\partial \delta^o}} \right]_k . \tag{4.13}$$

where the contact stiffness terms in the denominator are given in Eq. (3.61). This relation is iterated until the equilibrium equation in Eq. (4.5) is satisfied to a tolerance of 1×10^{-8} N. The initial guess $[u]_0$ was set to the elemental deflection in case of no centrifugal loading:

$$[r_b]_0 = \frac{C_o^{\frac{1}{n}}}{C_i^{\frac{1}{n}} + C_o^{\frac{1}{n}}} [r(\psi)]_+$$

Once the elemental deflection has been found, the contact stiffness at each ring is simply determined by the stiffness of the Hertzian contacts in series with each other:

$$K = \left(\left[\frac{\partial Q^i}{\partial \delta^i} \right]^{-1} + \left[\frac{\partial Q^o}{\partial \delta^o} \right]^{-1} \right)^{-1} \tag{4.14}$$

Eq. (4.14) gives a much more accurate estimate of the contact stiffness when the centrifugal loading on the elements is significant.

4.1.4 Load and stiffness

Due to the cyclic-symmetric nature of rolling-element bearings, the elastic properties vary with both rotation angle, as well as the bearing deflection. The two different methods for computing the load introduced in Sections 3.2.6 and 3.2.7 will be applied to the simplified case of a DGBB, which will allow these two effects to be decoupled. In addition, it is now possible to derive analytical expressions for the total bearing stiffness.

4.1.4.1 Time-varying load and stiffness

Once the contact loads Q_j^e and elemental stiffnesses K_j have been evaluated using the appropriate elemental compliance model from Section 4.1.3, the total load on the inner ring, $\boldsymbol{f}_b^i$, and outer ring, $\boldsymbol{f}_b^o$ can be computed. As in Section 3.2.6, the contributions from each element can be summed up, whilst taking their angular position into account [183]:

$$\boldsymbol{f}_b^e(\boldsymbol{x}_b, \psi_c) = \begin{bmatrix} f_x^e \\ f_y^e \end{bmatrix} = \sum_{j=1}^{Z} Q_j^e \begin{bmatrix} \sin \psi_j \\ -\cos \psi_j \end{bmatrix} \tag{4.15}$$

where $\boldsymbol{x}_b$ is the bearing displacement vector from Eq. (4.1). Note that this expression is much simpler than for the 4DOF model, since the contact angles are all fixed to 0.

This also means that, unlike in the general case, the bearing stiffness matrix $\boldsymbol{K}_b$ can be found by simply summing up all the previously introduced contributions from each element [183]:

$$\boldsymbol{K}_b(\boldsymbol{x}_b, \psi_c) = \begin{bmatrix} k_{xx} & k_{xy} \\ k_{yx} & k_{yy} \end{bmatrix} = \begin{bmatrix} \frac{\partial f_x^e}{\partial x} & \frac{\partial f_x^e}{\partial y} \\ \frac{\partial f_y^e}{\partial x} & \frac{\partial f_y^e}{\partial y} \end{bmatrix} = \sum_{j=1}^{Z} K_j \begin{bmatrix} \sin^2 \psi_j & -\sin \psi_j \cos \psi_j \\ -\sin \psi_j \cos \psi_j & \cos^2 \psi_j \end{bmatrix} \quad (4.16)$$

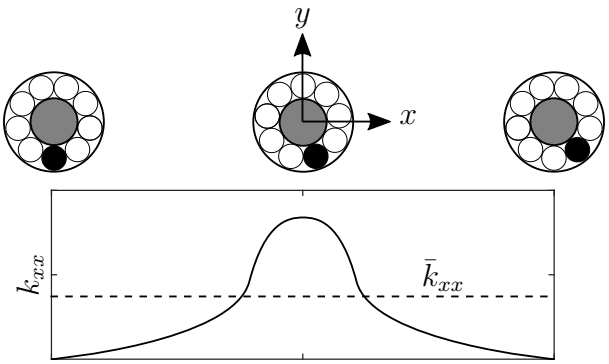
With expressions for the total load $\boldsymbol{f}_b^e$, and stiffness $\boldsymbol{K}_b$, available, the bearing model is now fully described. However, both the load and stiffness depend on the cage angle ψ_c, and will therefore vary over time which is known as "variable compliance" (VC). As an example, the variation of the horizontal, vertical and cross-stiffnesses with cage angle has been plotted in Fig. 4.4, in the case that a constant vertical load is applied; the horizontal stiffness is typically at a maximum when there are elements either side of the bearing centre as shown in Fig. 4.4a, and the vertical stiffness is at a maximum when there is a ball directly under the bearing centre shown in Fig. 4.4b.

The cross-stiffness is zero at both of these cage angles, because the elements are then symmetrically distributed either side of the vertical plane. However, it becomes non-zero at all other cage angles when the symmetry is broken. For this particular bearing, the horizontal stiffness was found to vary by around 20 %, and the vertical stiffness by around 3 %, so these effects are significant.

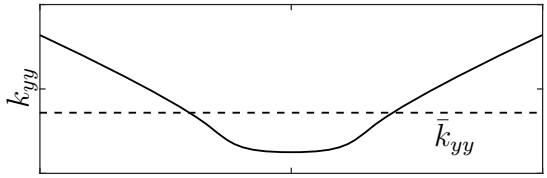
Due to the cyclic-symmetry of the cage, it should be noted that the bearing load and stiffness will oscillate at the BPF given in Eq. (3.96), which can excite the structures connected via the bearings. To identify the impact of this often neglected excitation source on the rotor dynamic response, a particular focus will be placed on this behaviour during simulation.

4.1.4.2 Average load and stiffness

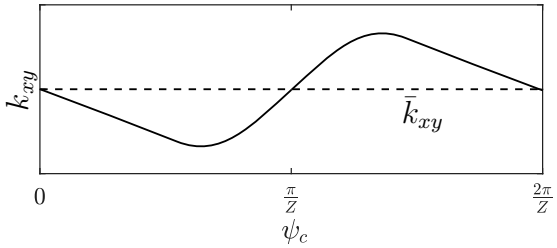
Although VC can be significant, the compliance oscillations are often ignored in the first instance, by computing the *average* load and stiffness in each direction using the Sjovall integral formulation in Section 3.2.7. The resulting average stiffnesses are overlaid on Fig. 4.4 as dotted lines. With this formulation the average load and stiffness is independent of the cage position, but may still depend on cage speed due to centrifugal loading on the elements.



(a) Horizontal stiffness



(b) Vertical stiffness



(c) Cross stiffness

Figure 4.4: Variation of bearing stiffness with cage position

4.1.4.3 Damping

REBs are typically quite lightly damped components, so the damping mechanisms are typically not as significant as the elastic non-linearities, which have been incorporated into the bearing model. For this reason, instead of a physical damping model, a simple viscous bearing damping term will be included. The damping load on each ring is given by:

$$\boldsymbol{f}^e_{b,d} = \begin{bmatrix} f^e_x \\ f^e_y \end{bmatrix}_d = \pm c_b \begin{bmatrix} \dot{x}_b \\ \dot{y}_b \end{bmatrix} = \pm \boldsymbol{C}_b \dot{\boldsymbol{x}}_b$$

where $\boldsymbol{C}_b = c_b \boldsymbol{I}$, and the positive sign is for the inner ring and the negative sign for the outer ring. This completes the derivation of the simplified bearing model, incorporating the effect of clearance, ring compliance centrifugal loads and variable compliance. The bearing model can now be integrated into a rotor model.

4.2 Jeffcott rotor

In order to assess the significance of the different bearing non-linearities on a rotor dynamic system, the response of a rigid Jeffcott rotor will be considered, as shown in Fig. 4.5. The rotor is assumed to spin at a constant speed Ω and is supported by the DGBB from Section 4.1. Gyroscopic effects were not included, as these could mask the influence of the bearing. The bearing is connected to ground via linear spring and viscous damping elements, representing a generic support structure, similar to the configuration considered in [62]. The horizontal and vertical deflections of the rotor centroid are denoted by x_r and y_r respectively in Fig. 4.5 while the stator deflection is expressed by x_s and y_s. The rotation angle of the rotor is denoted by $\Theta = \Omega t$. All the relevant rotor parameters are summarised in Table 4.3.

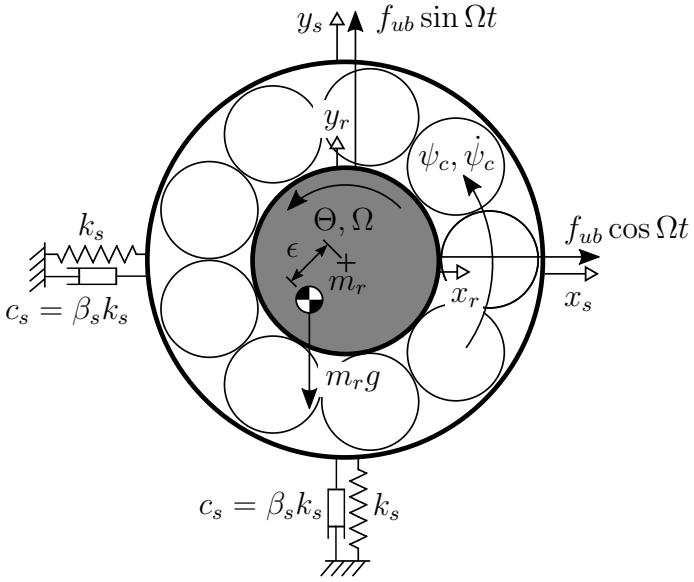


Figure 4.5: Jeffcott rotor mounted on a REB

4.2.1 Equations of motion

Denoting the rotor and stator displacements with vectors $\boldsymbol{x}_r = \begin{bmatrix} x_r & y_r \end{bmatrix}^T$ and $\boldsymbol{x}_s = \begin{bmatrix} x_s & y_s \end{bmatrix}^T$ respectively, the equations of motion of the rotor and stator can be written as:

$$\boldsymbol{M}_r \ddot{\boldsymbol{x}}_r + \boldsymbol{C}_b \left(\dot{\boldsymbol{x}}_r - \dot{\boldsymbol{x}}_s \right) + \boldsymbol{f}_b^i (\boldsymbol{x}_r - \boldsymbol{x}_s, \dot{\psi}_c t) = \boldsymbol{f}_{r,e}(t) \tag{4.17}$$

$$\boldsymbol{C}_s \dot{\boldsymbol{x}}_s + \boldsymbol{K}_s \boldsymbol{x}_s - \boldsymbol{C}_b \left(\dot{\boldsymbol{x}}_r - \dot{\boldsymbol{x}}_s \right) - \boldsymbol{f}_b^o (\boldsymbol{x}_r - \boldsymbol{x}_s, \dot{\psi}_c t) = \boldsymbol{0} \tag{4.18}$$

where $\boldsymbol{M}_r = m_r \boldsymbol{I}$, $\boldsymbol{C}_s = c_s \boldsymbol{I}$ and $\boldsymbol{K}_s = k_s \boldsymbol{I}$. The vectors $\boldsymbol{f}_b^i$ and $\boldsymbol{f}_b^o$ are the non-linear bearing forces from Eq. (4.15), and the terms involving $\boldsymbol{C}_b$ are due to the bearing

Table 4.3: Baseline Jeffcott rotor parameters

Symbol	Description	Value	Units
m_r	Rotor mass	6	kg
k_s	Stator stiffness	∞	$\mathrm{N\,m^{-1}}$
β_s	Stator Rayleigh damping	1×10^{-4}	-
g	Acceleration due to gravity	9.81	$\mathrm{m\,s^{-2}}$

damping. The vector $\boldsymbol{f}_{r,e}$ contains the external forces on the rotor. Eqs. (4.17) and (4.18) can then be combined to the general form:

$$\boldsymbol{M}\ddot{\boldsymbol{x}} + \boldsymbol{C}\dot{\boldsymbol{x}} + \boldsymbol{K}\boldsymbol{x} + \boldsymbol{f}_{nl}(\boldsymbol{x}, t) = \boldsymbol{f}_e(t) \tag{4.19}$$

where $\boldsymbol{M}$, $\boldsymbol{C}$, and $\boldsymbol{K}$ are the global mass, damping and stiffness matrices respectively, $\boldsymbol{x} = \begin{bmatrix} \boldsymbol{x}_r{}^T & \boldsymbol{x}_s{}^T \end{bmatrix}^T$ is the global position vector and $\boldsymbol{f}_e = \begin{bmatrix} \boldsymbol{f}_{r,e}^T & \boldsymbol{0} \end{bmatrix}^T$ is the global excitation vector. The non-linear forces $\boldsymbol{f}_{nl}$ depend on time due to the variable compliance of the bearing discussed in Section 4.1.4.1.

4.2.2 External forces

The rotor in Fig. 4.5 is excited by a small mass unbalance, which will be expressed in terms of an offset ϵ between the rotor Centre of Gravity (CoG) and centroid, leading to an unbalance force $f_{ub} = m_r \epsilon \Omega^2$. The rotor also experiences a static downward load $m_r g$ due to its self-weight. The total force on the rotor $\boldsymbol{f}_{r,e}$ in Eq. (4.17) can therefore be written as:

$$\boldsymbol{f}_{r,e}(t) = \boldsymbol{f}_g + \Re\left(\boldsymbol{f}_{ub} e^{i\Omega t}\right) \tag{4.20}$$

where $\boldsymbol{f}_g = \begin{bmatrix} 0 & -m_r g \end{bmatrix}^T$ is due to the self-weight and $\boldsymbol{f}_{ub} = f_{ub} \begin{bmatrix} 1 & -i \end{bmatrix}^T$ represents the rotating unbalance force.

4.2.3 Performance metrics

To quantify the vibration behaviour of the rotor, three different performance metrics will be used. The first will be the synchronous transmissibility, T_x, y, defined as the ratio between the unbalance force and the load transmitted to the stator. Mathematically, this can be written as:

$$T_x = \frac{\{f_x^o\}_{1X}}{f_{ub}} \qquad T_y = \frac{\{f_y^o\}_{1X}}{f_{ub}}$$

where only the synchronous component of the stator load is included, denoted by the subscript 1X. Note that the unbalance force is synchronous by definition. If the Jeffcott rotor were mounted on rigid bearings, this metric would be unity. If this metric is smaller than unity, it indicates attenuation of vibrations, and if it is greater than unity, it suggests amplification. The transmissibility will remain independent of the forcing amplitude if a system is linear, but this will no longer be true when non-linearity is present in the system.

The second metric assesses the self-excitation due to the variable compliance effect in the bearing. This may excite both the rotor and stator, and in turn impact the overall dynamic behaviour. The performance metric used here will be the load transmitted to the stator at the ball pass frequency (BPF):

$$F_x^b = \{f_x^o\}_{\mathrm{BPF}} \qquad F_y^b = \{f_y^o\}_{\mathrm{BPF}}$$

If the bearing had an infinite number of elements, or the average loads from Section 4.1.4.2 were used, this forcing would be 0 and hence no response would be expected at this frequency. However, if the time-varying loads from Section 4.1.4.1 are used, the load will vary as the cage rotates, leading to additional harmonic forcing and this metric will be non-zero.

The last metric is the position of the centre of the rotor orbit. This is given by the 0 Hz component of the horizontal x, and vertical y components of the rotor response, denoted by the subscript DC:

$$\bar{x} = \{x_r\}_{\mathrm{DC}} \qquad \bar{y} = \{y_r\}_{\mathrm{DC}}$$

For a linear system, this would not vary with excitation frequency or amplitude, since the response to static loads on the structure would be independent of the dynamic response. However, this is no longer true for non-linear systems.

4.2.4 Summary

A model of a Jeffcott rotor supported by non-linear bearings has been introduced. The physical bearing model allows the impact of a wide range of bearing parameters on the dynamic response of the system to be assessed, including the clearance, centrifugal loading or ring compliance, whilst incorporating the variable compliance effect. Various metrics

have been introduced to assess the impact of the bearings on the non-linear response of the system. However, due to the cyclic-symmetric and non-linear nature of the bearing, advanced numerical methods are required to analyse the frequency response in an efficient way.

4.3 Application of GHBM

The equations of motion for the Jeffcott rotor system in Eqs. (4.17) and (4.18) have a nonlinear form, preventing the use of standard linear solution techniques to compute the response. Time domain solvers, such as `ode15s` in MATLAB, are widely used to solve such nonlinear equations, and although they are a powerful tool for capturing all forms of response, convergence issues can make them very slow and computationally expensive. Alternatively the nonlinear response can be analysed much more efficiently in the frequency domain using the Harmonic Balance Method (HBM) [176]. Due to its high efficiency, standard HBM has been used successfully to compute the nonlinear dynamic response of rotor-bearing systems [102, 150] under the assumption that the response of the system will be periodic with the fundamental frequency equal to the rotation speed Ω.

However, if the VC effect from Section 4.1.4.1 is to be included in the analysis, as is the intention of this study, an additional periodicity is being introduced via the bearing stiffness matrix which varies at the BPF. Unless the BPF happens to be commensurate with the shaft rotation frequency, the response will in fact be quasi-periodic, for which conventional HBM is inadequate. Instead of resorting to computationally-expensive time-integration, an alternative approach is to apply the GHBM from Section 3.3 which can capture quasi-periodic responses. To the authors' knowledge no attempts have been made in the literature to date to study the combined effect of unbalance and VC on a rotor-bearing system using harmonic balance. A new approach to achieve this using GHBM will be introduced in the following sections.

4.3.1 Base frequencies

For a nonlinear dynamic rotor system with unbalance and VC excitation, two base frequencies will be present: (i) the rotation speed $\omega_1 = \Omega$, arising from the synchronous excitation, and (ii) the ball pass frequency $\omega_2 = \omega_{BPF}$. These two base frequencies can both be expressed in terms of the rotor speed Ω:

$$\boldsymbol{\omega} = \begin{bmatrix} \omega_1 \\ \omega_2 \end{bmatrix} = \begin{bmatrix} \Omega \\ \omega_{BPF} \end{bmatrix} = \Omega \begin{bmatrix} 1 \\ \nu_m Z \end{bmatrix} \tag{4.21}$$

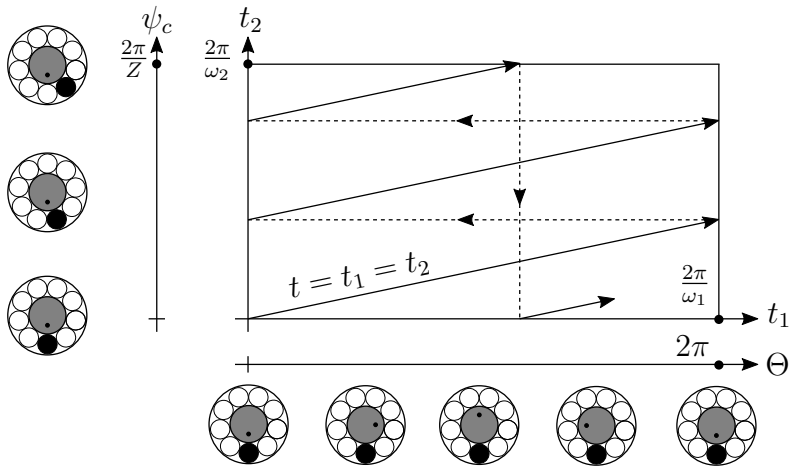


Figure 4.6: Depiction of hyper-time for the Jeffcott rotor

where the speed ratio ν_m can be computed from Eq. (3.83), and has the value of 0.4 for the SKF6002 bearing in this study, so that the BPF is around 3.6Ω. The rotor speed Ω was selected as the continuation parameter, since both base frequencies were proportional to Ω.

4.3.2 Application of AFT to cyclic-symmetric systems

As discussed in Section 3.3.4, a common approach for computing the contribution of the nonlinearities is to use the Alternating Frequency/Time (AFT) method [154]. One way this can be extended to quasi-periodic problems is to introduce a multi-dimensional time domain (or hyper-time) [153], as discussed in Section 3.3.4. This concept can be applied to a rotor-bearing system with unbalance and VC, in such a way as to exploit the cyclic-symmetry of the system. The rotor is assumed to spin at a speed $\Omega = \omega_1$ along the domain t_1, with the cage held fixed. Conversely the cage rotates along the domain t_2 at speed $\dot{\psi}_c = \frac{\omega_2}{Z}$, with the rotor held fixed. This idea is depicted in Fig. 4.6, where the x-axis represents t_1 with the rotor rotation, while the y-axis represents t_2 with the cage rotation. The true time domain, t, where both the rotor and cage will rotate but at different speeds, is represented by a diagonal line in hyper-time where $t = t_1 = t_2$.

It should be noted that the nonlinear bearing force $\boldsymbol{f}_b$ has an explicit dependence on t_2 and not t_1. This is because the nonlinear bearing forces vary with cage angle ψ_c, which varies with t_2 only according to the definition of hyper-time used here.

4.3.3 Simulation using HarmLAB

The response of the Jeffcott rotor was simulated using the novel application of GHBM using the HarmLAB toolbox presented in Section 3.3. The stability was computed using

Hill's method with adjusted HBM as described in Section 3.3.5. Applying this approach to the Jeffcott rotor in this paper, the ratio between the BPF and rotor speed $\nu_m Z$ was approximated as the ratio of two integers p and q (to an accuracy of 1×10^{-4}), such that $Z\nu_m \approx \frac{p}{q}$.

4.3.4 Summary

The proposed application of the GHBM, in combination with the pseudo arc-length continuation and Hill's method for stability, provides, for the first time, an efficient way to study the nonlinear unbalance response of a rotor-bearing system whilst including the VC effect. This therefore represents a more complete and accurate method for computing the nonlinear dynamic response of a rotor-bearing system than previous approaches.

4.4 Baseline system

The previously introduced model of the Jeffcott rotor from Section 4.2 supported by the non-linear time-varying DGBB model from Section 4.1 will be analysed in detail using the GHBM approach presented in Section 4.3. The aim is to better understand the influence of the bearing on the response of the system, with a particular focus on the effect of variable compliance and the non-linear bearing stiffness.

The input parameters of the baseline model are shown in Tables 4.1 to 4.3. Centrifugal loads were neglected at this stage and both rings and the stator were assumed to be rigid, in order to keep the complexity of the baseline to a minimum. The clearance was set to the C2 level shown in Table 4.1, corresponding to a radial clearance of 2.5 µm.

4.4.1 Validation of GHBM

The first step was to validate the novel application of the GHBM to the rotor-bearing system from Section 4.3, in order to ensure that the predictions were accurate. For this purpose, the solution from GHBM was compared to the solution from time integration of the equations of motion in Eqs. (4.17) and (4.18), with use of `ode15s` in MATLAB.

The number of harmonics M^H for each frequency $\omega_{1,2}$ in the GHBM computation was chosen so that the dominant peaks in the spectrum of the response could be captured, across a range of speeds and unbalance levels, ensuring the results would be sufficiently accurate. The number of discrete time points $N^T_{1,2}$ was set to be 4× the minimum dictated by the Nyquist frequency for each $\omega_{1,2}$, in order to minimise aliasing, leading to the GHBM parameters in Table 4.4. It is important to note that the multi-dimensional FFT/IFFT

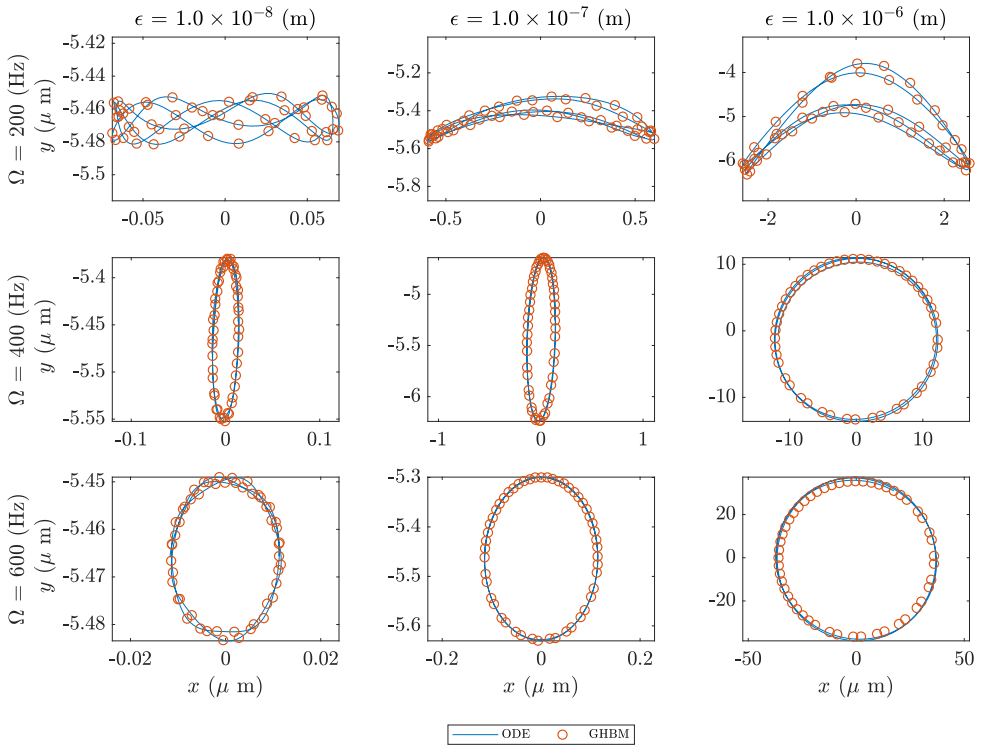


Figure 4.7: Comparison of the orbits obtained from integrating the ODE and GHBM

operations were evaluated over $M_1^T \times M_2^T = 40 \times 24 = 960$ points; leading to accurate results with relatively few points over each dimension [151].

The resulting rotor orbits from time-integration and GHBM are shown in Fig. 4.7 for three rotation speeds Ω and three unbalance levels ϵ. The two methods provide identical results for the first two excitation levels, and show a very similar behaviour at the highest excitation level, although small differences are visible. Both approaches accurately capture the clearly quasi-periodic nature of the response, which leads to the rotor never retracing exactly the same orbit. This is due to the time-dependence introduced by the variable compliance effect, which is in agreement with results from [90]. Based on the comparison of the solutions from GHBM and time solution, it can be concluded that GHBM, with

Table 4.4: Harmonic balance parameters for the Jeffcott rotor

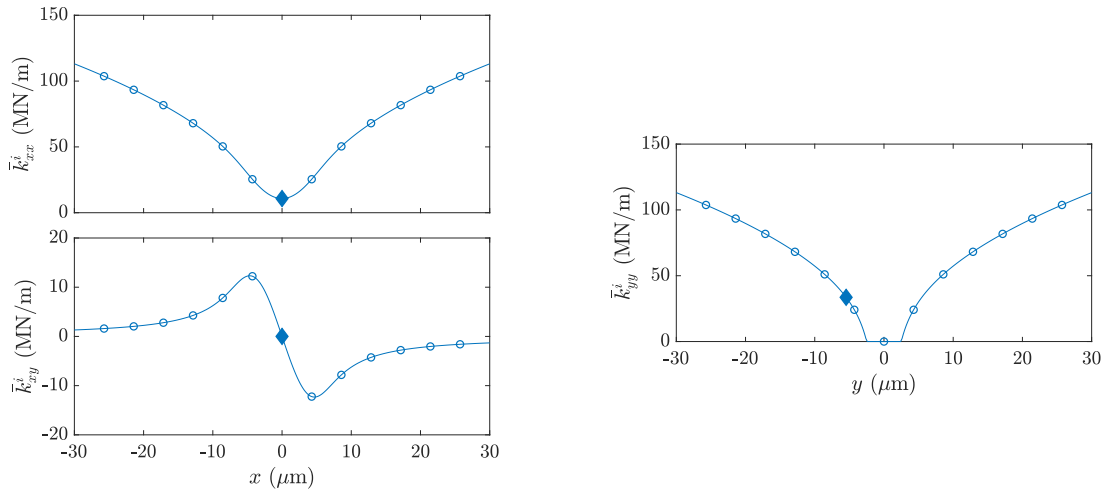
Symbol	Description	Value
M_1^H	No. of harmonics in ω_1	5
M_2^H	No. of harmonics in ω_2	3
M_1^T	No. of time points over t_1	40
M_2^T	No. of time points over t_2	24
$\frac{\omega_2}{\omega_1}$	Ratio between base frequencies	3.5885
p,q	Rational approximation of freq. ratio	750, 209

the selected number of harmonics, is indeed able to capture the quasi-periodic response of the rotor system accurately.

Both solutions were found on a Windows PC with an 8-Core i7 processor and 32GB of memory using MATLAB 2018b, where approximately 16 sec of computation time were needed to compute the solution at a given frequency using `ode15s`, while only 2 sec were needed using the GHBM approach. This 8x increase in computational speed, in combination with the ability to apply continuation to the analysis, highlighted the great potential the GHBM has for quasi-periodic rotordynamic problems, and all of the following results will be consequently based on the GHBM approach.

4.4.2 Bearing stiffness

The dynamic response of the rotor system is heavily dependent on the bearing stiffness, which in turn depends on the rotor deflection, and the cage angle of the bearing. In order to evaluate the non-linear stiffness characteristic of the baseline bearing, independent of the cage angle, the average bearing stiffness from Section 4.1.4.2 has been computed for different horizontal and vertical rotor positions and the results are shown in Fig. 4.8. The variation of the time-varying bearing stiffness from Section 4.1.4.1 was then computed in the equilibrium position, in order to quantify the variable compliance. This is plotted in Fig. 4.9.



(a) Horizontal sweep (b) Vertical sweep

Figure 4.8: Variation of the average bearing stiffness with rotor position for the baseline system

4.4.2.1 Rotor displacement

The variation of the average horizontal stiffness $\bar{k}_{xx}$ with rotor position was computed by varying the horizontal rotor position, whilst maintaining vertical equilibrium. It can be observed in the top graph of Fig. 4.8a that the stiffness increases monotonically as the rotor moves away from the centre, $x = 0$, in either direction. This is due to an increase in the size of the loaded zone, as well as the hardening characteristic of the Hertzian contacts. The variation of the cross-stiffness $\bar{k}_{xy}$ with horizontal rotor motion x is shown in the bottom graph of Fig. 4.8a. The cross-stiffness is zero when the rotor is in the centre, due to the symmetry of the system, but as the rotor moves horizontally away from the centre, the load distribution becomes asymmetric and the cross-stiffness becomes non-zero. As the rotor displaces even further, the coupling stiffness, $\bar{k}_{xy}$, tends back to zero, since the influence of the self-weight becomes negligible compared to the large horizontal rotor deflection, and the load distribution becomes symmetric about the x-axis once more.

The average vertical stiffness $\bar{k}_{yy}$ is plotted in Fig. 4.8b where the rotor was moved vertically while maintaining horizontal equilibrium. The position where the rotor is in vertical equilibrium with its self-weight is marked with a diamond. The rotor sags by approximately 6 µm due to the self-weight. When the rotor moves further downwards, the vertical stiffness increases due to an increase in the size of the loaded zone and Hertzian contact stiffening. However, when the rotor moves upwards from its equilibrium position, the stiffness initially reduces as the effect of the self weight is removed. When the rotor is near the central position $y = 0$, there is a deadband where the stiffness is zero, which is due to the radial clearance. If the rotor deflects even further upward, the stiffness increases once more as the elements at the top of the bearing become loaded. There is no such deadband in the horizontal stiffness, since the presence of the self-weight ensures that there is always some contact. The cross-stiffness $\bar{k}_{xy}$ remains zero if the rotor moves vertically because the load distribution remains symmetric about the y-axis, and has therefore not been plotted.

4.4.2.2 Cage position

The variation of the time-varying stiffness with cage angle at the equilibrium position of the rotor is plotted in Fig. 4.9. It is clear that the stiffness strongly depends on the cage angle, and can vary quite differently in each direction. In the vertical direction it reaches its maximum when a ball is directly under and over the rotor, while in the horizontal direction the maximum stiffness is reached when there are balls either side.

It is important to note that the variation in stiffness is larger in the horizontal direction (20 %) than in the vertical direction (3 %). The horizontal stiffness has its main contri-

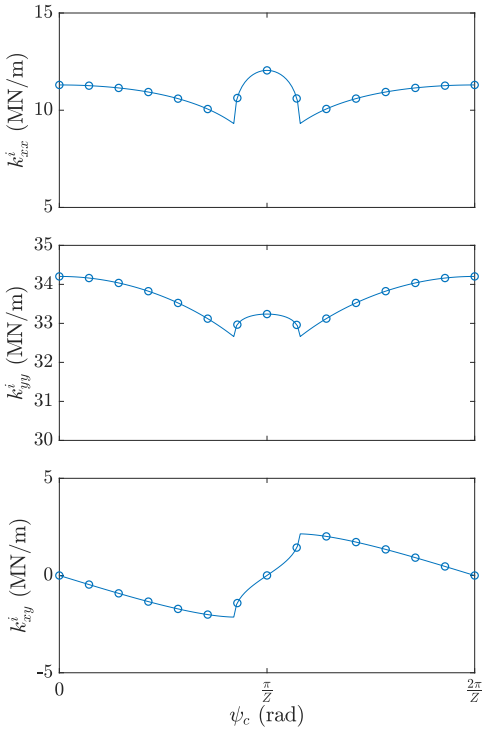


Figure 4.9: Variation of the stiffness with cage angle for the baseline system

bution from the elements at the edges of the loaded zone since these contact loads have the greatest horizontal component, and the overall stiffness is consequently very sensitive to their angular position since their contribution is proportional to $\sin^2 \psi_j$. The vertical stiffness on the other hand is mainly determined by the elements underneath the rotor, which have a small angle ψ_j. Their contribution to the vertical stiffness is proportional to $\cos^2 \psi_j$, but this is much less sensitive to variations in ψ_j.

The cross-stiffness is zero when the balls are positioned symmetrically about the vertical plane, but non-zero otherwise. This occurs when $\psi_c = 0$ or $\frac{\pi}{Z}$. The strong change in stiffness behaviour around $\psi_c = \frac{\pi}{Z}$ corresponds to a region where there is an extra element in the loaded zone. There is a non-smooth transition when an element enters or leaves the load zone.

4.4.2.3 Summary

The results show that the stiffness varies considerably as the rotor deflects leading to a highly non-linear characteristic. In addition, the bearing stiffness varies as the cage rotates, leading to the time-dependent variable compliance effect, which can further excite the rotor.

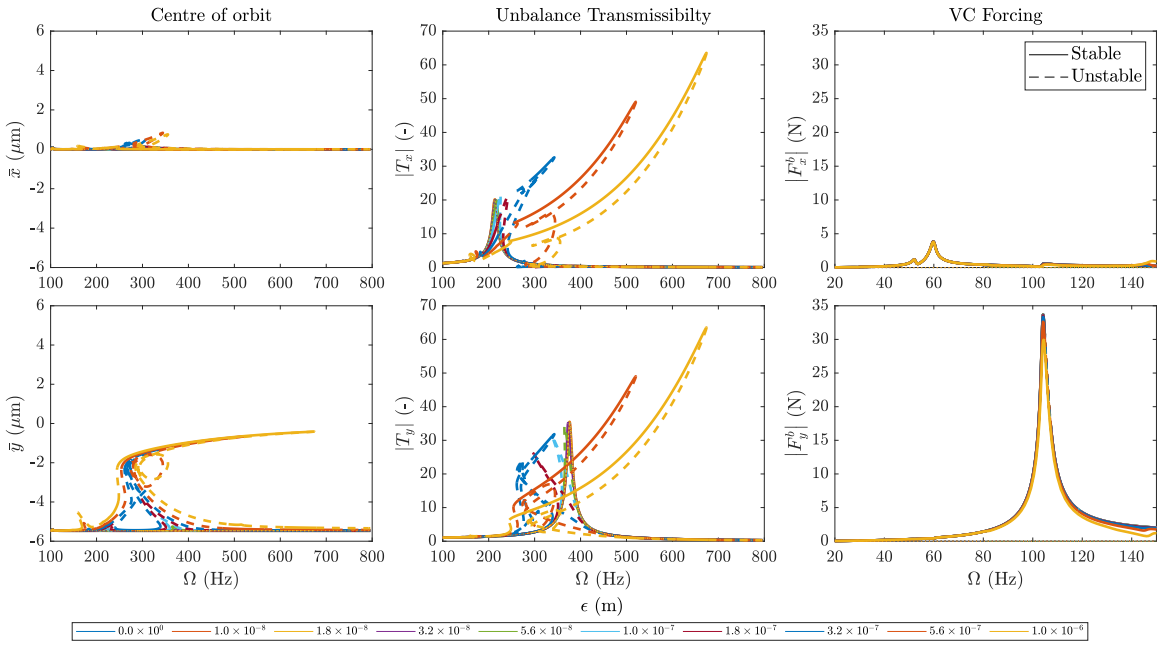


Figure 4.10: Frequency response of the baseline system

4.4.3 Frequency response

With the accuracy of the GHBM implementation confirmed, and an understanding of the bearing stiffness behaviour obtained, the frequency response of the baseline rotor was computed for increasing levels of rotor unbalance, leading to the results in Fig. 4.10. The displacement of the centre of the rotor orbit $(\bar{x}, \bar{y})$ is shown in the left hand column, the unbalance transmissibility across the bearing in the central column, and the self-excitation due to variable compliance in the right hand column. The dashed lines denote where the periodic solution is unstable.

It can be observed that there are distinct resonances in the horizontal (x) and vertical (y) directions. At low excitation levels, the horizontal resonance is at 213 Hz and the vertical resonance is higher at 376 Hz, which is consistent with the different stiffnesses in each direction discussed in the previous section. The vertical position of the centre of the rotor orbit $\bar{y}$ moves towards 0 at resonance. The horizontal position $\bar{x}$ is always zero, and only becomes non-zero when the quasi-periodic solution loses stability. It can also be observed that the forcing due to VC has resonances at speeds well below the primary resonances.

In order to condense and highlight the most important information contained in the frequency plots in Fig. 4.10 the variation of the resonance frequency, $\Omega_{\max}$, the peak horizontal/vertical transmissibility, $|T_x|_{\max}$ and $|T_y|_{\max}$, and the vertical position of the orbit centre $\bar{y}_{\max}$ can be plotted over the unbalance level, ϵ, which is shown in Fig. 4.11. Similarly the maximum forcing amplitude at the BPF due to VC, and the frequency at

which this occurs can be plotted over the unbalance level, ϵ, which is shown in Fig. 4.12. These results will now be discussed in more detail.

4.4.3.1 Synchronous Transmissibility

The unbalance transmissibility in the central column of Fig. 4.10 shows that the horizontal peaks start to lean to the right as the unbalance level is increased due to the horizontal stiffness increasing as the rotor oscillates with larger amplitudes, as shown in Fig. 4.8a. Interestingly, the vertical resonance leans to the left at low unbalance levels due to the initial reduction in stiffness as the rotor enters the deadband region in Fig. 4.8b. At higher unbalances, the rotor deflects so much that it passes through to the other side of the deadband, so that the effective stiffness is actually increased and the peak starts to lean to the right. This softening/stiffening effect of the non-linear bearing is in agreement with the literature [102] and highlights that the system is strongly non-linear.

The stiffening effect of the bearings is so strong that "jump phenomena" start to appear at the higher unbalance levels, where the periodic solution becomes unstable under the peak, denoted by the dotted lines. Additionally, both resonant peaks become unstable for certain medium excitation levels, before regaining stability at higher unbalance levels. Using time integration, the system was found to respond chaotically in these unstable regions which is in good agreement with the literature [64, 73, 75, 86, 101, 144]. These unstable regions are clearly identifiable in Fig. 4.11, where they are marked as dashed lines.

It can also be observed in Fig. 4.10 that cross-resonances start to appear at higher unbalance levels. At the horizontal resonance frequency, a peak starts to appear in the vertical response. In this case the cross-stiffness becomes non-zero as the rotor oscillates horizontally, which excites the rotor in the vertical direction. As the unbalance level is further increased, this cross-resonance becomes larger and the primary vertical resonance becomes smaller. Eventually the cross-resonance forms the dominant part of the vertical response, leading to a single resonance with circular orbits and equal motion in the horizontal and vertical directions. In this regime, the effect of the self-weight of the rotor is negligible compared to the dynamic loads, so the resonance frequencies and amplitudes are identical in both directions as clearly shown in Fig. 4.11. The resonance frequency more than doubles for the highest load case and the peak vibration transmission increases significantly in this regime. This can be attributed to the fact that the effective damping ratio is given by $\zeta_r \approx \frac{c_b}{2m\omega_n}$, where the bearing damping c_b is constant but the effective natural frequency ω_n increases due to the non-linear bearing stiffness, and therefore the effective damping ratio is reduced.

Another feature to observe in Fig. 4.10 are the small sub-resonances in the horizontal

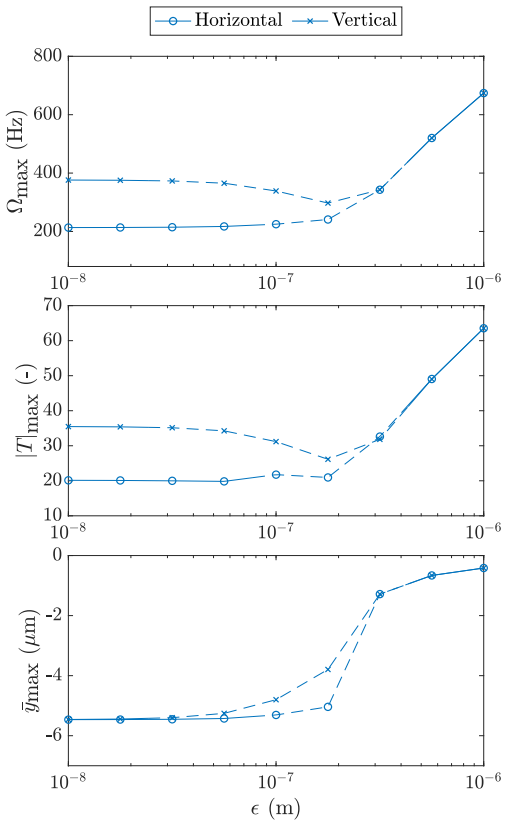


Figure 4.11: Unbalance transmissibility of the baseline system at resonance

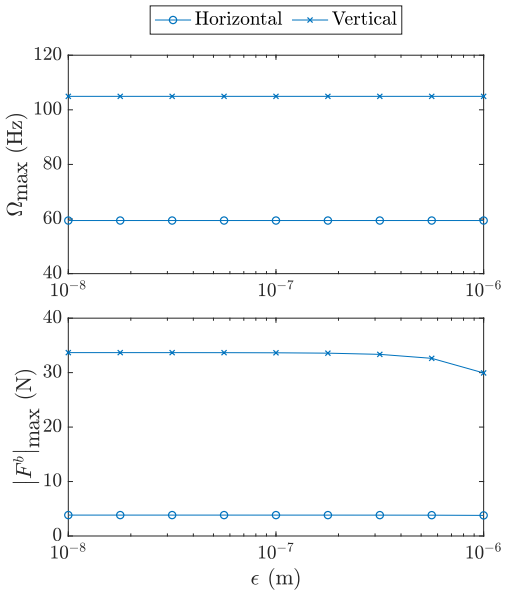


Figure 4.12: VC forcing of the baseline system at resonance

transmissibility around 180 Hz, which only appear at the highest excitation levels. This is approximately half of the vertical natural frequency, so is therefore evidence of $2\times$ components in the response.

4.4.3.2 Centre of rotor orbit

The position of the centre of the rotor orbit is shown in the left hand column of Fig. 4.10. The horizontal position $\bar{x}$ remains near zero due to the symmetry of the system, but the vertical position $\bar{y}$ varies considerably, which can be more clearly seen in Fig. 4.11. At higher unbalance levels, the rotor moves upward towards the centre position at resonance, because the self-weight becomes negligible compared to the dynamic loads, and no longer impacts the rotor motion. This is also visible on the bottom graph of Fig. 4.11.

4.4.3.3 Self-excitation due to variable compliance

Due to the novel use of the GHBM in this paper, the forcing due to variable compliance could be computed and is shown in the right hand column of Fig. 4.10. There are prominent peaks in the forcing in both the vertical and horizontal directions, when the

Ball Pass Frequency ω_{BPF} coincides with the natural frequency ω_n of the underlying linear system of either the vertical or horizontal mode. The mathematical relation is given by $\Omega = \frac{\omega_n}{\nu_m Z}$.

The frequency of maximum forcing varies very little with the excitation level, but the magnitude of the peaks reduces slightly at very high excitation levels as Fig. 4.12 shows more clearly. The latter indicates an influence of the unbalance forces even at these lower frequencies and suggests that the variable compliance phenomenon is most relevant for small unbalance levels. Surprisingly the forcing is greater in the vertical direction, despite the fact that the horizontal stiffness was found to be more sensitive to cage position (see Fig. 4.9). This effect could be attributed to the variations in cross-stiffness which can also excite the rotor in the vertical direction.

4.4.3.4 Summary

The results from the baseline configuration show that the rolling-element bearing leads to a highly non-linear unbalance response, with changes in the vibration transmission with the amplitude of excitation. In addition the variable compliance effect introduces further sub-synchronous forcing, leading to sub-resonances at low frequencies. In order to identify which of the bearing features particularly influence the observed behaviour, a parameter study will be presented next.

4.5 Parameter study

The influence of four key bearing features on the Jeffcott rotor response will now be investigated in more detail. In each section, the parameter of interest will be varied whilst keeping all others fixed at the baseline values, as outlined in Table 4.5. For each parameter, the impact on the bearing stiffness will be discussed initially, which will support the interpretation of the frequency response.

Table 4.5: Configurations for each section of the parameter study

Section	Clearance	Outer ring	C.f. loads	Stator
Section 4.4 Baseline	C2	Rigid	No	Rigid
Section 4.5.1 Clearance	Varied	Rigid	No	Rigid
Section 4.5.2 Ring Compliance	C2	Flexible	No	Rigid
Section 4.5.3 Centrifugal Loading	C2	Rigid	Yes	Rigid
Section 4.5.4 Stator Compliance	C2	Rigid	No	Flexible

4.5.1 Clearance

The clearance is one of the largest sources of non-linearity in a bearing, so the radial clearance c_r was chosen for the first parameter study. It was increased from its nominal C2 value of 2.5 µm to the C5 level of 20 µm, and decreased to 0 µm corresponding to a perfect fit. In addition the effect of a radial preload on the bearing was considered by setting c_r to -2.5 µm.

4.5.1.1 Stiffness

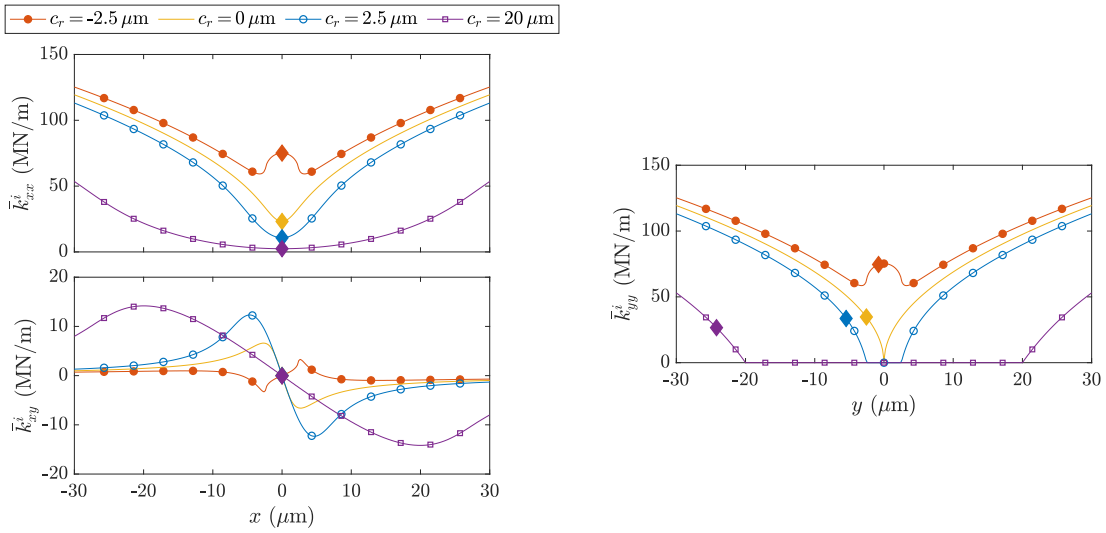
The horizontal and vertical stiffness variation was computed in the same way as outlined in Section 4.4. The results for the average horizontal stiffness in Fig. 4.13a show a high sensitivity to the clearance level.

The preload case ($c_r = -2.5$ µm) has a higher overall stiffness level as the loaded zone encompasses the whole of the bearing as shown in Fig. 4.14. The stiffness initially reduces as the rotor moves away from the centre as the loaded zone initially decreases in size due to loss of preload on the lightly loaded side of the bearing. At larger displacements the stiffness starts to increase again since the effect of the stiffening Hertzian contact dominates. For the cases of a loose bearing ($c_r > 0$ µm), the size of the loaded zone is smaller as seen in Fig. 4.14. This means the overall stiffness level is reduced. However, the stiffness increases monotonically in this case, since the loaded zone increases in size as the rotor moves horizontally.

The cross-stiffness in Fig. 4.13a is near zero for the preloaded case, but reaches higher values when the bearing is loose. This can be attributed to the load distribution becoming more asymmetric as the rotor moves horizontally. It is interesting to note that the maximum cross-stiffness is reached at a greater deflection as the clearance is increased, but the maximum value does not seem to be affected. As was found in the baseline case, the cross-stiffness tends back to zero for very large displacements.

The radial clearance has a very similar effect on the vertical stiffness, as shown in Fig. 4.13b. The most noticeable difference is that for the loose bearings, a deadband around the centre of the bearing where the stiffness is zero; the size of the deadband depends directly on the clearance level. For the preload case, it can also be observed that the vertical stiffness is very close to the horizontal stiffness in Fig. 4.13a. This is because the radial preload dominates over the self-weight, so the bearing stiffness is nearly axisymmetric.

In order to understand if the clearance changes the sensitivity of the bearing stiffness to cage angle, the stiffness in the rotor equilibrium position is plotted over a range of cage angles ψ_c in Fig. 4.15. It can be seen that larger clearances lead to a greater sensitivity to



(a) Horizontal sweep

(b) Vertical sweep

Figure 4.13: Variation of the average bearing stiffness with rotor position for different clearance levels

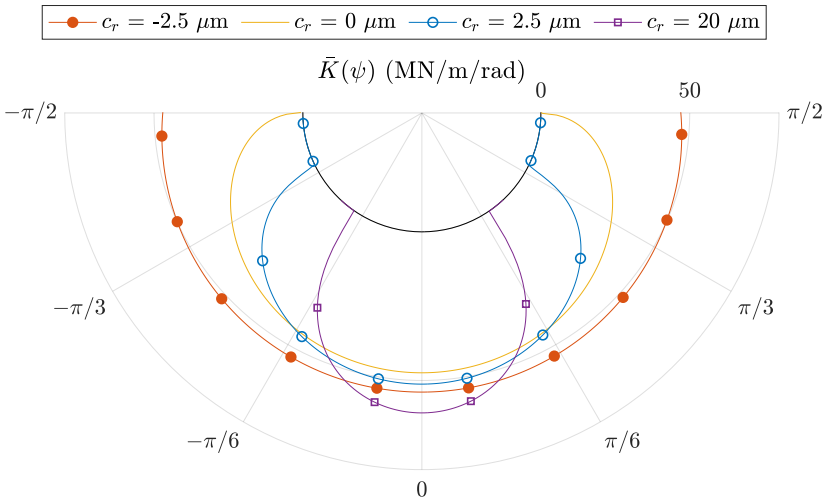


Figure 4.14: Variation of elemental stiffness distribution in equilibrium position for different clearance levels

cage angle. To explain this behaviour, Fig. 4.16 shows the number of loaded elements that are in contact as the cage rotates. When the bearing is preloaded, all elements remain in contact at all times, leading to a bearing stiffness independent of cage angle, while increasing clearance leads to a smaller and a changing number of loaded elements. There is a larger variation in *vertical* stiffness when the clearance is small ($c_r = 2.5\,\mu\text{m}$), but a larger variation in *horizontal* stiffness when the clearance is large ($c_r = 20\,\mu\text{m}$). This highlights a complex interaction between the clearance level and the variable compliance, since the variations in stiffness as the cage rotates are not only determined by the number of loaded elements at each cage angle, but also the angular positions of each element.

In general, the internal clearance appears to have a significant impact on the stiffness of

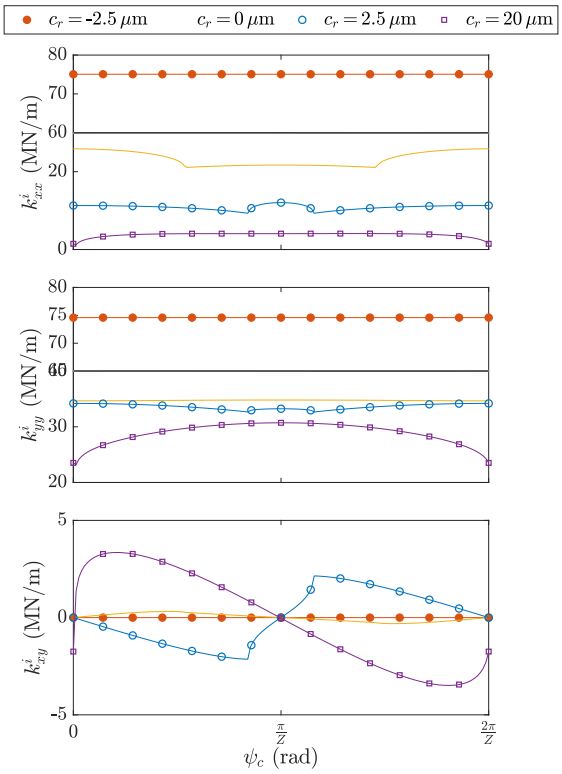


Figure 4.15: Variation of the bearing stiffness with cage angle for different clearance levels

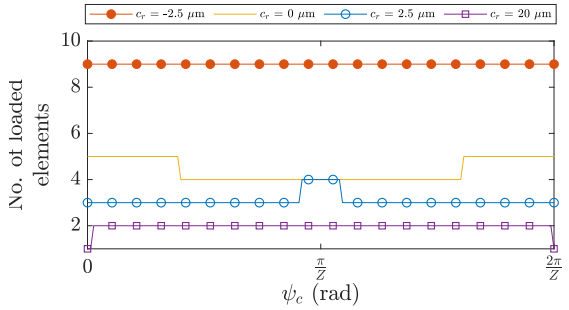
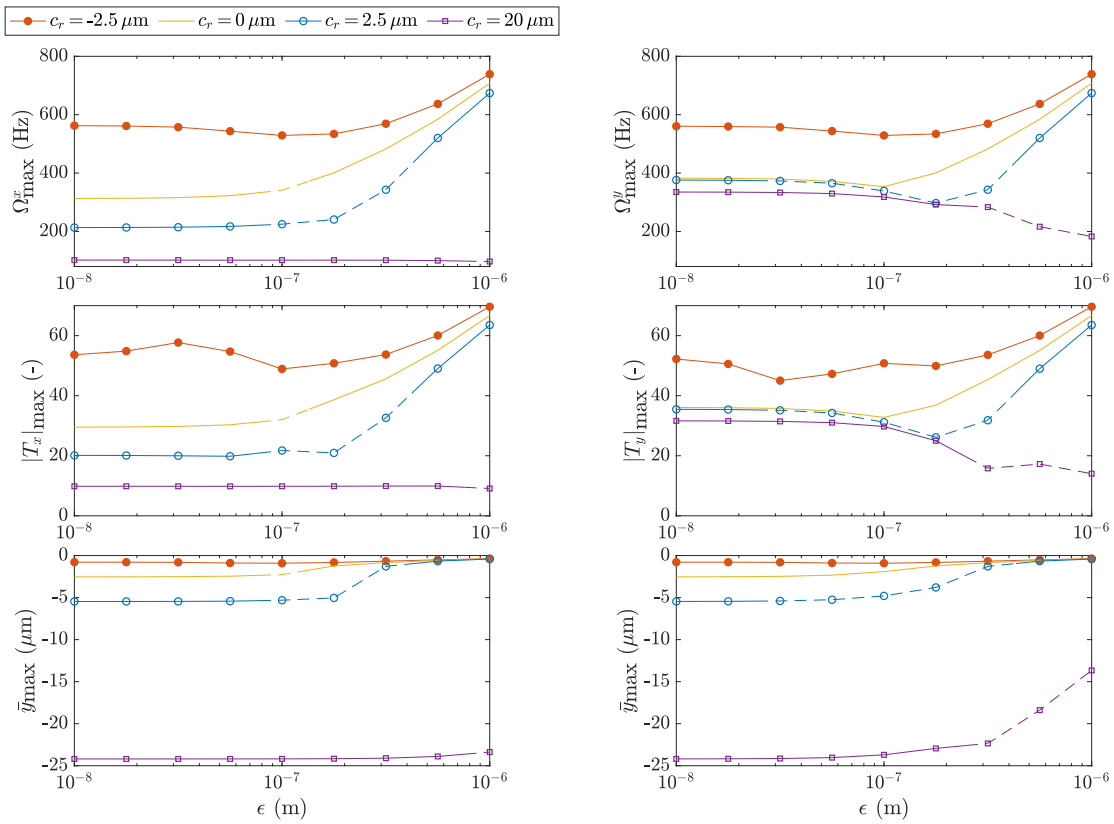


Figure 4.16: Variation of number of loaded elements with cage angle for different clearance levels

the bearing, and consequently it is expected to also have a strong impact on the frequency response of the system.

4.5.1.2 Frequency response

The frequency response was computed for all clearance levels, but only the condensed variation of the response at resonance is shown in Fig. 4.17. Considering first the linear response at low unbalance levels, ϵ, it can be seen that the resonance frequencies in both directions, Ω_{max}, are reduced when the bearing is loose, and increased when the bearing is preloaded. This behaviour can be attributed to the changes in the bearing stiffnesses observed in Fig. 4.13.



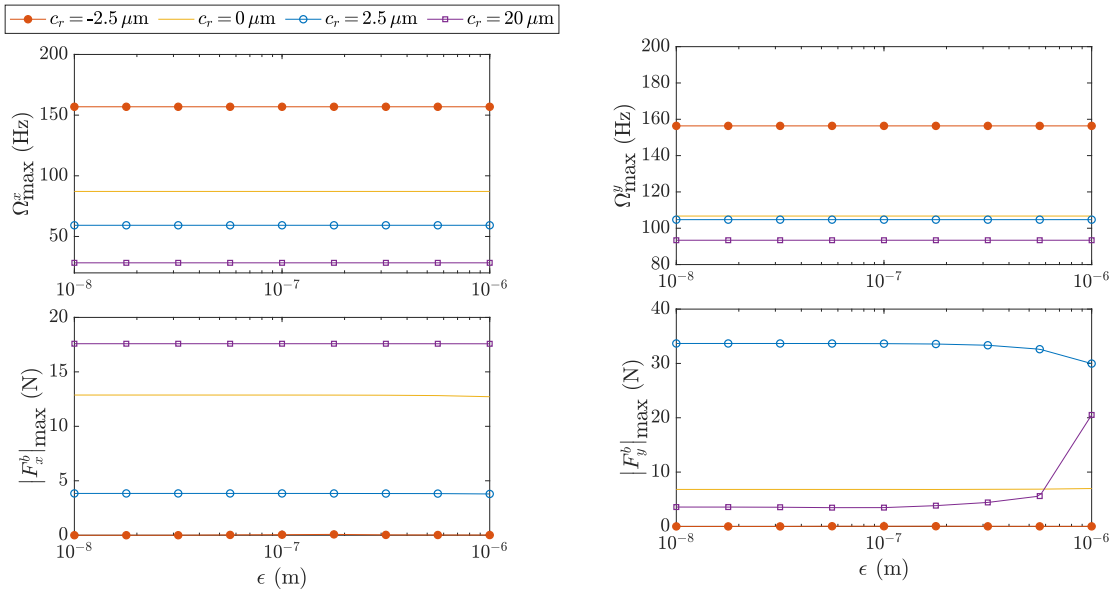
(a) Horizontal mode (b) Vertical mode

Figure 4.17: Variation of unbalance transmissibility at resonance with clearance

At higher excitation levels the resonance frequencies become much more dependent on the clearance. For the preload case ($c_r = -2.5\,\mu\text{m}$), some softening can be observed as the excitation increases, which is followed by a hardening effect, consistent with the more complex stiffness variation in Fig. 4.13. The resonance frequencies of the vertical and horizontal mode are similar for all unbalance levels, due to similar stiffness values in each direction.

For the cases without preload ($c_r \geq 0\,\mu\text{m}$), the resonance frequencies $\Omega_{\max}$, increase with the excitation level, which is consistent with the hardening effect shown in Fig. 4.13. When the clearance is very large ($c_r = 20\,\mu\text{m}$) the vertical mode shows a softening behaviour. This is because the size of the deadband in the vertical bearing stiffness is increased, so the rotor does not deflect enough to reach the stiffening regime. If the unbalance level was increased even further, it would eventually display a stiffening effect.

An unstable region appears for all clearance cases, indicated by a dashed line, which is caused by the deadband in the stiffness characteristic. As the clearance is increased, these unstable regions are shifted to higher excitation levels. This can be attributed to a smoother change in stiffness at the edges of the deadband so that the system must be excited harder to initiate instability. If the excitation level is further increased, the



(a) Horizontal mode

(b) Vertical mode

Figure 4.18: Variation of VC forcing at resonance with clearance

system is once more stabilised by the addition of the radial preload; this has been observed in other studies [65]. These results show that the instability induced by the bearing is strongly influenced by the radial clearance, but that it can be controlled by applying a preload.

The peak vibration transmission in Fig. 4.17 is reduced as the bearing clearance is increased. Since the damping in the system is kept constant, this increase in response amplitude can be directly linked to the change in resonance frequency, which is also quite apparent from Fig. 4.17. As the resonance frequency reduces, the effective damping ratio increases due to the simple relationship of $\zeta_r \approx \frac{c_b}{2m\omega_n}$.

It can also be observed from the bottom graphs in Fig. 4.17 that the centre of the rotor orbit at low unbalance levels moves downward as the clearance is increased. This is because the rotor must sag in order to load the bearing and support the weight of the rotor. However, the orbit centre moves upward towards 0 at high unbalance levels no matter the level of clearance, since the influence of the unbalance loading starts to negate the impact of the self-weight.

The variation of the VC forcing at resonance can be seen in Fig. 4.18 for different excitation and clearance levels. The magnitude of the forcing generally increases with the radial clearance, which can be attributed to the increased sensitivity of the stiffness to the cage position, as shown in Fig. 4.15.

When the bearing is preloaded, there is no VC forcing at all, since the stiffness does not vary with the cage angle. The frequency of the maximum forcing reduces with

clearance, which is consistent with the above mentioned reduction in bearing stiffness. The VC forcing generally remains constant for most of the excitation range, both in frequency and amplitude. Only at very large excitation levels in the vertical direction, some variations can be observed, where smaller clearance values ($c_r = 2.5\,\mu m$) lead to a small drop in VC forcing, while a large clearance ($c_r = 20\,\mu m$) leads to an increase in forcing. This is likely due to some interaction with the unbalance excitation. Another interesting point to note is that the vertical forcing is larger than the horizontal forcing for a small clearance ($c_r = 2.5\,\mu m$), whereas the converse is true for a larger clearance ($c_r = 20\,\mu m$). This is likely affected by the significant changes in the cross-stiffness shown in Fig. 4.15. Based on these results it can be observed that radial clearance generally amplifies the significance of variable compliance, and that non-negligible forces can be generated by it.

It has been shown that bearing clearance has a large influence on the rotor response. It controls whether there is a stiffening or softening effect in the response, strongly impacts the bearing stability, and it amplifies the VC forcing that a bearing experiences.

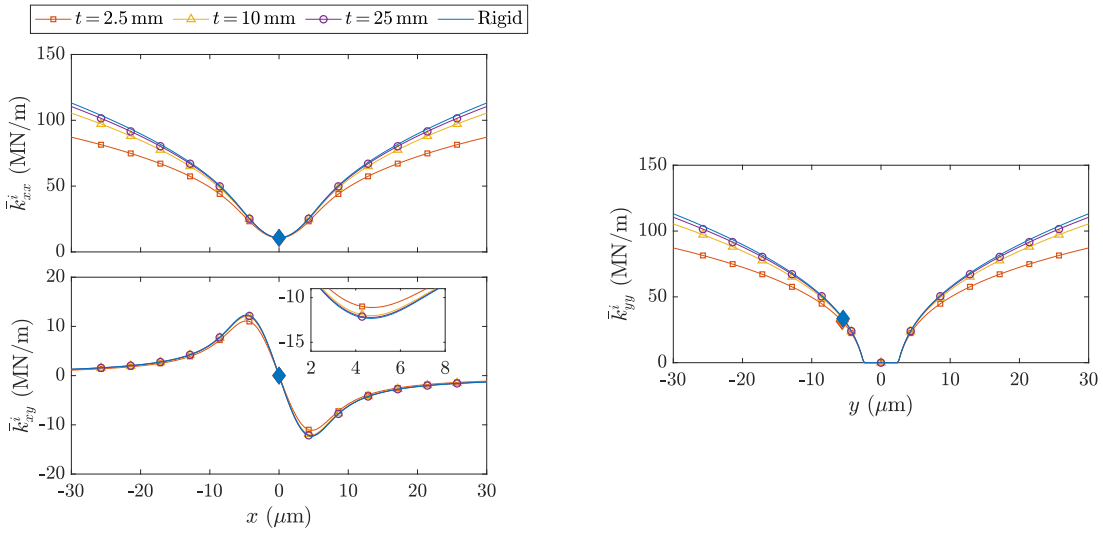
4.5.2 Ring Compliance

The influence of ring compliance on the dynamic response of the Jeffcott rotor will be investigated next. For this purpose, the outer ring of the bearing will be made compliant, and its thickness t will be varied from 2.5 mm to 25 mm to control its stiffness.

4.5.2.1 Stiffness

The average stiffness variation with rotor position is shown in Fig. 4.19. It can be seen that reducing the ring thickness, and hence increasing the ring compliance, leads to only a small reduction in bearing stiffness which applies in both the horizontal and vertical direction. The ring compliance has a tendency to reduce the maximum elemental load, as depicted in Fig. 4.20, which agrees with results from the literature [55, 78]. When the rotor moves very far in either direction, the contact loads and hence stiffnesses increase, which in turn makes the rings the dominant sources of compliance. This also means that the stiffness reduction increases as the ring thickness is reduced.

The cross-coupling reduces very slightly as the rings are made more compliant, as can be observed in Fig. 4.19a. This stiffness term mainly arises from a transfer of load from the most heavily loaded elements underneath the rotor to the adjacent ones, making the load distribution around the bearing asymmetric. However, the ring compliance distributes the loads between the elements more evenly so that the load distribution remains more symmetric as the rotor moves horizontally.



(a) Horizontal sweep

(b) Vertical sweep

Figure 4.19: Variation of the average bearing stiffness with rotor position for different levels of ring compliance

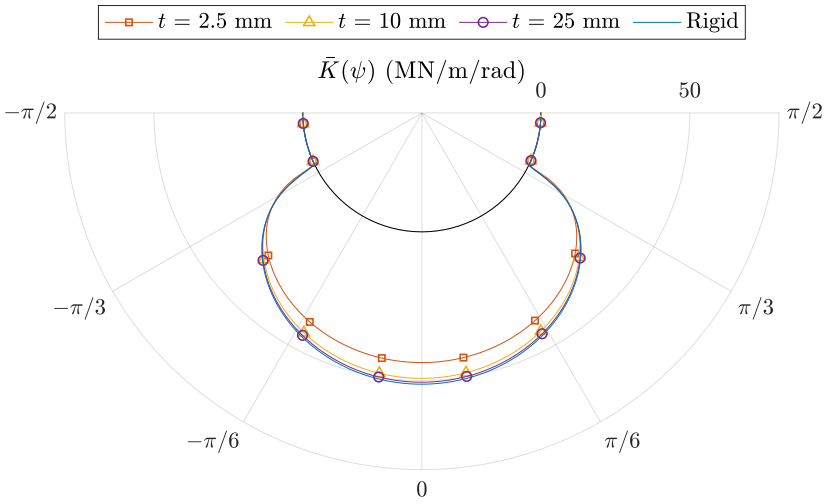


Figure 4.20: Elemental stiffness distribution in equilibrium position for different levels of ring compliance

The sensitivity of the bearing stiffness to cage angle is plotted in Fig. 4.21 for different ring thicknesses. It can be observed that the central lobes around $\psi_c = \frac{\pi}{Z}$ are wider when the rings are more compliant. The ring compliance transfers more load to the elements at the edge of the loaded zone as shown in Fig. 4.20, so that these elements remain loaded for a wider range of cage angles. This can be confirmed by examining the number of loaded elements which is shown in Fig. 4.22.

The peak horizontal stiffness k_{xx} at $\psi = \frac{\pi}{Z}$ is actually increased as the rings are made more compliant, which is again because more load is transferred to the elements at the edges of the loaded zone by the ring compliance, so they add a greater contribution to the horizontal stiffness. On the other hand, the horizontal stiffness $\psi = 0$ is reduced as the

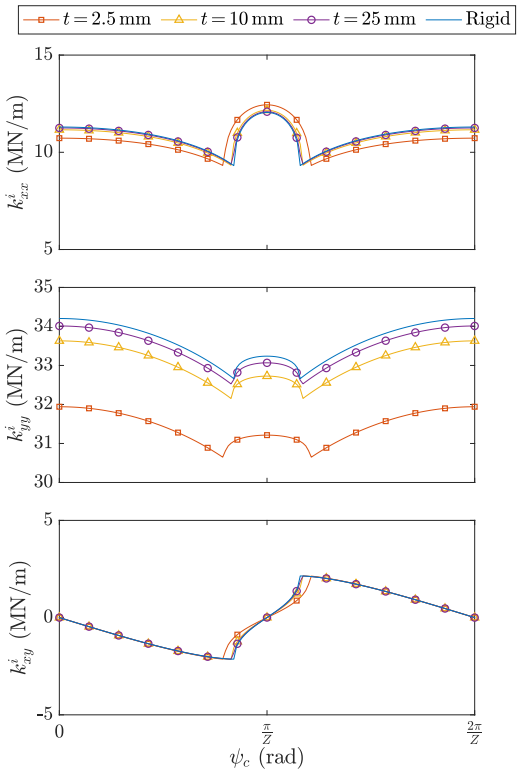


Figure 4.21: Variation of the bearing stiffness with cage angle for different levels of ring compliance

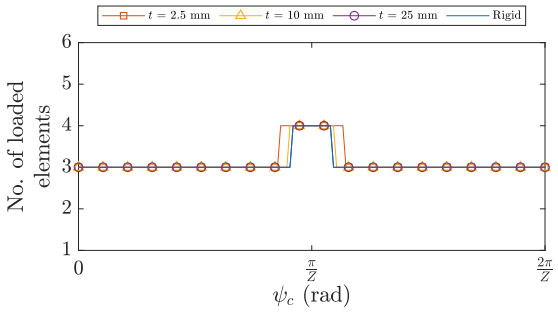
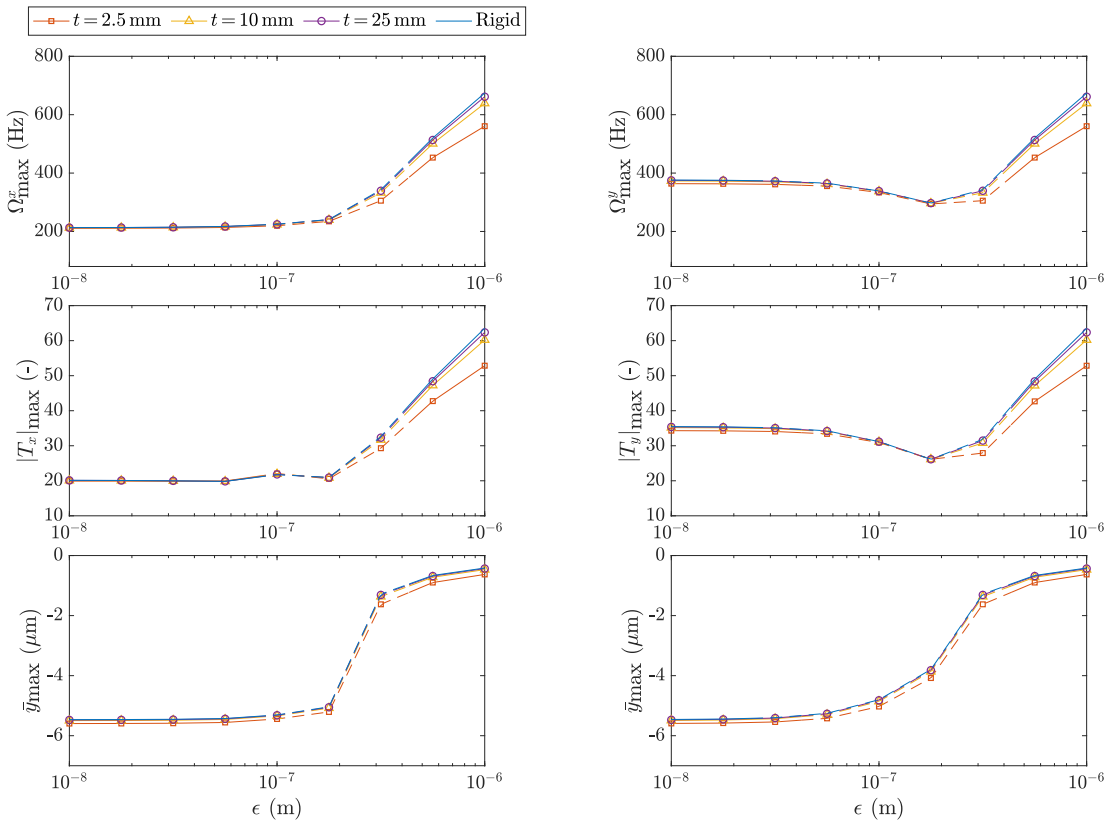


Figure 4.22: Variation of number of loaded elements with cage angle for different levels of ring compliance

rings are made more compliant, due to the general softening effect of the ring compliance. This means that the horizontal stiffness varies over a greater range as the rings are made more compliant. The absolute variation in vertical stiffnesses k_{yy} is reduced as the rings are made more compliant. However, the mean vertical stiffness also reduces with ring compliance, so that the relative variation in vertical stiffness actually increases, like the horizontal stiffness.

In summary it can be observed, that the bearing stiffness is reduced very slightly as the rings are made more compliant, but this becomes more significant as the rotor deflects further. The bearing stiffness becomes slightly more sensitive to cage position.



(a) Horizontal mode

(b) Vertical mode

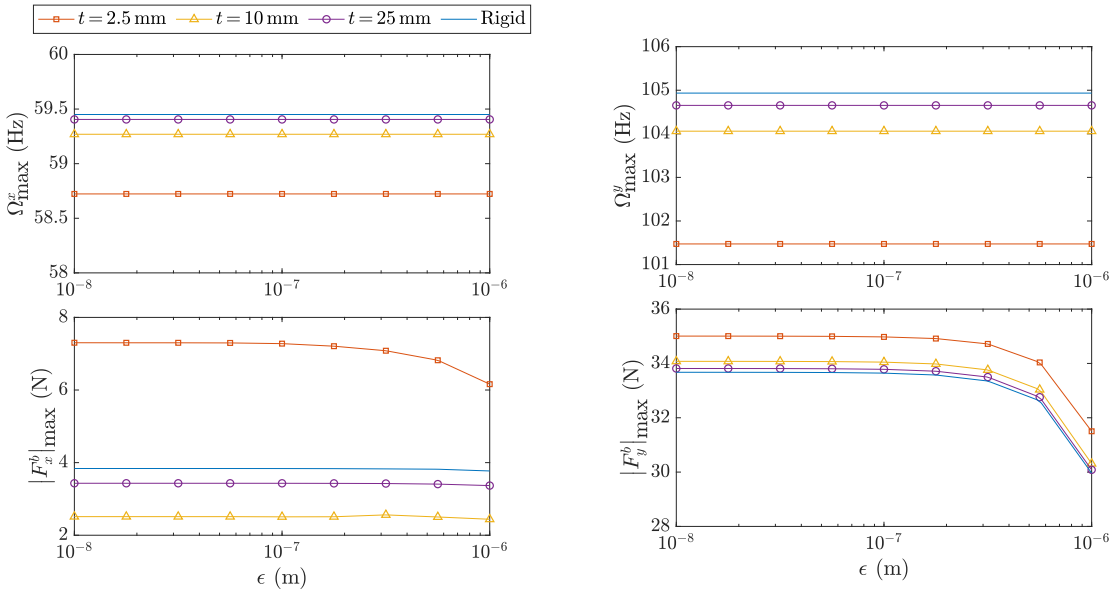
Figure 4.23: Variation of unbalance transmissibility at resonance with ring compliance

4.5.2.2 Frequency response

As with the previous cases, the frequency response was computed for different ring compliance levels, and the variation of the synchronous response at resonance is shown in Fig. 4.23. The resonance frequencies for the horizontal and vertical mode reduce slightly as the rings are made more compliant, but the effect only becomes of relevance at higher excitation levels. This is consistent with the larger stiffness reduction due to the ring compliance in Fig. 4.19. The peak transmissibility very much mirrors the frequency behaviour, which can once more be linked to the effective damping ratio in the system. The vertical position of the rotor, $\bar{y}_{\max}$, in Fig. 4.23 is slightly lower at resonance for more compliant rings due to an overall reduction in the bearing stiffness.

The stable region of the system is unchanged by ring compliance since the unstable regions appear at the same excitation levels as in the baseline case. This indicates that the ring compliance does not impact the stability of the system, and further supports the conclusions from Section 4.5.1 that the instability is mainly driven by the bearing clearance.

The variation of the VC forcing due to ring compliance is plotted in Fig. 4.24. The magnitude of the forcing increases slightly as the rings are made more compliant which



(a) Horizontal mode

(b) Vertical mode

Figure 4.24: Variation of VC forcing at resonance with ring compliance

is consistent with the larger variations in stiffness with cage position shown in Fig. 4.21. There is a drop in forcing at high excitation levels for all levels of ring compliance, due to an interaction with the unbalance excitation. The frequency of maximum forcing drops as the rings are made more compliant, since the linearised natural frequency of the system is reduced by the ring compliance.

Generally it can be said that the ring compliance leads to a small drop in the resonance frequency, which becomes more significant at higher amplitudes. It does not seem to affect the instability of the system, and its effect on the VC behaviour of the bearing is relatively small.

4.5.3 Centrifugal loading

No other studies in the literature were found to focus on the effect of centrifugal loading on the bearing elements in the context of rotating machines. Consequently their impact was investigated in some detail in this work, by artificially varying the ball density. This was first set to the true value for steel ($\rho_{steel} = 7800\,\mathrm{kg\,m^{-3}}$), and then doubled and quadrupled in order to scale the centrifugal loads. The baseline case was also included, where the centrifugal loads were neglected, which corresponds to setting $\rho = 0\,\mathrm{kg\,m^{-3}}$.

4.5.3.1 Stiffness

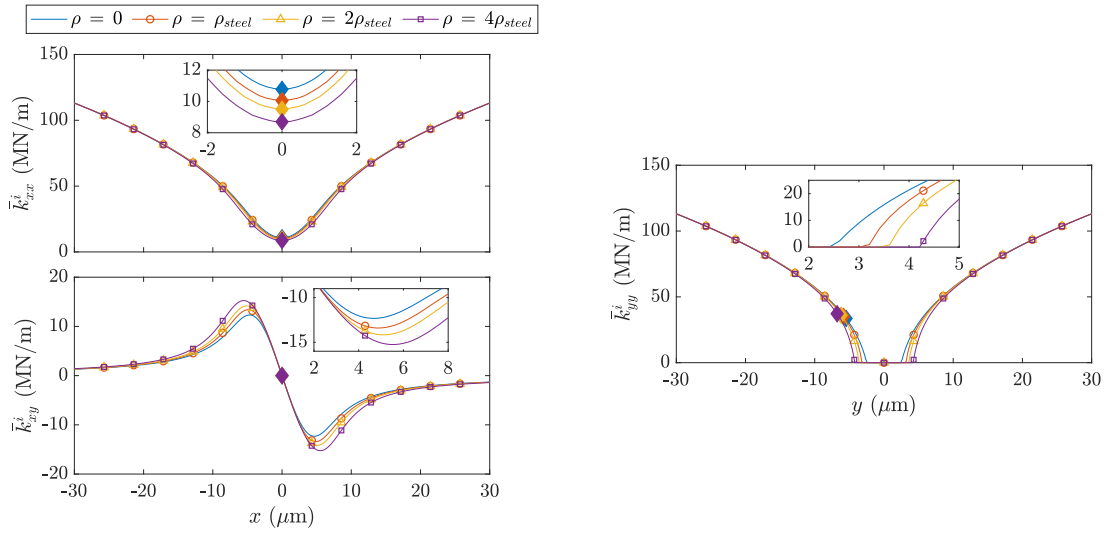
The stiffness computation was performed at a speed of $\Omega = 600\,\text{Hz}$ to ensure the centrifugal loads will be strong enough to influence the bearing behaviour. The resulting average horizontal stiffness, k_{xx}, in Fig. 4.25a shows only a small dependence on the centrifugal load, where higher centrifugal loading leads to a slightly softer behaviour. Looking at the load distribution plot in Fig. 4.26 it can be seen that higher centrifugal loads have a tendency to slightly unload the contacts at the edge of the loaded zone and hence reduce their contribution to the horizontal stiffness. With increasing horizontal rotor displacement, the reduction in stiffness becomes smaller, since the elastic loads in the bearing dominate over the centrifugal loads.

The cross-stiffness variation is shown in the bottom graph of Fig. 4.25a and is increased very slightly by the introduction of centrifugal loads. As the rotor moves horizontally, the more lightly loaded side of the bearing is further unloaded by the centrifugal loading on the elements, which increases the asymmetry of the load distribution around the bearing (see Fig. 4.26), thereby slightly increasing the cross-stiffness.

The average vertical stiffness in Fig. 4.25b shows that the deadband around the centre of the bearing is wider with centrifugal loads, leading to an increase in the effective clearance. This can be attributed to an unloading of the inner contacts due to the centrifugal forces, leading to a larger displacement of the inner ring before it comes into contact with the elements. As an interesting side effect, the rotor sags slightly further in the equilibrium position when centrifugal loads are introduced. Although the effective clearance is increased, the stiffness in the equilibrium position is counter-intuitively increased very slightly. This can be related to load distribution being more focused on the elements underneath the bearing (see Fig. 4.26), which provide the greatest contribution on the vertical stiffness.

The stiffness variation with the cage position is shown in Fig. 4.27. It can be seen that the bearing stiffness is much more sensitive to cage position when centrifugal loads are included. For the horizontal stiffness, k_{xx} the lobe of the baseline case around $\psi_c = \frac{\pi}{Z}$, where an extra element becomes loaded, is replaced by a flat region with a much lower stiffness. This behaviour can be attributed to a decrease in the number of loaded elements due to the centrifugal loading, as shown in Fig. 4.28 where higher centrifugal loads lead to wider areas of reduced element contact. As a result the load distribution is distorted in the presence of centrifugal loads (see Fig. 4.26), and consequently the cage must rotate further for the next contact to enter the loaded zone. This effect also amplifies the cross-stiffness in this regime. The maximum horizontal stiffness values are much less affected by the cage position.

The vertical stiffness is also heavily affected by the cage position, with a similar flat



(a) Horizontal sweep

(b) Vertical sweep

Figure 4.25: Variation of the average bearing stiffness with rotor position at $\Omega = 600\,\mathrm{Hz}$ for different levels of centrifugal loading

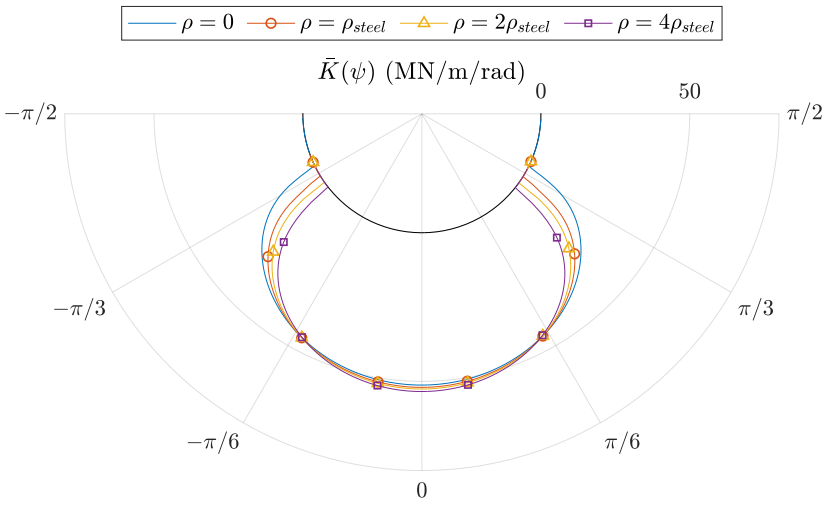


Figure 4.26: Elemental stiffness distribution in equilibrium position at $\Omega = 600\,\mathrm{Hz}$ for different levels of centrifugal loading

section around $\psi_c = \frac{\pi}{Z}$. The maximum vertical stiffness, which occurs at $\psi_c = 0$ and $\psi_c = \frac{2\pi}{Z}$, is increased by the centrifugal loads which once more can be linked to the previously discussed more focused load distribution in this case (see Fig. 4.26).

In summary the centrifugal loading has a very limited influence on the bearing stiffness, but it significantly increases the sensitivity towards cage position, potentially leading to greater self-excitation due to variable compliance.

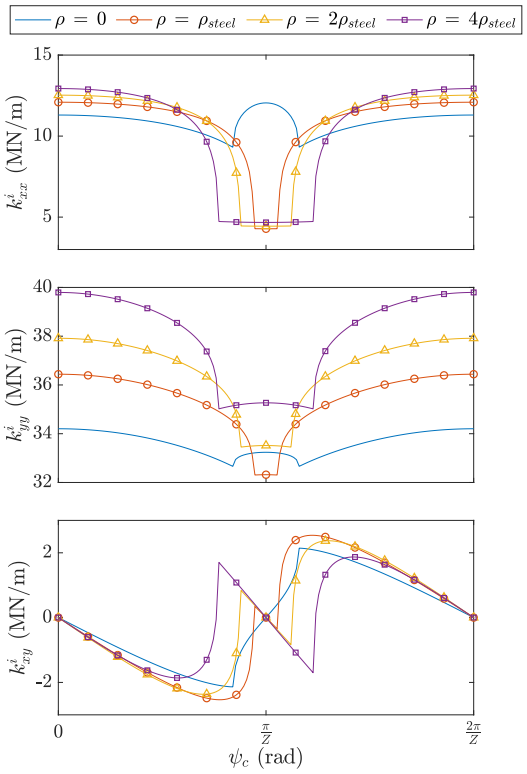


Figure 4.27: Variation of the bearing stiffness with cage angle at $\Omega = 600$ Hz for different levels of centrifugal loading

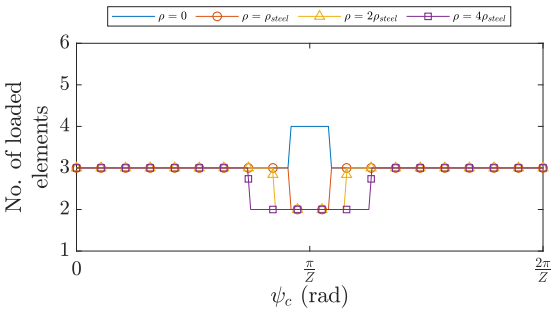
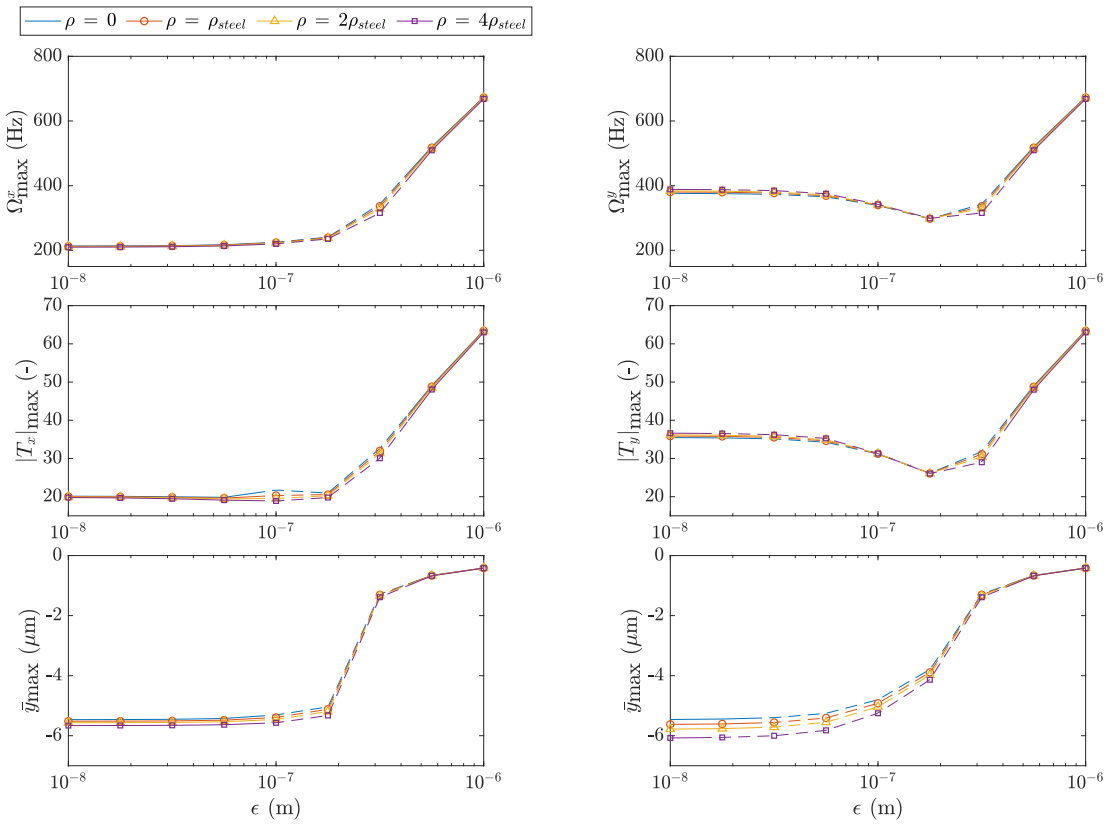


Figure 4.28: Variation of number of loaded elements with cage angle at $\Omega = 600$ Hz for different levels of centrifugal loading

4.5.3.2 Frequency response

The variation of the response at resonance in Fig. 4.29 shows that the centrifugal loads have a very small influence on the rotor response. As the centrifugal loading level is increased, there is a very slight reduction in the resonance frequencies for both modes, which is consistent with the drop in stiffness shown in Fig. 4.25. This reduction in the resonance frequency becomes less significant at the highest excitation levels where the elastic forces at the contacts start to dominate.

Although the resonance frequencies themselves are not affected much, the unstable regions at medium excitation levels are influenced by the centrifugal loading. Particularly for the



(a) Horizontal mode (b) Vertical mode

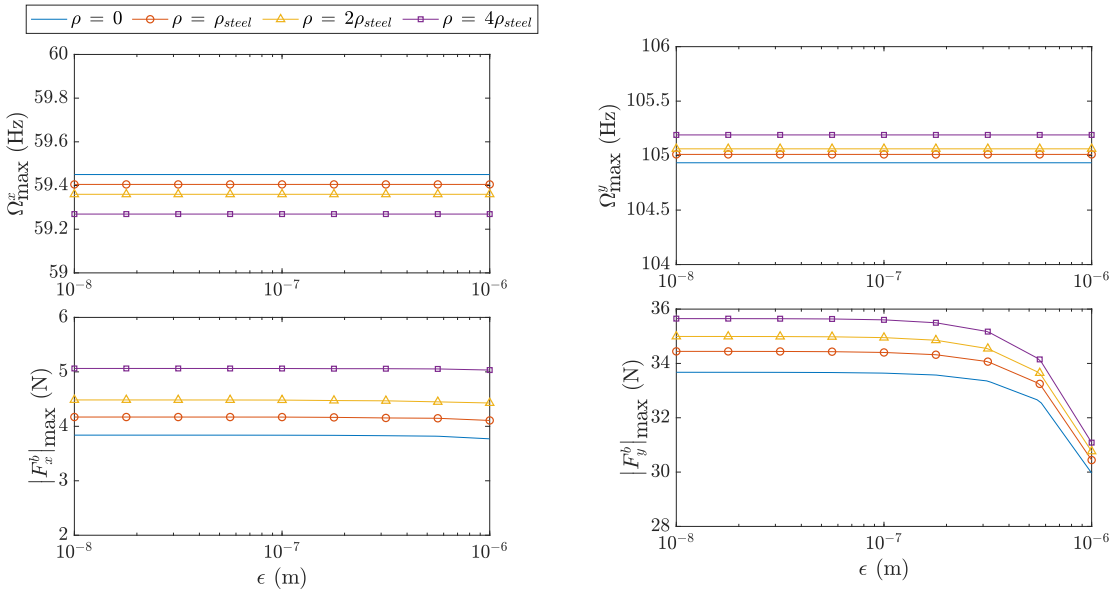
Figure 4.29: Variation of unbalance transmissibility at resonance with centrifugal loading

vertical mode in Fig. 4.29b, larger centrifugal loads lead to a loss of stability at smaller unbalance levels. This effect is driven by the centrifugal loads increasing the effective clearance which has previously been shown to destabilise the system (see Section 4.5.1). On the other hand, the stability of the horizontal mode in Fig. 4.29a is unaffected, as the self-weight of the rotor prevents the centrifugal loads from increasing the effective clearance in this direction.

The variation of the VC forcing with the level of centrifugal loading can be seen in Fig. 4.30 where an increase in the centrifugal loading leads to an increase in the VC forcing. The increase in forcing is smaller than might be expected from the relatively significant changes in bearing stiffness shown in Fig. 4.27. This is because the sub-resonances occur at low frequencies around 100 Hz, whereas the bearing stiffness in Fig. 4.27 was analysed at a much higher speed of 600 Hz. It should be kept in mind that this is application specific, and consequently this effect may be quite strong for other rotors and bearings.

Another feature of increasing the level centrifugal loading was a strong downward motion of the rotor with increasing rotational speed (see Fig. 4.31). This could be once more attributed to the speed dependent increase in clearance due to the centrifugal ball loading.

The inclusion of the centrifugal loading into the bearing model shows very small effect on



(a) Horizontal mode

(b) Vertical mode

Figure 4.30: Variation of VC forcing at resonance with centrifugal loading

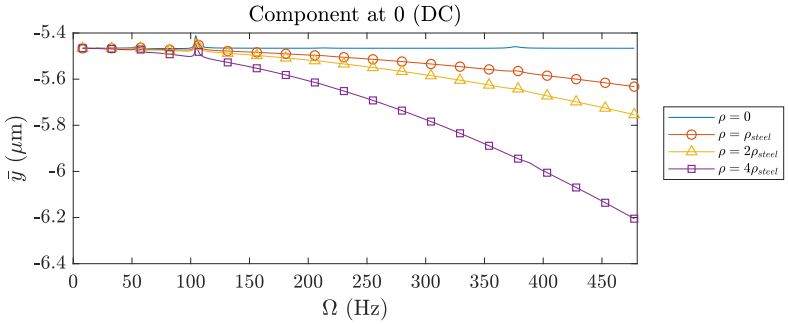
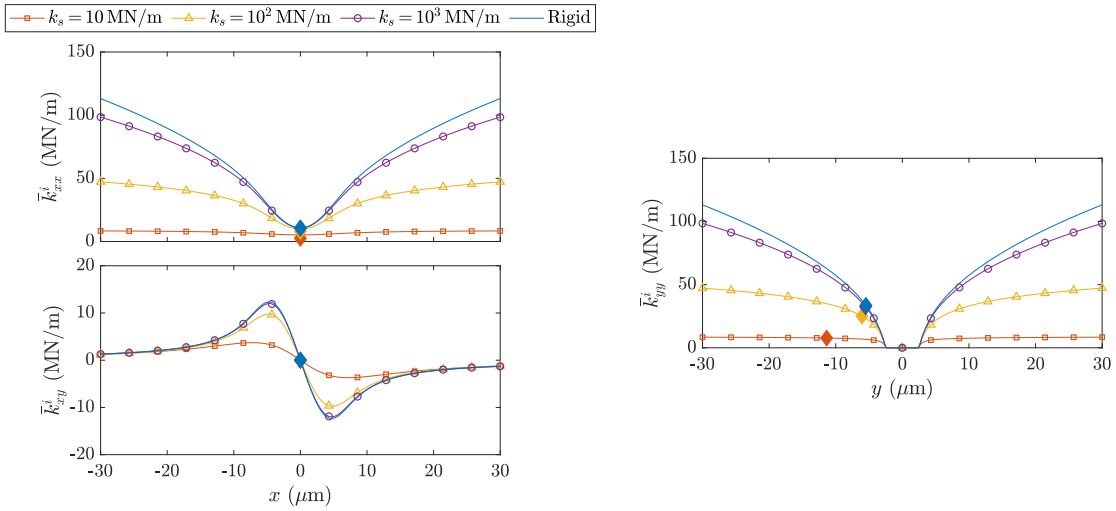


Figure 4.31: Variation of mean vertical rotor position with centrifugal loading for different speeds with $\epsilon = 1 \times 10^{-8}$ m

the actual dynamic response of the Jeffcott rotor, but it slightly destabilises the system and can lead to a different equilibrium position, potentially impacting the safe operation of the rotor.

4.5.4 Stator compliance

The final parameter study focused on the effect of a flexible stator. For this purpose the support stiffness k_s in horizontal and vertical direction was varied over a wide range. The limiting case of a rigid stator, as in the baseline configuration, was also considered by setting $k_s = \infty$.



(a) Horizontal sweep

(b) Vertical sweep

Figure 4.32: Variation of the average bearing stiffness with rotor position for different levels of stator compliance

4.5.4.1 Stiffness

The overall stiffness of the bearing in series with the stator has been plotted in Fig. 4.32. Not surprisingly, as the stator compliance is increased, the vertical and horizontal stiffnesses reduce considerably and become less and less dependent on the displacement since the linear stator compliance starts to dominate. This has the additional consequence that the cross-stiffness is also reduced and the behaviour is generally more linear. However, it should be noted that the deadband in the vertical stiffness remains, since this purely depends on the clearance of the bearing, which is not affected by the support stiffness.

Fig. 4.33 shows the variation of the overall bearing stiffness with cage angle. As the stator becomes more compliant, the sensitivity of all of the stiffness terms to the cage position is reduced. This is because the stator compliance dominates the behaviour, which is axisymmetric and independent of the cage position.

In summary, considerable changes to the stiffness behaviour of the bearing can be observed when the stator compliance is increased. The rotor support becomes much softer and more linear.

4.5.4.2 Frequency response

Given the strong changes in the bearing support stiffness due to stator compliance, a significant change in the frequency response would be expected. Fig. 4.34 shows that as the stator becomes more compliant, the resonance frequencies reduce and the linear regime extends to higher excitation amplitudes. For the softest case of $k_s = 1\,\mathrm{MN\,m^{-1}}$,

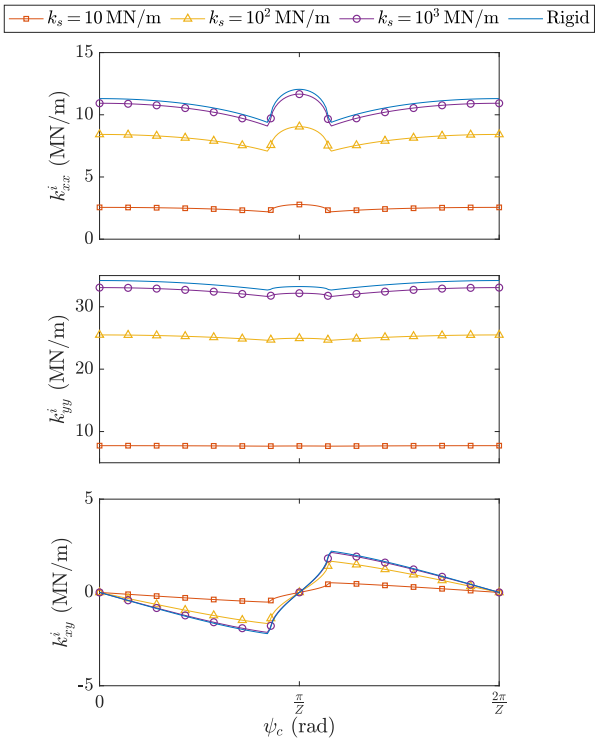


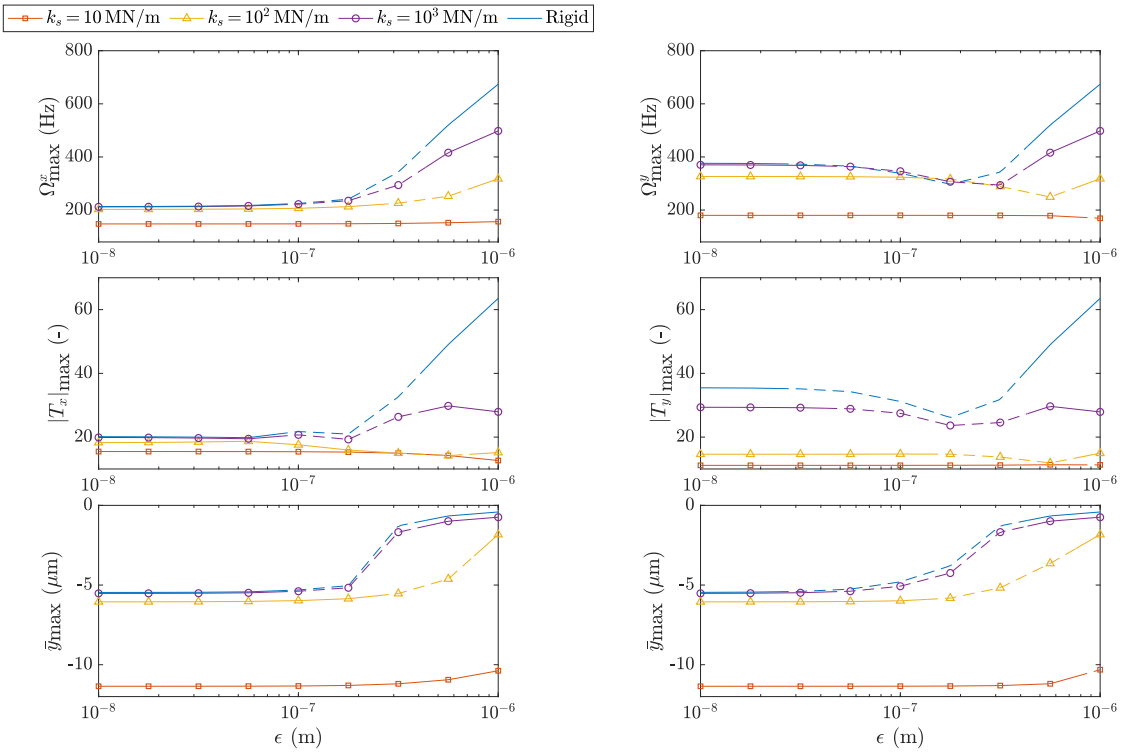
Figure 4.33: Variation of the bearing stiffness with cage angle for different levels of stator compliance

there is no change in the resonance frequency even at the highest excitation level, which is in agreement with the full linearisation of the stiffness characteristic in Fig. 4.32. This also means that the peak transmissibility remains constant. Stator compliance has the additional consequence that the mean rotor position, $\bar{y}_{\max}$, does not move upward so much at resonance, since the static response of the linearised system is unaffected by the unbalance response.

The unstable regions in Fig. 4.34 move to higher unbalance levels as the stator becomes more compliant with the lowest stiffness level $k_s = 1\,\mathrm{MN\,m^{-1}}$ leading to a totally stable system. Previous results in Section 4.5.1 have shown that the instability predominantly depends on the clearance and its effect on the stiffness behaviour (deadband). As the support gets softer, the transition from the deadband region to the contact zone in Fig. 4.32b becomes smoother and smoother, hence stabilising the system.

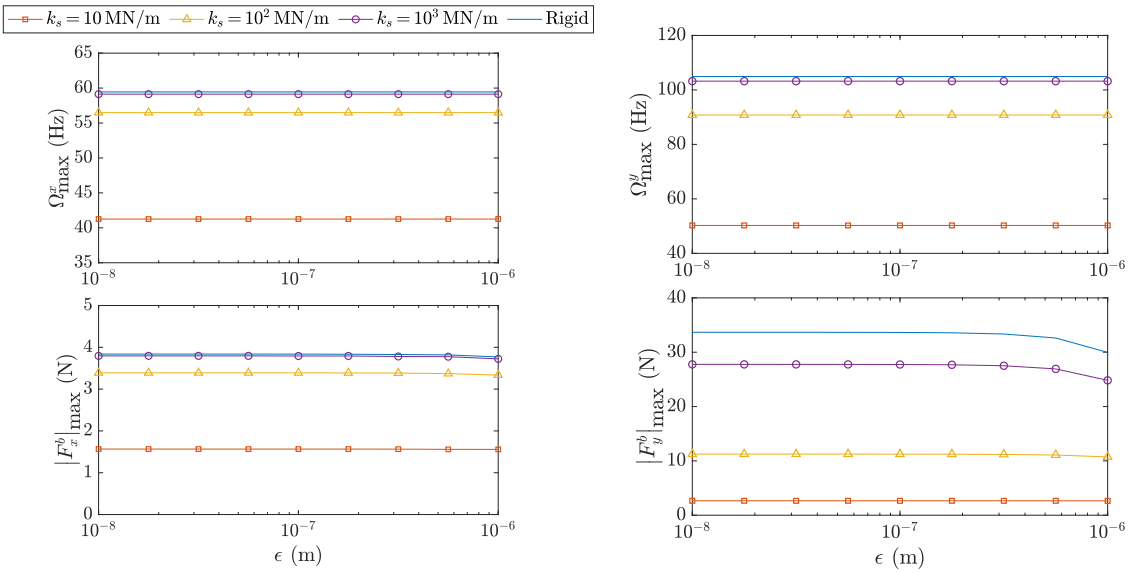
The maximum VC forcing is shown in Fig. 4.35. It reduces considerably when the stator becomes compliant since the stator compliance dominates, making the system less sensitive to the cage position (see Fig. 4.33). The frequency of maximum forcing also reduces significantly with increasing stator compliance, since the overall system is softer.

Increasing stator compliance has a significant effect on the rotordynamic response, by linearising the system and reducing the resonance frequency. In addition the system is also stabilised, and VC effects become less relevant.



(a) Horizontal mode (b) Vertical mode

Figure 4.34: Variation of unbalance transmissibility at resonance with stator compliance



(a) Horizontal mode (b) Vertical mode

Figure 4.35: Variation of VC forcing at resonance with stator compliance

4.6 Discussion

This study on the influence of a non-linear rolling-element bearing on the unbalance response of a Jeffcott rotor has highlighted the relative importance of different features from a modelling perspective.

When there is a static radial load on the bearing, it can no longer be considered symmetric, leading to different stiffnesses in the horizontal and vertical directions. In the case investigated in this paper, the vertical stiffness was approximately 2× higher than the horizontal direction due to the weight of the rotor, which agrees with the literature [5]. This asymmetry led to a splitting of the resonance frequencies, where the vertical mode had a higher frequency (376 Hz) than the horizontal mode (213 Hz). The frequency response displayed significant non-linear behaviour, where the vertical mode initially decreased in frequency as the unbalance load was increased, before eventually increasing significantly, whereas the resonance frequency of the horizontal mode increased monotonically. At the highest excitation levels, the two modes converged towards a single resonance frequency of 674 Hz.

At medium unbalance levels, the response of the horizontal and vertical modes can become unstable, which was attributed to the radial clearance. At very high unbalance levels the influence of the self-weight is negligible, so that the rotor exhibits circular orbits around the centre. This also means the effect of the clearance becomes negligible so that the response can regain stability.

A particular feature of this investigation was the inclusion of variable compliance (VC), and its effect on the rotor response was considered in detail. The General Harmonic Balance method proved to be an effective tool to study rotor-bearing systems which display quasi-periodic responses due to VC. It was shown that VC led to sub-synchronous excitation, which generated extra resonances at lower frequencies, where the VC frequency coincided with the natural frequency of the horizontal and vertical modes of the underlying linear system. The forcing due to variable compliance was generally insensitive to unbalance level, as it is driven purely by the cyclic-symmetry of the bearing. The resulting forcing amplitude was in the range 10 N to 40 N, and was determined by the sensitivity of the bearing stiffness to cage position.

4.6.1 Clearance

Clearance was found to have the largest influence on the bearing characteristic and is the greatest source of bearing non-linearity. It was found in Section 4.5.1 that when the bearing is loose, the response in the horizontal direction displayed hardening behaviour, whereas the vertical response displayed an initial softening then hardening behaviour. If

the bearing is radially preloaded, both modes were found to increase in frequency significantly (by around 300 Hz) and display softening then hardening behaviour. Clearance was identified as the main driver of instability in the system, due to the sudden change in stiffness when the clearance gap is closed. These unstable regions covered a wider range of unbalance levels as the clearance was increased, but could be controlled by radially preloading the bearing. It was also observed that increasing the bearing clearance magnified the variation in compliance as the cage rotates, leading to a 8× increase in VC forcing.

4.6.2 Ring compliance

Ring compliance is rarely included in bearing models, but the results in Section 4.5.2 showed that this phenomenon can lead to a small reduction in bearing stiffness (up to 7 % in the vertical direction). The reduction in stiffness became more significant as the bearing was more highly loaded (where there can be up to a 16 % drop in stiffness), so it is particularly important that attention is paid to how the rings are supported in applications where the vibration levels are high. Ring compliance was also found to increase the self-excitation from the VC effect somewhat (by up to 5 N), but was not found to change the overall softening/hardening characteristic of the non-linearity.

4.6.3 Centrifugal loading

Centrifugal loading on the bearing elements was found to have a very small effect on the rotor dynamic response in Section 4.5.3, and led to a very small reduction in resonance frequency (up to 2 %) and no change to the non-linear stiffness characteristic. For very heavy balls, the unstable region extended to higher unbalance levels due to an increase in effective clearance, but this corresponded to non-physical ball densities. The most significant effect of the centrifugal loading was that the rotor drifts downward as the rotor speed was increased (up to 15 % of the static deflection), which can strongly affect rotor and disc clearances in high accuracy applications. Centrifugal loading was found to slightly increase the self-excitation due to variable compliance (by around 2 N), due to the increase in effective clearance. It should be noted that centrifugal loading may have a greater influence in bearings with angled contacts, where the dynamic loads can lead to changes in the contact angle.

4.6.4 Stator compliance

It was found in Section 4.5.4 that increasing the level of stator compliance reduces the resonance frequency of both modes, and more importantly, the system becomes more

linear because the influence of the bearing is reduced. Additionally, the instability induced by the bearing clearance was found to disappear when the supports were very soft, and the self-excitation from variable compliance became negligible. As a result it is acceptable to model a relatively stiff bearing on a soft support as a linear system, as long as the support stiffness is significantly softer than the bearing stiffness; in this case, the system behaved linearly once the stator stiffness was approximately $\frac{1}{5}$ of the vertical bearing stiffness.

4.6.5 Summary

From the parameter study, it can be said that support stiffness and bearing clearance are the two most important features that need to be considered when attempting to accurately model the response of a rotordynamic system. The effect of the centrifugal loading on the bearing elements is most relevant for high precision or high speed applications, and ring compliance can generally be neglected as long as the bearing housing is significantly stiff and the rotor remains reasonably well balanced. Variable compliance can generate significant sub-synchronous excitation forces in the bearing, which may not directly impact the rotor dynamics due to their low frequency nature, but may lead to unexpected resonances on the rotor or support structure.

4.7 Conclusions

The bearing model from Section 3.2 was simplified for the case of a deep-groove ball bearing, and integrated into a model of a simple Jeffcott rotor system. The Generalised Harmonic Balance Method from Section 3.3 was applied in a novel way to predict the response of the system in an efficient manner, whilst incorporating the influence of the bearing non-linearities in conjunction with its variable compliance, which is otherwise often neglected.

The rotor-bearing system was found to have distinct horizontal and vertical resonances due to the asymmetry introduced by the bearing. The response was found to be highly nonlinear, with both softening and stiffening behaviour present, and zones of stability loss were identified. The application of GHBM was able to capture the sub-synchronous self-excitation from the VC effect, which led to sub-resonances where the Ball Pass Frequency coincided with the frequency of the horizontal and vertical modes. Such phenomena could not be captured with a linearised bearing model.

A systematic parameter study showed that bearing clearance has by far the largest influence on the dynamic response of the rotor, leading to strong nonlinear effects and

controlling the stability of the system. It was also found to amplify the self-excitation due to the VC effect. Only the addition of a soft support compliance around the bearing was found to limit this nonlinear behaviour by linearising the system. Ring compliance and centrifugal loading had only a small impact on the nonlinear dynamic response of the rotor, suggesting that they may generally be neglected in the analysis, although they may become of relevance for heavily unbalanced machines and high speed applications respectively. A much improved understanding of the different physical mechanisms within the bearing was developed.

The results from this chapter have highlighted the need to use a bearing model that can at least capture the radial clearance. However, if the support stiffness is very low, a linearised analysis may be sufficient. It was also shown that the VC effect can lead to significant super-synchronous forcing, which may lead to unexpected sub-resonances in a rotating machine. In the next chapter, a model of a test rig will be developed, which will eventually allow these phenomena to be investigated experimentally.

Chapter 5

The ARES test rig and model development

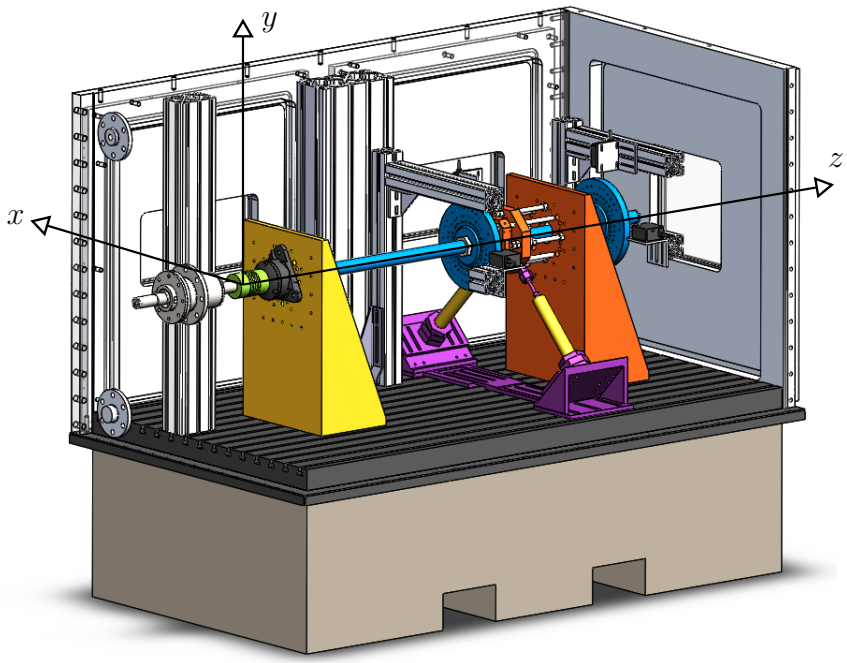
A general-purpose rotordynamics test rig known as the "Asynchronous Rotor Excitation System" (ARES) has been designed and built at Imperial College [184]. This can be used to explore a wide variety of rotordynamic phenomena, but was designed with investigations relating to rolling element bearing transmissibility in mind. The capabilities of the ARES test rig will first be described, as well as the key subsystems. It was necessary to develop an accurate model of the rig, in order to ensure that the response predicted by simulations would be comparable to the measured response. The results from experimental testing on each subsystem will be presented, including the bearing, rotor and stator. Suitable models of each system will be introduced, and the unknown parameters will be identified.

5.1 Overview of the ARES test rig

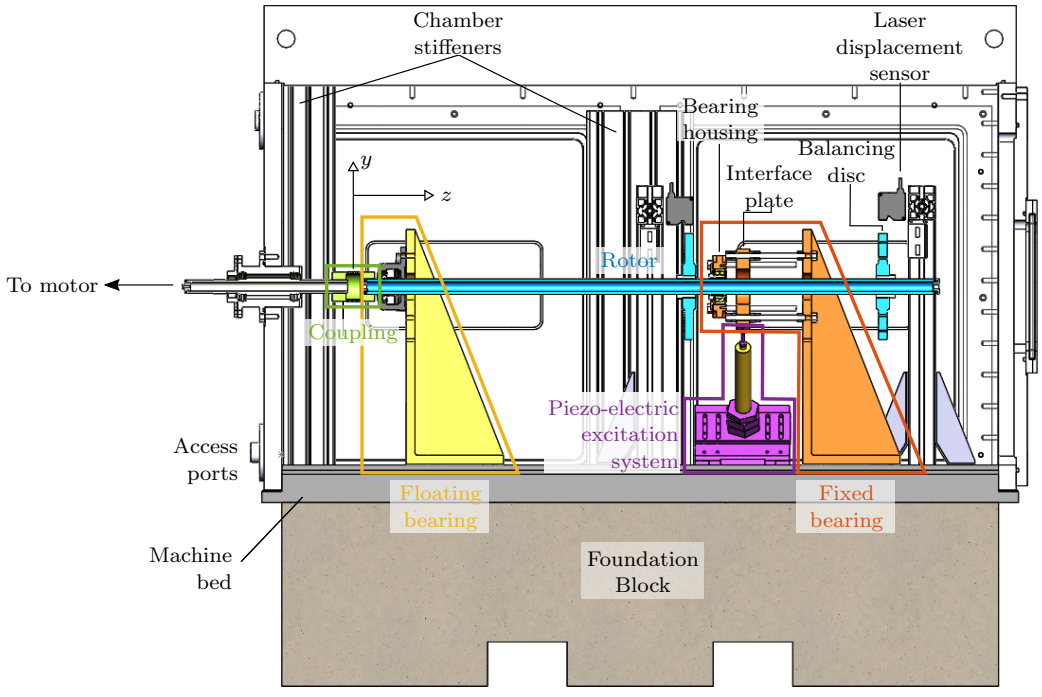
The ARES test rig consists of a single rotor supported by two self-aligning ball bearings (SABBs) as depicted in Fig. 5.1, where the key subsystems have been highlighted in different colours. The rotor consists of a flexible shaft, along which two rigid balancing discs are mounted (shown in blue). The axial location of both the discs and bearings can be varied, allowing the modes of the rig to be tuned as desired. The front bearing is supported by a flexible structure (shown in yellow), whose flexibility can be varied. This bearing can also be excited using an actuation system (shown in purple).

The rotor is housed within a steel containment chamber shown in Fig. 5.2a, which also allows the rotor to be operated in a vacuum if required. The rotor is driven by a Siemens motor as shown in Fig. 5.2b, with a maximum motor speed of 100 Hz. The drive shaft

from the motor is connected to the rotor by a flexible metal bellows coupling (shown in green in Fig. 5.1). The key subsystems will now be discussed in more detail.

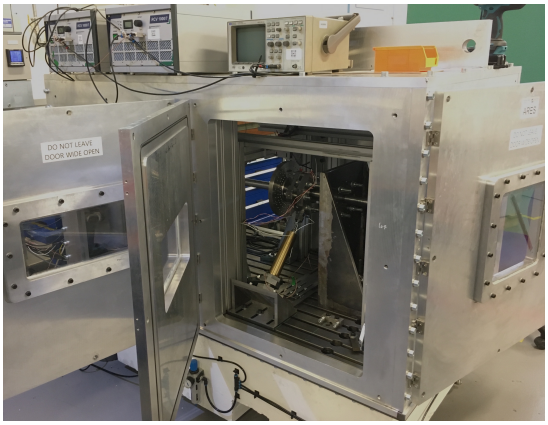


(a) Isometric view



(b) Cross-section view

Figure 5.1: CAD model of the ARES rig



(a) Chamber containing rotor



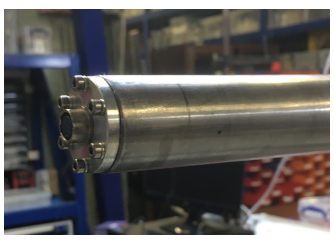
(b) Drive system

Figure 5.2: Photos of the ARES test rig

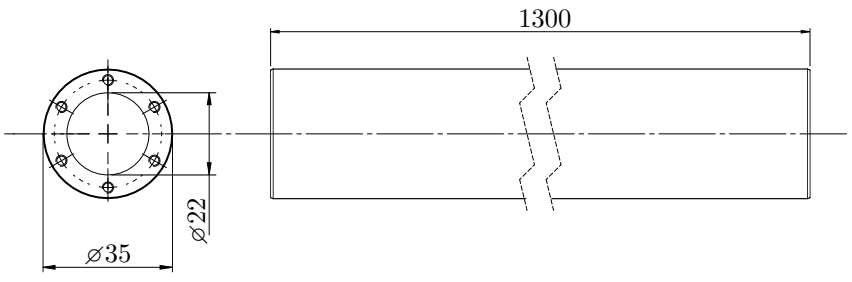
5.1.1 Rotor

The primary component of the ARES rotor is a 1300 mm long cylindrical shaft made from AISI 314 Stainless steel. It has a 35 mm OD and a 22 mm bore to allow cables to run through the shaft, as depicted in Fig. 5.3. This cabling is used to drive actuators or connect sensors on the rotor, such as piezo-electric patches or strain gauges on bladed discs. There are end caps at each end of the shaft, which house electrical connectors; one can be seen in Fig. 5.3a. Note that no instrumentation was placed on the rotor for the experimental tests in this project, although the cabling and electrical connectors remained.

Two solid balancing discs can be mounted on the shaft. These discs are made from AISI 314 Stainless steel like the shaft, and have an outer diameter of 240 mm as depicted in Fig. 5.4. These discs have three rows of threaded holes, which are spaced every 10°, to which balancing masses can be attached. Note that the middle row of bolts are offset by 5° from the inner and outer rows. The discs are fixed to the shaft using steel TranTorque GT adapters from Fenner Drives (model number 6202850UP). These are a form of keyless bushing, and rely on friction at the interfaces to hold the discs in place. They have the

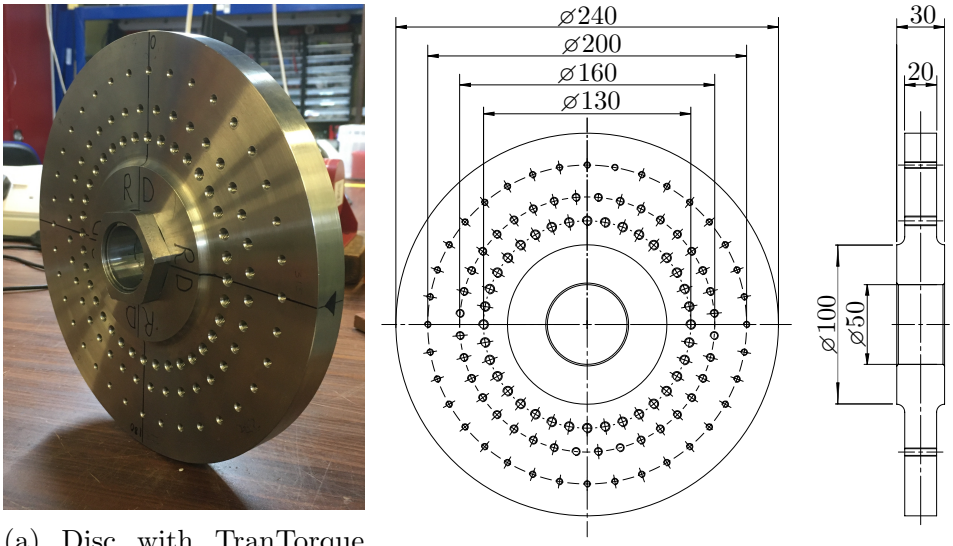


(a) Shaft with end cap



(b) Engineering drawing

Figure 5.3: ARES shaft



(a) Disc with TranTorque adaptor

(b) Engineering drawing

Figure 5.4: ARES balancing disc

additional advantage that the discs can be attached to the shaft at any axial location.

5.1.2 Rolling-element bearings

5.1.2.1 Floating bearing

The rear bearing is an SKF 1208-EKTN9 SABB. This bearing is housed within an SKF FNL 508 B housing, which was bolted directly to an L-shape pedestal, as shown in Fig. 5.5a. This bearing was therefore considered to be rigidly supported. The pedestal is bolted to the test bed with T-slots, so that the bearing can be moved axially. The SKF FNL 508 B housing fits the bearing loosely so that it is free to move axially; this bearing was therefore referred to as the "floating" bearing. The bearing is fixed to the shaft with an SKF H208 adaptor sleeve, which was tightened by an angle of 70° as specified by SKF.

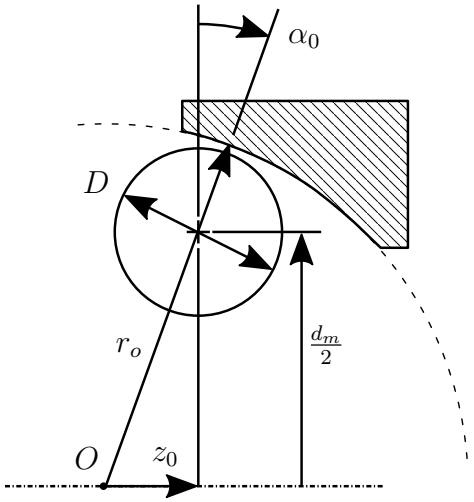
The dimensions of this bearing were obtained from the SKF website [185], and these values are listed in Table 5.1. However, SKF do not supply values for the radii of curvature of the races. Noting that the bearing is self-aligning, the radius of curvature of the outer race could be computed from geometry, as depicted in Fig. 5.5b. The outer radius of curvature is given by:

$$r_o = \sqrt{\left(\frac{d_m}{2} + \frac{D}{2}\cos\alpha_0\right)^2 + \left(z_0 + \frac{D}{2}\sin\alpha_0\right)^2} \tag{5.1}$$

The inner race, on the other hand, nearly conforms to the element. This means that the radius of curvature is very close to the radius of the elements, but has a very large influence on the contact stiffness. This can only be determined from experiments.



(a) Floating bearing in SKF housing



(b) Outer race geometry for a SABB

Figure 5.5: Floating ARES bearing

Table 5.1: ARES bearing dimensions

Parameter	Symbol	Floating SKF1208	Fixed SKF2208	Units
Number of balls	Z	36	36	-
Outer race width	B	18.0	23.0	mm
Ball diameter	D	8.73	8.73	mm
Diameter between ball centres	d_m	60.1	60.1	mm
Contact angle	α_0	8.5	10.8	°
Axial separation between rows	z_0	4.50	5.75	mm
Radius of curvature of outer race	r_o	34.8	35.0	mm

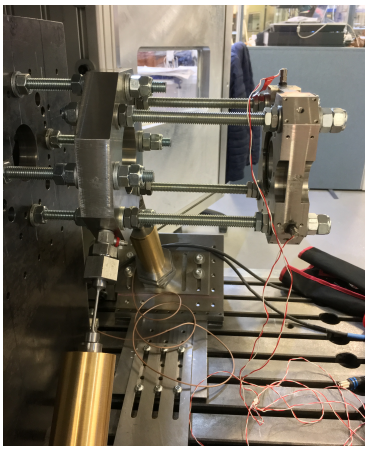
5.1.2.2 Fixed bearing

The rotor is supported by another SABB, which fixes the rotor in the axial direction. This bearing is a 2208 E-2RS1KTN9 SABB, which is very similar to the rear bearing except that it is sealed, and has a higher load capacity. This bearing is supported by custom designed structure, which will be introduced shortly, and was therefore considered to be the test bearing. The bearing is fixed to the shaft with an SKF H308E adaptor sleeve. The clearance of this bearing can be controlled with the tightening angle of the adaptor sleeve. However, in this thesis, it was tightened by a constant angle of 45°.

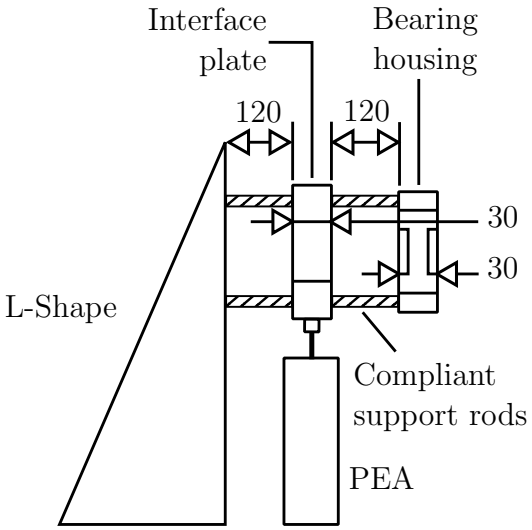
As with the floating bearing, the dimensions were obtained from the SKF website [186], and the radius of curvature of the outer race was computed from Eq. (5.1); these values are also listed in Table 5.1. Comparing the dimensions of the fixed bearing with those of the floating bearing, it can be observed that the only difference is that the fixed bearing is slightly wider in the axial direction, which also leads to a larger contact angle.

5.1.3 Bearing support structure

The fixed bearing on ARES is mounted in a custom bearing housing, which is in turn supported by a compliant support structure, as shown in Fig. 5.6, where the key components have been labelled. This bearing support structure is connected to the test bed via a vertical pedestal, known as the "L-shape". An intermediary solid block, known as the "interface plate" is connected to this via a set of flexible rods, which prevent any significant out-of-plane motion, but allow in-plane motion. The bearing housing is then connected to the interface plate via another set of axial support rods. These rods can be lengthened or shortened to vary the support compliance; they can be very long to create the "flexible" configuration shown in Fig. 5.6, or very short to create the "rigid" configuration shown in Fig. 5.7.



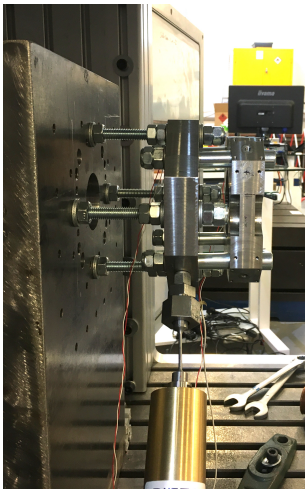
(a) Photo



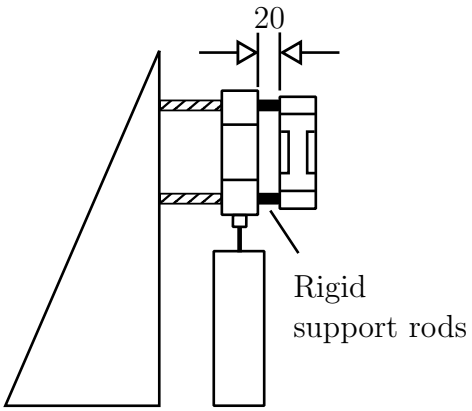
(b) Schematic

Figure 5.6: Structure supporting the fixed ARES bearing (flexible configuration)

The interface plate is also connected to ground by a pair of PiezoJena PSt 1000/35/200 VS45 piezo-electric actuators (PEA), as shown in Fig. 5.6. The PEAs are mounted at an inclination of 45° from the horizontal, as shown in Fig. 5.8. When the PEAs are inactive, they constrain the interface plate against any in-plane motion. However, they can also be driven by PiezoJena RCV 1000/7 switching amplifiers in order to excite the interface plate in the horizontal and vertical directions; thus, the interface plate acts as a base-exciter. The piezo-electric stacks in these actuators are preloaded, so that the PEAs are able to apply *both* tensile and compressive loads to the interface plate, whereas conventional PEAs could only apply compressive loads. Each PEA is connected to the interface plate via a stinger which contains a ball-joint; this is to minimise the bending moment reacted by the PEA. In addition, a force gauge is placed between each stinger and the interface plate, in order to measure the forces reacted by the PEAs. These components are labelled in Fig. 5.8.



(a) Photo



(b) Schematic

Figure 5.7: Structure supporting the fixed ARES bearing (rigid configuration)

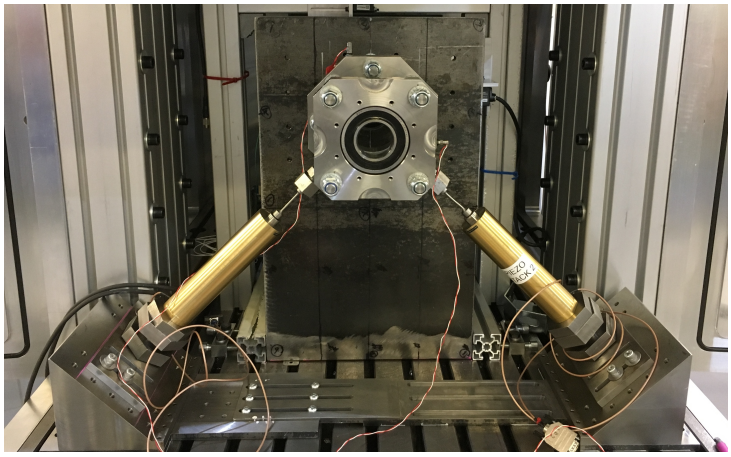
5.1.4 Excitation

The rotor can be excited synchronously with the addition of an unbalance mass to the discs. This is achieved by screwing in bolts into holes on the disc. The magnitude of the unbalance can be varied by choosing a longer or shorter bolt, or moving the mass to a ring of holes at a different radius on the disc.

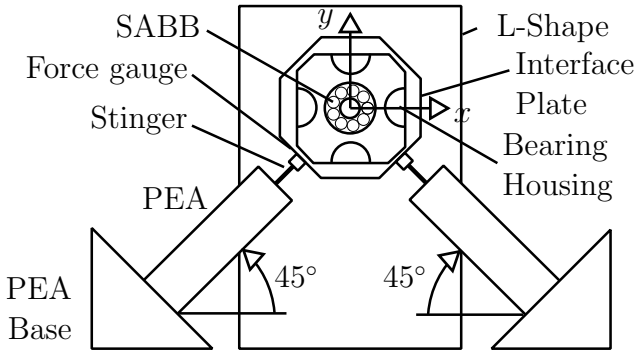
The rotor can also be excited by the PEAs connected to the interface plate on the fixed bearing support, as shown in Fig. 5.8. The displacement of the actuators scales with the applied voltage. The frequency of the PEA excitation is controlled independently of the rotor speed. It is therefore possible to excite the rotor asynchronously with the PEAs. The PEAs are able to excite the rotor at frequencies much higher than the rotor speed; they are typically operated up to a maximum of 200 Hz, although the actuators are capable of operating up to 4 kHz.

The phasing of each PEA can be varied to achieve a range of forcing patterns. The PEA voltages on each actuator are denoted by V_1 and V_2, and the displacement in each direction will scale with the applied voltage. However, it will be more convenient to rotate the voltages by 45° into the x-y co-ordinate system of the rotor, to yield an "effective voltage" in each direction, denoted by V_x and V_y. This can be written mathematically as:

$$V_x(t) = \frac{1}{\sqrt{2}}\left(V_1(t) - V_2(t)\right)$$
$$V_y(t) = \frac{1}{\sqrt{2}}\left(V_1(t) + V_2(t)\right)$$



(a) Photo



(b) Schematic

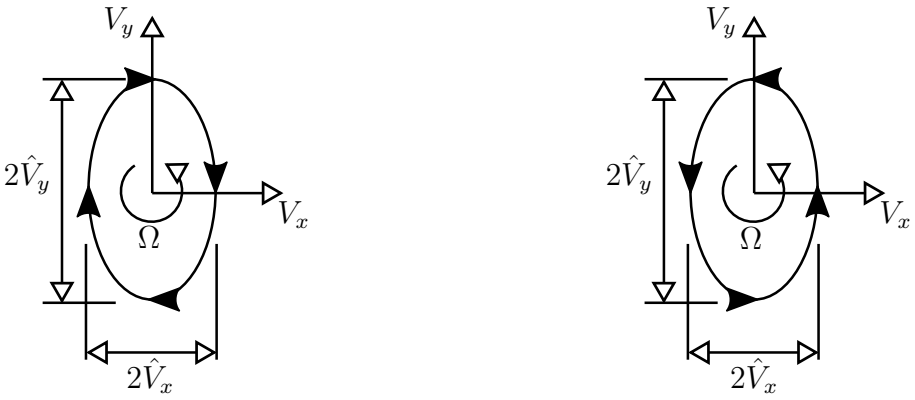
Figure 5.8: PEA excitation system attached to the ARES bearing support structure

For this project, a travelling wave excitation was used, whereby the applied voltage follows an elliptical orbit as shown in Fig. 5.9. It was assumed that the axes of the ellipse would remain aligned with the horizontal and vertical axes, with a width and height of denoted by $\hat{V}_x$ and $\hat{V}_y$. The amplitude $\hat{V}$ and phase ϕ of each PEA can then be written as a function of the dimensions of the ellipse:

$$\begin{bmatrix} \hat{V}_1 \\ \hat{V}_2 \end{bmatrix} = \frac{1}{\sqrt{2}} \sqrt{\hat{V}_x^2 + \hat{V}_y^2} \begin{bmatrix} 1 \\ 1 \end{bmatrix} \tag{5.2}$$

$$\begin{bmatrix} \phi_1 \\ \phi_2 \end{bmatrix} = \pm \arctan\left(\frac{\hat{V}_x}{\hat{V}_y}\right) \begin{bmatrix} 1 \\ -1 \end{bmatrix} \tag{5.3}$$

where the positive sign in the phase equation is for FW excitation, and the negative sign is for BW excitation. Some special cases are unidirectional excitation or circular excitation, for which the corresponding PEA voltage amplitudes and phases are listed in Table 5.2. Since the two actuators are identical, the horizontal and vertical displacement



(a) BW excitation (b) FW excitation

Figure 5.9: PEA voltage orbits

Table 5.2: PEA excitation types

Excitation type		Amplitude (V) PEA 1	Amplitude (V) PEA 2	Phase (°) PEA 1	Phase (°) PEA 2
Unidirectional	Vertical	$\hat{V}_y/\sqrt{2}$	$\hat{V}_y/\sqrt{2}$	0	0
	Horizontal	$\hat{V}_x/\sqrt{2}$	$\hat{V}_x/\sqrt{2}$	+90	−90
Circular	Forward	$\hat{V}$	$\hat{V}$	+45	−45
($\hat{V}_x = \hat{V}_y = \hat{V}$)	Backward	$\hat{V}$	$\hat{V}$	−45	+45

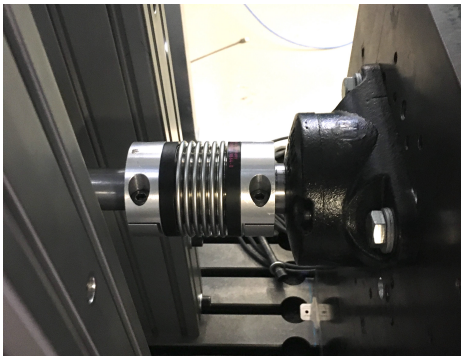
of the interface plate x_{IP} and y_{IP} will scale with V_x and V_y, although this relationship must be determined experimentally.

5.1.5 Coupling

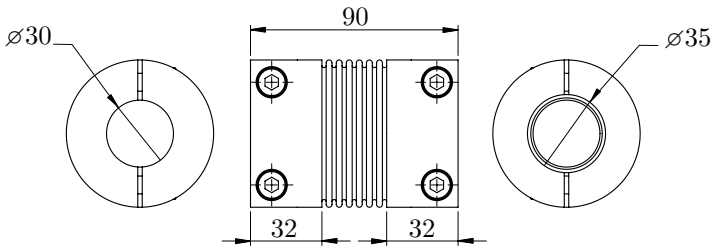
The ARES rotor is connected to the motor shaft by a R+W BKH/60/93/30/35 metal bellows coupling, which is depicted along with its geometry in Fig. 5.10. This coupling has split hubs on both ends to clamp it to both the rotor and motor shaft. This type of coupling was chosen for its low stiffness, so as to limit the influence on the dynamics of the rotor. It is able to accommodate both radial and angular misalignment between the shafts.

5.1.6 Instrumentation and control

The response of each disc in the horizontal and vertical directions is measured with non-contact laser displacement sensors (Keyence LK-H022). Accelerometers (PCB M353B17) are fitted to the non-rotating components in the horizontal and vertical directions; in this case, the bearing housing and interface plate. The forces applied by each PEA are measured with force gauges (PCB 208C04) between the PEAs and the interface plate.



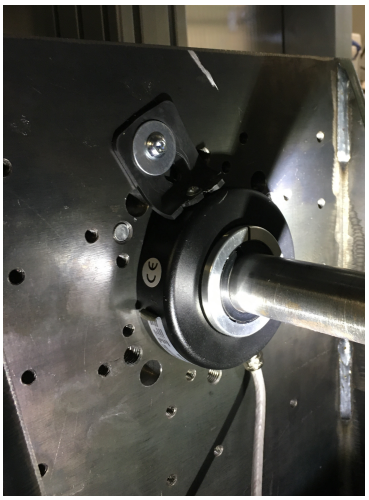
(a) Coupling in situ next to floating bearing



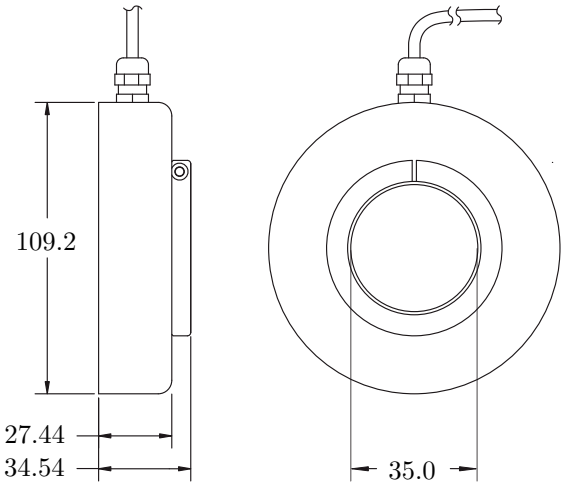
(b) Schematic [187]

Figure 5.10: BKH/60/93/30/35 coupling used to drive the ARES rotor

The rotor angle is measured with an incremental encoder (EPC Model 776), from which the speed can also be computed. This is depicted in Fig. 5.11a and the salient dimensions are shown in Fig. 5.11b. The encoder was mounted on the rotor, and was loosely attached to the floating bearing support via a rubber bracket. This was mounted on the rotor rather than the motor shaft, since the rotation speeds may differ if there are torsional vibrations.



(a) Encoder mounted to bearing support



(b) Schematic [188]

Figure 5.11: EPC Model 776 encoder used to measure the angle of the ARES rotor

The rig is controlled by a National Instruments cRio unit. This sends the motor speed target to the motor servo-amplifier and the desired voltage signals to the PEA amplifiers. The cRio also handles data acquisition, using a constant sampling rate of 5120 Hz. This is well above the maximum excitation frequency to avoid aliasing.

5.2 Stiffness of the fixed bearing

Since the ARES test rig is a complicated machine with many components, it was decided that it was necessary to first validate the bearing model in a simplified setting. To this end, a separate static bearing test rig was designed and built, which is known as the BEaring LOading System (BELOS). This was used to measure the non-linear bearing stiffness of the fixed bearing from ARES, which allowed some unknown bearing parameters to be identified. This work has already been presented in a conference paper [189].

5.2.1 Test setup

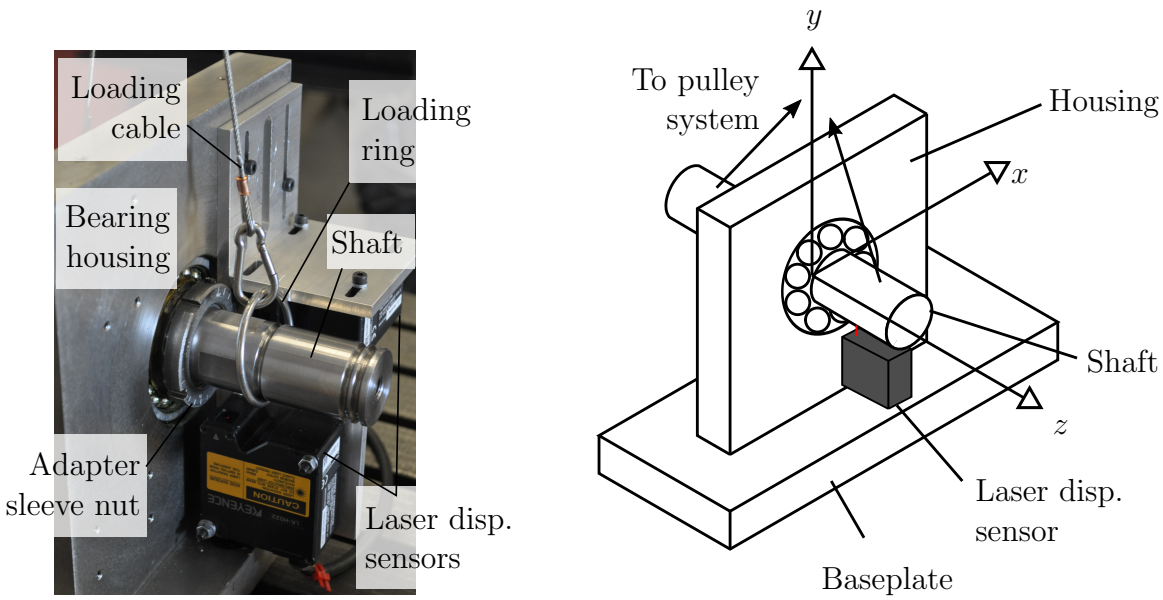
The BELOS test rig consists of an unsealed version of the fixed bearing on ARES, with a model number SKF 2208-EKTN9. This is fitted into a rigid steel housing block using a J7 ISO tolerance, which is the same as the tolerance on the bearing housing in ARES. The bearing is mounted in a horizontal orientation, so that the bearing is not axially loaded. The steel housing block is bolted to an interface plate using 8×M12 bolts, which is in turn bolted down firmly to a test bed using T-slots and 12×M10 bolts. This setup is depicted in Fig. 5.12.

A short 35 mm OD solid shaft runs through the bearing and is fixed using an SKF H308E adaptor sleeve, as used on ARES to fix the rotor. This device allows the internal clearance within the bearing to be varied, depending on how many turns it is tightened. The adaptor sleeve was tightened by an angle of 45° from where the nut was finger tight. This angle was kept constant across all tests, to ensure that the bearing clearance remained as consistent as possible. Since the bearing was self-aligning, the shaft was free to tilt around the x and y-axes (shown in Fig. 5.12b). The shaft was also not constrained against rotation around the z-axis, but the small amount of friction in the bearing was found to be adequate to prevent this during loading.

Loads are applied via a cable-pulley system connected to the short shaft running through the bearing, using calibrated weights. Loads can be applied in either the vertical or horizontal directions, and the shaft displacements are measured with laser displacement sensors. The acquired data allow force-displacement curves to be plotted, and the non-linear bearing stiffness to be measured. These systems will be discussed in more detail in the following sections.

5.2.1.1 Displacement sensors

The shaft displacement is measured by horizontally and vertically aligned sensors on each side of the bearing, so that the displacement in both orthogonal directions was measured



(a) Photo

(b) Schematic

Figure 5.12: BELOS bearing housing

Table 5.3: BELOS rig parameters

Parameter	Symbol	Value	Units
Laser separation	l_{laser}	40	mm
Shaft mass	m_{shaft}	1.57	kg
Pulley mass	m_{pulley}	0.367	kg

simultaneously. Keyence LK-H022 laser displacement sensors were used with a 0.01 µm precision. These were connected to a Keyence LK-G5001 controller, which interfaced with the PC over USB. Since the laser displacement sensors are designed to work on flat surfaces, the laser spots reflect off smooth flats machined into the shaft, which maximises the accuracy of the measurements.

5.2.1.2 Loading system

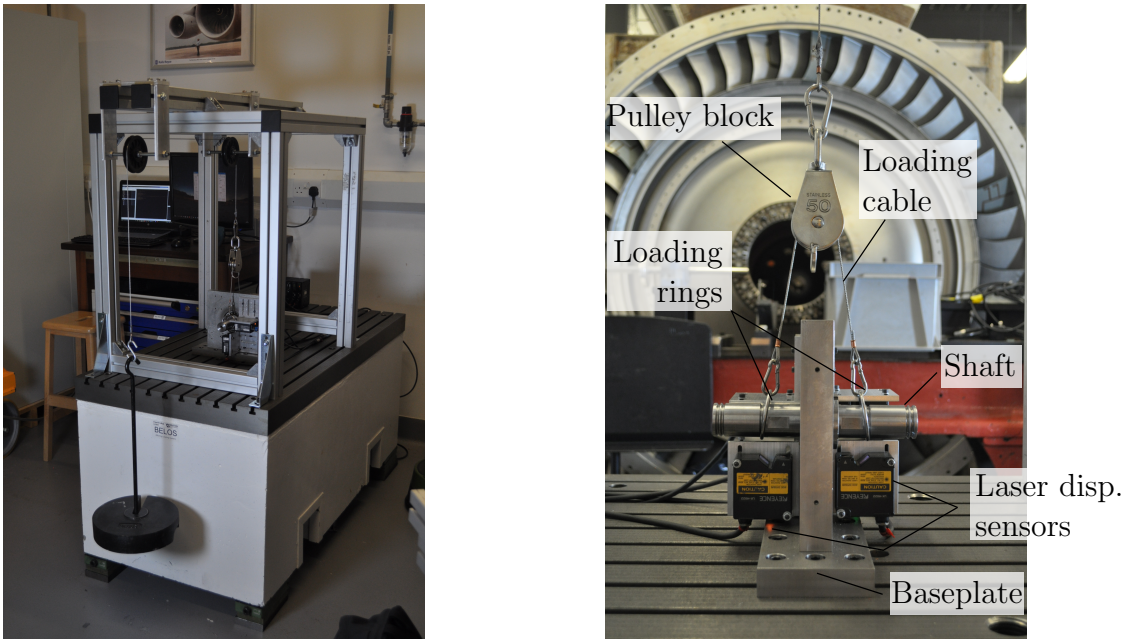
The bearing is loaded via steel rings encircling the shaft, which sit within machined grooves. This ensured that there was a single contact on the shaft and no torque could be applied, minimising any shaft rotation. Pre-calibrated weights applied loads to these rings via a cable-pulley system, as shown in Fig. 5.12. The loading system was designed to distribute loads evenly between each side of the bearing, to minimise any tilting motion.

5.2.1.3 Vertical loading configuration

The bearing was initially loaded vertically, since this was the simpler test setup, as shown in Fig. 5.13. The rig was only able to apply upward loads to the bearing in this

configuration, so that only the elements at the top of the bearing were in contact and loaded, while the elements at the bottom of the bearing remained unloaded. Therefore, the bearing never crossed the deadband due to its internal clearance, and it was not possible to measure this parameter from these tests. However, this test was found to have a lower uncertainty at high loads, thereby allowing any change in bearing stiffness with load to be measured more accurately.

Instead of directly connecting both sides of the bearing to the main loading cable, an intermediary pulley was used. This ensures that an equal load was applied to each side. The pulley was kept well greased to minimise the influence of friction. This is shown in Fig. 5.13.



(a) Front View (b) Detail View

Figure 5.13: BELOS test rig in the vertical loading configuration

The load applied to the bearing in the vertical direction is not in fact the same as the load applied to the loading cable. This is because a certain mass is required to offset the weight of the pulley and shaft. This can easily be compensated for by adding an offset to the applied load:

$$f_y^b = f_{\text{weights}} - (m_{\text{shaft}} + m_{\text{pulley}}) \tag{5.4}$$

where the shaft and pulley masses are shown in Table 5.3. Note that the cable mass was negligible compared to the weight of the other components. The bearing was loaded from an initial 10 N, which slightly exceeded the weight of the pulley and shaft, up to a maximum load of 1300 N in 50 N increments. One complete cycle of loading and unloading was completed in each test, so that any hysteresis could be measured.

The shaft was reinstalled 5 times, whereby the adapter sleeve was completely loosened, and then tightened by the same 45° angle each time. Each time the shaft was installed, two tests were carried out, whereby each test consisted of one complete loading and unloading cycle. This lead to a total of 10 tests, which allowed the uncertainty due to the setup and measurement error to be quantified.

5.2.1.4 Horizontal loading configuration

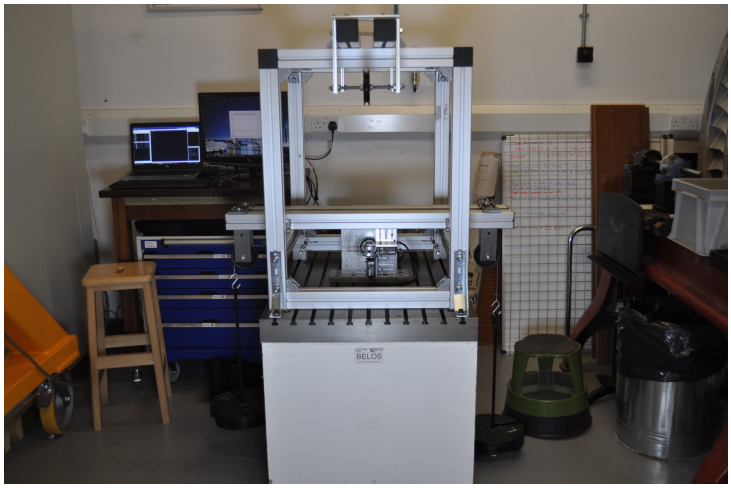
The rig setup was then adjusted to load the bearing in the horizontal direction. Since cables were connected to both sides of the bearing, it was possible to apply a net load to the bearing in both the positive and negative directions, unlike in the vertical tests. As a consequence of this, it is possible to directly observe any internal clearance in the bearing. However, there was a small constant vertical load due to the shaft weight in these tests, which complicates the analysis.

In this configuration, loading beams were used to distribute the load between the front and rear of the bearing, as shown in Fig. 5.14. Beams were used instead of a pulley block, in order to reduce the weight of the loading system, which would otherwise cause the loading cable to sag. Note that the horizontal loads had to be applied further out from the central plane of the bearing than the vertical loads, since the horizontal displacement sensors obstructed access.

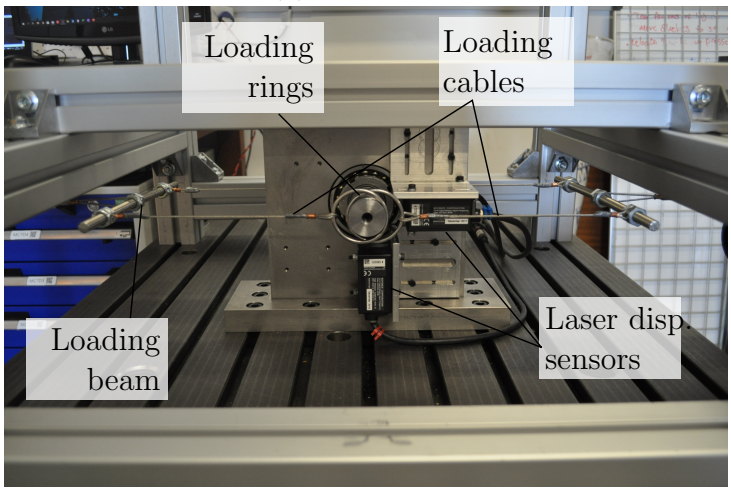
A constant 10 N load was applied to each side of the bearing to maintain tension in the cables. Additional masses were then hung from one side of the bearing from 0 N up to 1300 N in increments of 50 N, and then gradually unloaded down to 0 N. The masses were then applied in the same way to the other side of the bearing, so that the direction of loading was reversed, thus completing the loading cycle.

In this configuration, it was not necessary to offset the loads applied by the weights to compute the bearing loads, since the weight of the loading beams has little influence on the tension in the cables. However, the weight of the shaft was always present leading to a constant vertical load of $f_y = m_{\text{shaft}} g$. This must be included in the numerical model, in addition to the horizontal load f_x applied by the cable system, in order to accurately replicate the test conditions.

The shaft was fully removed, and reinstalled 5 times, like in the vertical configuration. However, each time the shaft was installed, only a single test was carried out. However, since both positive and negative loads were applied within each horizontal test, the total number of data points was approximately the same as in the vertical loading configuration.



(a) Front View



(b) Detail View

Figure 5.14: BELOS test rig in the horizontal loading configuration

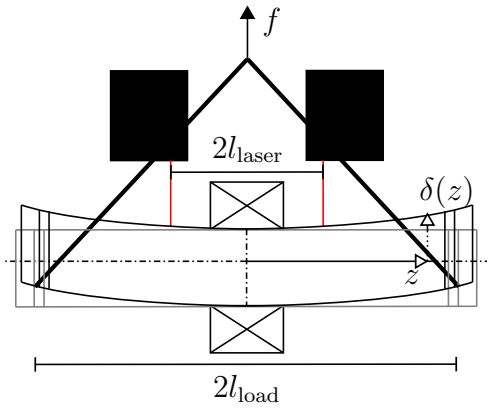
5.2.2 Data post-processing

5.2.2.1 Shaft rotation

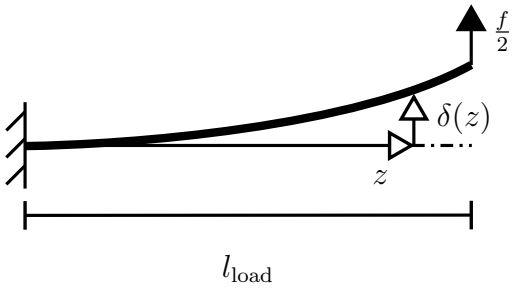
Since the shaft displacement was measured in both the horizontal and vertical directions on both sides of the bearing, it was possible to completely resolve the shaft translation in the horizontal (x) and vertical (y) directions removing the effect of any rotation around these axes. For example, in the horizontal (x-z) plane, the following transformation was applied:

$$\delta_x^{\text{shaft}} = \frac{\delta_x^f + \delta_x^r}{2} \tag{5.5}$$

$$\theta_y^{\text{shaft}} = \frac{\delta_x^f - \delta_x^r}{2l_{\text{laser}}} \tag{5.6}$$



(a) Schematic showing shaft deflection



(b) Equivalent beam model

Figure 5.15: BELOS shaft compliance model

where δ_x^f and δ_x^r are the displacements measured by the lasers on each side of the bearing, and δ_x^{shaft} and θ_y^{shaft} are the shaft translation and rotation respectively. The length l_{laser} is the axial separation between the lasers defined in Fig. 5.15a.

5.2.2.2 Shaft compliance

Although the shaft displacement was measured very close to the bearing using the laser displacement sensors (see Table 5.3), the compliance of the shaft could not be neglected. The bearing stiffness was predicted to be of the order of around $10 \times 10^8\,\text{N m}^{-1}$, whereas the shaft compliance was of the order of $10 \times 10^9\,\text{N m}^{-1}$. This means there could be up to a 10 % discrepancy between the deflection measured by the laser and the true bearing deflection, as depicted in Fig. 5.15a. This effect had to be compensated for in post-processing.

The shaft stiffness k_{shaft} seen at the laser was derived from beam theory, by considering the equivalent cantilevered beam model shown in Fig. 5.15b. The lateral deflection along the beam at a given axial location is given by [190]:

$$\delta(z) = \frac{f/2}{6EI} z^2 \left(3l_{\text{load}} - z\right)$$

where f is the total applied load, which is assumed to be split evenly between each side of the bearing. The deflection at the laser can be found by substituting in $z = l_{\text{laser}}$:

$$\delta\left(l_{\text{laser}}\right) = \frac{f}{12EI} l_{\text{laser}}^2 \left(3l_{\text{load}} - l_{\text{laser}}\right) \tag{5.7}$$

which can then be rearranged to yield the effective shaft stiffness k_{shaft}:

$$k_{\text{shaft}} = \frac{f}{\delta\left(l_{\text{laser}}\right)} = \frac{12EI}{l_{\text{laser}}^2 \left(3l_{\text{load}} - l_{\text{laser}}\right)} \tag{5.8}$$

Table 5.4: BELOS shaft compliance parameters

Parameter	Symbol	Vertical	Horizontal	Units
Cable loading position	l_{load}	110	200	mm
Shaft stiffness	k_{shaft}	884	425	MN m^{-1}

The shaft compliance can then be compensated for by introducing a simple load-dependent correction, to give the bearing deflection δ_b:

$$\delta_b = \delta_{\text{shaft}} - \frac{f}{k_{\text{shaft}}} \tag{5.9}$$

where δ_{shaft} is the shaft deflection from Eq. (5.5). This correction was applied to both the vertical and horizontal deflections. The values of the effective shaft stiffness from Eq. (5.8) were pre-computed for the loading in each direction, and are listed in Table 5.4. Note that the effective shaft stiffness was different in each direction, due to the different values of l_{load}.

5.2.3 Bearing model

The bearing was modelled using the quasi-static bearing model presented in Section 3.2, with the geometric parameters in Table 5.1. However, some key bearing parameters remained unknown. For example, the radii of curvature of the races are not typically supplied by the manufacturer. These values are required in order to compute the Hertzian stiffness coefficient of each contact using Eq. (3.62), which in turn allows the combined Hertzian stiffness coefficient C to be computed using Eq. (3.71). The Hertzian coefficient relates the contact deflection to contact loads, and therefore plays a key role in determining the bearing stiffness. Although the outer race curvature of the SABB could be calculated from Eq. (5.1), the inner race curvature r_i remained unknown.

In order to get an initial estimate of the bearing stiffness, the inner race curvature was set to the value shown in Table 5.5, which was slightly larger than the ball radius $D/2$. The Hertzian contact stiffness coefficient C could then be estimated, assuming appropriate values for the material properties of steel ($E = 210\,\text{GPa}, \nu = 0.3$), and this value is also shown in Table 5.5.

The bearing clearance also has a large influence on the bearing stiffness. This is typically expressed in terms of a radial clearance value c_r. Although manufacturers sometimes supply typical values for the clearance, it will also depend on many other variables such as the bearing housing tolerance and how much the adapter sleeve is tightened. Therefore, to get an accurate value, it needs to be measured in situ. It was initially assumed that there was no clearance (ie $c_r = 0\,\mu\text{m}$), as shown in Table 5.5.

Table 5.5: Estimated values of unknown bearing parameters

Parameter	Symbol	Value	Units
Radial clearance	c_r	0	µm
Radius of curvature of the inner race	r_i	4.5	mm
Hertzian contact stiffness coefficient	C	4.6×10^9	$\mathrm{N\,m^{-3/2}}$

It should be noted that since this bearing has many elements, it was expected that the bearing stiffness would be insensitive to rotation angle, and the so-called "variable compliance" would be negligible. To verify this, the vertical displacement of the bearing was computed with a radial preload of $f_y = 1.25\,\mathrm{kN}$ over a range of cage angles ψ_c, using the initial estimates of the unknown parameters in Table 5.5. From the results plotted in Fig. 5.16, it can be observed that the variation in the vertical displacement is less than 0.01 %. Tests could therefore be carried out at a single cage position, and the influence of the cage angle was consequently neglected in the model updating process.

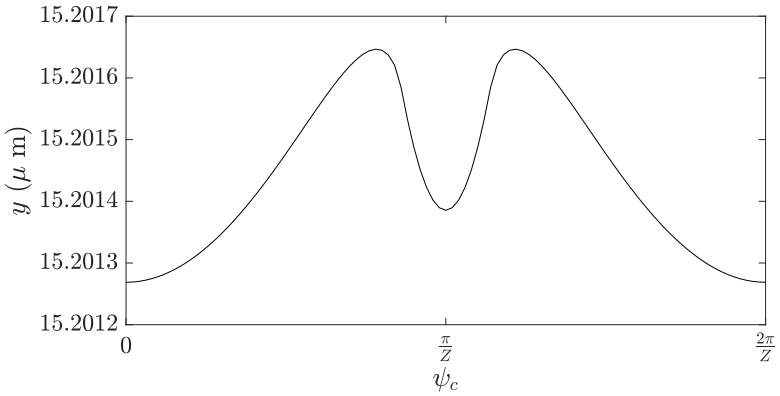


Figure 5.16: Predicted variation of vertical bearing displacement y with cage angle ψ_c for a load $f_y = 1.25\,\mathrm{kN}$

In order to fully parameterise the bearing model, both the Hertzian contact stiffness coefficient C and the radial bearing clearance c_r were extracted from the experimental data. This process will be discussed later in Section 5.2.5.

5.2.4 Results

5.2.4.1 Vertical loading configuration

The results from the vertical loading setup are shown in Fig. 5.17. The laser displacements were converted into shaft translations using Eq. (5.5) and the bearing load was computed from Eq. (5.4). The effect of shaft compliance was then compensated for using Eq. (5.9).

Even though great care was taken when setting up the rig, the displacements from each of the individual tests were found to be offset slightly from each other. This was the case

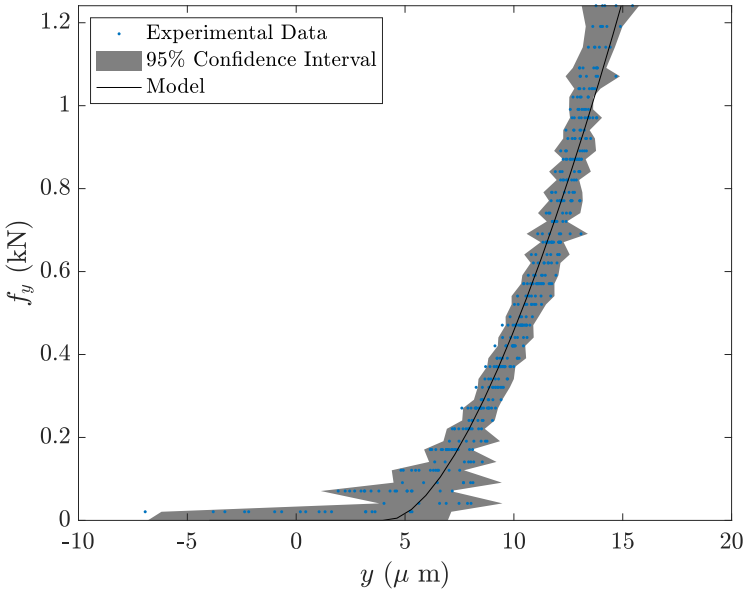


Figure 5.17: Results from vertical loading tests on BELOS

even when the shaft was left untouched between 2 tests. After taking photos of the shaft during loading, it was found that the shaft would tilt slightly as the bearing was initially loaded, so the shaft would never start from *exactly* the same position. Therefore, it was necessary to offset each test in post-processing so that they would align at high loads where the behaviour was more consistent.

There is a strong stiffening characteristic with increasing load in Fig. 5.17, demonstrating that the bearing is non-linear. The bearing is also very stiff, since the maximum observed deflection was only 10 µm. There are many points where the load is very low, which is where the bearing is just in contact. However, since the bearing was not loaded downwards, these points do not necessarily cover the whole deadband region due to clearance. Unfortunately, this meant that it was not possible to extract the radial clearance from this data.

The experimental uncertainty was estimated by computing the standard deviation of the bearing deflection at each load level, and assuming a normal distribution. The 95 % confidence interval is denoted by the shaded region in Fig. 5.17. The uncertainty is quite low at high loads, but very large at the lowest loads, where the bearing just starts to become loaded. This is likely due to the titling motion of the shaft, as explained previously. For a different bearing which would provide some constraint against titling, such as a deep-groove bearing, it would be expected that this uncertainty would be reduced.

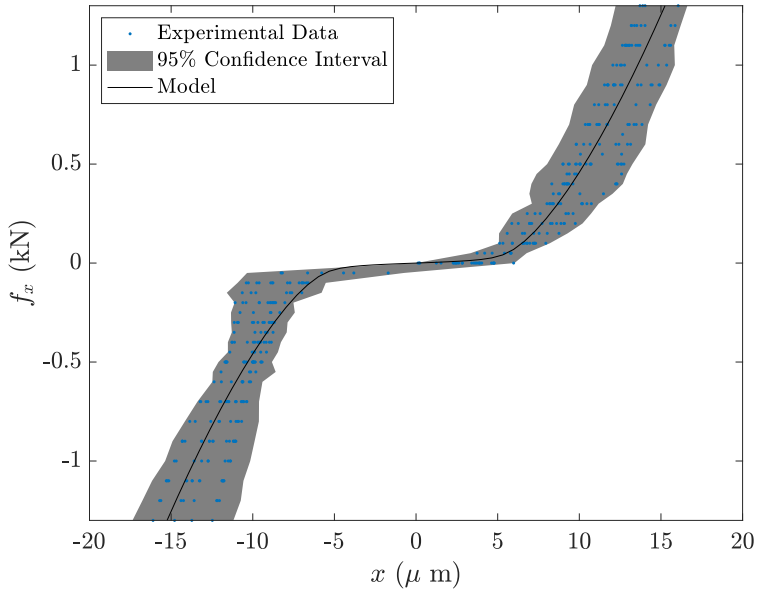


Figure 5.18: Results from horizontal loading tests on BELOS

5.2.4.2 Horizontal loading configuration

The load-displacement relation for this loading configuration, after post-processing the deflections using Eqs. (5.5) and (5.9), is plotted in Fig. 5.18. The data from each test was offset so that the data was centred around $x = 0\,\mu\text{m}$. This removed the effect of any drift in the measured displacements between each test.

The radial bearing clearance is immediately obvious in Fig. 5.18, leading to a deadband around $x = 0\,\mu\text{m}$ with a width of around $8\,\mu\text{m}$ where the stiffness is very low. Outside of these regions, there is a clear stiffening characteristic. The horizontal stiffness appears to be very similar to the vertical stiffness, since the bearing displaces from $4\,\mu\text{m}$ at the edge of clearance to around $14\,\mu\text{m}$ at a load of $1300\,\text{N}$, which is similar to the $10\,\mu\text{m}$ deflection observed in the vertical loading case. This is as expected, since the bearing should be approximately axisymmetric.

The experimental results do show some slight asymmetry, with a slightly higher stiffness for loading in the positive direction than in the negative direction. This could be due to the bearing being slightly anisotropic due to manufacturing tolerance, or that the balls have failed to settle into their quasi-static equilibrium position. However, the asymmetry could also stem from the rig, due to the separate loading systems used to load the bearing in each direction.

The experimental uncertainty was estimated in the same way as for the vertical loading. It can be observed that the experimental uncertainty is much higher in the case of horizontal loading, even for the same applied loads; for example at a load of $500\,\text{N}$, the $95\,\%$ confidence interval is around $5\,\mu\text{m}$ for the case of horizontal loading, compared to

Table 5.6: Identified bearing parameters

Parameter	Symbol	Value	Units
Radial clearance	c_r	4.1	µm
Radius of curvature of inner race	r_i	4.9	mm
Hertzian contact stiffness coefficient	C	5.0×10^9	$\mathrm{N\,m^{-3/2}}$

around 2 µm in the vertical direction. Unlike in the vertical loading case, the bearing was unloaded twice within one complete loading cycle, which was found to increase the tilting motion of the shaft. This explains why the uncertainty is particularly high around $f_x = 0\,\mathrm{N}$. This means the bearing clearance can only be identified with a large confidence interval of around 0.5 µm. This highlights that the vertical loading configuration is a more accurate setup, once the bearing is fully in contact.

5.2.5 Parameter identification

In order to estimate the unknown bearing parameters, a two stage process was applied. The unknown Hertzian contact stiffness coefficient C was first identified by minimising the least-squares error between the predictions from the model and the experimental data. Only the data from the vertical loading test was used for this, since this was believed to be the most accurate test at higher loading levels, where the stiffening effect of the Hertzian contacts was most visible. The radius of curvature of the inner race r_i, could then be back-computed from the Hertzian stiffness coefficient. The second stage was to identify the radial clearance using the results from the horizontal test, where the deadband due to clearance was clearly visible. These values are listed in Table 5.6.

The bearing model was updated with the identified parameters in Table 5.6, and the bearing stiffness was computed for the same load ranges covered in the experiments. The results from the model are overlaid on Fig. 5.17 and Fig. 5.18. The correlation with the experimental data will now be discussed.

5.2.5.1 Vertical loading configuration

The model and experimental data agree well at higher loads, which is also the region where the experimental uncertainty was lowest, as shown in Fig. 5.17. However, the model appears to stiffen more rapidly than the experimental data at lower loads. It was found that varying the Hertzian contact stiffness coefficient did not improve the agreement any further in this region, indicating that the model was not able to capture all the features of the bearing loading. One explanation could be that imperfections in the bearing races caused some elements to become loaded sooner than the idealised case

assumed in the model. It is also possible that the elements may "jam" due to friction, and therefore do not reach the quasi-static equilibrium position assumed by the model. However, this is also the region where the experimental uncertainty is quite large, so this was not deemed a concern.

5.2.5.2 Horizontal loading configuration

It can be observed from Fig. 5.18 that there is good agreement with experimental data, with the model predicting the same clear deadband region where the bearing is in clearance. It can be observed that stiffness in the clearance region is non-zero in both the experimental data and from the model. This is due to the presence of the small vertical load from the shaft weight. Outside of this region, the bearing stiffness rises rapidly as the shaft moves away from the central position, which is due to the Hertzian contacts.

It is interesting to note the experimental data shows a much sharper change in horizontal stiffness (in either direction) as the bearing starts to become loaded than in the vertical loading case (as plotted in Fig. 5.17). The agreement was found to be poor in this region in the vertical loading configuration, but since the agreement is now much improved in the case of horizontal loading, there is evidence that the very soft transition observed in the case of vertical loading may just be due to experimental uncertainty.

5.2.6 Summary

The BELOS test rig has allowed the quasi-static bearing model to be validated, and two key unknown bearing parameters to be identified. The resulting bearing model provides a good agreement with the experimental results. Attention can now move onto the other subsystems of the ARES test rig.

5.3 Rotor

The rotor was chosen as the next sub-system of ARES to be analysed, since it is mechanically very simple. The rotor consists of only the flexible shaft and solid balancing discs, which means that it could be modelled very easily with the ROLADYN toolbox. This also has the biggest impact on the natural frequencies of the rig once assembled. The parameters of the rotor model were updated using results from hammer tests, as will now be discussed in more detail.

5.3.1 ROLADYN model

A 1D FE model of the ARES rotor was created using the ROLADYN toolbox outlined in Section 3.1; the rotor model is depicted in Fig. 5.19. The rotor was left unsupported in the model, without any joint elements fixing it to ground. The shaft was modelled with 20 shaft elements along its length. The mass of the end caps was lumped into the nodes at the end of the shaft. This is depicted in Fig. 5.19.

It was assumed the frequencies of the discs are well above the range of the shaft, so that they can be modelled as rigid bodies. The exact geometric properties of the discs were extracted from the Solidworks model, so that all of the details were accounted for; this includes the volume and radius of gyration. The inertia from the TranTorque was lumped into the shaft node at the location of the disc root, so that it does not rotate with the disc itself.

From the experimental data, it was observed that the discs appeared to tilt slightly w.r.t the shaft, which was assumed to be due to some rotational compliance from the TranTorque adapters. As the disc tilts, this induces high tensile stresses at the edges of the disc root, which may overcome the radial preload from the tightening torque, and lead to separation between the shaft and disc. Thus, the TranTorque adapters can never provide a truly rigid connection, particularly in the case of rotational motion. This was modelled as a rotational spring between the shaft and disc, as depicted in Fig. 5.19. However, the TranTorque adapters were still assumed to provide a rigid connection in the radial direction.

Although the shaft and disc are made of AISI 314 Stainless steel, the exact density and Young's modulus are unknown and must be identified. For the discs, it was only necessary to identify their density, since they were modelled as rigid. Note that different density values were to be identified for the shaft and discs.

There were two sources of damping in the rotor model. The material damping in the shaft was modelled using a Rayleigh damping model. For the cases where the shaft was fitted with the instrumentation cabling, it was assumed that the cable running through the shaft would introduce some extra damping. This additional damping was lumped into the shaft damping, and modelled using a different set of Rayleigh damping coefficients. The other source of damping was frictional losses at the disc root, as the disc tilts w.r.t the shaft. This was modelled with a viscous damping term. These damping parameters must be identified from experiments.

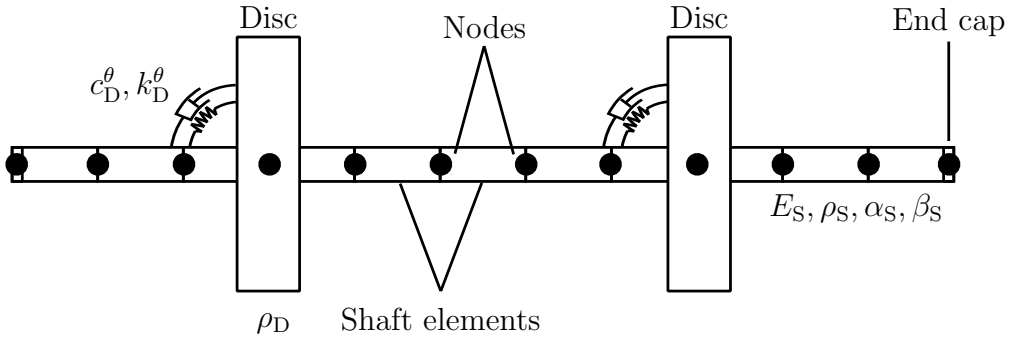


Figure 5.19: Schematic of FE model of ARES rotor

5.3.2 Component weights

The constituent components of the rotor were first weighed, and these values are listed in Table 5.7. Since the shaft and discs are quite heavy, these components could only be weighed with an analogue force gauge with a 1 N precision, whereas high accuracy digital scales with 1 g resolution were used for the smaller components. These values allow the density of the shaft and disc to be identified.

Table 5.7: Measured rotor component weights

(a) Measured using analogue force gauge

Component	Weight (N)	Mass (kg)
Shaft	58	5.91
Disc	70	7.14

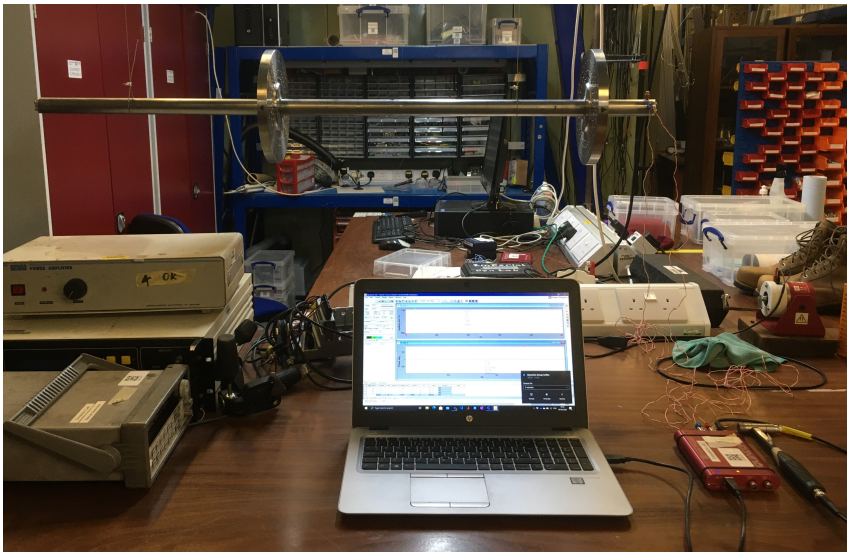
(b) Measured using digital scales

Component	Mass (g)
Shaft end cap	46
Disc TranTorque adaptor	309

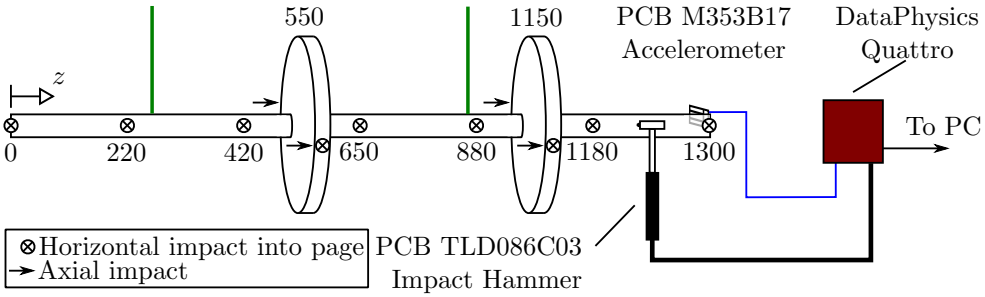
5.3.3 Hammer tests

In order to provide data to allow the elastic and damping parameters of the rotor to be identified, a hammer testing campaign was carried out. The rotor was hung from nylon wire in two locations, and an accelerometer was placed on the shaft in a position which was far from a node for all of the modes of interest. This test setup is depicted in Fig. 5.20.

A roving hammer test was performed, hitting the shaft in the lateral direction at multiple locations along its length, as indicated in Fig. 5.20b. The shaft was excited in the horizontal direction, perpendicular to the wires holding the shaft, in order to minimise their contribution to the stiffness of the system. For the tests with discs, additional axial impacts were applied to the faces of the discs, thereby allowing the disc rotation to be resolved. This is denoted by the arrows in Fig. 5.20b.



(a) Physical setup



(b) Schematic

Figure 5.20: ARES rotor hammer test setup

5.3.3.1 Data acquisition

A DataPhysics Quattro DAQ was used to acquire the data, which interfaces with a PC running the DataPhysics SignalCalc software over USB. Since the structure was very lightly damped, each impact required a long acquisition window of 32 s in order to get sufficient resolution around the resonances. Due to the limited memory of the Quattro, the usable bandwidth was capped to 1 kHz. SignalCalc is able to automatically compute the FRF from each impulse response; a rectangular window was specified. Each impact was repeated three times, and the average of the three FRFs was taken using SignalCalc, thereby removing some of the experimental variability.

The modal properties were then identified from the SignalCalc FRFs in MATLAB. It was assumed that the modes were sufficiently well-separated that the response around each peak is dominated by a single mode. This means that a peak-picking method could be used, whereby each peak can be analysed as an SDOF system [191]. The least-squares method from [192] was used to estimate the natural frequency, damping ratio and amplitude of each mode from each measured FRF. Note that the peak-picking method yielded N_{loc} estimates of the natural frequency and damping ratio for each mode, where

N_{loc} is the number of hammer test locations [191]. In order to yield a single estimate of the natural frequency and damping ratio for each mode, any outliers were removed and the average of these values was taken. The mode shapes were found from the amplitudes at the given mode from each hammer test.

The modal extraction routine was implemented within a MATLAB toolbox known as ModeLAB [193]. This was written in a generic way, so that it could also be used to post-process hammer test data from other structures later on in this project. The geometry of the test, as well as the frequency bands containing the modes, were specified in a configuration file. This configuration file was then passed to ModeLAB, which then automatically read in the SignalCalc FRFs from the ASCII files and processed the FRFs to yield the modal properties of the system.

5.3.3.2 Rotor configurations

Tests were carried out in a variety of configurations, so that the influence of the shaft, cabling and discs could be identified. Tests were first carried out on only the shaft, both with and without the cabling, in order to be able to quantify the effect of the cabling and end caps. Tests were then carried out with different numbers of discs, in order to highlight the effect of the many disc parameters. The complete set of rotor configurations considered in the hammer tests is listed below. The results from all the hammer tests will be presented in Section 5.3.3.3.

- Shaft only - Plain (ie. without cabling)
- Shaft only - Instrumented (ie. with cabling and end caps fitted)
- Shaft with rear disc (with cabling and end caps fitted)
- Shaft with two discs (with cabling and end caps fitted)

The position of the discs is also shown in Fig. 5.20; both discs were placed away from the nodes of the shaft, so that they would influence all of the modes. Note that this configuration was chosen arbitrarily, and was not the same as the final rig configuration considered in Chapter 6, which had not yet been chosen. Instead, it was assumed that if the updated ROLADYN model could accurately predict the modes of the rotor in this arbitrary configuration, then the model should be able to predict the modes in *any* rotor configuration, since the system is mechanically very simple. Note that it was only possible to detect the first 4 modes when no discs were fitted, due to the limited sampling frequency. To allow comparison across configurations, only the first 4 modes were analysed for the cases with discs as well.

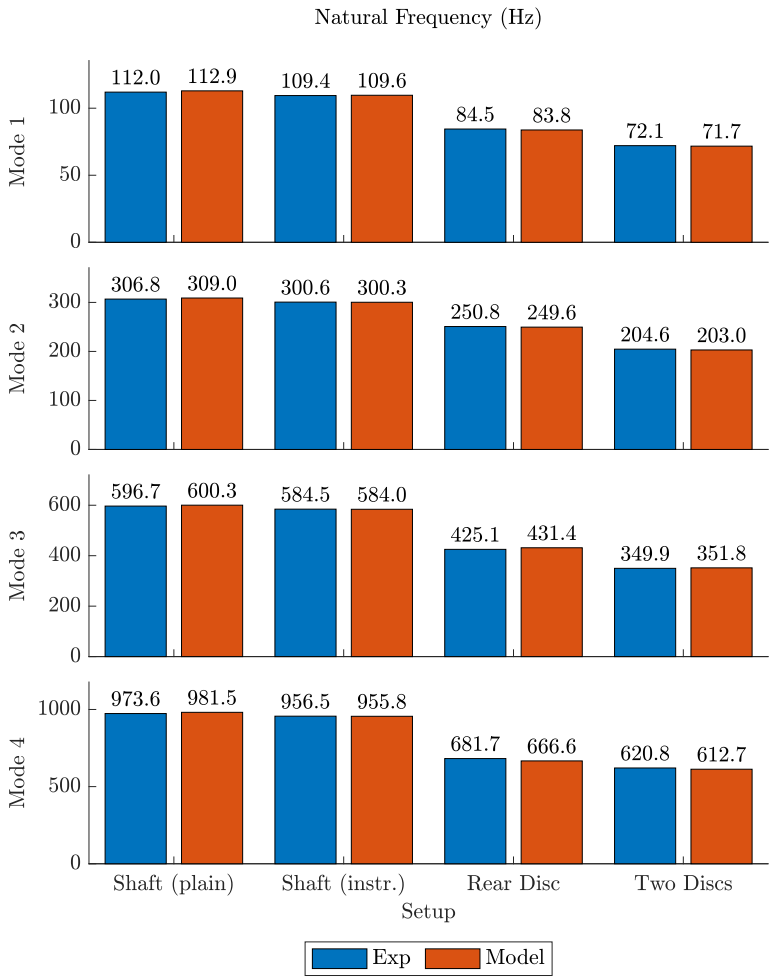


Figure 5.21: Comparison of the natural frequencies of the ARES rotor from experiments and the numerical model

5.3.3.3 Results

The natural frequencies of the first four modes obtained from the hammer tests are shown in Fig. 5.21, along with the associated damping ratios in Fig. 5.22. In Fig. 5.23, the mode shapes have only been plotted for the two disc configuration, since the mode shape are visually very similar for the other configurations. Smoothing splines were fitted through the experimental data at the impact locations for improved visualisation. For the full set of mode shapes, please refer to Appendix B.1.

Plain shaft Starting with the case of the plain shaft first, since this is the simplest configuration, it can be observed that the gap in frequency between each pair of adjacent modes increases with the order of the mode. This is what would be expected from a beam-like system such as the shaft. There also appears to be a general trend that the damping increases monotonically with the frequency of the mode. This is because there are more bends in the shaft in the higher order modes, as shown in Fig. 5.23, which leads

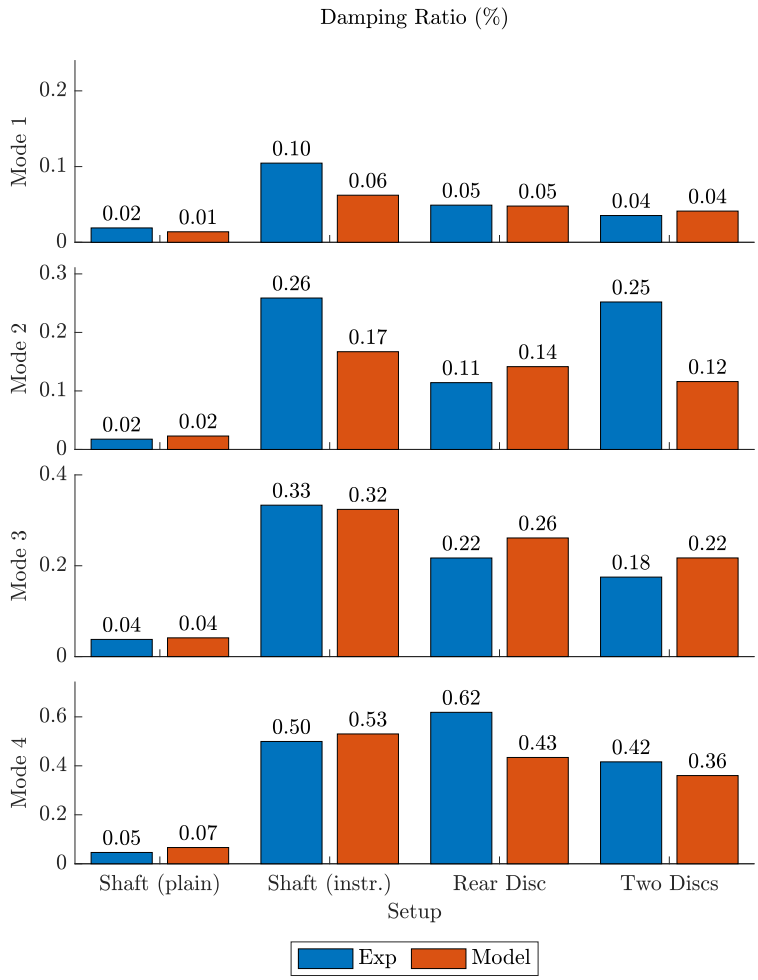


Figure 5.22: Comparison of the damping ratios of the ARES rotor from experiments and the numerical model

to more energy dissipation from material damping in the shaft.

Effect of cabling The cabling and end caps leads to a small drop in the natural frequencies of the shaft, starting at 3 Hz in the first mode, and slightly greater in the higher modes, as shown in Fig. 5.21. The end caps are located at the ends of the shaft, where there is significant motion for all modes, as can be observed in Fig. 5.23. However, there is a much more significant increase in damping once the cabling is fitted, with the damping ratio raising by an order of magnitude, as shown in Fig. 5.22. The material damping in the shaft is so very low, and therefore this is easily dwarfed by the addition of the cabling, which introduces many energy dissipation mechanisms. The damping continues to increase with the frequency with the mode.

Effect of discs It can be observed from Fig. 5.23 that the 1st order modes have 2 nodes along the shaft, and there is an additional node for the 2nd order modes, and so

on. This behaviour would be expected from a beam-like system such as a rotor. Once the discs are added, the extra inertia reduces the motion at the discs, so the modes look as if there was a pin joint at the disc roots. This becomes more significant in the higher order modes; for example, it can be observed in the 3rd and 4th modes in Fig. 5.23 that there is a lot of shaft motion away from the discs, but very little at the disc roots. This also means that the drop in the natural frequencies due to the discs increases with the order of the mode, as shown in Fig. 5.21; eg. the addition of the rear disc leads to a 23 % drop in the frequency of the 1st mode, compared to a 29 % drop in the frequency of the 4th mode.

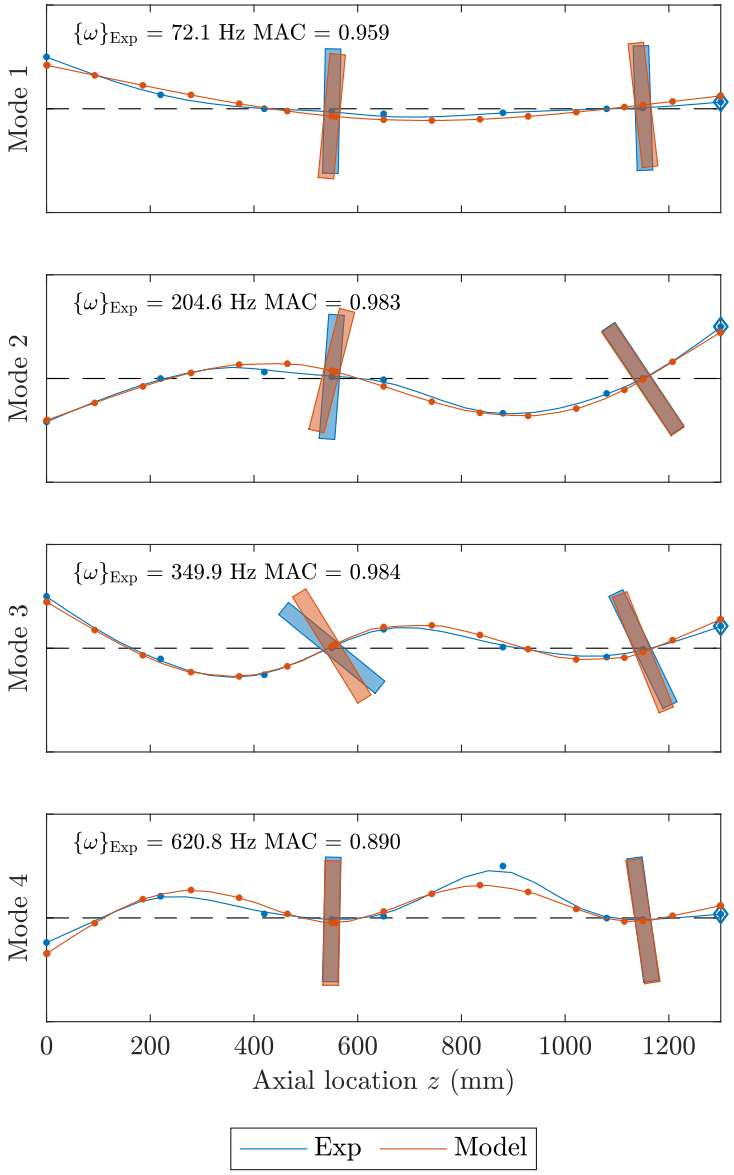


Figure 5.23: Comparison of experimental and numerical mode shapes of the ARES rotor with two discs

For the configurations without discs, there is a monotonic increase with damping with

frequency. Once the discs are added, there is a reduction in the damping ratio as shown in Fig. 5.22, which initially appears to be counter intuitive as the discs introduce extra energy dissipation at their roots. However, the addition of the discs also reduces the amount of shaft bending, since they increase the inertia of the system, thereby reducing the damping contribution from the shaft. As with the shaft only configurations, there continues to be a general increase in damping with the natural frequency of the mode.

5.3.4 Parameter identification

The next stage was to identify the unknown rotor parameters using the experimental results. A naive approach would be to individually tune the shaft parameters to match the shaft hammer tests, and similarly for the disc parameters. However, this has a tendency to over-fit the data, whereby the parameters will be heavily skewed by outliers in the experimental data. Instead, an alternative approach was used, where all of the unknown parameters were tuned together in order to best match the identified modes from all tests. This tends to lead to solutions which generalise better.

The unknown parameters can be split into two categories; elastic and inertial properties (which influence the natural frequencies), and damping-related parameters. Since the two are decoupled for lightly damped systems such as the rotor, the two sets of parameters were identified separately.

5.3.4.1 Inertial and elastic parameters

The inertial and elastic parameters were identified first, since these control the natural frequencies of the system. These were tuned to minimise the error in the component weights, and natural frequencies from the ROLADYN model. Mathematically, this can be written as the following minimisation problem:

$$\begin{aligned} \underset{\boldsymbol{\theta}}{\text{minimize}} \quad & \sum_i \left(\frac{\{\omega\}_i^{\text{Exp}} - \{\omega\}_i^{\text{Model}}}{\{\omega\}_i^{\text{Exp}}} \right)^2 + \sum_j \left(\frac{\{m\}_j^{\text{Exp}} - \{m\}_j^{\text{Model}}}{\{m\}_j^{\text{Exp}}} \right)^2 \\ \text{subject to} \quad & \boldsymbol{\theta} > 0 \end{aligned} \tag{5.10}$$

where the vector $\boldsymbol{\theta}$ contains the parameters to be optimised, which included the shaft and disc parameters in Table 5.8. The constraint on the parameters $\boldsymbol{\theta}$ ensures that the optimal parameters are positive and therefore have physical meaning. The term $\{\omega\}_i^{\text{Exp}}$ in the cost function is the natural frequency of the ith mode from the hammer test, and $\{\omega\}_i^{\text{Model}}$ is the frequency of the same mode from the ROLADYN model. The term $\{m\}_j^{\text{Exp}}$ represents the measured weights of the shaft and disc in Table 5.7a, and $\{m\}_j^{\text{Model}}$

represents the corresponding terms from the model. The denominator terms normalise each residue, so that they are all equally weighted.

This optimisation problem was solved using a Genetic Algorithm (GA) using the function `ga` in MATLAB. On each iteration, the ROLADYN was updated with the current set of parameters $\boldsymbol{\theta}$, which were then used to estimate the value of the natural frequencies, $\{\omega\}_i^{\text{Model}}$, and component masses, $\{m\}_j^{\text{Model}}$. This process was repeated many times by the GA, resulting in the optimal set of parameters $\boldsymbol{\theta}^*$ listed in Table 5.8.

Table 5.8: Identified inertial and elastic rotor parameters

Property	Symbol	Value	Units
Shaft Young's modulus	E_{S}	211	MPa
Shaft density	ρ_{S}	7815	$\text{kg}\,\text{m}^{-3}$
Disc root stiffness	k_{D}^{θ}	17	$\text{MN}\,\text{m}\,\text{rad}^{-1}$
Disc density	ρ_{D}	7950	$\text{kg}\,\text{m}^{-3}$

5.3.4.2 Damping parameters

Once the inertial and elastic properties were identified, such that the natural frequencies and components matched the experimental data to a suitable degree of accuracy, attention moved onto identifying the damping parameters. These were identified by solving another optimisation problem, this time penalising the error in the damping ratio:

$$\begin{aligned} &\underset{\boldsymbol{\theta}}{\text{minimize}} \quad \sum_i \left(\frac{\{\zeta\}_i^{\text{Exp}} - \{\zeta\}_i^{\text{Model}}}{\{\zeta\}_i^{\text{Exp}}} \right)^2 \\ &\text{subject to} \quad \boldsymbol{\theta} \geq 0 \end{aligned} \tag{5.11}$$

where $\boldsymbol{\theta}$ contains the damping parameters in Table 5.9. The term $\{\zeta\}_i^{\text{Exp}}$ is the natural frequency of the ith mode from the hammer test, and $\{\zeta\}_i^{\text{Model}}$ is the frequency of the same mode from the ROLADYN model. The optimal damping parameters were then found in the same way as the inertial and elastic properties, with use of a GA. The optimal damping parameters obtained from this procedure are shown in Table 5.9.

5.3.4.3 Correlation of updated ROLADYN model

The ROLADYN was finally updated with the identified set of parameters from Tables 5.8 and 5.9. The modes were then computed from the model, and these predictions have been overlaid in orange on Figs. 5.21 to 5.23. In addition, the masses of the shaft and disc were computed from the ROLADYN model. The correlation of the updated model with the experimental model will now be discussed.

Table 5.9: Identified rotor damping parameters

Property	Symbol	Value	Units
Shaft (Plain)	α_S	0.090	s^{-1}
	β_S	2.1×10^{-7}	s
Shaft (Instr.)	α_S	0.023	s^{-1}
	β_S	1.8×10^{-6}	s
Disc root damping	c_D^θ	10	$N\,m\,s\,rad^{-1}$

Component weights The mass of the shaft and disc were computed using the identified densities and these are listed in Table 5.10 along with the measured values. It can be observed while the shaft weight from the model agrees very well with the measured value, the disc mass is over-predicted by 0.3 kg. This discrepancy can partly be attributed to experimental error, since the masses could only be measured to a precision of 0.1 kg. However, since the error is larger than the precision of the measurements, this suggests that the model has also compensated for some other deficiency in the model by increasing the disc density. The most likely explanations are that the TranTorque model is overly simplistic, or that the compliance of the discs themselves has some influence, but this has been neglected. However, this wasn't deemed a major concern, since the natural frequencies and mode shapes were predicted very well, as will now be discussed.

Table 5.10: Measured rotor component weights

	Mass (kg)	
Component	Measured	Model
Shaft	5.91	5.91
Disc	7.14	7.44

Natural frequencies The natural frequencies from the ROLADYN model match the experimental results very well for all configurations, as shown in Fig. 5.21; the maximum error is less than 1 % across all modes. The natural frequencies of the higher order modes are generally under-predicted by the model, but since even the 3rd order modes are well above the critical speeds of the ARES test rig once assembled, this level of correlation was deemed acceptable.

Damping ratios The ROLADYN model predicts the rotor damping much less accurately than the natural frequencies, as shown in Fig. 5.22. The level of damping in the plain shaft is captured reasonably well across all modes. However, the damping of the instrumented shaft is under-predicted for the 1st and 2nd modes, suggesting that the Rayleigh model is not sufficient to capture the frequency dependence of the damping in

this case. This is not unsurprising given that a lot of the damping from the cabling will be due to frictional losses, which are non-linear in nature.

For the configurations with discs, the damping ratio of the 1st modes is captured well by the model with an error of less than 20 %, but the damping of the higher order modes is over- or under-predicted by varying amounts, with a maximum error of around 50 % and no general trend. It appears that the experimental damping ratios for these higher order modes is less consistent when the discs are fitted; for example, the damping ratio of the 2nd mode for the two disc configuration is much higher than the 1st and 3rd modes, and is not in line with the trend of an increase in damping with frequency. It is possible that the damping from the disc root is non-linear due to the friction at the interface with the TranTorque, and therefore it is not valid to assess the damping using the FRF approach assumed here.

Although the ROLADYN model does not predict the damping as well as the natural frequencies, the order of magnitude of the damping is predicted accurately, which was deemed to be sufficient at this stage. Once the ARES rig is fully assembled, it was expected that the bearings and supports would be much more significant sources of energy dissipation, and therefore the rotor only has a very small contribution to the damping in the complete system.

Mode shapes The mode shapes from the ROLADYN model have been overlaid for the two disc configuration on Fig. 5.23. It can be observed that the ROLADYN model predicts the general shape of each mode very well, with the same number of nodes long the shaft for each mode, and the same localisation of motion around the discs for the higher order modes. In the 2nd and 3rd modes, the experimental data suggests the rear disc rotates much more than the model, which could indicate the disc root was looser than the front disc in the experiments. However, since the rotation of the front disc is predicted very well, and the discs were tightened in the same way, this perhaps indicates some other error during the axial impacts on the front disc or in the post-processing carried out using ModeLAB.

The mode shapes were assessed more quantitatively by computing the MAC [194] between the experimental and numerical mode shapes, using the deflection along the shaft. The MAC values from all rotor configurations are listed in Table 5.11. It can be observed that it is above 0.95 for the first 3 modes, with a minimum value of 0.89 in the 4th modes, which suggests that the model accurately captures the physics of the rotor.

Table 5.11: MAC for the mode shapes of the rotor

	Configuration			
Mode	Shaft (plain)	Shaft (instr.)	Rear Disc	Two Discs
1	0.999	0.981	0.965	0.959
2	0.998	0.989	0.989	0.983
3	0.994	0.966	0.976	0.984
4	0.996	0.981	0.920	0.890

5.3.5 Summary

The ROLADYN model of the ARES rotor has successfully been validated using hammer testing and weighing the components. The unknown shaft and disc parameters were identified using a least-squares approach, and the resulting model correlates well with the experimental results. This model is therefore now ready to be integrated into a model of the complete ARES test rig.

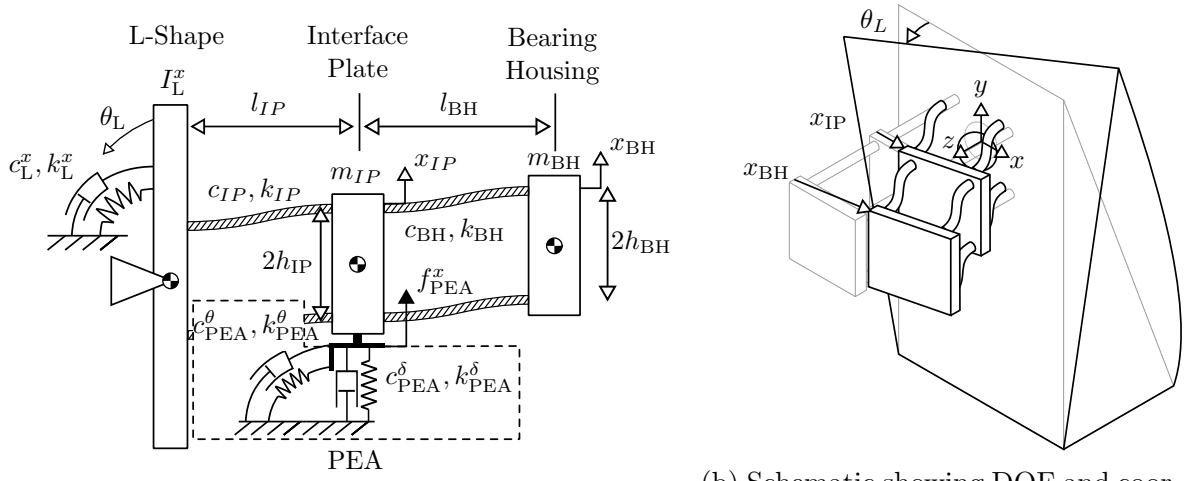
5.4 Bearing support structure

The fixed ARES bearing is supported by a complex support structure, which allows the influence of stator compliance to be investigated. In addition, this structure allows the rotor to be excited with base excitation using the PEAs. This bearing support structure therefore has a large influence on the dynamics of the ARES rig. For this reason, an extensive test programme was carried out in order to develop an accurate model of this subsystem. Hammer tests were carried out in various configurations, as well as a quasi-static loading test using the PEAs. These tests will be explained in more detail in the following sections. As with the rotor model, the unknown parameters were then identified using a least-squares approach.

5.4.1 Equivalent model

To create a physical model of the support structure would require a 3D FE model of the key components, as well as the fixtures joining them. However, such a model would be unlikely to correlate well without significant model updating, particularly due to the non-linear behaviour of the joints between the components. In addition, such a detailed analysis would be well beyond the scope of this project.

Instead, a simplified approach was taken whereby the system was modelled as the 3 DOF system depicted in Fig. 5.24a. Only the horizontal (x) DOF are depicted in Fig. 5.24, but there will be another identical 3 DOF in the vertical (y) plane, leading to a total



(a) Equivalent 3DOF model

(b) Schematic showing DOF and coordinate system

Figure 5.24: Simplified model of the bearing support structure (horizontal plane)

of 6 DOF. Since the system is completely symmetrical in the vertical (y-z) plane, it is assumed that the motion in the horizontal and vertical directions are decoupled, and therefore each can be analysed and modelled independently.

The interface plate and bearing housing were approximated as rigid lumped masses, with springs representing the support rods. It is assumed that the support rods are axially rigid, so that both the interface plate and bearing housing must rotate with the L-shape. This means that only one rotational DOF is required, which is represented by the L-shape rotation θ_L. Torsional and axial motion were neglected, since little motion was observed in these directions in the modes of interest.

5.4.1.1 L-shape

If the L-shape were rigid, then only 2DOF for the interface plate and bearing housing would be required, and the model would be axisymmetric; ie. the natural frequencies would be the same in the horizontal and vertical directions. However, some asymmetry was observed from the experimental testing, which can only arise from the L-shape. As the interface plate displaces horizontally, the L-shape primarily twists about the vertical axis. Similarly, the L-shape bends about the horizontal axis, as the interface plate is loaded vertically. Therefore one rotational DOF was included for the L-shape in each plane, with a corresponding stiffness and moment of inertia.

Since the support rods are all assumed axially rigid, both the interface plate and bearing housing must rotate with the L-shape. The L-shape parameters therefore have an influence on the properties of the whole system. The stiffness and inertia of the L-shape will likely be quite different in the horizontal and vertical directions, in contrast to the bearing housing and interface plate. This model is therefore able to introduce the asymmetry

observed in the experimental tests. The L-shape parameters in Fig. 5.24a have therefore been given a superscript to denote that they apply for motion in the horizontal plane; there will be another different set of L-shape parameters for vertical motion.

5.4.1.2 Interface plate

Since the interface plate was very thick, it was modelled as a rigid body. The inertia of this rigid body was assumed to have two components; one due to the mass of the main body of the interface plate, termed the "block", which can be measured directly, as well as an additional contribution due to the support rods:

$$m_{\mathrm{IP}} = m_{\mathrm{IP}}^{block} + m_{\mathrm{IP}}^{rods}$$
$$I_{\mathrm{IP}} = I_{\mathrm{IP}}^{block} + m_{\mathrm{IP}}^{rods} h_{\mathrm{IP}}^2$$

The interface plate block was weighed using scales with a precision of 1 g, and this value is listed in Table 5.13a. The moment of inertia of the interface plate block was then estimated using the radius of gyration from the CAD model, and this is listed in Table 5.13b.

The effective rod inertia term m_{IP}^{rods} cannot be measured directly, and must be identified from the experimental data. Note that this is not simply half of the mass of the support rods, because not all sections of the rod move fully with the interface plate. The rods also have a contribution to the moment of inertia due to the offset of the rods from the centroid of the interface plate, denoted by h_{IP}, as defined in Fig. 5.24a. The key dimensions of the rods are shown in Table 5.12a.

The rods were modelled as linear springs and dampers, with a stiffness k_{IP} and viscous damping constant c_{IP}. These terms were also identified from the experimental data. It was assumed that they were axisymmetric so that $k_{\mathrm{IP}}^x = k_{\mathrm{IP}}^y = k_{\mathrm{IP}}$ and similarly for the damping constants and inertia.

Table 5.12: Support rod dimensions (mm)

(a) Interface plate

Property	Symbol	Value
Rod separation	h_{IP}	49.5
Rod length	l_{IP}	135.0

(b) Bearing housing

Property	Symbol	Value
Rod separation	h_{BH}	49.5
Rod length (rigid)	l_{BH}	50.0
Rod length (flexible)	l_{BH}	150.0

Table 5.13: Inertia of different support components

(a) Measured masses (kg)

Component	Symbol	Weight
Interface plate	m_{IP}^{block}	4.26
Bearing housing	m_{BH}^{block}	2.82
SKF bearing	$m_{\mathrm{BH}}^{bearing}$	0.50

(b) Estimated moments of inertia ($\mathrm{kg\,m^2}$)

Component	Symbol	Inertia
Interface plate	I_{IP}^{block}	10.134×10^{-3}
Bearing housing	I_{BH}^{block}	5.548×10^{-3}
SKF bearing	$I_{\mathrm{BH}}^{bearing}$	0.226×10^{-3}

5.4.1.3 Bearing housing

The bearing housing was also modelled as a rigid body. Its inertia was assumed to have a similar form to the interface plate:

$$m_{\mathrm{BH}} = m_{\mathrm{BH}}^{block} + m_{\mathrm{BH}}^{bearing} + m_{\mathrm{BH}}^{rods}$$
$$I_{\mathrm{BH}} = I_{\mathrm{BH}}^{block} + I_{\mathrm{BH}}^{bearing} + m_{\mathrm{BH}}^{rods} h_{\mathrm{BH}}^2$$

where there is now an additional term $m_{\mathrm{BH}}^{bearing}$ due to the bearing. The "block" and "bearing" terms are independent of the setup, but the last terms due to the rods will depend on the setup, and will be different for the rigid and flexible configurations.

The bearing housing block and rolling-element bearing were weighed in the same way as the interface plate, and these values are listed in Table 5.13a. The moment of inertia of the housing was then estimated using the radius of gyration from the CAD model. The radius of gyration of the rolling-element bearing was estimated using the diameter between ball centres d_m (defined in Fig. 3.6):

$$I_{\mathrm{BH}}^{bearing} \approx m_{\mathrm{BH}}^{bearing} \frac{d_m^2}{4}$$

where the value of d_m can be found from Table 5.1. The estimated moments of inertia are listed in Table 5.13b.

In the rigid configuration, the support rods were assumed to be infinitely stiff, so it was not necessary to identify any elastic or damping rod parameters; however, an inertial term was still identified. In the flexible configuration, it was necessary to identify both the rod stiffness k_{BH} and damping c_{BH}, as well as another inertial term. The flexible bearing housing support rods were assumed to be axisymmetric, like the interface plate support rods. The dimensions of the support rods are shown in Table 5.12b.

5.4.1.4 Piezo-electric actuator model

When the PEAs are fitted, they will add some stiffness to the system. These were modelled as springs and dampers between the interface plate and ground as shown in Fig. 5.24. Both radial springs (with stiffness k^{δ}_{PEA}) and rotational springs (with stiffness k^{θ}_{PEA}) were included. Note that these springs and dampers represent not only the PEA stacks, but also the stingers and PEA bases, as shown in Fig. 5.8. Since the PEAs are identical, and inclined at 45°, they will add the same stiffness in the horizontal and vertical directions. Therefore, only a single set of PEA parameters needs to be identified, which apply in both the horizontal and vertical directions. Since the PEAs are connected to the bottom of the interface plate, they could introduce some axial-lateral coupling. However, it was assumed that the L-shape provides adequate constraint against axial motion, since little axial motion was observed experimentally. Therefore, this effect was neglected.

5.4.1.5 Equations of motions

The equations of motion of the system depicted in Fig. 5.24 were derived using a Lagranian approach. These equations will not be reproduced here for brevity, but have been derived in Appendix D.1. These equations will be used later in Section 5.4.4 to find the modal properties of the system using eigenvalue analysis.

5.4.2 Quasi-static loading test

In order to identify the elastic properties of the L-shape and interface support rods, as well as the PEA voltage gain, a quasi-static loading test was carried out. The interface plate was fixed to the L-shape, and then the two PEAs were attached, as shown in Fig. 5.25. The actuators were then used to excite the interface plate in the horizontal and vertical directions. The frequency of excitation was kept very low ($< 20\,\text{Hz}$), so that it approximated static loading and inertial loads could be neglected. The displacement of the interface plate was measured in both directions using the Keyence laser displacement sensors, and the loads applied to the plate were measured using the force-gauges on the PEAs. The loads from each force gauge were converted into horizontal and vertical components in post-processing.

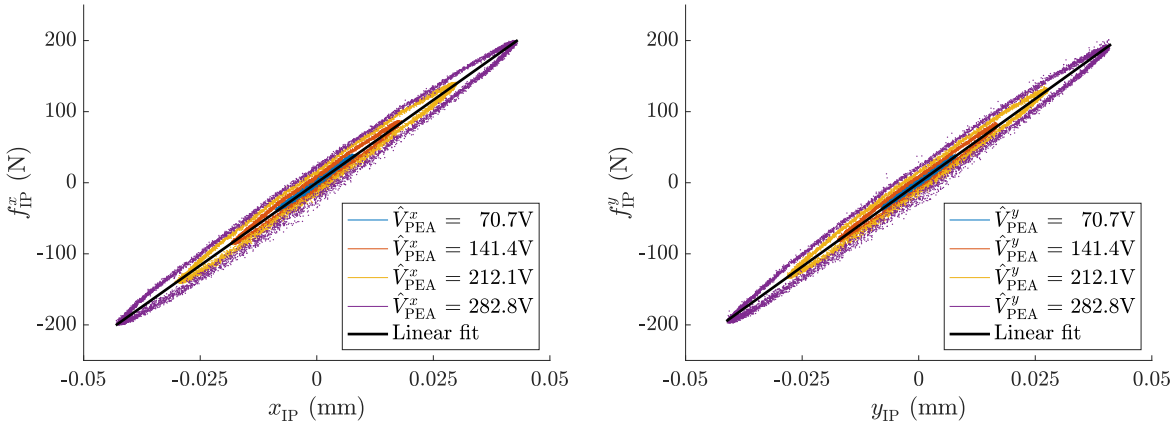
5.4.2.1 Effective interface plate stiffness

The relation between the interface plate displacement and the load applied by the PEAs was used to extract an effective interface plate stiffness. This was repeated for multiple excitation voltages, in order to be able to verify that the measured stiffness remained



Figure 5.25: Experimental setup to measure the interface plate stiffness

independent of the applied load. The load-displacement relation measured in the experiments is plotted in Fig. 5.26. The effective interface plate stiffness clearly remains constant, although there is a small amount of hysteresis due to friction. Linear polynomials were fitted to the load-displacement relation in each direction, and these are overlaid. The effective interface plate stiffness was found from the gradient of these lines.



(a) Horizontal (b) Vertical

Figure 5.26: Experimental results from interface plate stiffness test

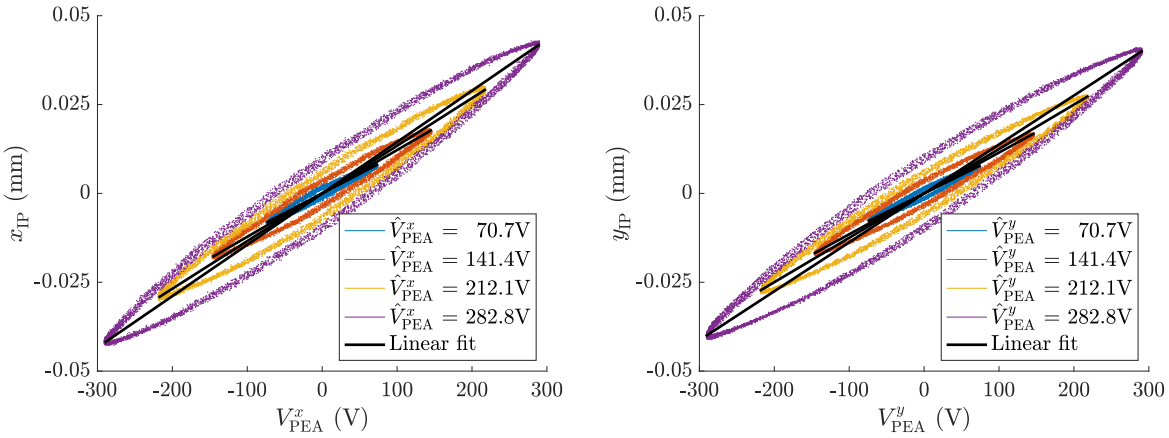
It should be noted that the measured stiffness is not simply the stiffness of the flexible rods supporting the interface plate. In Appendix D, the expression for stiffness measured in this test was derived as follows:

$$k_{\mathrm{IP}}^{test} = \left(\frac{1}{k_{\mathrm{IP}}} + \frac{l_{\mathrm{IP}}^2}{k_{\mathrm{L}} + k_{\mathrm{PEA}}^{\theta}} \right)^{-1} \tag{5.12}$$

where k_{L} is L-shape stiffness in the direction of the loading test. It becomes apparent that there is one component due to the interface plate rod compliance as expected. However, there is an additional term due to the rotational compliance from the L-shape and PEAs, which are in series with the support rods. Note that the radial PEA stiffness has no influence on the measured stiffness, since the load was measured in series with the PEAs.

5.4.2.2 PEA voltage gain

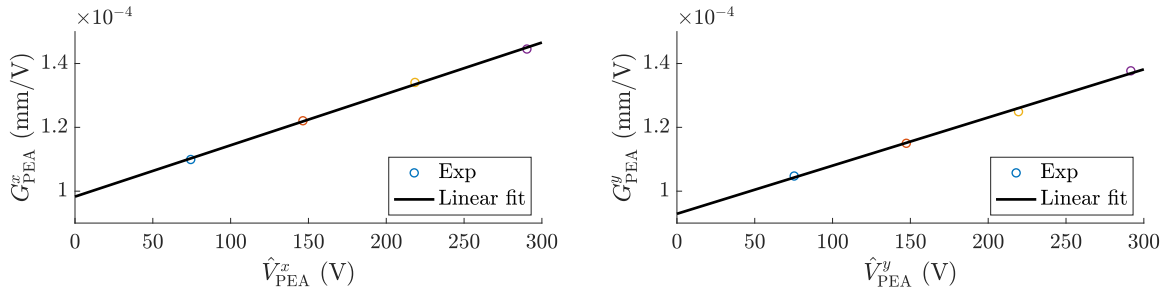
The relation between the applied PEA voltage and interface plate displacement was also extracted from the quasi-static tests. The interface plate displacement is plotted against the applied voltage in Fig. 5.27 for both horizontal and vertical loading. It can be observed that for each voltage, there is a linear relationship between the applied voltage and interface plate displacement. Some hysteresis is visible, which is due to friction within the joints of the bearing support structure. However, when comparing the results from each voltage level, it can also be observed that the gain from voltage to displacement increases varies with the voltage amplitude.



(a) Horizontal (b) Vertical

Figure 5.27: PEA voltage-displacement relation from quasi-static loading test

The voltage-displacement gain was determined at each amplitude by fitting a line through the experimental data points. The gradient of these lines can then be plotted against the applied voltage amplitude, as shown in Fig. 5.28. It becomes clear that the voltage-displacement increases with the amplitude of the PEA voltage. This is a well-known phenomenon in PEAs, and is due to the electrical hysteresis within the piezo-electric material being overcome [195]. For this project, it was not necessary to understand the origin of this PEA behaviour. Instead, a line was fit through the measured points on Fig. 5.28, which is plotted in black, to yield an amplitude dependent voltage gain which is valid for harmonic excitation. Since the PEAs are clearly non-linear, this voltage-displacement gain will not necessarily extend to other types of excitation, but this was



(a) Horizontal (b) Vertical

Figure 5.28: Variation of PEA voltage-displacement gain from quasi-static loading test with amplitude of PEA voltage

not an issue since only harmonic excitation was considered in this project. It should be noted that the voltage-displacement gain is very similar in the horizontal and vertical directions, but differences are visible at lower voltage levels.

This amplitude-dependent gain can then be evaluated to find the corresponding gain for a given PEA voltage amplitude. This can then be used to find the resulting interface plate displacement. For example, the horizontal interface plate displacement is given by:

$$x_{\mathrm{IP}}(t) = G^x_{\mathrm{PEA}}\left(\hat{V}^x_{\mathrm{PEA}}\right) * V^x_{\mathrm{PEA}}(t) \tag{5.13}$$

where $\hat{V}^x_{\mathrm{PEA}}$ is amplitude of the effective horizontal PEA voltage. The vertical gain can be applied in the same way to yield the vertical interface displacement.

5.4.3 Hammer tests

Although the quasi-static test revealed some information about the elastic properties of the system, it did not reveal how much compliance is introduced by the L-shape or flexible rods, but only the total compliance. Moreover, no tests were carried out with the bearing housing fitted yet, so the compliance of the bearing housing support rods was unknown. In addition, the inertial and damping contributions from the support rods remained unknown. Further information was therefore required.

An extensive hammer test campaign was therefore carried out, in order to identify the remaining unknown parameters. Tests were carried out in many multiple support configurations, so that it was possible to glean information about all of the different components. Roving hammer tests were carried out in each configuration, using the same data acquisition method as the rotor hammer tests explained in Section 5.3.3.1. The only difference was that the acquisition window was reduced to 16 s, since the support structure was much more heavily damped. The modal parameters were identified using the ModeLAB

toolbox, as with the rotor. The different hammer tests will now be explained in more detail.

5.4.3.1 L-shape

A roving hammer test was first carried out on the L-shape only, without the interface or bearing housing fitted. This was to allow accurate determination of the L-shape modal parameters, without any extra contributions from the other components. Two accelerometers were fitted to the front face of the L-shape on the top edge, so that both flexural and torsional modes could be detected, as shown in Fig. 5.29. There was a grid of impact locations over the front face of the L-shape.

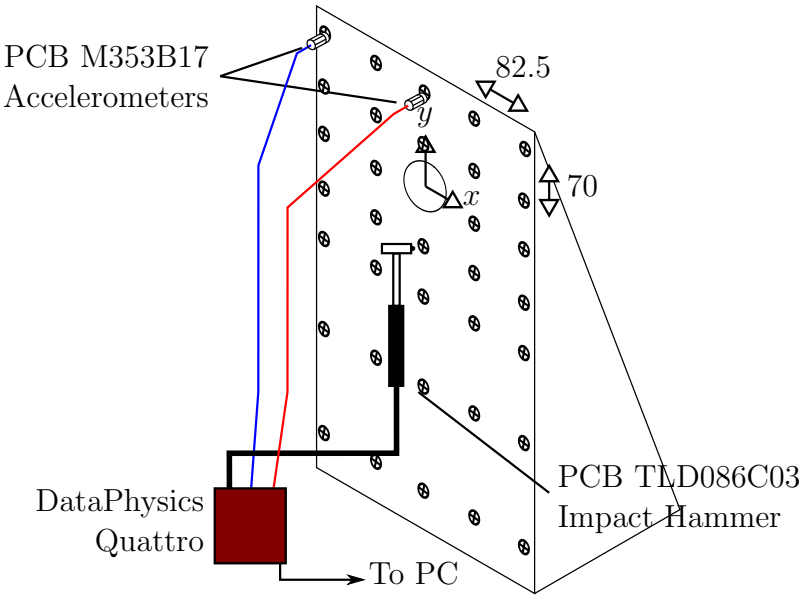


Figure 5.29: Schematic of L-shape hammer tests

5.4.3.2 Interface Plate

The interface plate was then attached to the L-shape via its compliant support rods, as shown in Fig. 5.31. The rods were tightened to a torque of 60 N m. Two accelerometers were attached to the interface plate itself; one in the horizontal and one in the vertical direction. A roving hammer test was then carried out, with impact locations on both the interface plate and L-shape, as depicted in Fig. 5.30.

The mode shapes were post-processed to resolve all 6 displacements of the interface plate, assuming it was a rigid body. The displacements at the six in-plane impact locations on the interface plate were used to resolve the horizontal, vertical and torsional displacement of the interface plate. Similarly, the displacement at the four axial impact locations were

used to resolve the axial displacement and rotations about the horizontal and vertical axes.

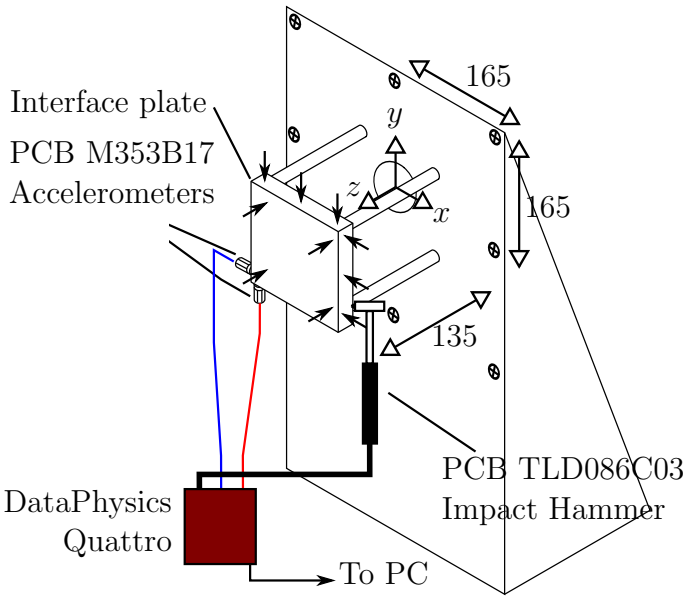


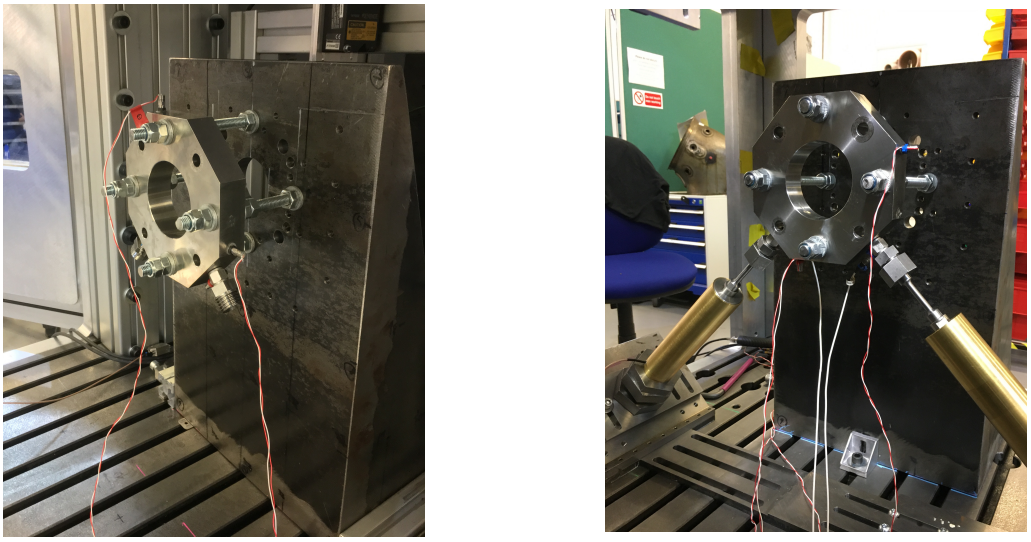
Figure 5.30: Schematic of interface plate hammer tests

Tests were carried out first without the PEAs fitted, as shown in Fig. 5.31a; this was referred to as the "free" configuration. Another hammer test was attempted with the PEAs fitted, as shown in Fig. 5.31b, known as the "fixed" configuration. However, no modes could be observed in the FRF for the fixed configuration, so no information could be gleaned from this test. It was later understood that this was because the PEAs constrained the interface plate in the horizontal and vertical directions, so the modes of interest would have only contained out-of-plane motion. This meant that these modes could not be detected by the horizontal and vertical accelerometers used in the hammer test. However, sufficient information about the interface plate could be gleaned from the "free" test.

5.4.3.3 Bearing housing

The bearing housing was then fitted, in both the rigid and flexible configurations, as shown in Fig. 5.33 and Fig. 5.34. These rods were also tightened to 60 N m. Roving hammer tests were carried out in the same way as with the interface plate, except there were additional impact locations on the bearing housing, as shown in Fig. 5.32. The 6 bearing housing displacements were resolved in the same way as the interface plate. Tests were carried out in both the "free" and "fixed" configurations like the interface plate.

Rigid configuration The bearing housing was first installed in the "rigid" bearing configuration, with very short support rods, as shown in Fig. 5.33. In this case, the



(a) Free configuration

(b) Fixed configuration

Figure 5.31: Experimental setup for hammer tests on interface plate

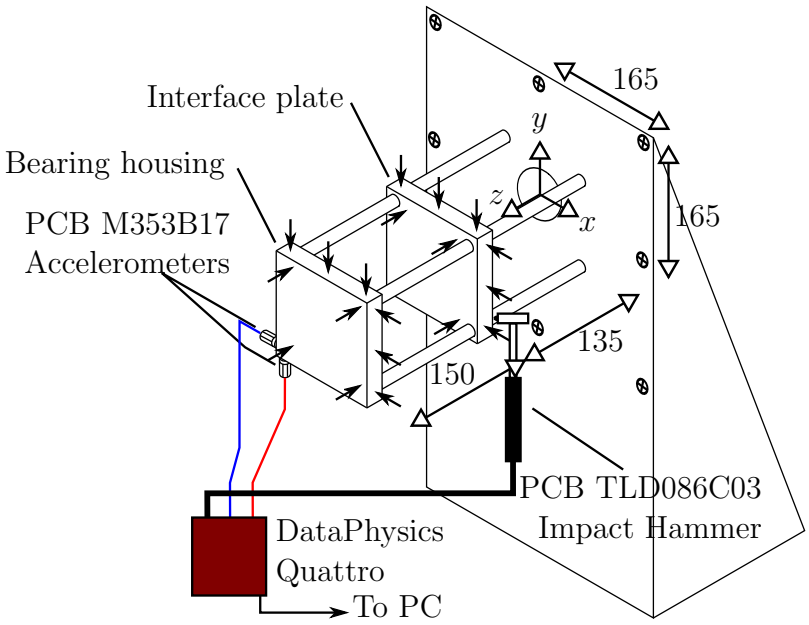
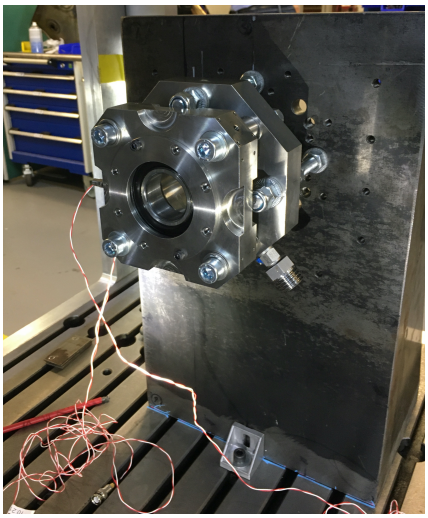


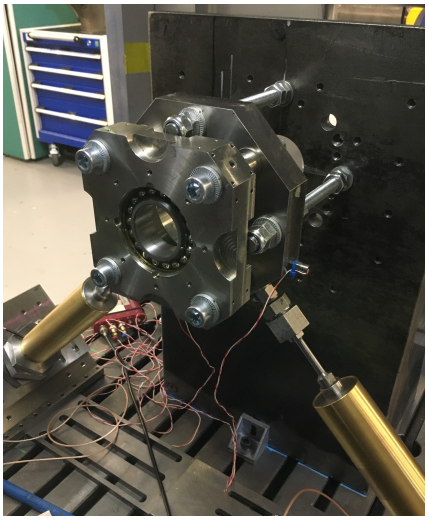
Figure 5.32: Schematic of bearing housing hammer tests

bearing housing and interface plate move as one body, and can therefore be considered to be rigidly connected.

Flexible configuration Flexible bearing housing support rods were then installed as shown in Fig. 5.34. This introduces a significant amount of compliance between the interface plate and bearing housing, so that they can no longer be considered rigidly connected.

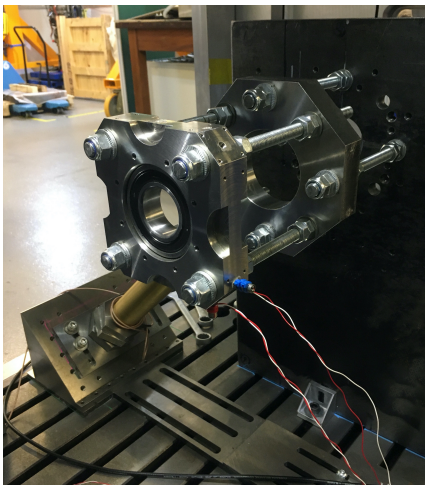


(a) Free configuration

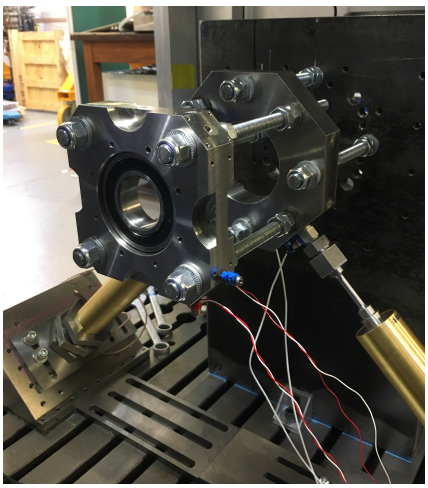


(b) Fixed configuration

Figure 5.33: Experimental setup for hammer tests on rigid bearing housing



(a) Free configuration



(b) Fixed configuration

Figure 5.34: Experimental setup for hammer tests on flexible bearing housing

5.4.4 Parameter identification

In order to identify the unknown bearing support parameters, the same least-squares approach as with the rotor model in Section 5.3.4 was used. As before, a two stage identification process was adopted, whereby the inertial and elastic parameters were identified first, followed by the damping parameters.

The cost function for determining the inertial and elastic parameters from the rotor in Eq. (5.10) was modified slightly, as shown below in Eq. (5.14). The natural frequency term was maintained, but the other terms were replaced using the available information about the supports.

$$\begin{aligned} \underset{\boldsymbol{\theta}}{\text{minimize}} \quad & \sum_i \left(\frac{\{\omega\}_i^{\text{Exp}} - \{\omega\}_i^{\text{Model}}}{\{\omega\}_i^{\text{Exp}}} \right)^2 + \sum_j \left(\frac{\{I_{\text{L}}\}_j^{\text{Exp}} - \{I_{\text{L}}\}_j^{\text{Model}}}{\{I_{\text{L}}\}_j^{\text{Exp}}} \right)^2 \\ & + \sum_j \left(\frac{\{k_{\text{IP}}^{test}\}_j^{\text{Exp}} - \{k_{\text{IP}}^{test}\}_j^{\text{Model}}}{\{k_{\text{IP}}^{test}\}_j^{\text{Exp}}} \right)^2 \\ \text{subject to} \quad & \boldsymbol{\theta} > 0 \end{aligned} \tag{5.14}$$

In Eq. (5.14) there is one term involving the effective L-shape inertia, and another involving the effective interface plate stiffness. The former term encourages the model to match the L-shape inertia measured from the hammer test, which is the most accurate estimate of this inertia. The latter term ensures that the identified L-shape stiffness introduces enough asymmetry to match the results from the quasi-static interface plate test. This stiffness term was computed from the model using Eq. (5.12). To identify the damping parameters, the same cost function from the rotor case was used as in Eq. (5.11), involving only the damping ratios.

5.4.4.1 L-shape parameters

The L-shape was the only component for which all of its parameters had to be identified indirectly by fitting to all of the available experimental data. In addition, the L-shape was the only component with different properties in the horizontal and vertical directions due its inherent asymmetry, so it was necessary to identify 2 sets of inertial, elastic and damping parameters. The identified parameters are listed in Table 5.14.

Table 5.14: Identified L-shape parameters

Property	Symbol	Horizontal	Vertical	Units
Effective stiffness	k_{L}	10.3	1.76	MN m rad^{-1}
Effective inertia	I_{L}	1.30	0.09	kg m^2
Effective damping	c_{L}	70.2	11.2	N m s rad^{-1}

The asymmetry between the two directions is quite pronounced, with the horizontal stiffness approximately 6× the vertical stiffness. Since there is also much more damping in the vertical direction, this can likely be attributed to a gap opening up between the L-shape and test bed, which will also dissipate energy due to friction. On the other hand, the inertia is also much larger in the horizontal direction, so the natural frequencies will be closer than the difference in stiffnesses would suggest.

5.4.4.2 Interface plate rod parameters

The identified elastic, damping and inertial properties of the interface support rods are listed in Table 5.15. These properties apply in both the horizontal and vertical directions. The identified support rod stiffness is very similar in magnitude to the stiffness measured in the quasi-static stiffness test; this implies that the compliance from the support rods dominates over the contributions from the L-shape and PEAs as would be expected. The effective mass is also similar to the measured mass of the support rods which was 1.15 kg.

Table 5.15: Interface plate support rod parameters

Property	Symbol	Value	Units
Effective mass	m_{IP}^{rods}	1.08	kg
Effective damping	c_{IP}^{rods}	52.1	$\mathrm{N\,s\,m^{-1}}$
Effective stiffness	k_{IP}^{rods}	4.68	$\mathrm{MN\,m^{-1}}$

The identified damping value is relatively high, and equates to 0.5 % damping of the interface plate, if the L-shape were rigid.

5.4.4.3 Bearing housing rod parameters

The identified bearing housing rod parameters are shown in Table 5.16 for both the rigid and flexible bearing configurations. It can be observed that the effective rod inertia is higher in the flexible configuration, due to the increased rod length. The rod parameters in the flexible configuration are very similar to the values for the interface plate support rods, which would be expected since the rods has the same free length.

Table 5.16: Identified bearing housing rod parameters

(a) Rigid configuration

Property	Symbol	Value	Units
Effective mass	m_{BH}^{rods}	0.60	kg

(b) Flexible configuration

Property	Symbol	Value	Units
Effective mass	m_{BH}^{rods}	0.94	kg
Effective damping	c_{BH}^{rods}	71.6	$\mathrm{N\,s\,m^{-1}}$
Effective stiffness	k_{BH}^{rods}	4.74	$\mathrm{MN\,m^{-1}}$

5.4.4.4 Piezo-electric actuator parameters

The effective stiffness and damping from the PEAs are listed in Table 5.17. The identified radial stiffness is considerably lower than the value for the actuator stiffness of $150\,\mathrm{MN\,m^{-1}}$ given by the manufacturer. However, the PEAs are not in fact perfectly axially loaded by the interface plate, and there will be some additional compliance from the stingers and the angled mounts connecting the PEAs to the test bed. Therefore it is not entirely unexpected that the values do not agree.

Table 5.17: Identified PEA parameters

Property	Symbol	Value	Units
Effective radial stiffness	$k^{\delta}_{\mathrm{PEA}}$	38.7	$\mathrm{MN\,m^{-1}}$
Effective rotational stiffness	$k^{\theta}_{\mathrm{PEA}}$	0	$\mathrm{MN\,m\,rad^{-1}}$
Effective radial damping	$c^{\delta}_{\mathrm{PEA}}$	857	$\mathrm{N\,s\,m^{-1}}$
Effective rotational damping	$c^{\theta}_{\mathrm{PEA}}$	13	$\mathrm{N\,m\,s\,rad^{-1}}$

The optimiser has set the rotational stiffness of the PEAs to the lower bound of $0\,\mathrm{MN\,m\,rad^{-1}}$. Since the L-shape is very stiff, any additional rotational stiffness from the PEA has very little influence. However, the identified rotational damping term from the PEAs is non-zero, since this is able to account for the increase in stiffness observed once the PEAs are fitted. This is likely due to friction in the stingers.

5.4.5 Results from the L-shape and interface plate

The results from the hammer tests on the L-shape and interface plate will now be presented, along with the predictions from the equivalent model, using the parameters from Section 5.4.4. The results from the quasi-static loading test will also be compared to the predictions from the model.

5.4.5.1 Quasi-static interface plate stiffness

The interface plate stiffnesses measured in the quasi-static loading test with PEAs have been listed in Table 5.18 from both the experiments and the equivalent model. It can be observed that the stiffness is slightly different in each direction, due to the asymmetrical compliance introduced by the L-shape. The L-shape is in fact softer in the vertical direction, in which the L-shape bends, than the horizontal direction in which the L-shape twists, as shown in Table 5.14. Therefore the measured interface plate stiffness is higher in the horizontal direction than in the vertical direction. The model predicts both this asymmetry very well, as well as the overall stiffness level, indicating that the L-shape and interface plate support rods stiffnesses have been identified correctly.

Table 5.18: Comparison of effective interface plate stiffness from the quasi-static loading test and equivalent numerical model

	Stiffness (MN m^{-1})	
Direction	Experiment	Model
Horizontal	4.64	4.64
Vertical	4.44	4.46

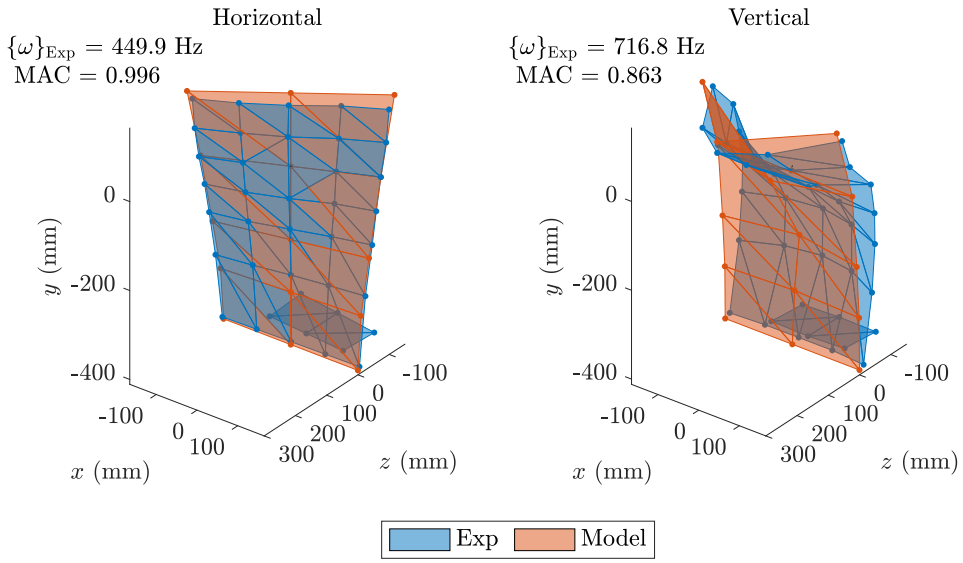


Figure 5.35: Mode shapes of the L-shape

5.4.5.2 L-shape hammer test

The mode shapes obtained from the hammer tests on the L-shape are plotted in Fig. 5.35 and the corresponding modal properties are plotted in Fig. 5.36. In order to reproduce the full displacement field over the L-shape from the model of the support structure, a static FE analysis was performed using Solidworks, where a moment was applied about the x and y axes, as shown in Appendix D.3. These displacement fields were then scaled appropriately by the L-shape rotation from the equivalent support model, in order to reconstruct the deflection of the complete L-shape.

From Fig. 5.35, it can be observed that the L-shape displaces torsionally in the mode which will couple with horizontal interface plate motion, and flexurally in the mode which couples with vertical motion. Without the interface plate fitted, the frequencies of the modes are at their highest, and are well above the running range of the rig. The MAC has been computed over the impact locations on the front face of the L-shape from the hammer test, and this is displayed on Fig. 5.35. Since the mode shape from the model relies on the FE analysis from Solidworks, it is unsurprising that the MAC is high, particularly in the horizontal mode.

Table 5.19: Comparison of L-shape inertia from hammer test and equivalent numerical model

		Inertia ($\mathrm{kg\,m^2}$)	
Direction	Symbol	Experiment	Model
Horizontal	I_{L}^{x}	1.22	1.3
Vertical	I_{L}^{y}	0.15	0.09

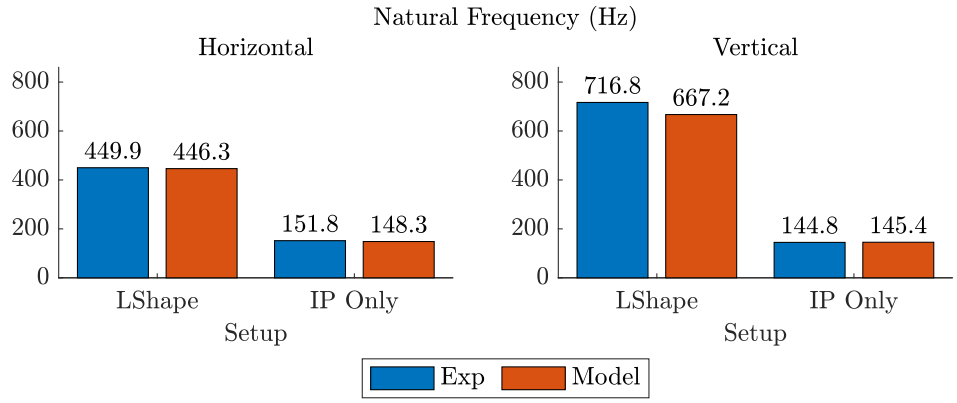
Despite the fact that the L-shape was observed to be stiffer in the horizontal direction from the quasi-static loading test, the horizontal mode is significantly lower than the vertical mode, as shown in Fig. 5.36a. This is because the torsional mode engages more of the front panel as well as the webs on the side compared to the flexural mode, which therefore introduces extra inertia, which is reflected in the measured values from the hammer test listed in Table 5.19.

The L-shape inertias identified from the procedure in Section 5.4.4 are close to the measured values, but show an even greater level of asymmetry than the values extracted from the hammer test. It is possible that there are additional sources of asymmetry in the support, which have been lumped into the L-shape during the parameter identification procedure. However, a more likely explanation is that there is non-linear damping in the L-shape due to friction between the L-shape and the test bed, and therefore the estimate of the modal mass from the FRFs is not accurate. This perhaps explains why the model under-predicts the L-shape damping ratio in Fig. 5.36b.

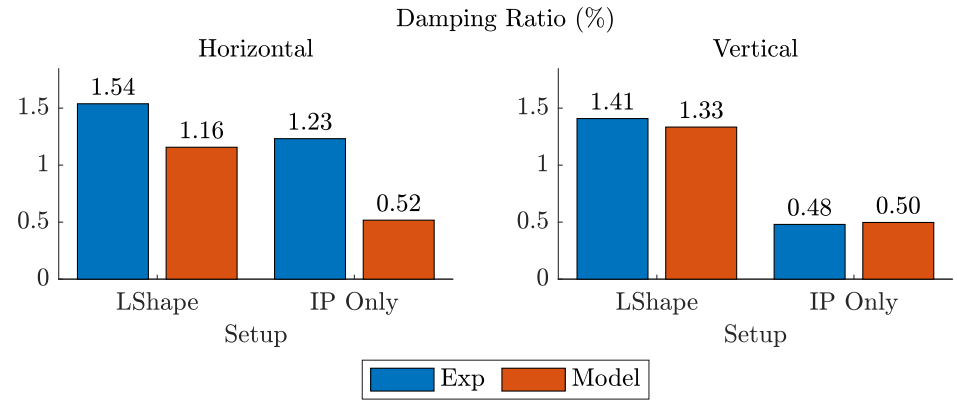
Overall, the model correlates quite well, with a maximum error in the natural frequencies of 7 % in the vertical mode. The damping ratios are also well predicted with a maximum error of 25 % in the horizontal mode. Given that the focus of this work was to be able to accurately predict the bearing housing motion, this level of correlation was deemed acceptable. In the next sections, it will become clear that these small discrepancies become less significant once the other components are added.

5.4.5.3 Interface plate hammer test

Once the interface plate is fitted, the natural frequencies reduce significantly. The interface plate moves in-plane with very little torsional or titling motion, as depicted in Fig. 5.37. The L-shape deflects very slightly with the interface plate; the L-shape twists slightly in the horizontal mode, and bends slightly in the vertical mode. This leads to some asymmetry, with a small gap of 5 Hz between the frequencies, as shown in Fig. 5.36a. It is interesting to note that the horizontal mode now has a higher frequency, which is the opposite of what was observed in the L-shape hammer test; the addition of the interface plate has brought the frequencies into the regime where the L-shape stiffness has more



(a) Natural frequencies



(b) Damping ratios

Figure 5.36: Modal properties of the L-Shape and interface plate supports (PEAs disconnected)

influence than its inertia, so that the horizontal mode has a higher frequency since the L-shape is stiffer in this direction. In addition to this, the L-shape now has a smaller contribution to the damping, and therefore the damping ratio has reduced considerably, as shown in Fig. 5.36b.

These modes are very well predicted by the equivalent model, both in terms of the mode shapes and natural frequencies. The MAC was computed using the deflections of both the L-shape and interface plate, and this is displayed on Fig. 5.37. It can be seen that the MAC remains above 0.9 for both modes; the frequencies are also within 1 % of the measured values. The damping in the vertical direction has reduced significantly, and this is well predicted by the model. However, the model over-predicts the reduction in damping for the horizontal mode, suggesting that the damping contribution from the L-shape may in fact be higher than the model predicts. However, the overall level of damping is captured well, with a maximum error of 50 %.

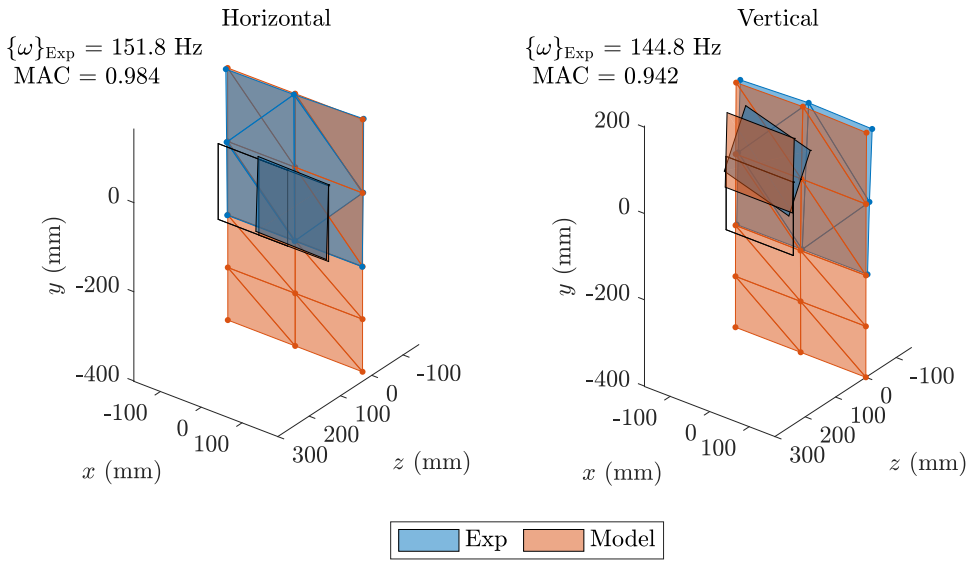


Figure 5.37: Mode shapes of the interface plate (PEAs disconnected)

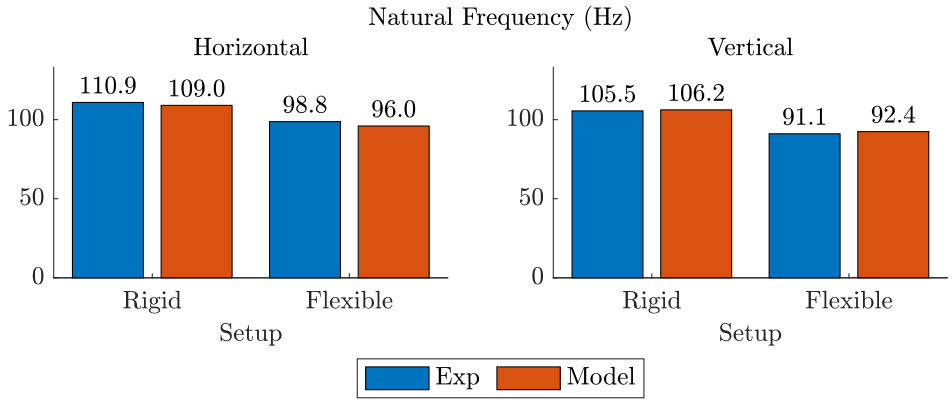
5.4.6 Results from the bearing housing hammer tests

The results from the hammer test with the bearing housing attached will now be presented, which have the most relevance for predicting the response of the ARES rig, once fully assembled. First, the "'free" case without the PEAs connected will be examined, before moving on the "fixed" case with PEAs connected, which is the configuration which will be used on ARES once assembled. Only the first order modes will be discussed here, but in some of the configurations, a second set of modes with a higher frequency could be observed. The full set of modes are presented in Appendix B.2.

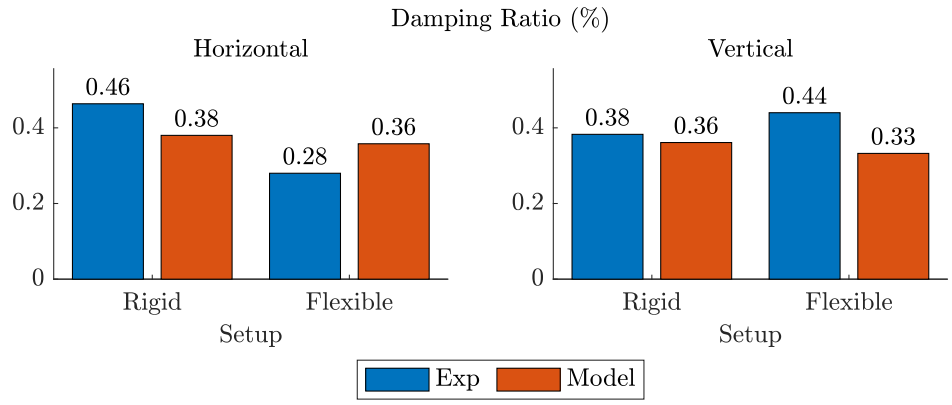
5.4.6.1 Free case with the PEAs disconnected

The modal properties for the case without the PEAs are shown in Fig. 5.38. It can be observed immediately that the frequencies are reduced by the addition of the extra bearing housing inertia. However, the additional compliance between the bearing housing and interface plate in the flexible configuration only leads to a drop in frequency of around 20 Hz from the rigid configuration. This will now be explained in more detail.

Rigid configuration It would be expected that adding the bearing housing with the rigid support rods would reduce the frequencies due to the additional inertia. Indeed it can be observed from Fig. 5.38a that the frequency of the first mode depicted in Fig. 5.39 has been reduced by approximately 40 Hz. The interface plate and bearing housing displace by approximately the same amount, validating the assumption that the two are rigidly connected together. The frequency gap between the modes has remained



(a) Natural frequencies



(b) Damping ratios

Figure 5.38: Modal properties of the rigid and flexible bearing configurations (PEAs disconnected)

at around 5 Hz, with the horizontal mode slightly higher due to the increased L-shape stiffness in this direction.

The agreement with the model is again very good, with the model predicting the same 40 Hz drop in the first pair of modes from the case with only the interface-plate. The MAC has increased slightly to above 0.95. The model generally predicts the damping levels well, as shown in Fig. 5.38b. The damping level remains similar to the case with only the interface plate, since the rigid bearing housing support rods add little damping.

Flexible configuration As would be expected, the natural frequencies reduce considerably when moving to the flexible bearing configuration, as shown in Fig. 5.38a. This is due to the extra compliance introduced by the support rods, which allows the bearing housing to deflect w.r.t interface plate, as depicted in Fig. 5.40. It can be observed that the bearing housing and interface plate move in phase, with the bearing housing displacing further.

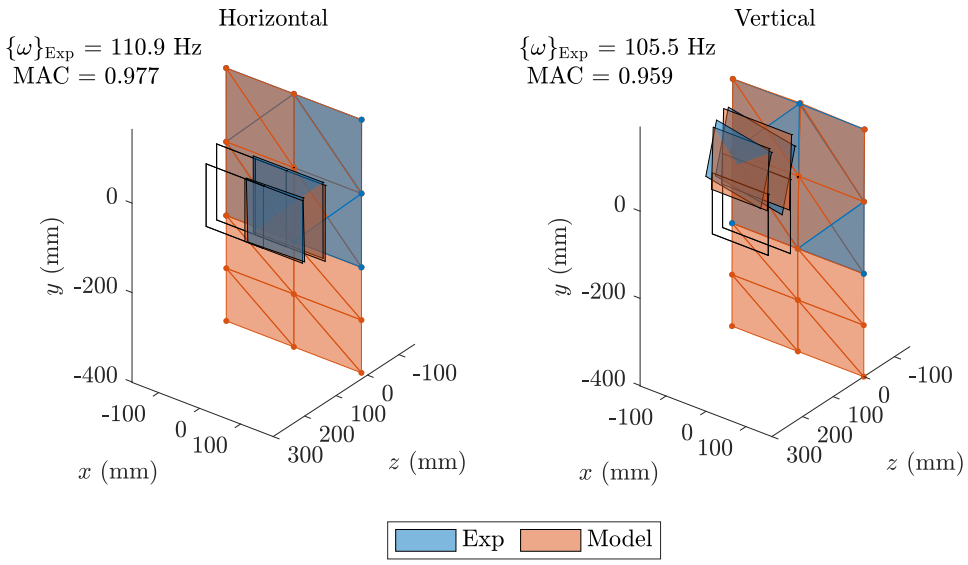


Figure 5.39: Mode shapes of the rigid bearing configuration (PEAs disconnected)

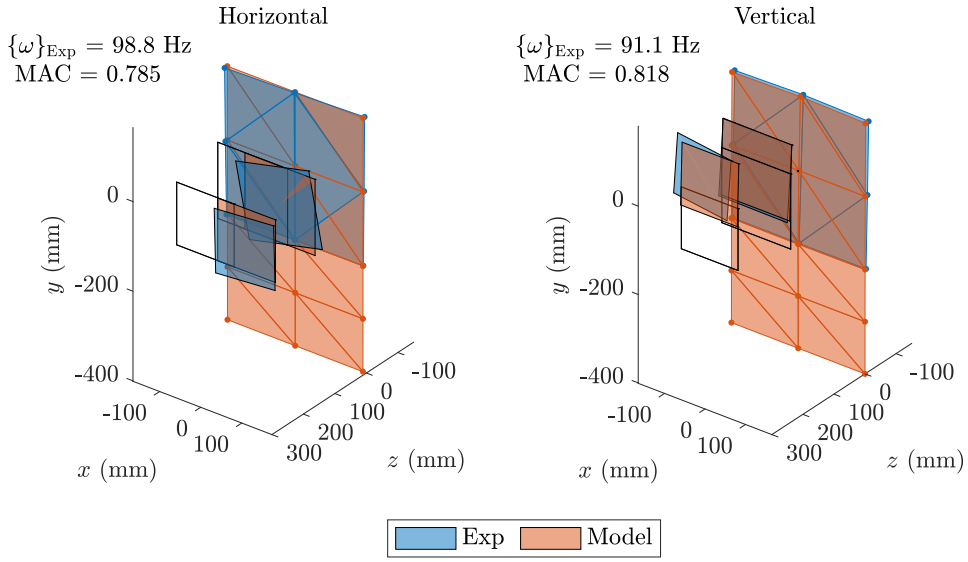


Figure 5.40: Mode shapes of the flexible bearing configuration (PEAs disconnected)

It is interesting to note that the frequency gap between the horizontal and vertical modes has increased from 5 Hz for the rigid bearing housing, to around 9 Hz in the flexible configuration. It would be expected that the frequency gap should *decrease* since the influence of the L-shape will be reduced by the introduction of further compliance. This is why the model predicts that the frequency gap should reduce to around 4 Hz. This discrepancy suggests that some extra asymmetry was introduced during the installation of the flexible support rods. This could also explain the large difference in the measured damping in the horizontal and vertical modes, which is not captured by the model, as well as the drop in the MAC down to around 0.8.

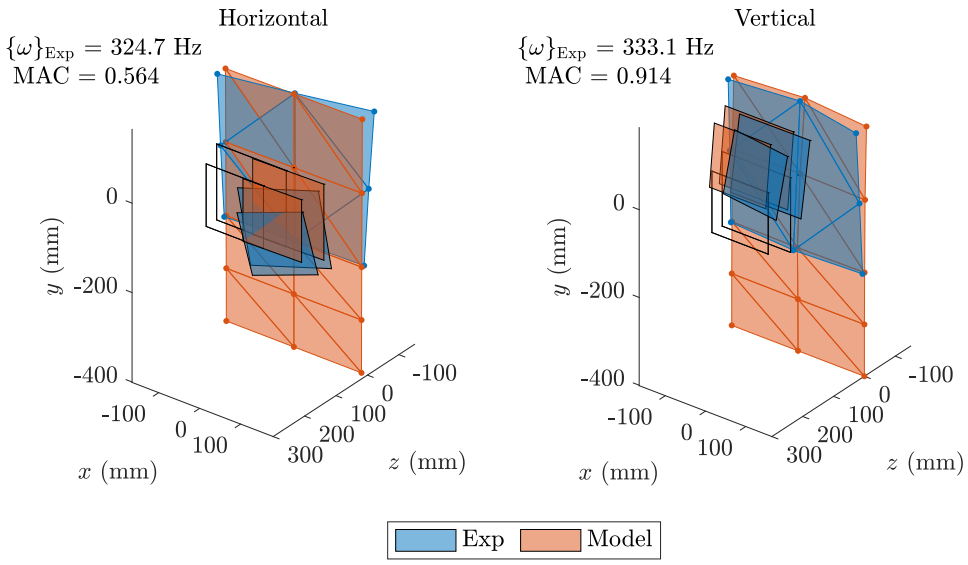


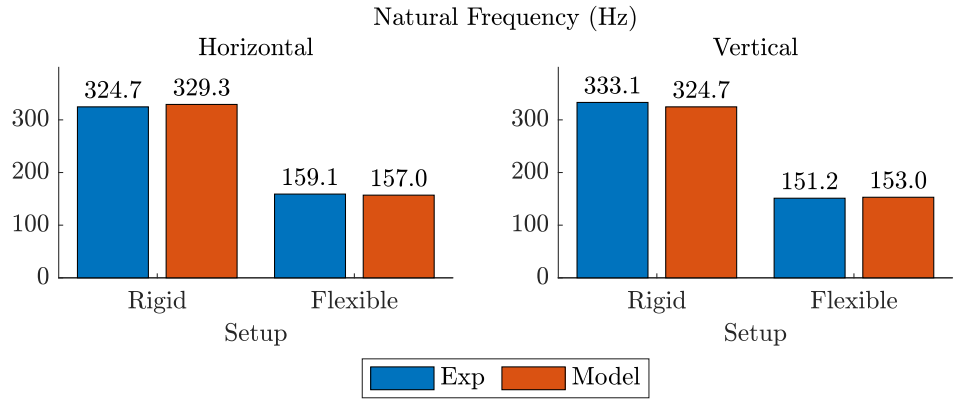
Figure 5.41: Mode shapes of the rigid bearing configuration (PEAs connected)

5.4.6.2 Fixed case with PEAs connected

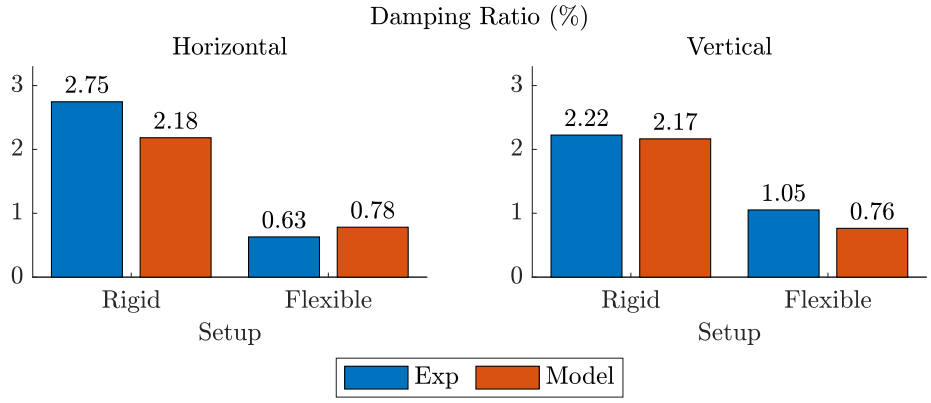
The modal properties obtained from the hammer tests with the PEAs attached are shown in Fig. 5.42. It can be observed that the frequency gap between the rigid and flexible bearing configurations has increased significantly, as will now be discussed in more detail.

Rigid configuration After attaching the PEAs, the frequencies of the first set of modes has increased by over 200 Hz as shown in Fig. 5.42a. This would be expected since the stiffness of the PEAs (shown in Table 5.17) was identified to be approximately 8× higher than the interface plate rod stiffness (shown in Table 5.15). The horizontal mode continues to have a slightly higher frequency due to the increased L-shape stiffness in this direction. The damping of these modes has increased from around 0.4 % in the "free" case to around 2 % in the "fixed", which can likely be attributed to the joints between the interface plate and PEA stingers, or possibly due to hysteretic losses within the PEAs themselves.

The model predicts the increase in both frequency and damping of these modes due to the PEAs very well. However, the MAC value of the horizontal mode has dropped significantly, most likely because the additional L-shape motions appears to have lead to some torsional coupling which is neglected in the model. The damping of the horizontal mode is slightly over-predicted, and the vertical mode under-predicted. This could indicate that there is another damping mechanism in the PEAs and stingers which cannot be captured with a simple viscous damper. However, the overall damping level is captured well. The model was deemed to agree sufficiently well with the experimental data, especially since these modes are unlikely to be significantly excited on the rig because their frequencies



(a) Natural frequencies



(b) Damping ratios

Figure 5.42: Modal properties of the rigid and flexible bearing configurations (PEAs connected)

are so high.

Flexible configuration Attaching the PEAs has a much smaller influence when the bearing is in the flexible configuration. The natural frequencies only increase by around 50 Hz, and this increase is predicted very well by the model. The interface plate was found to move considerably less than the bearing housing in the "free" configuration, so that there is only a small increase in the frequency once the PEAs are attached, even though they are very stiff. Thus, the PEAs simply constrain the interface plate and leave the bearing housing free to deflect, as shown in Fig. 5.43. However, this will likely isolate the bearing from base excitation with the PEAs.

Unlike with the rigid bearing housing, the vertical mode continues to have a lower frequency than the horizontal mode, with a gap of around 8 Hz. This is because the frequencies are much lower with the flexible bearing rods, so that they are in the regime where the L-shape inertia has negligible effect and its compliance dominates. This asymmetry is predicted by the model, but the frequency gap is under-predicted at 4 Hz. As was

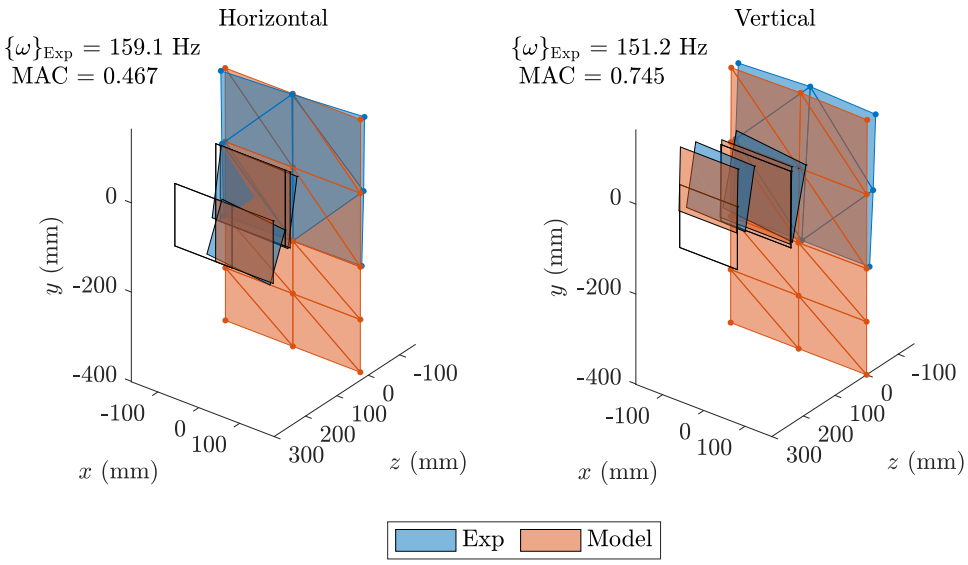


Figure 5.43: Mode shapes of the flexible bearing configuration (PEAs connected)

found with the rigid configuration, the MAC has dropped when compared to the "free" configuration; for example, in the horizontal mode, the MAC was around 0.8 in the "free" configuration, but has reduced to around 0.5 in the "fixed" configuration. This is likely related to the large L-shape motion observed in the experimental results, which is not captured by the model.

The measured damping level appears to have increased with the addition of the PEAs, when comparing the damping from the "free" and "fixed" cases. This is also predicted by the model. However, as was observed in the "free" configuration, there is a large discrepancy between the damping in the horizontal and vertical modes, which cannot be captured by the model because the support rods are assumed symmetric. This is further evidence that the behaviour of the system is sensitive to how it is assembled. Despite this, the overall damping level is captured reasonably well.

5.4.7 Summary

A simplified 6DOF model of the ARES bearing support structure has been developed, which can accurately predict the first two modes of the system. It has been fully parameterised using data from multiple hammer tests and a quasi-static loading test. It is able to accurately predict the modal properties of the bearing housing in both the rigid and flexible configurations, and is now ready to be integrated into a model of the complete ARES rig.

5.5 Ancillary components

Since the shaft within ARES is both quite light and flexible, the influence of other ancillary components such as the coupling and encoder cannot be neglected. Therefore some additional tests were carried out to assess the impact of the other accessories and identify the relevant parameters.

5.5.1 Coupling

Although the metal bellows coupling which drives the rotor was expected to have a low flexural stiffness, it will still exert elastic forces on the end of the shaft. Since the shaft is quite compliant, there was a concern that the forces from the coupling could still have a significant influence on the rotor's dynamic properties, and therefore a procedure was developed to experimentally measure the lateral stiffness matrix of the coupling. In addition, the coupling will add some inertia to the shaft, so the relevant inertial terms were estimated by weighing the coupling.

5.5.1.1 Test setup

The coupling was mounted on a solid 35 mm OD shaft, which was in turn clamped to a workbench with 2 large G-clamps. Another 30 mm shaft was connected to the motor end of the coupling, and cantilevered off the end of the workbench. The coupling was loaded by hanging weights from the cantilevered shaft. The loading cable could be placed at different axial locations, where loading groves were cut into the shaft at 50 mm intervals. Small masses were hung from the loading cable in increments of 250 g, up to a maximum of 1.5 kg.

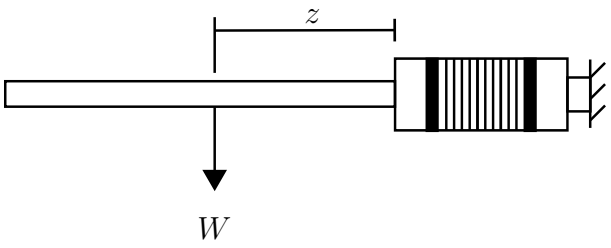
Since the deflections of the loading bar were large, its rotation and deflection were measured by using a Logitech C920 webcam and a point tracking algorithm from the Computer Vision toolbox in MATLAB. To improve the reliability of the point tracking, a speckle pattern was applied to the surface of the shaft, and it was placed in front of a black background. The setup is shown in Fig. 5.44. Once the position and orientation of the loading bar was known, the deflection at the end of the coupling could be computed in post-processing.

5.5.1.2 Coupling Model

The coupling can exert both lateral forces and moments on the shaft, and these loads will depend on both the translation and rotation at the coupling. This can be written in the following matrix form:



(a) Experimental setup



(b) Schematic of coupling test setup

Figure 5.44: Coupling test setup

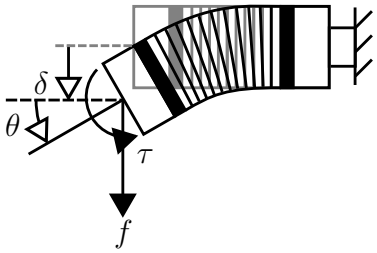


Figure 5.45: Coupling deflections and loads during test

$$\begin{bmatrix} f \\ \tau \end{bmatrix} = \begin{bmatrix} k_{\mathrm{C}}^{\delta,\delta} & k_{\mathrm{C}}^{\delta,\theta} \\ k_{\mathrm{C}}^{\theta,\delta} & k_{\mathrm{C}}^{\theta,\theta} \end{bmatrix} \begin{bmatrix} \delta \\ \theta \end{bmatrix} = \boldsymbol{K} \begin{bmatrix} \delta \\ \theta \end{bmatrix} \tag{5.15}$$

where the loads and deflections are defined in Fig. 5.45, and $\boldsymbol{K}$ is the stiffness matrix. It can be shown that this must be symmetric so that $k_{\mathrm{C}}^{\theta,\delta} = k_{\mathrm{C}}^{\delta,\theta}$. This matrix can be inverted to give the compliance matrix $\boldsymbol{C}$:

$$\boldsymbol{C} = \boldsymbol{K}^{-1} \tag{5.16}$$

which allows Eq. (5.15) to be rewritten as:

$$\begin{bmatrix} \delta \\ \theta \end{bmatrix} = \begin{bmatrix} c_{\delta}^{f} & c_{\delta}^{\tau} \\ c_{\theta}^{f} & c_{\theta}^{\tau} \end{bmatrix} \begin{bmatrix} f \\ \tau \end{bmatrix} = \boldsymbol{C} \begin{bmatrix} f \\ \tau \end{bmatrix} \tag{5.17}$$

With reference to Fig. 5.10, the load and moment applied to the coupling via the cantilevered beam is given by:

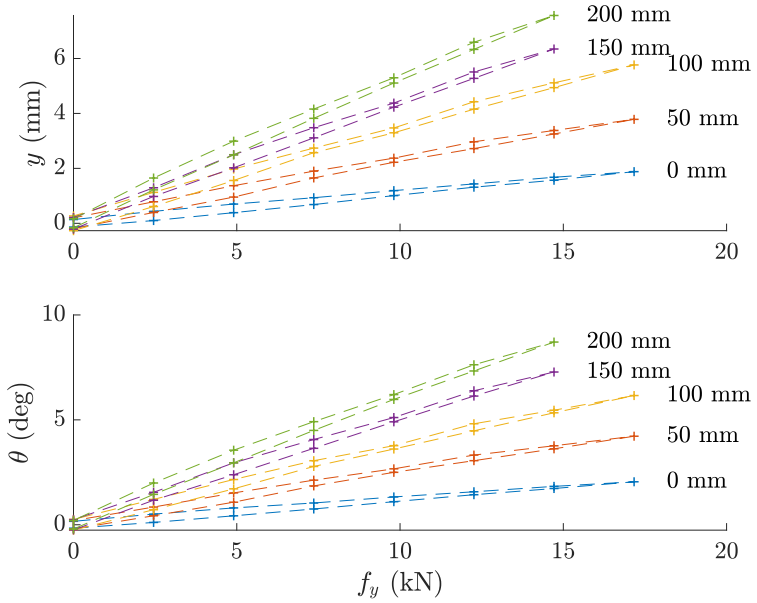


Figure 5.46: Coupling load-displacement relation for different loading positions

$$\begin{bmatrix} f \\ \tau \end{bmatrix} = \begin{bmatrix} 1 \\ z \end{bmatrix} W$$

where W is the weight of the masses hung from the cantilevered beam at a distance z from the coupling, as shown in Fig. 5.44b. This expression can be substituted into Eq. (5.17) to yield expressions for the compliance's measured in the test:

$$\begin{bmatrix} \delta \\ \theta \end{bmatrix} = \boldsymbol{C} \begin{bmatrix} 1 \\ \mathrm{z} \end{bmatrix} W = \begin{bmatrix} c_\delta^f + z c_\delta^\tau \\ c_\theta^f + z c_\theta^\tau \end{bmatrix} W = \begin{bmatrix} c_\delta^W \\ c_\theta^W \end{bmatrix} W \tag{5.18}$$

Thus it is clear that the translational and rotational compliance measured from the cantilever test, denoted by c_δ^W and c_θ^W respectively, should vary linearly with the loading position z. Therefore, if the compliance is measured for many different values of z, the contribution from the terms c_δ^τ and c_θ^τ will vary, and it is therefore possible to determine all the terms in the compliance matrix.

5.5.1.3 Results

The coupling was loaded and unloaded for various different loading locations, and the corresponding coupling displacement and rotation has been plotted in Fig. 5.46. It can be immediately observed that the coupling is very linear, with some small hysteresis due to friction. In addition, the measured compliance appears to increase as the load was applied further out from the coupling.

The lateral and rotational compliance was extracted from each test by finding the gradient of each of the lines in Fig. 5.46. These can then be plotted against the axial loading position z to yield Fig. 5.47. It can be observed that both the lateral and rotational compliance vary linearly with the axial loading position, as expected from Eq. (5.18).

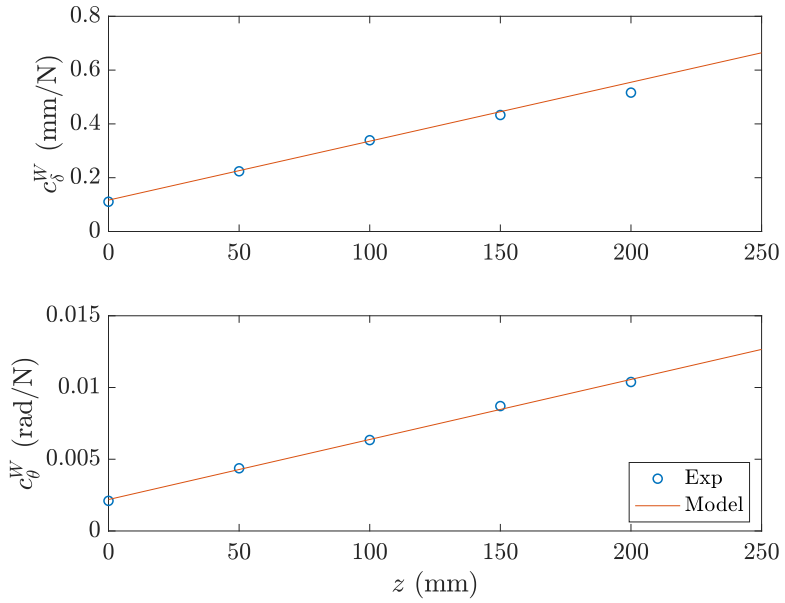


Figure 5.47: Variation of coupling compliance with loading position

5.5.1.4 Parameter identification

There are many possible approaches for extracting the unknown stiffness matrix $\boldsymbol{K}$ from the experimental data. One approach would be to fit linear models to the data in Fig. 5.47 to determine the terms in the compliance matrix. This can then be inverted to yield the stiffness matrix. However, this was found to be an ill-posed problem due to the matrix inversion. An alternative approach is to solve the following constrained non-linear optimisation problem, which attempts to find the terms in the stiffness matrix $\boldsymbol{K}$ directly:

$$\begin{aligned} \underset{\boldsymbol{K}}{\text{minimize}} \quad & \sum_i \left(\left\{ c_\delta^W \right\}_i^{\text{Exp}} - \left\{ c_\delta^W \right\}_i^{\text{Model}} \right)^2 \\ \text{subject to} \quad & k_{\text{C}}^{\theta,\delta} = k_{\text{C}}^{\delta,\theta}, \\ & k_{\text{C}}^{\theta,\delta} < 0, \\ & k_{\text{C}}^{\delta,\delta} > 0, k_{\text{C}}^{\theta,\theta} > 0 \end{aligned} \tag{5.19}$$

where $\left\{ c_\delta^W \right\}_i^{\text{Exp}}$ is the lateral compliance measured from the experiment with the loader at z_i and $\left\{ c_\delta^W \right\}_i^{\text{Model}}$ is the same compliance predicted from the model using Eqs. (5.16)

Table 5.20: Identified coupling stiffnesses

Description	Symbol	Value	Units
Radial stiffness	$k_{\mathrm{C}}^{\delta,\delta}$	459	$\mathrm{kN\,m^{-1}}$
Cross stiffness	$k_{\mathrm{C}}^{\theta,\delta}, k_{\mathrm{C}}^{\delta,\theta}$	-26.5	$\mathrm{kN\,rad^{-1}}$
Rotational stiffness	$k_{\mathrm{C}}^{\theta,\theta}$	1.56	$\mathrm{kN\,m\,rad^{-1}}$

and (5.18). This is very similar to the approach used to identify the rotor and support parameters.

One advantage of this non-linear formulation is that it allows the parameters of the stiffness matrix to be constrained directly. The first constraint enforces that the stiffness matrix is symmetric, whilst the second ensures that cross-stiffness terms are of the correct sign for the given co-ordinate system. The last constraints ensure that the coupling has positive radial and bending stiffnesses, so the identified stiffness matrix is physical.

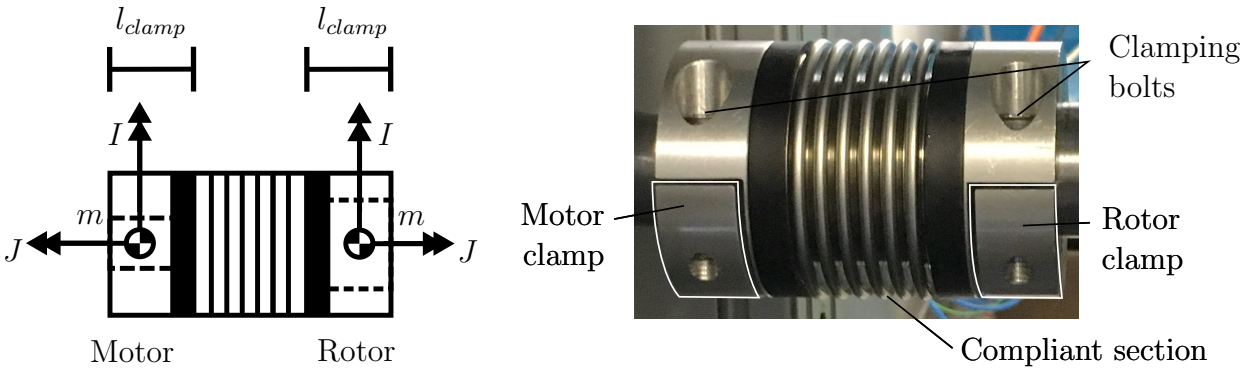
The values for the compliance stiffness found using this approach are shown in Table 5.20, and the corresponding compliances are plotted in Fig. 5.47. It can be observed that the fit between the model and the experimental data is very good. The lateral stiffness $k_{\mathrm{C}}^{\delta,\delta}$ is within 10 % of the manufacturer's value of $420\,\mathrm{kN\,m^{-1}}$; unfortunately, this is the only term of the stiffness matrix supplied by the manufacturer.

These tests have confirmed that the overall stiffness level is of the coupling quite low. It would be expected that only the radial stiffness is large enough to have a significant influence on the dynamics of the rotor. Since these tests were static, it was not possible to identify the damping from the coupling at this stage. However, this will be considered at a later stage, once the rig is fully assembled in Section 6.4.

5.5.1.5 Inertial properties

The coupling also adds some inertia to the shaft, so it was necessary to incorporate this into the model. A further complication is that the coupling has different inertial properties on each side, because the motor shaft and rotor shaft have different ODs. It was assumed that the central bellows section is light, so that most of the inertia arises from the end sections. The coupling inertia was therefore lumped to the two ends of the coupling, as shown in Fig. 5.48a.

The complete coupling assembly was first weighed using digital scales to yield the complete coupling mass, denoted as m_{tot}. The clamps at each end of the coupling were then removed from the body of the coupling, as shown in Fig. 5.48b, and each clamp was weighed by itself. The complete coupling mass was then distributed to each end of the coupling as follows:



(a) Lumped mass model

(b) Split-hub clamps

Figure 5.48: Coupling inertia

$$m_{rotor} = r_{rotor} m_{tot}$$
$$m_{motor} = (1 - r_{rotor})\, m_{tot}$$

where r_{rotor} is the ratio of the clamp masses given by:

$$r_{rotor} = \frac{m_{rotor}^{clamp}}{m_{rotor}^{clamp} + m_{motor}^{clamp}}$$

An estimate of the polar moment of inertia of the coupling is provided by the manufacturer, which was denoted by J_{tot}. This was also distributed to each end of the coupling using the clamp mass ratio:

$$J_{rotor} = r_{rotor} J_{tot}$$
$$J_{motor} = (1 - r_{rotor})\, J_{tot}$$

Lastly, the diametral polar moment of inertia was estimated by summing the "disk" term due its circular cross-section, to the "rod" component due to its length:

$$I_{rotor} = \frac{J_{rotor}}{2} + \frac{m_{rotor} l_{clamp}^3}{12}$$
$$J_{motor} = \frac{J_{motor}}{2} + \frac{m_{motor} l_{clamp}^3}{12}$$

where the length $l_{clamp} = 32\,\text{mm}$, as can be observed from Fig. 5.10b. The inertia values obtained using this approach are listed in Table 5.21. It can be observed that the inertia

terms are lower on the rotor side of the coupling, due to the increased bore size.

Table 5.21: Estimated coupling inertia

Inertia	Symbol	Motor side	Rotor side	Units
Mass	m_{C}	0.257	0.244	kg
Diametral moment of inertia	I_{C}	7.17×10^{-5}	6.83×10^{-5}	$\mathrm{kg\,m^2}$
Polar moment of inertia	J_{C}	1.33×10^{-4}	1.27×10^{-4}	$\mathrm{kg\,m^2}$

5.5.2 Encoder

The encoder used to measure the rotor angle is quite large, and it will therefore add some inertia to the shaft. The encoder was modelled as a rigid body with its CoG coincident with the centroid of the coupling, as depicted in Section 5.5.2. It was assumed that the encoder was rigidly connected to the shaft, and therefore its diametral moment of inertia and mass contribute to the inertia of the rotor. However, it was assumed that the encoder has a negligible contribution to the polar moment inertia of the shaft, since the body of the encoder does not spin. Therefore it was not necessary to estimate this value.

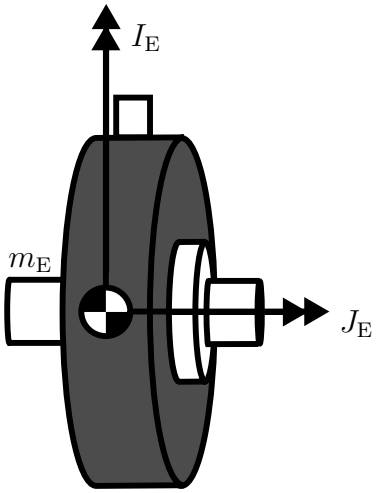


Figure 5.49: Encoder inertia

The encoder was weighed using digital scales. The diametral moment of inertia was estimated by assuming the weight of the encoder was evenly distributed over the body of the encoder. Both of these values are listed in Table 5.22.

Table 5.22: Estimated encoder inertia

Inertia	Symbol	Value	Units
Mass	m_{E}	0.498	kg
Diametral moment of inertia	I_{E}	4.41×10^{-4}	$\mathrm{kg\,m^2}$

The encoder is loosely connected to ground via a rubber mount, and therefore adds negligible stiffness to the system, unlike the coupling. However, it would be expected that the rubber mount may introduce some damping to the system. It was not possible to identify the effect of this without fully assembling the rig, but this damping will be quantified later in Section 6.4.

5.6 Summary

In this chapter, the ARES rotordynamic test rig has been introduced. Well-correlated models of each of the key subsystems have been developed. The fixed rolling-element bearing was loaded statically using a separate test rig known as BELOS, and this was used to parameterise the quasi-static bearing model from Section 3.2. The rotor was modelled using the ROLADYN toolbox and parameterised using the modes obtained from roving hammer tests. A simplified model of the flexible bearing support structure was developed, and this was parameterised using results from further hammer tests. Lastly, the properties of the ancillary components were determined; in particular, the stiffness matrix of the flexible coupling which drives the rotor was successfully measured using a cantilever test. This model of the ARES rig should now be able to accurately capture the linear dynamics of both the rotor and stator, as well as any non-linear effects due to the bearings. This will be investigated in the next chapter.

Chapter 6

Forced response of the ARES test rig

Over the course of Chapter 5, accurate models of each subsystem of the ARES rig were developed, and fully parameterised using results from experiments. In this chapter, these component models will be incorporated into a model of the complete rig using ROLADYN, which can then be used to analyse the forced response. First, a procedure will be developed for optimising the rig setup using the ROLADYN model, in order to maximise the influence of the non-linearity from the fixed bearing. This was so that the rig would operate in the non-linear regime, where it was expected the bearing transmissibility would be most difficult to predict. It was hoped that this would also allow some of non-linear effects from the Jeffcott rotor study in Chapter 4 to be observed in an experimental setting.

The ARES rig will then be assembled in the optimised configuration, and the ROLADYN model will be validated in the linear regime, both with the rotor stationary (using hammer tests) and rotating (using PEA excitation). The forced response of the rotor will then be investigated. The variable compliance of the bearing will be quantified by analysing the spectrum of the response of the rig. Most significantly, the unbalance response will be investigated over a range of excitation levels, and compared to predictions from the ROLADYN model using HBM.

6.1 Complete rig model using ROLADYN

The models of the different sub-systems developed in Chapter 5 first had to be integrated into a ROLADYN model of the complete ARES test rig, as depicted in Fig. 6.1. Some of the components were already modelled using ROLADYN so this was trivial, but for some of the other components, some work was required to implement them within the ROLADYN framework. This will now be explained in more detail.

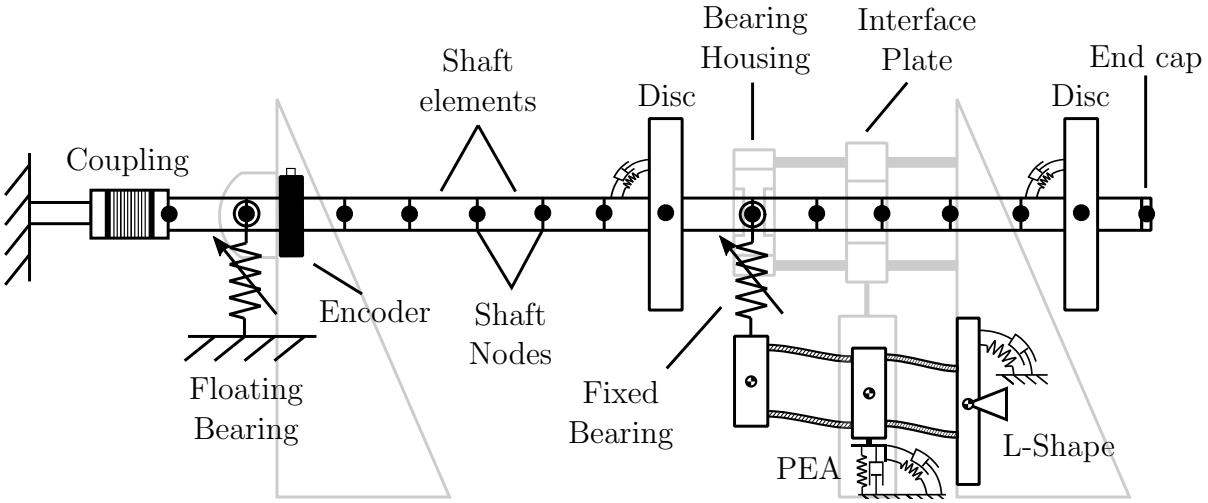


Figure 6.1: Schematic ROLADYN model of ARES rig

6.1.1 Rolling-element bearings

The quasi-static model of the rolling-element bearing from Section 3.2.5 was implemented as a non-linear joint element within ROLADYN. This element was dependent on the rotor speed, due to the effect of dynamic loads on the elements, and the rotor angle due to variable compliance.

The fixed bearing was parameterised using the values identified from BELOS in Section 5.2.5. This includes the radial clearance ($c_r = 4.2\,\mu\text{m}$) and radius of curvature of the inner race ($r_i = 4.9\,\text{mm}$). This bearing was connected to the model of the bearing support structure, which will be discussed shortly.

On the other hand, the properties of the floating bearing were not measured directly using BELOS, so had to be estimated. Since the two bearings contain identical ball elements, the inner race curvature of the floating bearing was set to the same value as the fixed bearing ($r_i = 4.9\,\text{mm}$). However, the floating bearing has a completely different housing from the fixed bearing, so the radial clearance from BELOS will not necessarily carry over. Since the adapter sleeve of this bearing was tightened by a larger angle than the fixed bearing (70° compared to 45°), the clearance of the floating bearing was arbitrarily set to $c_r = 0\,\mu\text{m}$. The floating bearing was assumed to be rigidly connected to ground.

6.1.2 Ancillary components

The metal bellows coupling was modelled using a linear joint element, using the measured stiffness matrix from Section 5.5.1. The rubber mount supporting the encoder was modelled using another linear joint element to ground, except this joint had zero stiffness. The damping of both the coupling and encoder mount were unknown at this stage. The

inertia of both the coupling and encoder was lumped into solid disc elements at the CoG of the coupling clamp and encoder respectively.

6.1.3 Bearing support structure

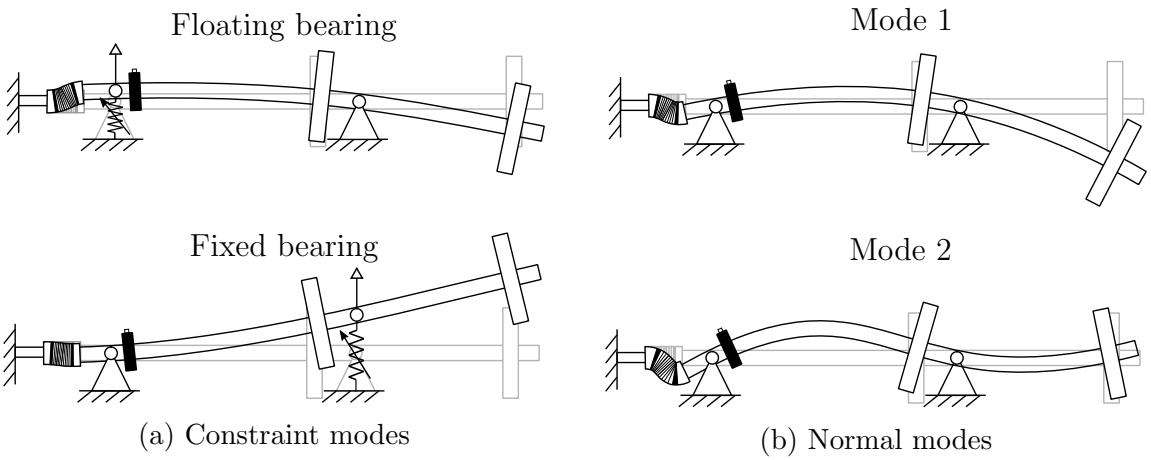
The simplified model of the fixed bearing support structure outlined in Section 5.4.1 was implemented within ROLADYN by modelling the L-shape, interface plate, and bearing housing with solid stator elements. The L-shape compliance and support rods were represented with joint elements, which were defined such that any relative rotation between the L-shape, interface plate and bearing housing was prevented. This model was validated against the support model derived in Appendix D, and was confirmed to give identical results. The support model has 6 DOF for the flexible bearing configuration, but only 4 DOF in the rigid configuration since the bearing housing and interface plate are constrained to move as one rigid body. The effect of PEA excitation was modelled as displacement control of the horizontal and vertical interface plate DOF.

6.1.4 Model reduction of the rotor

The rotor was already modelled within ROLADYN with shaft and disc elements in Section 5.3.1, using a relatively fine 1D mesh with around 20 nodes along its length. This model could have been integrated in a model of the complete rig as it was, but it was relatively large with around 80 DOF. This is acceptable for linear modal analysis on the rotor itself, but becomes computationally expensive when performing more advanced analysis. To mitigate this, component mode synthesis outlined in Section 3.1.2.4 was used to reduce the number of rotor DOF.

Since the two rolling-element bearings have negligible tilt-stiffness, they could be thought of as pin joints supported by non-linear spring, as shown in Section 5.3.1. This leads to 2 constraint DOF at each bearing, one horizontal and one vertical; these are depicted in Fig. 6.2a. The normal modes of the rotor were then computed with the rotor fixed to ground at the bearing locations. The first 2 pairs of normal modes were retained, with one horizontal mode and one vertical mode within each pair, as depicted in Fig. 6.2b. The normal modes added another 4 rotor DOF, leading to a total of 8 rotor DOF once the constraint DOF were included.

Note that for this analysis, the encoder and coupling were included as part of the rotor system. This means that the coupling stiffness was included when computing the constraint modes due to the bearing DOF. In addition, the coupling and encoder inertia was included when computing the normal modes. For this reason, the coupling and encoder



(a) Constraint modes (b) Normal modes

Figure 6.2: Application of CMS to ARES rig

are included in the normal modes depicted in Fig. 6.2. It was therefore unnecessary to include any extra constraint DOF for the coupling or encoder.

6.1.5 Mode pairs

Unlike the rotor, the complete ARES rig is anisotropic due to the bearing support structure and rolling-element bearings, and therefore the modes appear in pairs, with one horizontal and one vertical mode. For example, the first and second mode shapes are shown in Fig. 6.2b. Typically the horizontal modes have a lower frequency since the support structure and bearings are softer in this direction. Each mode was referred to by its mode pair, and whether it was horizontal or vertical. For example, the natural frequencies were denoted as $\omega_{1,H}, \omega_{1,V}, \omega_{2,H}, \omega_{2,V}$ and so on.

6.1.6 MATLAB Implementation

It has been shown how the ARES rig could be modelled using ROLADYN, with only 12 DOF, for the rigid bearing configuration (or 14 DOF in the flexible configuration). The ROLADYN model was made re-parameterisable, so that both the bearings, discs and ancillary components could be moved axially, and the configuration of the bearing support structure could be varied. In addition, it allowed for the coupling, encoder or discs, to be removed. This model could now be used to both perform modal analysis on the rig, and to predict the forced response.

6.2 Setup optimisation

The first use for the newly developed ARES rig model was to decide which configuration should be used for experimental testing. It was expected that the influence of the bearing non-linearities would be significantly smaller than in the Jeffcott rotor study Chapter 4, due to the compliance from both the rotor and stator. Therefore, the logical first step was to find a rig configuration that would maximise the non-linearity of the system.

It was decided that the influence of the fixed bearing non-linearities should be maximised, since this bearing is much better understood. The stiffness of this bearing was measured using the BELOS rig in Section 5.2, and a high-fidelity model of its support was developed in Section 5.4. In addition, the fixed bearing is more heavily instrumented with accelerometers and force gauges, and can be excited asynchronously with PEAs. On the other hand, the floating bearing was poorly understood by comparison, so its influence was to be minimised. Therefore the fixed bearing was chosen as the test bearing. In order to find a setup which satisfies these objectives, whilst ensuring that the rig can be run safely, a setup optimisation procedure was applied. This will be explained further in the following sections.

6.2.1 Excitation

It was first necessary to specify how the rig will be excited, in order to be able to later impose constraints on the natural frequencies, as well as magnitude of the response. The rotor was to be configured so that it is possible to excite the first pair of critical speeds with an unbalance. This means that these critical speeds must lie below the maximum motor speed of 100 Hz. This will allow the effect of the bearing non-linearity on different modes to be observed. A maximum unbalance mass of 2.1 g in the outer ring was assumed, which was applied to the front disc and rear disc separately.

The second pair of modes were to be excited asynchronously using the PEAs, which can excite the rotor asynchronously at higher frequencies. An excitation voltage amplitude of 150 V was assumed, which was within the range investigated in the quasi-static tests on the interface plate in Section 5.4.2.2. A FW circular excitation pattern was assumed, which would excite both the horizontal and vertical modes. This was converted into an equivalent interface plate displacement using the relation in Eq. (5.13).

6.2.2 Rigid bearing approximation

To impose constraints on the critical speeds and natural frequencies of the rotor, as well as the response at resonance (e.g bearing loads and shaft stresses), it was necessary

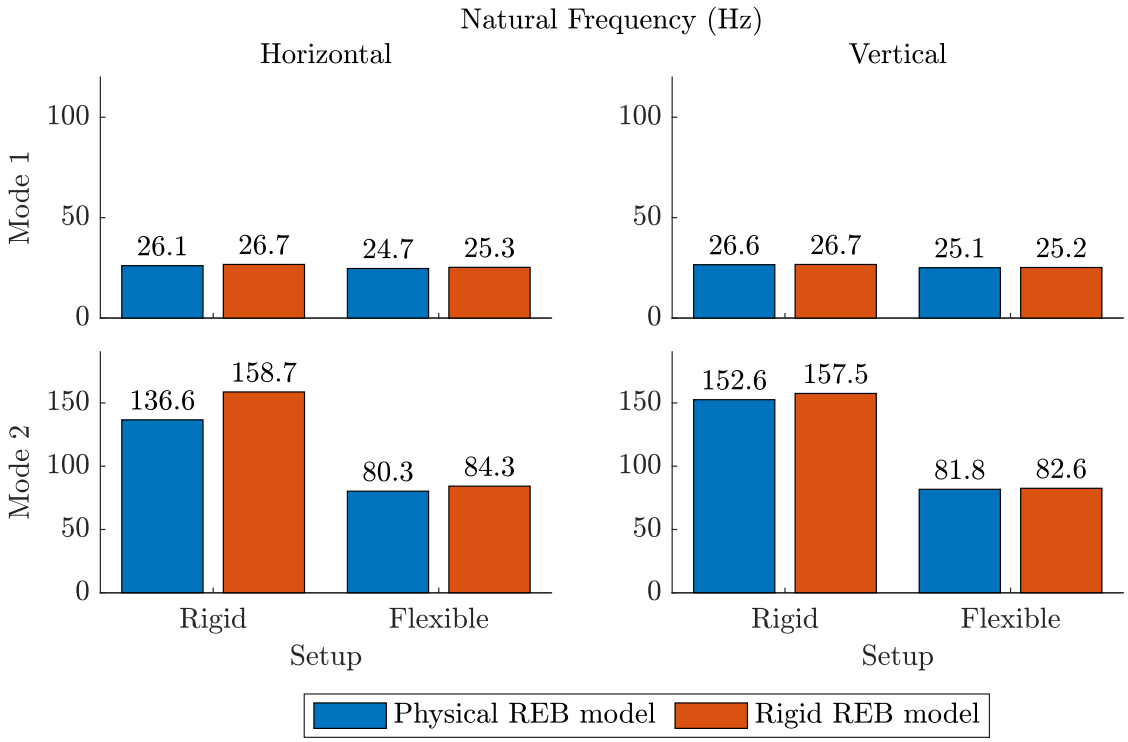
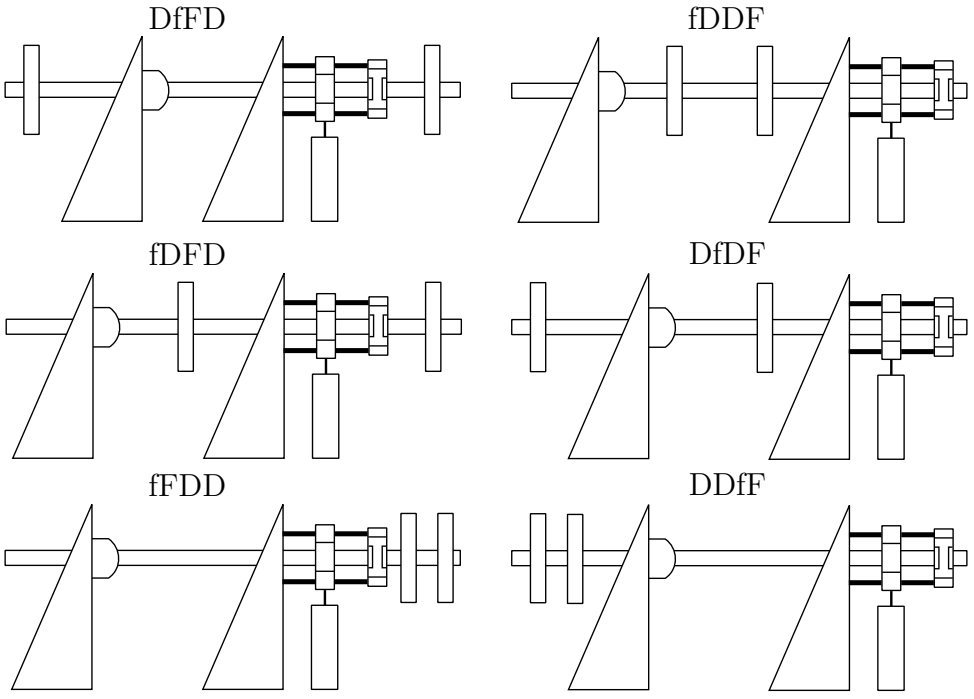


Figure 6.3: Comparison of natural frequencies with and without the rigid bearing approximation

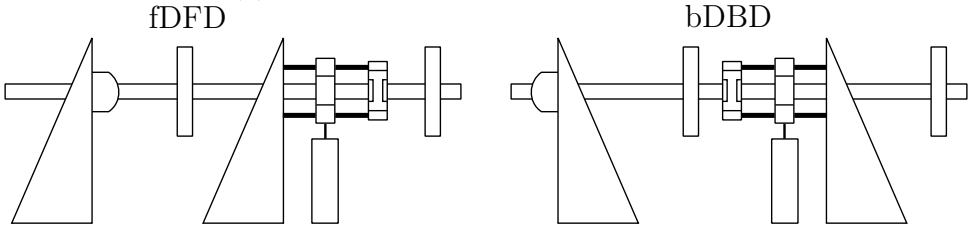
to perform modal analysis on each potential configuration. This is a computationally expensive operation, and therefore it was necessary to make some approximations to reduce the cost of the rig optimisation routine.

It was observed that the rolling-element bearings primarily introduce further asymmetry between the horizontal and vertical mode within each pair. However, whilst the frequency of the horizontal modes are lowered by the reduced horizontal bearing stiffness, the frequency of the vertical modes reduce only very slightly. This is because the bearings have a higher vertical stiffness due to the preload from the weight of the rotor. This means that the frequencies of the vertical modes can be approximated by modelling the self-aligning bearings as pin joints, which are radially rigid.

A comparison of the frequencies of the ARES rig using the physical bearing model and simplified rigid pin model is shown in Fig. 6.3. Although the horizontal modes are over-predicted by the rigid bearing model, the vertical modes are predicted much more accurately with an error of around 2 %. This model therefore yields an accurate upper bound on the natural frequencies of the rig, whilst being around 4× faster to evaluate, since no calls to the expensive physical bearing model are required. Even though this simplified model is not sufficient for an accurate forced analysis, it was sufficiently accurate to be used to impose constraints on the critical speeds and resonance frequencies, which will be discussed further in Section 6.2.4.



(a) Different order of discs and bearings



(b) Different bearing orientations

Figure 6.4: Potential ARES configurations

6.2.3 Rig configurations

The ARES test rig has been designed to be highly configurable, and therefore many parameters are required to uniquely define each possible setup. The axial position of both bearings can be varied, and the discs can be moved along the shaft using the TranTorque adaptors. In addition to this, each bearing support can be orientated to face forwards or rearwards. Some different configurations are depicted in Fig. 6.4. In total, there are 48 possible ways in which to configure the rig.

A naming convention was developed to refer to the different rig configurations. The discs were denoted by the letter D, the bearings were denoted by B or F, depending on whether the bearings face backwards (B) or forwards (F). The fixed bearing was denoted by an uppercase B or F, whilst the floating bearing was denoted by a lowercase b or f. The configuration was then identified by listing the components from most rearwards to the frontmost. The names of the configurations have been shown in Fig. 6.4.

In addition to the rotor and bearing configuration, the support configuration also had

to be specified. It was assumed that the rig would be run in both the rigid and flexible bearing configurations considered in Section 5.4. Therefore, for a given rotor setup, any constraints must be satisfied in *both* the rigid bearing and flexible bearing configurations. Note that when moving between the rigid and flexible configurations, the bearing housing is kept in the same location, and the L-shape, interface plate and PEAs are moved to accommodate the new bearing housing support bar length.

6.2.4 Constraints

The most complex part of optimising the setup was the specification of the different constraints, in order to ensure the resulting solution was safe to run and could be physically assembled. There were various geometric, structural and practical constraints, which will now be discussed in more detail.

6.2.4.1 Geometric constraints

The most obvious constraint on the rig configuration is that the components along the rotor must not clash with each other. There must be sufficient separation between them so that there is enough access to be able to assemble the rig. In addition, the components must keep within the bounds of the rotor and chamber. Using the bDBD configuration as an example, the rear bearing must remain a certain distance from the rear of the shaft to avoid clashing with the coupling. The rear disc must have sufficient separation from the two bearings so that there is access to its TranTorque adapter. The front disc must be sufficiently far from the front end of the shaft, to ensure it can be fixed tightly on the shaft. These constraints can be written mathematically as:

$$\begin{aligned} z_{\mathrm{B}}^{r} &> \Delta_1 \\ z_{\mathrm{D}}^{r} - z_{\mathrm{B}}^{r} &> \Delta_2 \\ z_{\mathrm{B}}^{f} - z_{\mathrm{D}}^{r} &> \Delta_3 \\ l_{\mathrm{S}} - z_{\mathrm{D}}^{f} &> \Delta_4 \end{aligned}$$

where z_{B}^{f} and z_{B}^{r} are the axial locations of the front and rear bearings, and z_{D}^{f} and z_{D}^{r} are the locations of the discs. These geometric constraints are depicted in Fig. 6.5. The values of the various axial separation distances Δ are listed in Table 6.1.

There are some additional constraints which depend on the bearing housing configuration, due to the dependence on the L-shape position z_{L}. The front disc must be sufficiently far in front of the front L-shape so that there is enough space for the stands for the

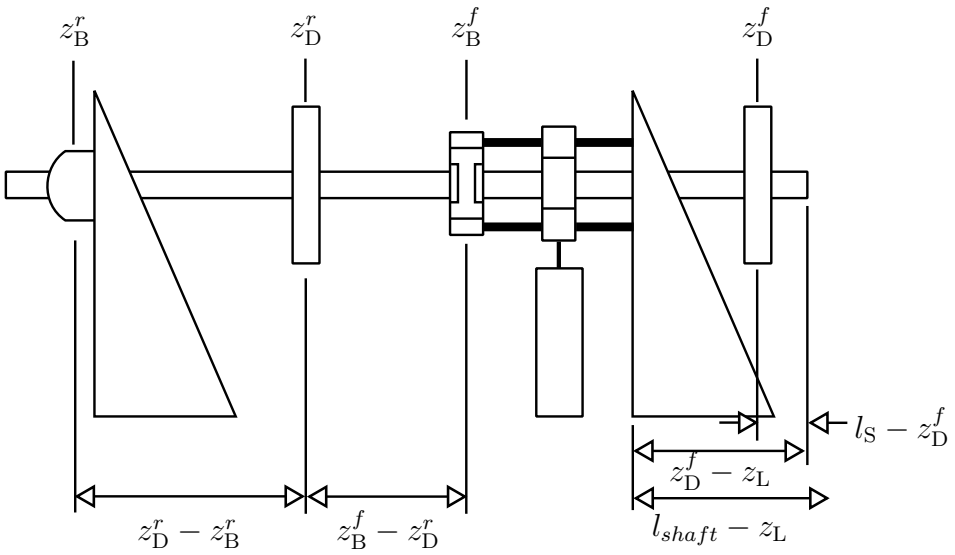


Figure 6.5: Degrees of freedom and geometric constraints in bDBD configuration

laser displacement sensors. In addition, the front L-shape must be sufficiently rearward so that it keeps within the bound of the chamber. These constraints can be written mathematically as:

$$z_{\mathrm{D}}^{f} - z_{\mathrm{L}} > \Delta_5 \tag{6.1}$$

$$l_{\mathrm{S}} - z_{\mathrm{L}} > \Delta_6 \tag{6.2}$$

where the axial location of the front L-shape z_{L} is given by:

$$z_{\mathrm{L}} = z_{\mathrm{B}}^{f} + l_{\mathrm{BH}} + l_{\mathrm{IP}}$$

The values of the separation distances Δ_5 and Δ_6 are also listed in Table 6.1. The complete set of constraints can be written more succinctly in vector form:

$$\begin{bmatrix} -1 & 0 & 0 & 0 \\ 1 & -1 & 0 & 0 \\ 0 & 1 & -1 & 0 \\ 0 & 0 & 0 & 1 \\ 0 & 0 & 1 & -1 \\ 0 & 0 & 1 & 0 \end{bmatrix} \begin{bmatrix} z_{\mathrm{B}}^{r} \\ z_{\mathrm{D}}^{r} \\ z_{\mathrm{B}}^{f} \\ z_{\mathrm{D}}^{f} \end{bmatrix} < \begin{bmatrix} -\Delta_1 \\ -\Delta_2 \\ -\Delta_3 \\ l_{\mathrm{S}} - \Delta_4 \\ -\Delta_5 - (l_{\mathrm{BH}} + l_{\mathrm{IP}}) \\ l_{\mathrm{S}} - \Delta_6 - (l_{\mathrm{BH}} + l_{\mathrm{IP}}) \end{bmatrix} \tag{6.3}$$

These equations are linear in the axial disc positions z_{D} and bearing positions z_{B}. For a different rig configuration, there will be a slightly different set of constraints, due to the different ordering of the components. However, another very similar set of equations can be derived.

Table 6.1: Component separation distances in linear geometric constraints

Parameter	Components being separated		Value (mm)
Δ_1	Rear bearing	End of shaft	63.5
Δ_2	Rear disc	Rear bearing support	81.5
Δ_3	Rear disc	Front bearing	55.0
Δ_4	Front disc	End of shaft	25.0
Δ_5	Front disc	Front bearing support	13.9
Δ_6	Front bearing support	Edge of chamber	15.0

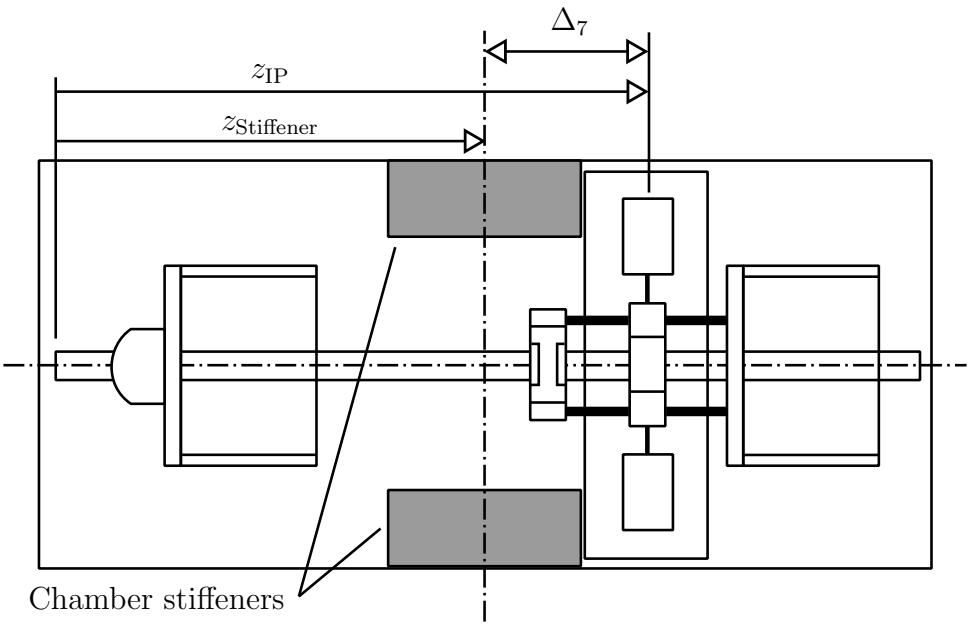


Figure 6.6: Non-linear geometric constraints due to chamber stiffeners

6.2.4.2 Chamber stiffeners

There were further constraints on the position of the fixed bearing, due to the vertical stiffeners within the chamber. These restricted the range of possible locations of the PEAs and, in turn, the fixed bearing. This is depicted in Fig. 6.6, again using the bDBD configuration in Fig. 6.5 as an example. This constraint can be written mathematically in the following form:

$$|z_{\text{IP}} - z_{\text{Stiffener}}| > \Delta_7 \tag{6.4}$$

where z_{IP} denotes the centre of interface plate and is given by:

$$z_{\text{IP}} = z_{\text{B}}^{f} + l_{\text{BH}}$$

where the constants $z_{\text{Stiffener}}$ and Δ_7 are listed in Table 6.2. This constraint is a non-linear

Table 6.2: Chamber stiffener geometric constraint parameters

Parameter	Description	Value (mm)
$z_{\text{Stiffener}}$	Stiffener position	627.5
Δ_7	Separation distance	26

function of the design variables due to the absolute operation.

6.2.4.3 Resonance frequencies

In order to be able to excite the first pair of modes with an unbalance, it was necessary to constrain the first critical speed $\Omega_{1,V}^{\text{crit}}$ to be within the running range of the motor. For safety reasons, and to reduce the ramp up time, it was decided that the first pair of critical speeds should be in the lower half of the running range, which can be written as:

$$\Omega_{1,V}^{\text{crit}} < 50\,\text{Hz} \tag{6.5}$$

which constrains the critical speed where the vertical mode is excited to be within the specified range. Note that since the horizontal mode within each pair of modes is always lower in frequency due to the asymmetry from the bearing support, it was not necessary to also constrain the horizontal mode.

The second pair of modes were to be excited with the PEAs only, and were therefore able to exceed 100 Hz. A loose constraint was imposed on the second pair of critical speeds, to ensure that it remains well below the natural frequency of the rigid bearing support at around 300 Hz, which could otherwise lead to a lot of unwanted L-shape motion. Assuming the damping is small, this can be expressed in terms of a constraint on the natural frequency of the second mode, denoted by $\omega_{2,V}^{\text{nat}}$:

$$\omega_{2,V}^{\text{nat}} < 150\,\text{Hz} \tag{6.6}$$

Note that, for simplicity, this constraint was placed on the natural frequency of the rotor when stationary (ie $\Omega = 0\,\text{Hz}$). However, if the rig is excited with the PEAs at a higher rotor speed, the resonance frequency may slightly exceed 150 Hz, due to the stiffening effect from gyroscopic loads. As with the constraint on the critical speed, this constraint was also only applied to the vertical mode, since the horizontal mode is always lower than this due to the asymmetry in the system.

It was only necessary to impose the constraints on the critical speed and natural frequencies with the bearing support in the rigid configuration. This is because the critical

speeds and natural frequencies will always reduce when the extra support flexibility is added.

6.2.4.4 Shaft stresses

The most likely mode of failure in the rotor is high-cycle fatigue of the shaft. To mitigate this, the maximum shaft stress was computed at the resonances. The bending stress is maximum on the outer edge of the shaft, and can be calculated from the resultant bending moment τ at a given node:

$$\sigma_{\mathrm{S}} = \frac{\tau r_o}{I_{rr}} \tag{6.7}$$

where r_o is outer radius of the shaft, and I_{rr} is second moment of area of the shaft cross-section. The maximum stress was then constrained to remain within the high-cycle fatigue (HCF) limit for the shaft:

$$\max_z |\sigma_{\mathrm{S}}(z)| < \sigma_{\mathrm{HCF}} \tag{6.8}$$

where the HCF stress was $\sigma_{\mathrm{HCF}} = 240\,\mathrm{MPa}$ for AISI 304 stainless steel. Since this is well below the ultimate tensile strength of $\sigma_{\mathrm{UTS}} = 505\,\mathrm{MPa}$, this also ensures the shaft should not fail.

6.2.4.5 Coupling deflections

The coupling which connects the rotor to the motor shaft can only accommodate certain levels of radial and rotational misalignment. The manufacturer specifies maximum allowable values, which are listed in Table 6.3.

Table 6.3: Maximum allowable misalignments for BKH/60/93/30/35 coupling

Parameter	Description	Value
$\theta_{\mathrm{C}}^{\mathrm{rated}}$	Maximum rotational misalignment	1.5°
$\delta_{\mathrm{C}}^{\mathrm{rated}}$	Maximum radial misalignment	0.25 mm

The values in Table 6.3 apply for continued operation, but can be exceeded by 50 % for brief overloads according to the manufacturer. Since the maximum coupling deflection will occur as the rig passes quickly through resonance, it is appropriate to treat this as a brief overload, and therefore it is allowable for the rig to slightly exceed the rated limits:

$$|\theta_{\mathrm{C}}| < 1.5\,\theta_{\mathrm{C}}^{\mathrm{rated}} \tag{6.9}$$

$$|\delta_{\mathrm{C}}| < 1.5\,\delta_{\mathrm{C}}^{\mathrm{rated}} \tag{6.10}$$

where the constraints were imposed on the coupling deflection at the resonances.

6.2.5 Objectives

It was demonstrated in Chapter 4 that the non-linearity in the bearings increases with the applied load. Therefore, in order to maximise the fixed bearing non-linearity, the dynamic load on the fixed bearing at resonance was to be maximised. Conversely, the dynamic load on the floating bearing was to be minimised, so it would be more likely to remain in the linear regime. These two objectives can be encapsulated in the following dynamic load ratio:

$$r_{\mathrm{B}} = \frac{f_{\mathrm{B}}^{r}}{f_{\mathrm{B}}^{f}} \tag{6.11}$$

where f_{B}^{f} and f_{B}^{r} are the loads on the front and rear bearings respectively. At resonance, the rotor response will closely resemble the mode shape of the mode being excited, since the system was assumed linear for this analysis. Although magnitude of the bearing loads will depend on the method of excitation, as well as the level of damping, the load *ratio* is purely a property of the mode.

This objective was computed at the first critical speed of the rotor, and second resonance due to PEA excitation. Both of these objectives were to be minimised, yielding a multi-objective problem.

6.2.6 Method of solution

Once that the constraints and objectives had been defined, it was necessary to express these in a form which can be passed to an optimiser. This required the design variables to be defined, and the constraints to be split into linear and non-linear constraints.

6.2.6.1 Genetic algorithm

This problem for finding the optimal setup is likely to have many local minima due to the many constraints, so it necessary to use a global optimisation method. Since no analytical expression for the Jacobian was available, gradient-based approaches like interior-point

algorithms will be very slow. Instead, as with the rotor and support parameter identification procedures in Sections 5.3.4 and 5.4.4, a genetic algorithm (GA) was chosen. This is a gradient-free method for finding global minima, and is parallelisable so is fast to run. The genetic algorithm interface `gamultiobj` in MATLAB was used, which solves for the Pareto front for problems with multiple objectives.

6.2.6.2 Mathematical representation

The position of the two discs and bearings were chosen as design variables, as depicted in Fig. 6.5. The vector of design variables is given by:

$$\boldsymbol{z} = \begin{bmatrix} z_{\mathrm{B}}^{r} & z_{\mathrm{D}}^{r} & z_{\mathrm{B}}^{f} & z_{\mathrm{D}}^{f} \end{bmatrix}^{T} \tag{6.12}$$

Although it would have been possible to optimise the rig setup whilst considering all possible configurations (order of discs/bearing and orientation of supports), this would have increased the complexity of the problem. The number of geometric constraints would be large, since every disc and bearing would have to be prevented from clashing with all of the rest, because it cannot be known a priori which components will be adjacent to each other. In addition, all of the geometric constraints would then be non-linear functions of the design variables, which can only be written in the following generic form:

$$f\left(\boldsymbol{z}\right) < 0 \tag{6.13}$$

Since the genetic algorithm cannot enforce that the population satisfies the non-linear constraints, it must explore many infeasible solutions, which therefore slow the rate of convergence. Instead, the type of configuration (eg. bDBD or bFDD) was fixed by the user before calling the optimiser. This reduces the number of active geometric constraints considerably since only adjacent discs and bearings need to be considered. This also allows the geometric constraints to be expressed as linear functions of the design variables. This means the GA is able to restrict the search to solutions which meet the geometric constraints, which increases rate of convergence. Substituting the vector of design variables in Eq. (6.12) into Eq. (6.3) allows the geometric constraints to be written more succinctly as:

$$\boldsymbol{A}\boldsymbol{z} < \boldsymbol{b} \tag{6.14}$$

which are a set of *linear* inequality constraints. The only drawback is that the user must find the most promising configuration manually, by running the setup optimiser for each type of configuration, and then comparing the solutions.

Even with this choice of design variables, the constraints on the critical speeds, shaft stresses and so on, can only be expressed as *non-linear* constraints as in Eq. (6.13). In addition, the objective also remains a non-linear function. However, it was found that the GA was able to reliably find optimal solutions which satisfies the non-linear constraints, now that it could restrict its solution space to geometrically feasible configurations. The optimisation problem was now ready to be solved by the GA, to find the best rig configuration.

6.2.7 Optimal setup

The proposed setup optimisation algorithm was run for a variety of configurations, and it became clear very quickly that the rated limits on the coupling deflection were the most restrictive constraints. Therefore the optimiser chose to move the rear bearing as rearwards as possible, in all configurations, in order to minimise the shaft deflection at the location of the coupling. The coupling deflection can be further minimised by ensuring that the bearing is the most rearwards component on the shaft, and mounting the floating bearing support facing rearwards. The search therefore focused on configurations of the form bXXX. This left three promising types of solution; one with the two discs between the two bearings (bDDB or bDDF), placing the discs either side of the fixed bearing (bDBD or bDFD) or placing the discs in front of the fixed bearing (bBDD or bFDD).

The Pareto front of solutions for each of these 6 types of configuration is shown in Fig. 6.7; the solution with the lowest $\mathcal{L}_2$-norm are denoted with a cross. It can be observed immediately that the bDBD and bFDD have by far the best performance with the smallest rear-to-front load ratios. These two configurations were selected for further consideration, and the other configurations were immediately disregarded. The bDBD configuration has a slightly lower load ratio in mode 2, whereas bFDD has a slightly lower load ratio in mode 1.

The mode shapes in each of the two most optimal configurations are shown in Fig. 6.8. It can be observed that in the bDBD configuration, the two discs move out of phase with each other whereas in the bFDD configuration, they always move in phase with each other. In addition, the discs are much closer together in the bFDD configuration, so that they almost behave as one single disc. However, the most significant difference is that the second mode is more sensitive to the bearing support compliance in the bDBD configuration, where more bearing motion is observed. On the other hand, the second mode in the bFDD configuration is much less sensitive to the level of support compliance.

The first critical speeds and second natural frequencies in these two configurations are shown in Fig. 6.9a. It can be observed that the first critical speed in the bDBD configuration is much lower than in the bFDD configuration. This has practical benefits,

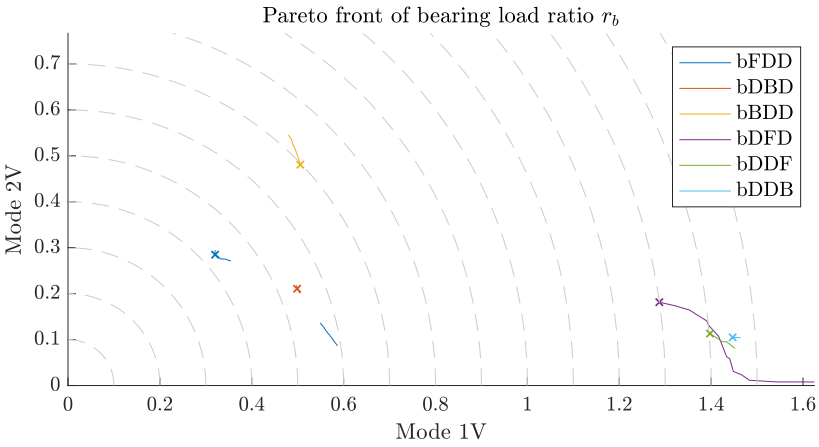
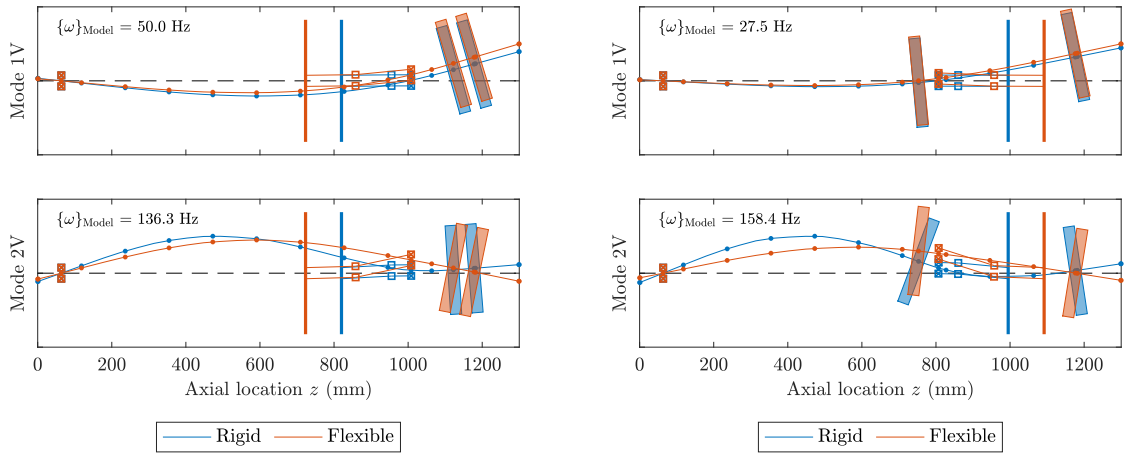


Figure 6.7: Bearing load ratios for different rig configurations



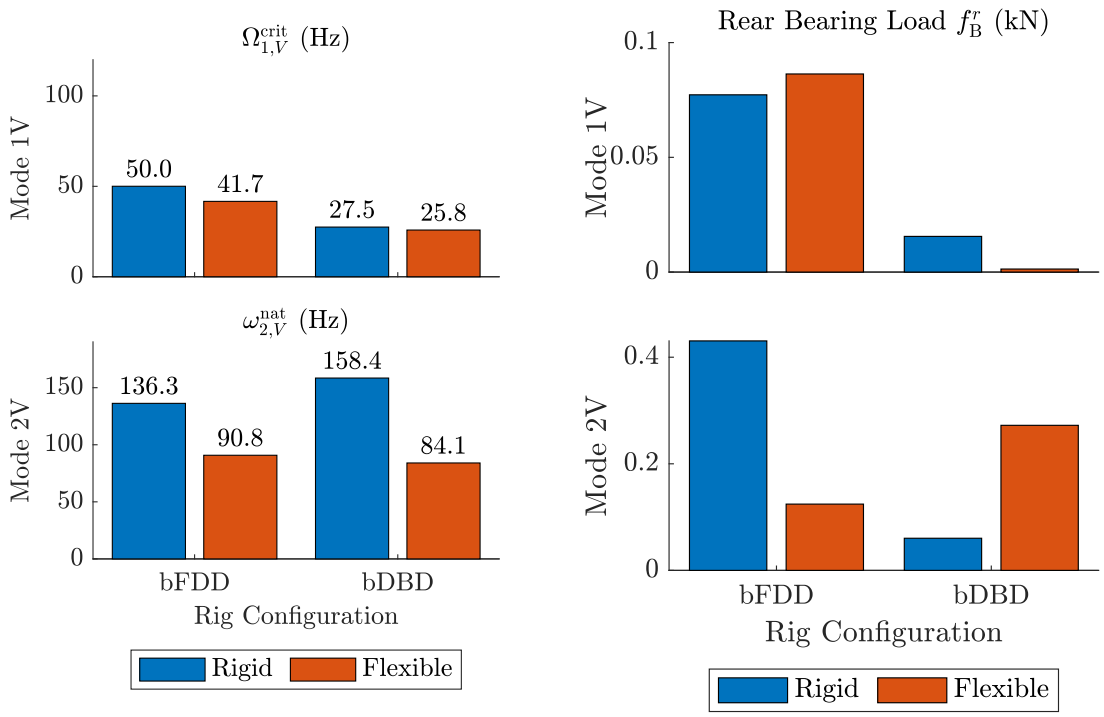
(a) bFDD configuration

(b) bDBD configuration

Figure 6.8: Mode shapes for different rig configurations (V denotes vertical mode)

since it reduces the ramp up time, which is important when balancing the rotor. The frequency of the second mode is much more sensitive to the support flexibility in the bDBD configuration than in the bFDD configuration, which agrees with larger change in mode shape observed in Fig. 6.8. In the bDBD configuration, the frequency drops by 74 Hz when moving from the rigid to flexible configurations, whereas in the bFDD configuration, it only drops by 45 Hz. The bearing loads on the floating bearing at resonance have been plotted in Fig. 6.9b. It can be seen that the floating bearing is much more lightly loaded in the bDBD configuration than the bFDD configuration, which should significantly reduce the influence of its non-linearities.

After analysing the results, the bDBD configuration was chosen over the bFDD configuration. This was primarily for practical reasons; both the lower first critical speed, and larger separation between the discs should make it easier to balance the rotor. The re-



(a) Critical speeds and natural frequencies

(b) Floating bearing loads

Figure 6.9: Performance metric for different rig configurations

duced load on the floating bearing should increase the likelihood that it will operate in the linear regime, so that it is more likely any observed non-linearity can be attributed to the fixed bearing as desired. The position of the components in the chosen configuration are listed in Table 6.4.

Table 6.4: Position of components in chosen rig configuration (bDBD)

Component	Symbol	Axial location (mm)
Floating bearing	z_{B}^{r}	64
Fixed bearing	z_{B}^{f}	807
Rear disc	z_{D}^{r}	738
Fronts disc	z_{D}^{f}	1176

6.2.8 Summary

The configuration of the ARES test rig has been optimised so as to maximise the influence of the fixed bearing whilst minimising the influence of the floating bearing. It was ensured that the resulting solution was physically realisable and safe to run, by imposing suitable geometric constraints on the position of the bearing and discs, and limits on the maximum shaft stress and coupling deflection. In addition, the first pair of critical speeds were

constrained to remain within the running range of the motor, so that they could be excited with unbalance. This setup will now be analysed in more detail.

6.3 Prediction of frequency response using HBM

Now that the ARES setup had been chosen, it was necessary to couple the HBM approach from Section 4.3 with the ROLADYN model, in order to compute the non-linear forced response. Firstly, this will allow the influence of the floating bearing to be investigated, to confirm whether the effect of its non-linearity on the rotor response has indeed been minimised by the setup optimisation procedure in Section 6.2. In addition, this will eventually allow the results from the model to be compared with the measured forced response from experiments. However, it was necessary to reselect some of the HBM parameters for analysis of the ARES rig.

6.3.1 Ball pass frequencies

The ball pass frequencies of both the front and rear bearings were first computed using the expression Eq. (3.96), assuming outer-raceway control. Knowledge of the BPF allows the spectrum of the rig response to be better interpreted. The computed values are tabulated in Table 6.5. The cage speed ratios were evaluated in the setup position using Eq. (3.83), as explained in Section 3.2.6.1.

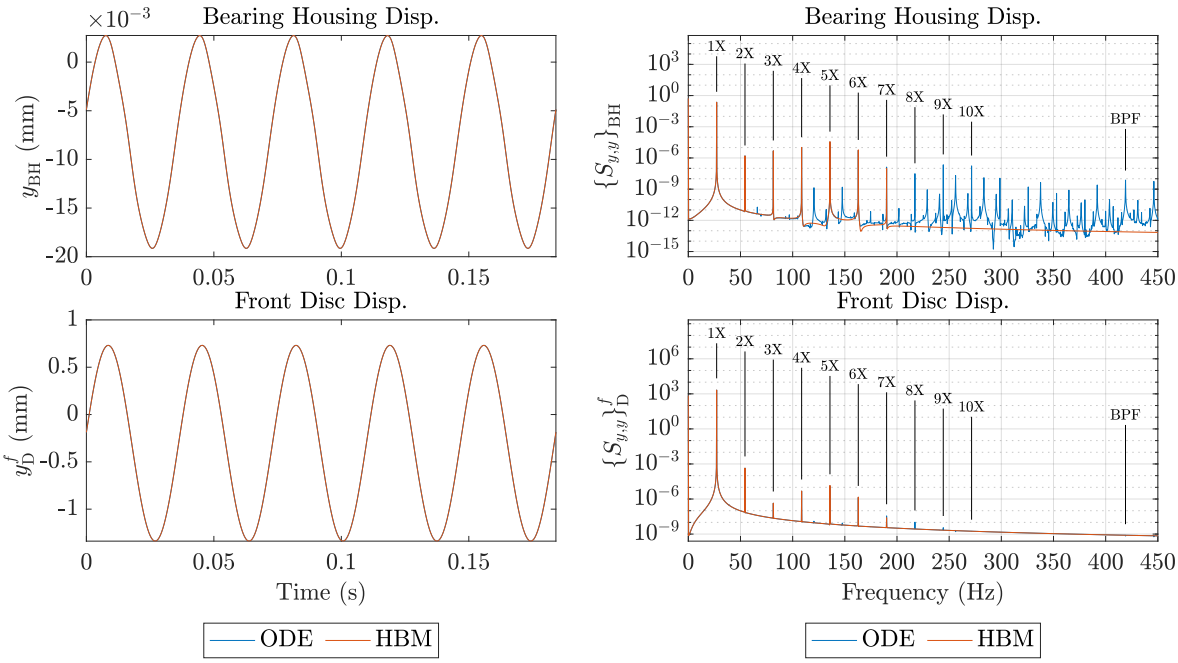
Table 6.5: ARES ball pass frequencies

Bearing	Type	BPF
Fixed	SKF 2208	15.433Ω
Floating	SKF 1208	15.416Ω

It can be observed that the BPF of the two bearings are nearly identical. This is because the bearings have the same number of elements, and a very similar geometry. They are so close that it would be expected that only a single peak at around 15.4Ω would be observed in the spectrum of the response, due to the finite frequency resolution. It can also be observed that the order of the BPF excitation is very high, and will therefore excite the modes of the rig at very low rotor speeds.

6.3.2 Determination of number of harmonics

In order to be able to apply HBM, it first was necessary to define which harmonics to include. If too few harmonics were included, the accuracy of the solution would be poor,



(a) Time response

(b) Spectrum

Figure 6.10: Response of the ARES rig for $m_{\mathrm{UB}} = 2.1\,\mathrm{g}$ at resonance ($\Omega = 27.25\,\mathrm{Hz}$)

but if too many were included, this would increase the simulation time. The ROLADYN model was set up in the optimal bDBD configuration listed in Table 6.4, with the rigid bearing housing configuration. The response of the rotor at the first critical speed was first computed using time integration with `ode15s`. An unbalance mass of 2.1 g was applied on the front disc, which was the maximum allowable level of unbalance and should therefore be the most non-linear case. The resulting bearing housing and front disc displacement at resonance are shown in Fig. 6.10a. The spectra of the responses was then found using the function `periodogram` in MATLAB and a Hanning window, which is shown in Fig. 6.10b.

It can be observed that for both the disc and bearing housing, nearly all of the energy is within the first harmonic of the rotor speed. For the bearing housing, there are contributions from the higher harmonics, which is due to the slightly non-sinusoidal nature of the time response. However, these higher order harmonics have an increasingly small contribution. There is some content in the front disc response up to the 7th harmonic, although the higher harmonics are much less significant than for the bearing housing, since this is physically further from the non-linear bearing, and the response is linearised by the rotor compliance. It can be concluded from these spectra that a reasonably accurate solution could be obtained using HBM with only the first harmonic of the fundamental, since this captures nearly all of the signal power. However, it was decided that the first 7 harmonics should be included to slightly improve the accuracy, since this captures the most significant harmonics in the bearing housing response.

Table 6.6: Harmonic balance parameters for the ARES rig

Symbol	Description	Value
M^H	No. of harmonics in Ω	7
M^T	No. of time points	64

The component at the BPF in both the disc and bearing housing response is negligible, demonstrating that variable compliance is insignificant in this regime, which explains why the response appears to be periodic. Therefore, it can be concluded that it is not necessary to include harmonics of the BPF within the HBM problem, which is quite unlike the Jeffcott rotor system considered in Section 4.3. This means that GHBM is no longer necessary, and standard HBM can be used to solve for the periodic response, which reduces the computational cost considerably.

In order to validate the application of HBM to the ARES rig, the periodic response for the same case as in Fig. 6.10 was computed using standard HBM. The rotor speed was chosen as the base frequency, and 7 harmonics were included. The number of discrete time points was set very high at 64, to guarantee aliasing should not occur. These values are listed in Table 6.6. The resulting time histories and spectra are overlaid with the solution from time-integration on Fig. 6.10. It can be observed that the solution from HBM matches the ODE solution very accurately. It was found that the inclusion of the additional harmonics increased the computation time only very slightly, likely because their contribution is small.

6.3.3 Computation of frequency response using HarmLAB

In order to construct the complete non-linear frequency response function, the HarmLAB toolbox from Section 3.3 was used. Since some of the nodes in the model move considerably more (eg. front disc) than others (eg. interface plate), so the DOF were normalised so that they had the same order of magnitude, which ensured the steps taken by the predictor-corrector algorithm were not too large. Note that in this case, since standard HBM was used, it was not necessary to adjust the base frequencies before applying Hill's method to assess the stability.

6.3.4 Influence of the floating bearing

In order to verify that the optimisation procedure had indeed minimised the influence of the floating bearing, the non-linear frequency response to a front disc unbalance was computed using HBM. The floating bearing was represented with 3 different models:

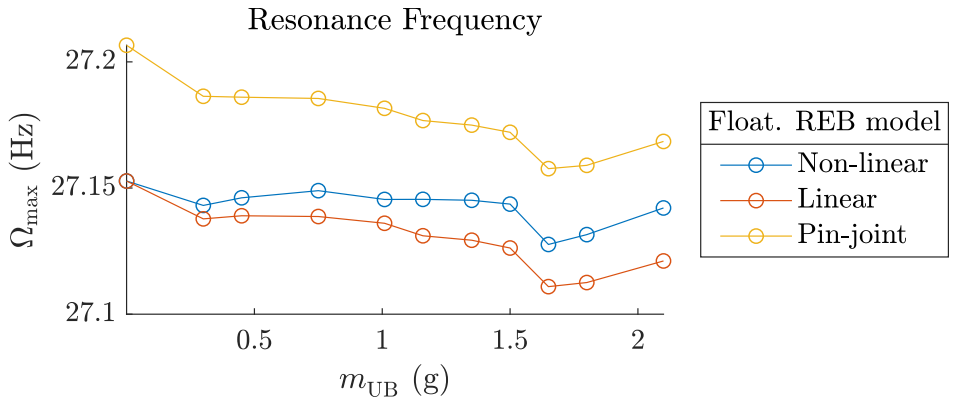


Figure 6.11: Backbone curve for different floating bearing models

- *Non-linear model:* The bearing is modelled using the quasi-static bearing model in Section 3.2, which inherently captures the non-linearities from clearance and the Hertzian contacts.

- *Linear model:* The quasi-static bearing model is linearised about the rotor equilibrium position, and these linear properties are then assumed constant.

- *Pin-joint model:* The bearing is assumed radially rigid, and can therefore be modelled as pin joint. This eliminates the two constraint DOF associated with the floating bearing from the model.

The response to a front disc unbalance was computed for a range of unbalance masses at the critical speed corresponding to the first FW mode. The resonance frequency can then be plotted against unbalance mass to yield the backbone curve, which has been in Fig. 6.11 for all three floating bearing models. If the system were linear, the resonance frequency would be independent of amplitude. However, it can be observed that the resonance frequency initially drops as the unbalance mass is increased, due to internal bearing clearance, before increasing due to the stiffening behaviour of the Hertzian contacts.

It is also possible to attribute most of the non-linearity to the front bearing, since the behaviour is nearly identical, even if the floating bearing is linearised. Moreover, the floating bearing also has a minimal influence on the dynamics of the underlying linear system, since there is only a small shift in frequency when the floating bearing is modelled as a rigid pin-joint. From these results, it can be concluded that firstly, the optimisation routine has successfully minimised the influence of the floating bearing. This means that any non-linearity can be attributed to the fixed bearing. In addition, the floating bearing can be modelled as a pin-joint with only a small loss of accuracy. This reduces the number of DOF by 2, and avoids evaluation of the quasi-static bearing model for the floating bearing, thereby reducing the computational load.

6.3.5 Summary

An appropriate set of harmonics has been chosen in order to accurately predict the response of the rig using HBM, and the results have been validated against the results from time-integration. It was demonstrated that the setup chosen in Section 6.2 has indeed minimised the influence of the floating bearing, so much so that it can be modelled as a pin-joint with minimal loss of accuracy. The floating bearing will now be modelled as a pin-joint for the remainder of this chapter. Experimental testing on the chosen ARES setup can now begin.

6.4 Hammer tests

The first type of experimental testing carried out on ARES were hammer tests, with the rotor non-rotating. This allowed the complete ROLADYN model to be validated, as well as the remaining unknown parameters to be identified. The test procedure will now be explained in more detail.

6.4.1 Test procedure

Hammer tests were carried out on the assembled rig in a very similar way to the rotor hammer tests. A roving hammer test was then carried out, with impact locations on the shaft and discs, as well as additional axial impacts on the discs when fitted. An accelerometer was mounted at the front end of the shaft, since there was a lot of motion here in all of the modes of interest. However, some additional impact locations were included on the bearing housing and interface plate, so that the effect of the bearing support structure could be observed. Unlike the rotor which was axisymmetric, the rig was expected to be asymmetric, so there were impact locations and an accelerometer in both the horizontal and vertical planes. The same acquisition settings as the rotor hammer tests in Section 5.3 were used, and the modal parameters were identified using the ModeLAB toolbox. The hammer test setup is depicted in Fig. 6.12.

The ARES rig was gradually assembled in the configuration found from the setup optimisation procedure in Section 6.2. The bearings were first installed in desired locations. The front bearing support was set up in the rigid configuration, with short rods between the interface plate and bearing housing. The rotor was then installed *without* any discs. The fixed bearing adapter sleeve was tightened by the same 45° angle used on BELOS in Section 5.2. From this initial configuration, the rig was then assembled in stages with hammer tests carried out in each configuration, to validate all parts of the model. The

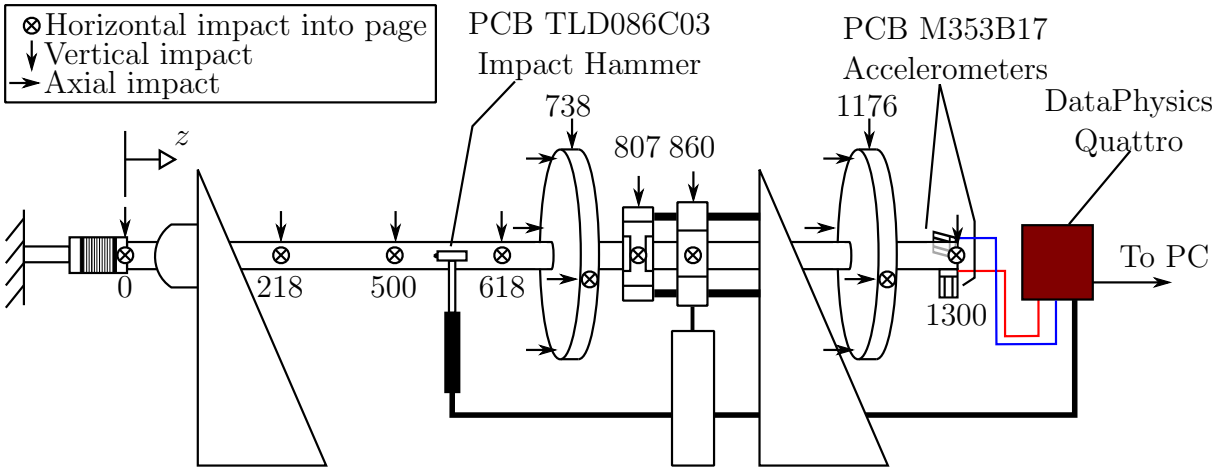
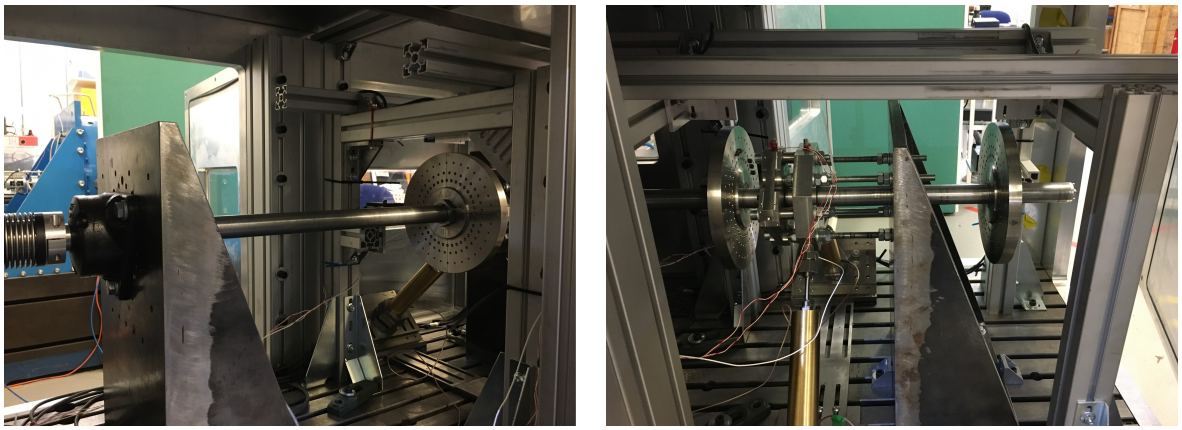


Figure 6.12: Experimental setup for hammer tests on fully assembled ARES test rig



(a) Rear floating bearing (b) Front fixed bearing

Figure 6.13: ARES test rig configured in optimised bDBD setup

final rig configuration with the PEAs, ancillaries and discs fitted is shown in Fig. 6.13. The different stages of assembly will now be briefly outlined.

6.4.1.1 Installation of PEAs

The first tests were carried out with only the shaft mounted on the bearings. Tests were then carried out with both the PEAs disconnected (in the "free" configuration), and then connected (in the "fixed" configuration). Since no discs were fitted, the rotor frequency was closer to that of the bearing support structure, so this highlights any deficiencies in the bearing support model. It was found that in the "free" configuration, the support properties have a large influence on both the first and second pairs of modes. Once the very stiff PEAs are fitted, the first pair of modes become insensitive to the bearing support parameters. However, the second pair of modes is still affected by the bearing support.

6.4.1.2 Installation of ancillary components

The next stage of assembly was to install the coupling and encoder, to verify that these have minimal influence on the modal properties. Since only the shaft was fitted, this amplified the effect of any additional inertia and damping added by these components, which could otherwise be masked by the much larger disc inertia, and significant damping from the disc roots. It was found that the coupling had a negligible effect on the both the frequencies and damping in the system, which is desirable behaviour. Similarly, the encoder led to a very small drop in the natural frequencies of the system. However, the encoder was found to introduce a significant amount of damping into the system.

6.4.1.3 Installation of rotor discs

Since the rotor was the most well understood sub-system from the previous rotor hammer testing, the balancing discs were the last components to be installed. The front disc was installed first, followed by the rear disc. The discs were found to have by far the largest influence on the frequencies of the rig.

6.4.2 Results

For sake of brevity, only the modes from the final stage of assembly will be presented here, when the discs were added. The modal properties are shown in Figs. 6.14 and 6.16, and the mode shapes for the two disc case are depicted in Fig. 6.15. For the complete set of hammer test results from each stage of rig assembly, please refer to Appendix B.3.

The natural frequencies have been plotted in Fig. 6.14, and it can be seen that the first pair of modes drop substantially in frequency as the front disc is fitted, but they then drop only very slightly as the rear disc is fitted. This is because the front disc deflects much further in the first pair of modes, whilst the rear disc is near a nodal point, as depicted in Fig. 6.15. However, the addition of the rear disc reduces the frequency of the second pair of modes quite significantly, since the rear disc is no longer near a nodal point in these higher order modes.

The gap between the horizontal and vertical natural frequencies in the second pair of modes is much larger than in the first pair of modes. This is because the bearing support structure has more influence on the second pair of modes, which introduces asymmetry into the system. Interestingly, the gap between the horizontal and vertical modes reduces from 17 Hz in the shaft only configuration to 6.2 Hz once the front disc is fitted, but then increases to 10.4 Hz once the rear disc is fitted. This is due to the influence of the discs on the mode shapes. As the front disc is fitted, the motion is localised to the section of shaft

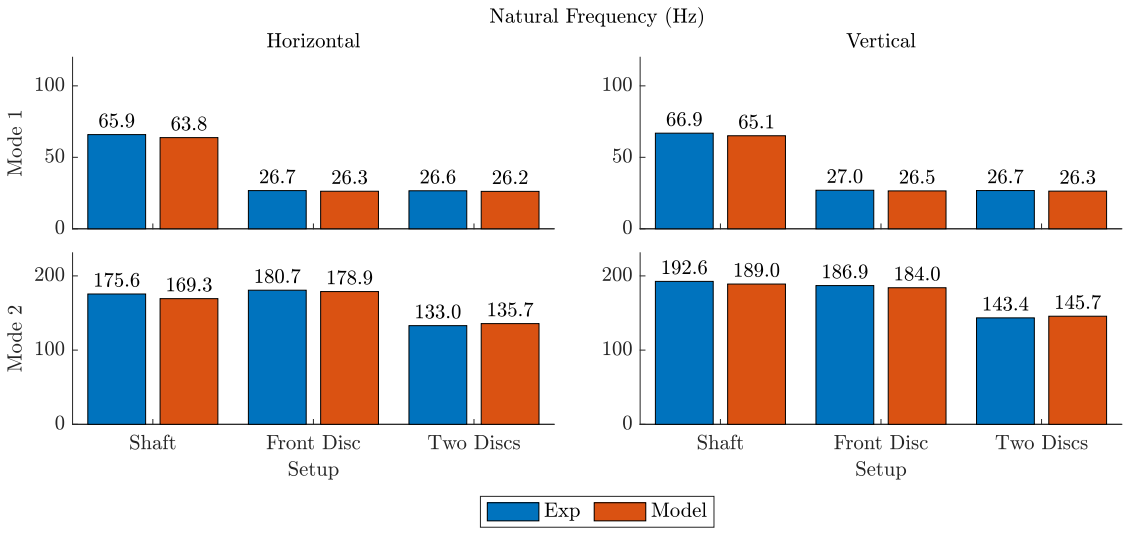


Figure 6.14: Comparison of the experimental and numerical natural frequencies of the assembled ARES rig

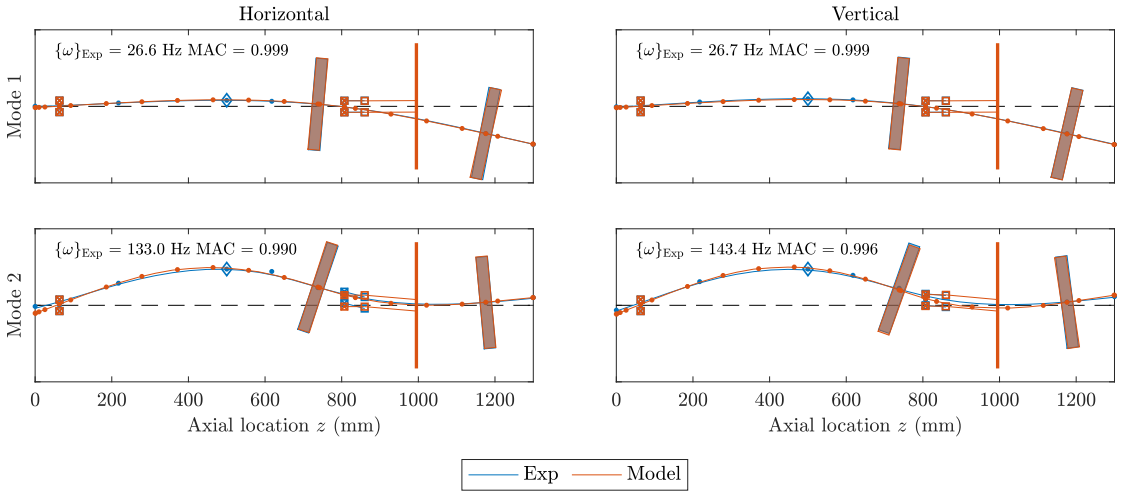


Figure 6.15: Comparison of the experimental and numerical modal properties of the ARES rig

between the bearings in the second pair of modes, so the bearing support has reduced influence. However, the rear disc counteracts this effect, so that the shape of the second pair of modes looks much more similar to the shaft only case, as shown in Fig. B.10.

The corresponding damping ratios are shown in Fig. 6.16. It can be observed that there is a general trend for the damping ratio to reduce as more discs are added. This suggests that the dominant source of damping does not originate from the discs, and remains constant. However, since the discs also increase the inertia in the system, this means that the damping ratio reduces.

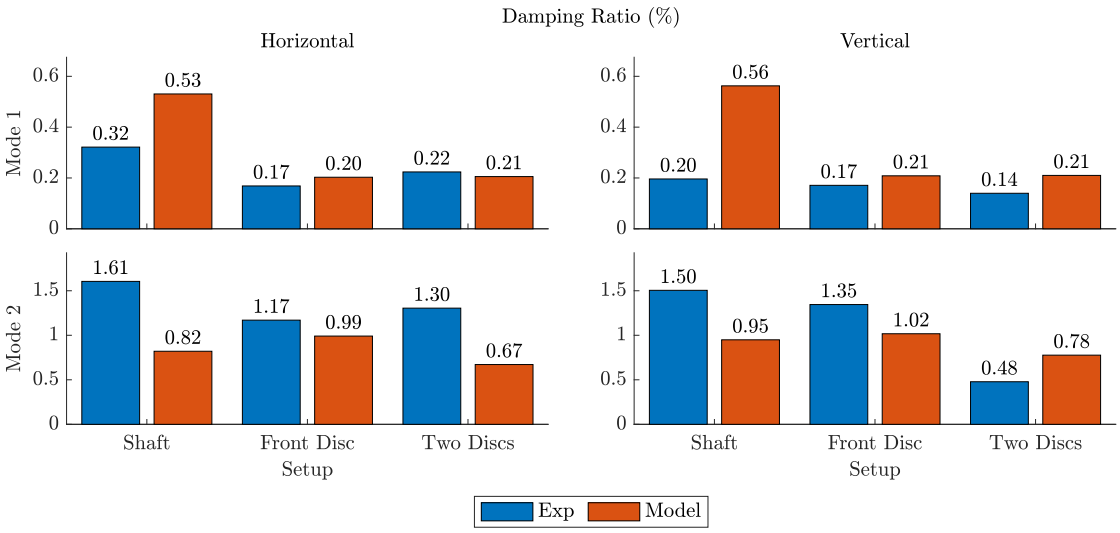


Figure 6.16: Comparison of the experimental and numerical damping ratios of the assembled ARES rig

6.4.3 Parameter identification

As with the rotor hammer testing in Section 5.3.3, these hammer tests were used to update the ROLADYN model. All of the relevant elastic and inertial parameter were identified from component tests in Chapter 5, and it was found that no further tuning of these parameters was required. However, significantly higher damping levels were observed in the experimental tests on the full assembly, than predicted by the ROLADYN model parameterised by component-level testing. This was believed to be due to a damping contribution from the bearings and ancillaries, which could not be determined from the previous component-level tests. Therefore, these damping parameters were identified from the hammer test data from the fully assembled rig. The same approach as in Section 5.3.4 was used, whereby the parameters were tuned to minimise the least-squares relative error in the predicted damping ratios from the various configurations. The damping models for each component will now be described.

6.4.3.1 Bearing damping

It was assumed that the joints between the outer ring of each bearing and their housing, and between the inner ring and shaft, were sufficiently rigid so as not to introduce any frictional losses. This meant that the primary source of damping in the bearing was the lubricant. Since the titling stiffness of the SABBs is negligible, there is significant squeeze flow around the elements as the shaft rotates which can introduce a lot of damping. On the other hand, the bearing is very stiff in the radial direction that the damping in this direction would be expected to be negligible in comparison [96]. Therefore, only tilting

terms were included in the bearing damping matrix:

$$\boldsymbol{C}_{\mathrm{B}} = \begin{bmatrix} 0 & 0 & 0 & 0 \\ 0 & 0 & 0 & 0 \\ 0 & 0 & c_{\mathrm{B}}^{\theta} & 0 \\ 0 & 0 & 0 & c_{\mathrm{B}}^{\theta} \end{bmatrix} \tag{6.15}$$

It was assumed that the two bearings would have similar levels of damping, since their construction is very similar, and therefore a common set of damping parameters was identified for both bearings. The identified bearing damping is listed in Table 6.7.

6.4.3.2 Coupling damping

The damping from the coupling was assumed to originate from material damping within the flexible metal bellows section. This implies that the coupling damping is proportional to the stiffness matrix of the coupling:

$$\boldsymbol{C}_{\mathrm{C}} = \beta_{\mathrm{C}} \boldsymbol{K}_{\mathrm{C}} \tag{6.16}$$

However, the parameter identification procedure yielded a value of $\beta_{\mathrm{C}} = 0$, as shown in Table 6.7, indicating that the coupling introduces little damping into the system. This is likely due to the way the rotor configuration was chosen; the rig was configured so that the coupling deflections would remain within the rated limits, and as a consequence, there is little relative motion between the rotor and motor shaft.

6.4.3.3 Encoder damping

The major source of damping from the encoder was assumed to be the rubber mount connecting the encoder to the floating bearing support; this is shown in Fig. 5.11a. The damping matrix was assumed to be diagonal, with different terms for the radial and rotational damping:

$$\boldsymbol{C}_{\mathrm{E}} = \begin{bmatrix} c_{\mathrm{E}}^{\delta} & 0 & 0 & 0 \\ 0 & c_{\mathrm{E}}^{\delta} & 0 & 0 \\ 0 & 0 & c_{\mathrm{E}}^{\theta} & 0 \\ 0 & 0 & 0 & c_{\mathrm{E}}^{\theta} \end{bmatrix} \tag{6.17}$$

The identified encoder parameters are listed in Table 6.7. It can be observed that the optimiser identified negligible radial damping, which is likely because the encoders displaces little in the radial direction as it is near the floating bearing. However, the rotational

damping term is very large, and is responsible for around a fifth of the damping in the rotor.

Table 6.7: Identified rig damping parameters

Parameter	Symbol	Value
Bearing rotational damping	c_{B}^{θ}	$8.25\,\mathrm{N\,s\,m^{-1}}$
Coupling damping coefficient	β_{C}	0
Encoder radial damping	c_{E}^{δ}	$0\,\mathrm{N\,s\,m^{-1}}$
Encoder rotational damping	c_{E}^{θ}	$4.5\,\mathrm{N\,s\,m^{-1}}$

6.4.3.4 Correlation of updated ROLADYN model

The ROLADYN model was updated with the identified parameters, and the modes were computed using eigenvalue analysis. The results have been overlaid on Figs. 6.14 to 6.16. The correlation with the experimental results will now be discussed in more detail.

Natural frequencies Considering the natural frequencies in Fig. 6.14 first, the maximum error between the model and experimental results is around 3 % in the shaft only configuration. However, the error reduces as the discs are added, and is only 1.5 % once both discs are fitted. This is because the influence of the discs tends to dominate over the ancillary components and any other uncertainties. This is further confirmed by examining the MAC values in Table 6.8, which generally move closer to unity as each disc is added.

It can also be observed that the model predicts the frequencies of the first and second pairs of modes to similar level of accuracy. The first set of modes are primarily determined by the rotor, whereas the bearing support structure has a large influence on the second pair of modes. Therefore, this provides evidence that both the rotor and bearing support have been accurately modelled.

Damping ratios The damping ratios from the ROLADYN model have been overlaid on Fig. 6.16. It is clear that the model predicts the damping much less accurately than the natural frequency. This is consistent with the results from the hammer testing on both the rotor in Section 5.3 and support structure in Section 5.4, the damping. However, once the encoder and bearing damping is included, the overall damping level is captured well. In the final configuration with two discs, the maximum error is around 50 %, which is inline with the damping predictions from the support model in Section 5.4.

Table 6.8: MAC for mode shapes of the assembled ARES rig

	Configuration		
Mode	Shaft only	Front Disc	Two Discs
1H	0.988	0.998	0.999
1V	0.998	1.000	0.999
2H	0.969	0.995	0.990
2V	0.969	0.992	0.996

Mode shapes The ROLADYN model also appears to predict the mode shapes for the two disc case accurately as shown in Fig. 6.15, with some small bearing housing motion in the second pair of modes. This good correlation extends to the other cases with different numbers of discs, as indicated by the high MAC values in Table 6.8. Therefore, these results provide further evidence that both the rotor and stator have been modelled accurately.

6.4.4 Summary

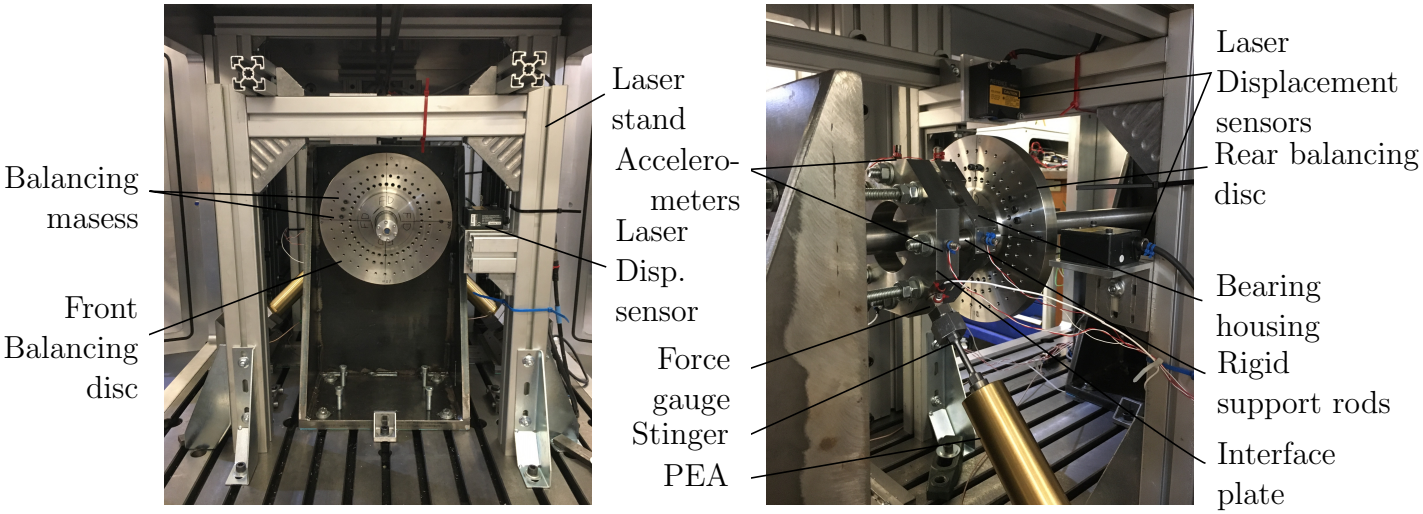
The ROLADYN model of the fully assembled ARES test rig has now been validated in the linear regime using hammer tests. The unknown damping parameters have been identified using a least-squares approach, in the same way as the rotor and bearing support structure. The next step is to validate the model in the rotating case, thereby introducing gyroscopic loads.

6.5 Rotating tests

The rig was now fully assembled in the chosen configuration, so that it was possible to begin rotating testing. The rig was first commissioned for rotating tests, and then the Campbell diagram was measured experimentally using the PEAs, which then was compared with the predictions from the ROLADYN model. Attention will then move onto the forced response, in both the balanced and unbalanced cases. These results will be compared to simulations using HBM.

6.5.1 Commissioning the rig for rotating tests

It was necessary to first prepare the rig for rotating tests, by fitting additional sensors to both the rotor and stator. This allows the response of the key components to be measured, and then compared to the model. The rotor must also be balanced, so that the rig can safely pass through the resonances within the speed range of the motor. However, it was



(a) Front view of disc (b) Detail view of bearing support

Figure 6.17: ARES test rig instrumentation

found that, even after balancing, the response of the rotor remained significant, so the residual unbalance and shaft runout were estimated from the data.

6.5.1.1 Instrumentation

Since the rotor spins, a contact free method for measuring its displacement was required. Keyence laser displacement sensors were mounted on aluminium extrusion stands around each disc, with one sensor measuring the horizontal displacement and another measuring the vertical displacement, as depicted in Fig. 6.17a. These sensors have a relatively small operating window of $\pm 3\,\text{mm}$, so care was taken to install them in the centre of their range.

For the non-rotating components, conventional accelerometers could be used. Accelerometers were fitted to the bearing housing and interface plate in both the horizontal and vertical directions. In addition, the force gauges between the PEAs and interface plate were connected. The sensors on the bearing support structure are shown in Fig. 6.17b.

The rotation angle of the rotor was measured using the encoder mounted to the pedestal of the floating bearing. This was numerically differentiated on the cRIO, which controls the rig as explained in Section 5.1, to give an estimate of the instantaneous rotation speed. The complete set of sensors is listed in Table 6.9.

6.5.1.2 Balancing the rotor

The rig was balanced using the Influence Coefficient method [196], using the two discs as balancing planes, and the vertical displacement of the two discs as response terms to

Table 6.9: List of ARES sensors

(a) Digital sensors

Channel	Sensor	Type	Precision	Range
Front Disc Disp.	Keyence LK-H022	Laser disp. sensor	0.1 µm	±3 mm
Rear Disc Disp.	Keyence LK-H022	Laser disp. sensor	0.1 µm	±3 mm
Shaft rotation	EPC Model 776	Rotary encoder	4096 inc. per rotation	

(b) Analogue sensors

Channel	Sensor	Type	Sensitivity
Bearing Housing Acc.	PCB M353B17	Accelerometer	$1\,\mathrm{mV\,m^{-1}\,s^{-2}}$
Interface Plate Acc.	PCB M353B17	Accelerometer	$1\,\mathrm{mV\,m^{-1}\,s^{-2}}$
PEA Force	PCB 208C04	Force gauge	$1.2\,\mathrm{mV\,N^{-1}}$

be minimised. The rig was first spun up to 27 Hz, which was the maximum speed which could be reached whilst keeping within the maximum allowable shaft displacement, and one balancing iteration was then carried out. The rotation speed could then be safely increased to 27.5 Hz, and another balancing iteration was carried out. The rotor was now sufficiently balanced that the rotor could be re-balanced at the critical speed at 28 Hz, which corresponds to the first FW mode. Balancing corrections were then applied at this speed until no further reduction in the response at resonance could be obtained. This yielded what was termed the "nominally balanced" condition.

6.5.1.3 Runout and residual unbalance estimation

The front disc response in the nominally "balance" case is plotted in Fig. 6.18. It can be observed that the rig vibrates significantly, even without the addition of any unbalance masses, and two resonances are clearly visible, which correspond to the BW and FW modes of the rotor. This was found to be due to the runout of the shaft. Although the rotor response at the first critical speeds was significantly reduced by applying the balancing procedure, it is not possible to fully eradicate the runout using balancing masses alone, and the response therefore remains significant even away from the resonances. Unfortunately, a replacement shaft was not available.

The influence of the shaft runout and residual unbalance will be particularly significant when the applied unbalance mass is small. This is because the response of the rotor due to its runout and residual unbalance can exceed the response due to the applied unbalance. Therefore, unless the runout and residual unbalance are identified, the predictions from the numerical model will be very inaccurate in this regime. For this reason, the shaft runout and residual unbalance had to be identified from the experimental data, and then incorporated into the model.

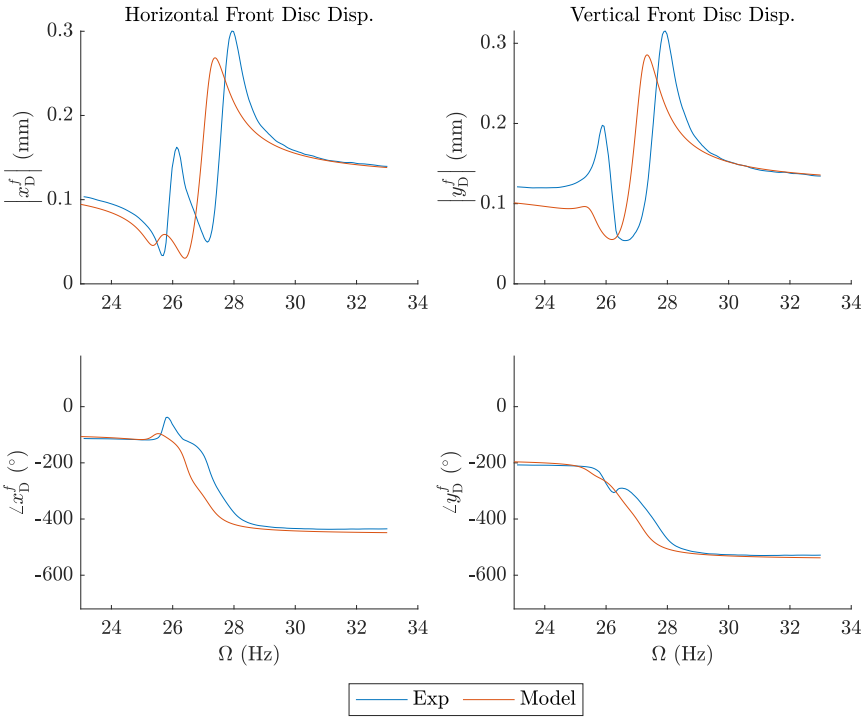


Figure 6.18: Numerical and experimental front disc response in the nominally "balanced" case

It was assumed that the rig remains in the linear regime in the nominally "balanced" case, so a linear-treatment can be used. Using the approach from [133], it will be assumed that the shaft runout can be expressed as a linear supposition of the modes of the rotor. The residual unbalance will be assumed to be lumped into the balancing discs. Under these assumptions, the response of the rotor to runout and residual unbalance can be written in the following form:

$$\boldsymbol{Z}(\Omega)\boldsymbol{x} = \left(\boldsymbol{K}_r\boldsymbol{\beta} + \Omega^2\boldsymbol{M}_d\boldsymbol{\epsilon}\right) \tag{6.18}$$

where $\boldsymbol{Z}(\Omega)$ is the dynamic stiffness of the complete rig. The matrix $\boldsymbol{K}_r$ is the stiffness matrix due to the rotor and the vector $\boldsymbol{\beta}$ represents the shaft runout, in terms of the complex magnitude of each normal mode. The second excitation term is due to the residual unbalance, and therefore scales with Ω^2. The matrix $\boldsymbol{M}_d$ contains the mass matrix contributions from the discs (where the unbalance is assumed to be located), and the vector $\boldsymbol{\epsilon}$ represents the residual unbalance in terms of the unbalance on each disc.

Only a subset of the rig displacement vector $\boldsymbol{x}$ was measured experimentally. Focusing only on the response at the discs by substituting $\boldsymbol{x}_d = \boldsymbol{S}_d\boldsymbol{x}$ into Eq. (6.18) and rearranging yields:

$$\begin{aligned}\boldsymbol{x}_d = \boldsymbol{S}_d\boldsymbol{x} &= \boldsymbol{S}_d\boldsymbol{Z}(\Omega)^{-1}\begin{bmatrix}\boldsymbol{K}_r & \Omega^2\boldsymbol{M}_d\end{bmatrix}\begin{bmatrix}\boldsymbol{\beta}\\ \boldsymbol{\epsilon}\end{bmatrix}\\ &= \begin{bmatrix}\boldsymbol{S}_d\boldsymbol{Z}(\Omega)^{-1}\boldsymbol{K}_r & \Omega^2\boldsymbol{S}_d\boldsymbol{Z}(\Omega_1)^{-1}\boldsymbol{M}_d\end{bmatrix}\begin{bmatrix}\boldsymbol{\beta}\\ \boldsymbol{\epsilon}\end{bmatrix}\end{aligned}$$

where $\boldsymbol{S}_d$ extracts the disc response from the global displacement vector of the machine. It should be noted that the dynamic stiffness $\boldsymbol{Z}$ and excitation matrices $\boldsymbol{K}_r$ and $\boldsymbol{M}_d$ can be computed from the ROLADYN model. On the other hand, the values of $\boldsymbol{x}_d$ were measured by the displacement sensors focused on the discs. In order to solve for the values of $\boldsymbol{\beta}$ and $\boldsymbol{\epsilon}$, the measured disc displacements at each frequency can be stacked together as follows:

$$\begin{bmatrix}\boldsymbol{x}_d(\Omega_1)\\ \vdots\\ \boldsymbol{x}_d(\Omega_N)\end{bmatrix}_{\text{Exp}} = \begin{bmatrix}\boldsymbol{S}_d\boldsymbol{Z}(\Omega_1)^{-1}\boldsymbol{K}_r & \Omega_1^2\boldsymbol{S}_d\boldsymbol{Z}(\Omega_1)^{-1}\boldsymbol{M}_d\\ \vdots & \vdots\\ \boldsymbol{S}_d\boldsymbol{Z}(\Omega_N)^{-1}\boldsymbol{K}_r & \Omega_N^2\boldsymbol{S}_d\boldsymbol{Z}(\Omega_N)^{-1}\boldsymbol{M}_d\end{bmatrix}_{\text{Model}}\begin{bmatrix}\boldsymbol{\beta}\\ \boldsymbol{\epsilon}\end{bmatrix}_{\text{Est}} \tag{6.19}$$

The response is measured at many more frequencies than there are unknowns, so that Eq. (6.19) is an over-constrained problem. This equation was solved in a least-squared sense to yield an estimate of the shaft runout $\boldsymbol{\beta}$ and residual unbalance $\boldsymbol{\epsilon}$.

The parameters identified using this approach are listed in Table 6.10. It is interesting to note that the residual unbalance masses are of the same order of magnitude to the masses applied during the rotor balancing procedure. This suggests that a significant proportion of these balancing masses are in fact reducing the effect of the runout, rather than actually counteracting any unbalance in the rotor. The shaft runout contribution from each mode has been expressed in terms of the displacement of the front disc. The shaft runout is mostly composed of the first rotor mode, indicating that it is the front section of the shaft which is bent.

Table 6.10: Identified rotor runout and residual unbalance parameters

(a) Residual unbalance

Disc	Mass @ 100 mm	Angle
Front	11.83 g	83.16°
Rear	12.92 g	70.02°

(b) Shaft runout

Mode	Amp. @ front disc	Angle
1	0.1165 mm	263.26°
2	0.0004 mm	222.91°

These parameters were then used to compute the linear frequency response using the ROLADYN model, and the results are overlaid on Fig. 6.18. There is a small frequency offset between the experimental and numerical results, but this is only around 2 % and is

consistent with the error in the natural frequencies from the hammer tests in Section 6.4. The disc responds with a constant amplitude away from resonance, which is due to the runout of the rotor, which is captured well by the model. There are significant resonances at both critical speeds, although the response is larger at the FW mode. The model accurately predicts the response around the dominant FW mode, but significantly under-predicts the response at the BW mode. This is because the unbalance and runout excitation are FW in nature, so such a large response at the BW mode is unexpected. Between the resonances, there is a large drop in the response, which is where the residual unbalance excitation partially cancels out the runout excitation. This feature is captured well by the model. With the incorporation of the residual unbalance and shaft runout, a fully valid linear model of ARES was now available, and proper dynamic testing could commence.

6.5.2 Campbell diagram

In order to verify that the ROLADYN model captures gyroscopic effects accurately, it was decided that the Campbell diagram should be measured experimentally using low amplitude asynchronous excitation from the PEAs. These results could then be compared to the predicted Campbell diagram from the ROLADYN model.

However, before the Campbell diagram could be computed from the ROLADYN model, it was first necessary to investigate whether the stiffness of the fixed bearing was sensitive to rotor speed due to centrifugal loading on the elements; this was investigated in detail on the Jeffcott rotor in Section 4.5.3. If this found to be the case, it would be necessary to re-linearise the system at each rotation speed when computing the Campbell diagram. However, if the bearing stiffness is insensitive to rotation speed, any changes in frequency will be purely due to gyroscopic effects.

6.5.2.1 Bearing stiffness

The average stiffness of the fixed bearing in the equilibrium position was computed for a range of rotation speeds using the high-speed contact model from Section 3.2.5. The horizontal and vertical stiffnesses are plotted in Fig. 6.19. The stiffness of the bearing itself is shown in orange, whilst the stiffness of the bearing in series with the supporting structure (in the rigid configuration) is shown in blue. The effective support structure stiffness at the bearing housing, using the parameters identified in Section 5.4.4, was computed to be $42.7\,\mathrm{MN\,m^{-1}}$.

Both the horizontal and vertical stiffnesses initially increase with speed, since the centrifugal loads lead to a reduction in the contact angle, which in turn increases the radial

stiffness of the bearing. However, at speeds above 100 Hz, both the horizontal and vertical stiffness decrease significantly, although this is particularly significant in the horizontal direction. This is because the centrifugal loads start to unload the contacts at the edge of the loaded zone, which have the largest contribution to the horizontal bearing stiffness. Even so, the drop in the total stiffness becomes much less significant once the support compliance is included. This is because the influence of the bearing is attenuated by the flexible support structure.

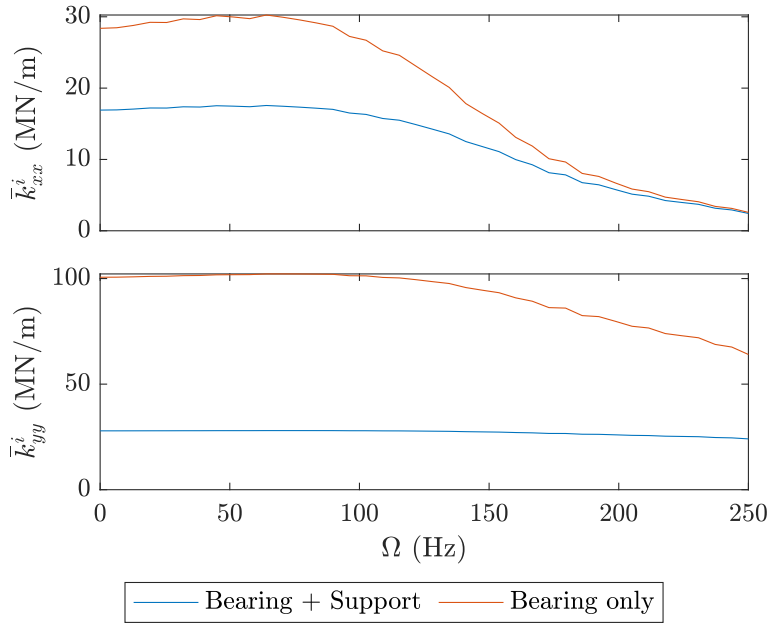


Figure 6.19: Predicted variation of ARES fixed bearing stiffness with rotor speed

It was concluded from this analysis that dynamic loading on the elements can be neglected, since the rig will only operate at speeds lower than 50 Hz, where the total stiffness remains almost constant. It is therefore acceptable to use the simpler low-speed contact model from Section 3.2.4 to model the rolling-element bearings. The bearing stiffness can be considered to be independent of rotation speed.

6.5.2.2 Computation of Campbell diagram using ROLADYN

Now that it had been established that the bearing stiffness is insensitive to rotor speed, the Campbell diagram could be computed. For this analysis, the system was linearised around the equilibrium position with the rotor non-rotating. The first two pairs of modes are plotted in Fig. 6.20. Two engine order lines have been plotted; the synchronous engine order corresponding to unbalance excitation denoted by 1X, and the frequency of self-excitation due to variable compliance frequency which occurs at the BPF. The corresponding mode shapes have been plotted in Fig. 6.21; note that the mode shapes

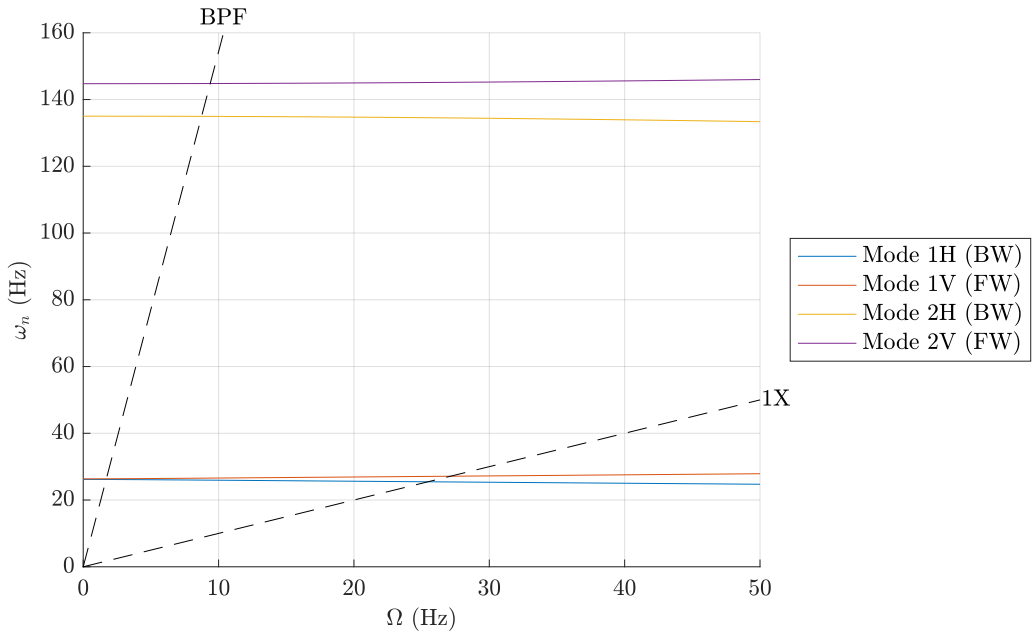


Figure 6.20: Predicted Campbell diagram of the ARES rig

have been plotted at a rotor speed of 50 Hz, so that the whirl is clearly visible.

It can be observed from Fig. 6.20 that the first pair of modes show very little asymmetry, whilst the second pair of modes are separated even at $\Omega = 0$. This is because the fixed bearing and its support have a much larger influence on the higher order modes, which both have asymmetric properties in the horizontal and vertical directions. This also explains why the first pair of modes are nearly circular, whilst the second pair of modes are highly elliptical, as shown in Fig. 6.21. As the rotor speed increases, each pair of modes diverge in frequency, due to the gyroscopic forces on the rotor. This effect is equally strong in both pairs of modes; the first pair of modes diverge in frequency by 6.5 Hz at $\Omega = 100$ Hz, while the second pair of modes diverge by 8.5 Hz.

It can be observed that the 1X engine order line only crosses the first pair of modes, and therefore it is only possible to excite the first pair of modes with unbalance excitation, within the speed range of the motor. However, the BPF line crosses the first pair of modes at 1.6 Hz and the second pair of modes at 5.3 Hz, and therefore it is possible for variable compliance oscillations to excite both pairs of modes.

6.5.2.3 Experimental measurement of the Campbell diagram using asynchronous PEA excitation

The PEAs connected to the front bearing support on ARES can be used to excite the rotor asynchronously across a range of frequencies. If the rotor speed is held constant, this corresponds to traversing a vertical line on the Campbell diagram. This can then be

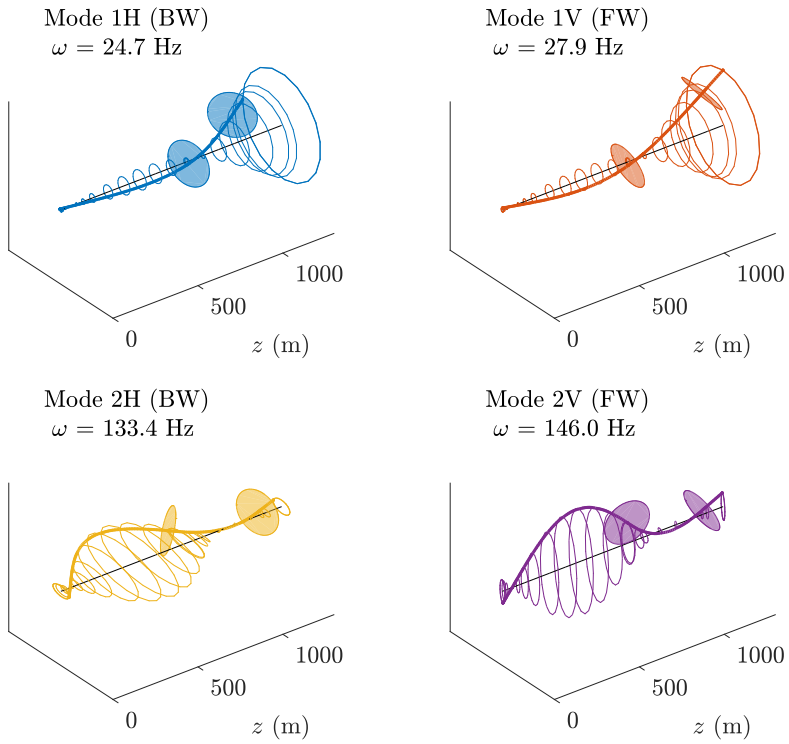


Figure 6.21: Predicted mode shapes of the ARES rig at $\Omega = 50$ Hz

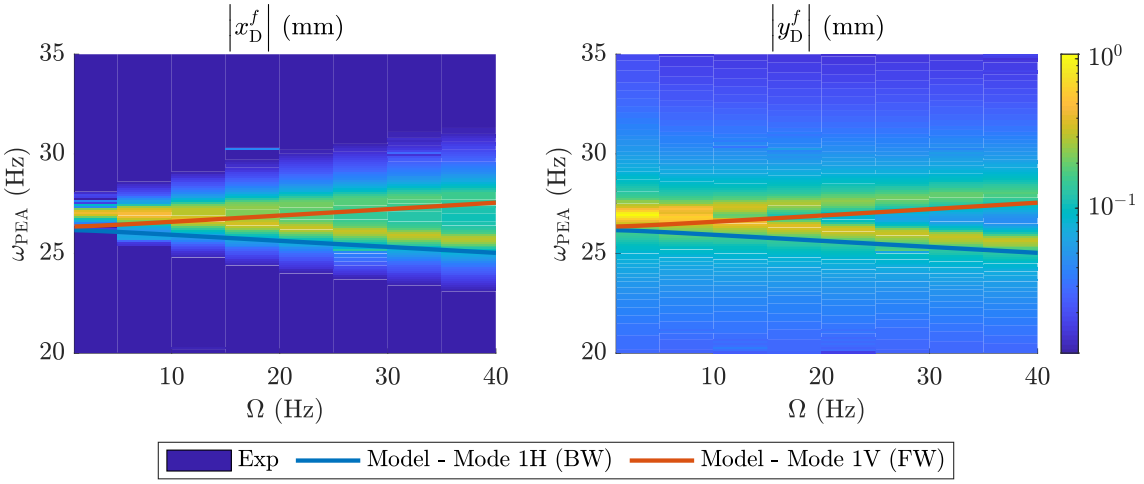
repeated for different rotor speeds to build up the complete Campbell diagram.

The PEAs were driven with a stepped-sine sweep, ranging from a frequency of 20 Hz up to 35 Hz, so as to cross the first pair of modes. The frequency step was set to 0.1 Hz, and each step lasted 1 s which was found to be sufficient for the response to reach steady-state at each excitation frequency. A vertical excitation pattern was applied by the PEAs, so as to excite both the FW and BW modes. A very low amplitude voltage of 50 V was applied, so that the system remains in the linear regime. Within each step, the amplitude and phase of the response at the excitation frequency was found using the FFT of the signal.

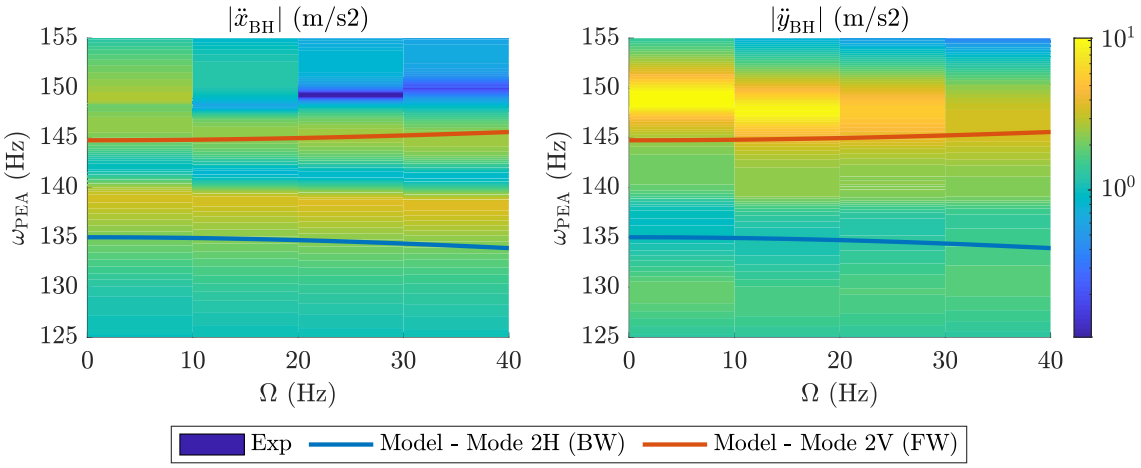
This was then repeated at higher-frequencies from 125 Hz up to 155 Hz in order to excite the second pair of modes. These modes are more elliptical than the first pair of modes due to the asymmetry from the bearing support, so a FW excitation was applied this time, which was expected to excite both modes significantly. The voltage amplitude was reduced to 10 V, since the front L-shape was found to vibrate considerably when passing through these resonances. The data was post-processed in the same way.

The resulting spectra are plotted in Fig. 6.22, and the predicted natural frequencies from the ROLADYN model have been overlaid. The disc response when passing through the first pair of modes has been plotted in Fig. 6.22a. The two resonances corresponding to the FW and BW modes are very clear in the experimental data. It can be observed that

at $\Omega = 0\,\text{Hz}$, the 2 frequencies coincide as predicted, at a frequency of 27 Hz. As the rotation speed increases, they diverge due to gyroscopic forces, which is predicted well by the model. However, the natural frequencies are slightly offset (by around 0.3 Hz) from the experimental values, which remains constant for all rotor speeds. This offset agrees with the small discrepancy seen from the hammer tests shown in Fig. 6.14.



(a) Front disc displacement with vertical PEA excitation (Modes 1H and 1V)



(b) Bearing housing acceleration with FW PEA excitation (Modes 2H and 2V)

Figure 6.22: Response of the ARES rig to PEA excitation

The bearing housing response as the rig passes through the second pair of modes has been plotted in Fig. 6.22b. As expected, there is a larger response in the horizontal direction in the lower frequency BW mode, and a larger vertical response in the higher frequency FW mode. Unlike the first pair of modes, there is a clear gap between the resonances, even when the rotor is not rotating. The resonances appear to diverge as the speed is increased, due to gyroscopic effects, like the first pair of modes.

However, the resonance due to the higher-frequency vertical mode starts at a frequency around 4 Hz higher than what was observed from the hammer tests in Fig. 6.14. To

further complicate things, the resonance appears to initially drop in frequency for rotor speeds below 20 Hz, before eventually increasing at would be expected due to gyroscopic effects. This initial drop in frequency is unexpected, but this is likely due to a frictional non-linearity in the bearing support structure. Since this phenomenon was not believed to be associated with the bearings, it was not investigated in more detail.

The lower frequency horizontal mode (2H) is very well predicted by the model, including the increasing reduction in frequency with speed. Similarly, the vertical mode (2V) appears to match the experimental data well at higher speeds. However, the model under-predicts the resonance frequency at low speeds, which is the region where the resonance was higher than expected from the hammer tests. Since this phenomena was believed to be non-linear in nature, it would not be captured by the model, since a linearised analysis was used to compute the Campbell diagram. Even so, the maximum error between the natural frequency from the model and the resonance frequency from the experimental data is only around 1.5 Hz, which was deemed acceptable. It can be concluded that the physics of the rig are accurately represented.

6.5.2.4 Summary

The validation of the ROLADYN model of the assembled ARES rig in the linear regime is now complete. The modal properties of the rig in the rotating case were investigated using PEA excitation, and it was verified that gyroscopic effects are accurately captured by the model. It is expected that this model is capable of predicting the transmissibility of vibrations across the bearing in the linear regime. The forced response can now be considered.

6.5.3 Variable compliance

The first phenomenon to be investigated was self-excitation due to the variable compliance (VC) of the fixed bearing. It was observed in the Jeffcott rotor study in Section 4.4 that the variable compliance of the bearing excites the rotor synchronously at the Ball-Pass Frequency (BPF). This can lead to sub-resonances where the BPF line crosses one of the natural frequencies of the system. In an industrial rotating machine, VC could synchronously excite both the rotor and stators connected by the bearing, even if the machine is perfectly balanced. To investigate whether this effect could be observed on ARES, the sensitivity of the bearing stiffness to cage angle was analysed using the quasi-static bearing model. The conclusions were then verified experimentally, by spinning the rotor through the speeds where the sub-resonances should occur.

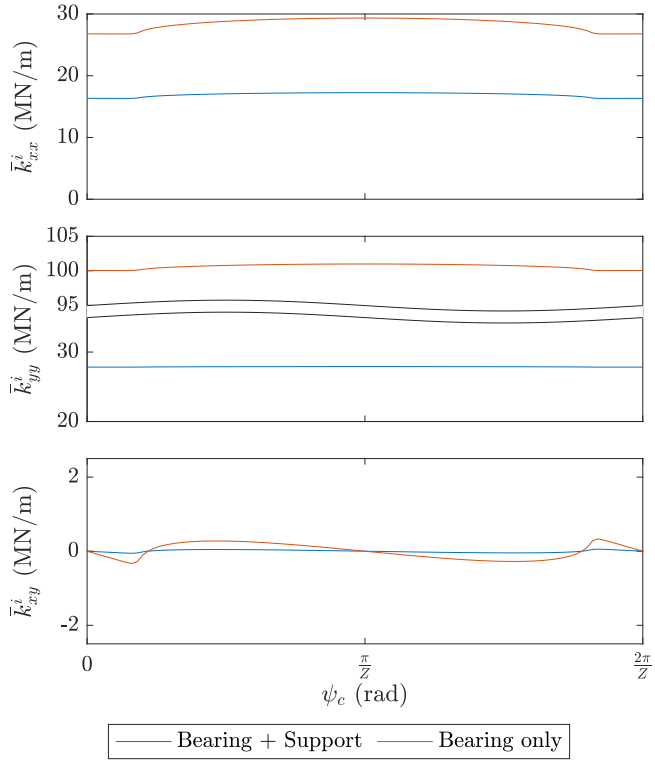


Figure 6.23: Predicted variation of ARES fixed bearing stiffness with cage position

6.5.3.1 Bearing stiffness

The time-varying stiffness of the fixed bearing was computed over a range of cage angles with the bearing in its equilibrium position, in the same way as in Section 4.4. It would be expected that if the variable compliance effect is significant on ARES, then large variations in both the bearing stiffness (and combined bearing and support stiffness) should be observed. The results have been plotted in Fig. 6.23.

It can be observed immediately that the stiffness of the SABB on ARES is much less sensitive to cage angle than the DGBB analysed in Section 4.4.2. The horizontal stiffness of the ARES bearing varies by around 6 % compared to around 20 % for the DGBB supporting the Jeffcott rotor. Similarly, the vertical stiffness varies by around 1 % compared to around 6 % on the DGBB. This is primarily because the SABB on ARES has many more elements ($Z = 36$) than the DGBB ($Z = 9$) in the Jeffcott rotor study.

The vertical and horizontal stiffness vary in a very similar way to each other, and both reach a maximum at $\psi = 0$ and $\psi = \frac{2\pi}{Z}$, when there is an element underneath the shaft. This is quite different from the case for the DGBB analysed in Section 4.4.2, where the horizontal stiffness was at a maximum of $\psi = \frac{\pi}{Z}$ where there were elements either side of the shaft centreline. The angle where the stiffness is at a maximum is determined by the number of elements in the loaded zone, as well as the load distribution between the

elements. This in turn depends on both the clearance and number of elements, and is therefore highly dependent on the particular bearing.

The cross-stiffness is again very sensitive to the clearance level, but one key feature from the Jeffcott rotor remains. The cross-stiffness is zero at $\psi = 0$, $\psi = \frac{\pi}{Z}$ and $\psi = \frac{2\pi}{Z}$, when the elements are symmetrically distributed around the bearing. At all other cage angles, the cross-stiffness becomes non-zero, since the symmetry is broken, as was found in Section 4.4.2.

Once the compliance from the bearing support is included, the stiffness becomes even less sensitive to cage angle. Since the bearings are so stiff, even the rigid bearing configuration introduces sufficient compliance to linearise the system. Therefore, this suggests that VC is negligible on ARES, and that the sub-resonances associated with the BPF will not be detected.

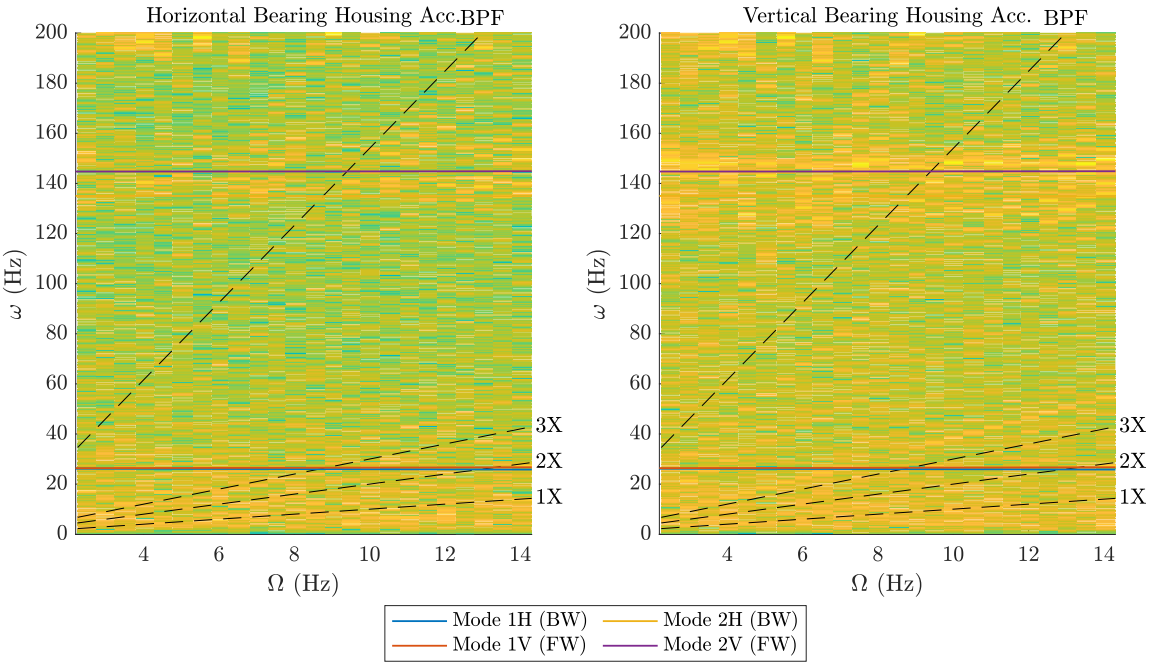
6.5.3.2 Experimental observations of the BPF during rotor ramp-up

From the Campbell diagram in Fig. 6.20, the critical speeds from self-excitation due to variable compliance are all below 10 Hz. The motor speed was therefore ramped slowly from 1 Hz up to 15 Hz at a rate of $0.25\,\mathrm{Hz\,s^{-1}}$, which ensured that the rotor would pass through all of the critical speeds due to BPF excitation. The spectrum of the rig response was then computed using `spectrogram` in MATLAB. It would be expected that the effect of variable compliance should be most detectable in the bearing housing and interface plate response, since there is negligible compliance between the bearing and these components, which would otherwise attenuate this content. Therefore the bearing housing acceleration, and interface plate forces (measured by the PEA force gauges), have been plotted in Fig. 6.24.

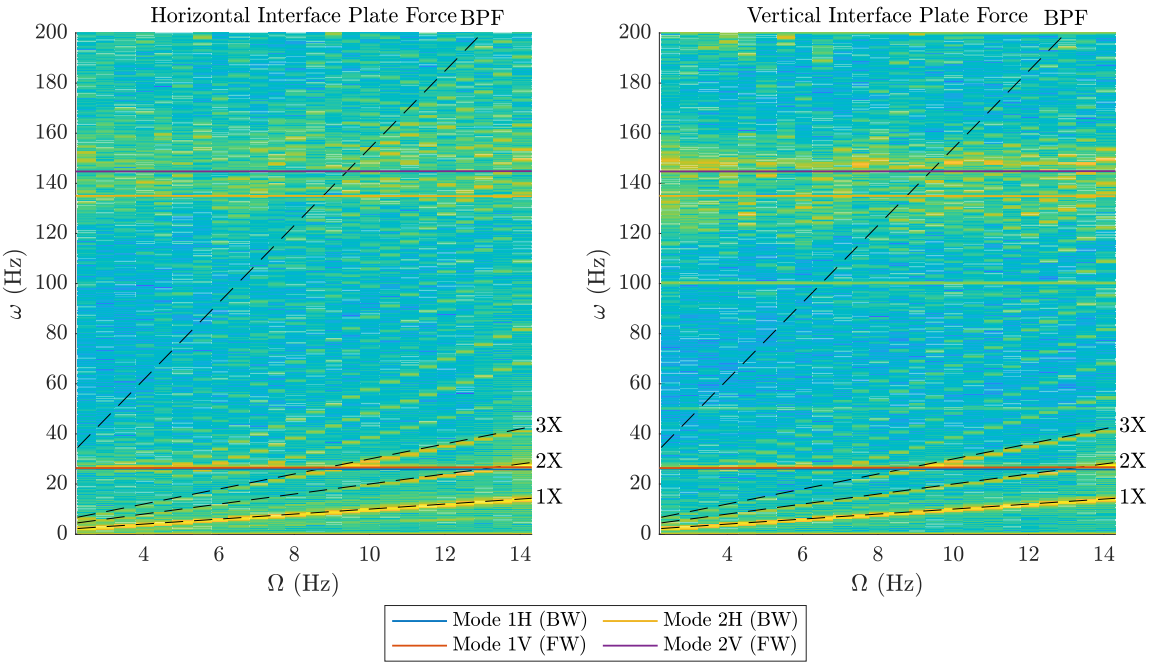
It can be observed that there is significant content at the first 3 engine orders, particularly in the interface plate force in Fig. 6.24b. These higher order harmonics suggest that there is some non-linearity on the rig which is excited by the runout and residual unbalance of the rotor. However, there appears to be no content along the BPF line, and no resonances are visible where it was expected that the variable compliance will excite the modes of the system. Therefore, these results confirm the conclusion drawn from the quasi-static bearing model that variable compliance is not significant on ARES.

6.5.3.3 Summary

It has been demonstrated that the instrumented bearing on ARES is much less sensitive to cage angle than the previously analysed bearing in the Jeffcott rotor study in



(a) Bearing housing acceleration



(b) Interface plate force

Figure 6.24: Spectrum of ARES response during ramp-up

Chapter 4. This is primarily because it has many more elements, which reduces the fluctuations in bearing stiffness. In addition, the bearing support structure introduces some additional compliance in series with the bearing, which further reduces these fluctuations and linearises the system. Therefore, it not necessary to include the VC when simulating the forced response.

6.5.4 Unbalance response

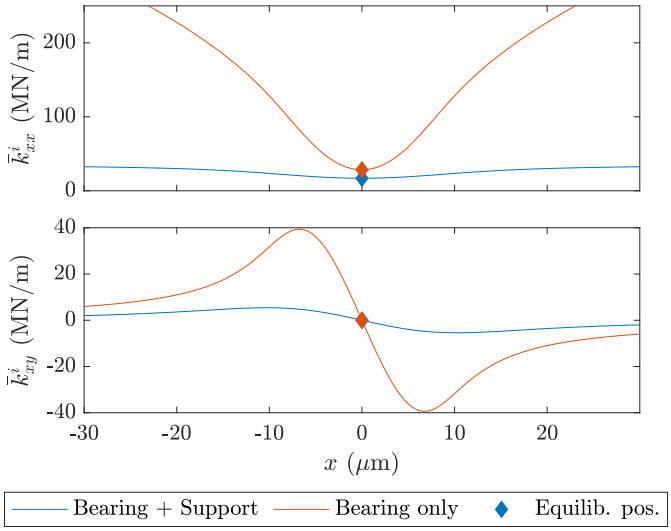
Although it has been established that the variable compliance of the bearing is negligible on the ARES rig, it is possible that the other sources of non-linearity in the bearing remain significant; namely the clearance and Hertzian contacts. The bearing stiffness around the equilibrium position was first analysed, to provide insight into the significance of these non-linearities. The rotor was then excited with a range of unbalance masses, and the disc response and vibration transmission through the bearing was analysed. The level of non-linearity in the system was assessed by examining how the response varies with the excitation amplitude. The results were compared to predictions from the ROLADYN model, in order to determine whether the observed non-linearity could be attributed to the fixed bearing.

6.5.4.1 Bearing stiffness

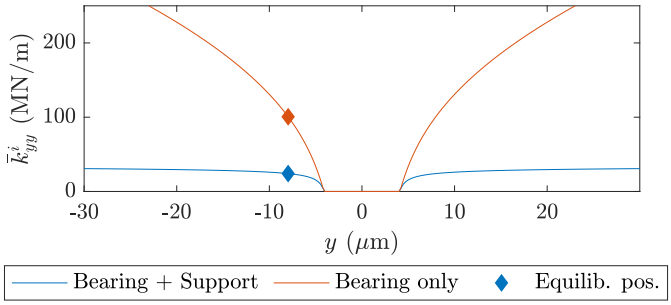
Before analysing the forced response of the system, the sensitivity of the stiffness of the fixed bearing was analysed using the model in the same way as in Section 4.4.2, which will provide insight into the non-linear response later on. The shaft was perturbed vertically and horizontally, and the average stiffness was computed in each position. The shaft tile angle was fixed to zero (ie $\theta_x = \theta_y = 0$), but the constant vertical load due to the self-weight of the rotor was maintained throughout. The results are plotted in Fig. 6.25, where the equilibrium position has been marked with a diamond.

The overall trends are very similar to the results from the Jeffcott rotor in Section 4.4.2. The horizontal stiffness in Fig. 6.25a increases monotonically as the shaft is moved away from the centre, due to the Hertzian contacts. However, there is no deadband since the vertical preload takes up the clearance. On the other hand, there is a clear deadband in the vertical stiffness centred around $y = 0\,\mu\text{m}$, as shown in Fig. 6.25b, where no elements are in contact. Outside this region, the vertical stiffness increases monotonically, again due to the stiffening characteristic of the Hertzian contacts.

The cross-stiffness in Fig. 6.25a is zero in the centre, due to symmetry. It initially increases as the rotor moves horizontally which breaks the symmetry of the load distribution around the bearing. However, the cross-stiffness returns towards zero again for large horizontal



(a) Horizontal sweep



(b) Vertical sweep

Figure 6.25: Predicted variation of ARES fixed bearing stiffness with displacement

displacements, because the horizontal load becomes so large that the effect of the vertical preload is negligible, and a symmetrical load distribution returns.

The addition of the compliance from the bearing support reduces the level of non-linearity considerably; this agrees with the results from the Jeffcott rotor study in Section 4.5.4. Even though the bearing housing was in the rigid configuration, the bearing is so stiff that even this small additional compliance leads to a significant drop in the combined stiffness. The variation in the horizontal stiffness is considerably reduced as the bearing displaces horizontally, and the stiffness converges to that of just the bearing support, as shown in Fig. 6.25a. The same effect occurs in the vertical direction, except that the deadband remains, as shown in Fig. 6.25b.

From this analysis, it would be expected that an initial softening effect should be observed when the ARES rotor is excited by an unbalance, due to the internal bearing clearance. However, at higher excitation levels, only a limited hardening effect would be expected, which will eventually saturate due to the support compliance.

6.5.4.2 Test procedure

To measure the unbalance frequency response of the rig, the motor speed was increased slowly from 23 Hz up to 33 Hz which passes through the first pair of critical speeds. The speed was increased in 0.05 Hz increments so that the resonance frequency could be identified accurately. The response at the motor speed was then extracted from the response using the FFT. Bolts of various sizes were attached to the front disc in order to introduce unbalance excitation. The bolts were attached to the outer ring at 0°, up to a maximum bolt mass of 2.1 g.

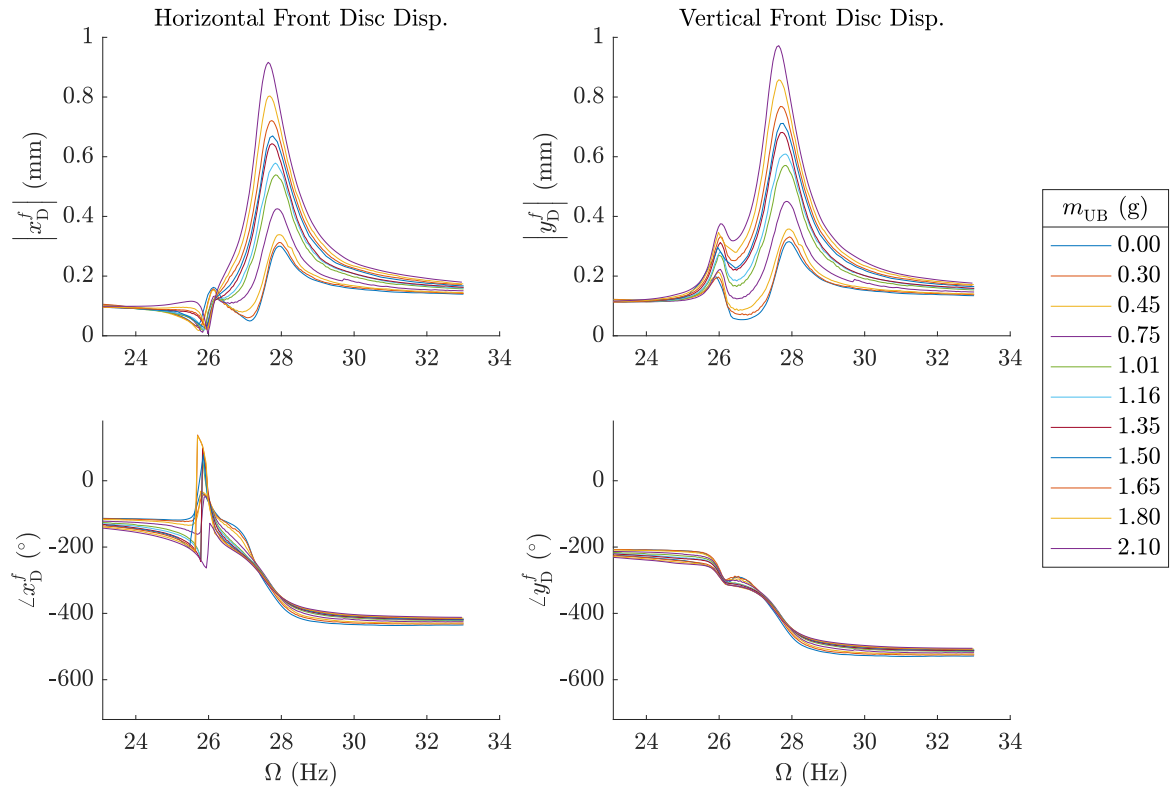
6.5.4.3 Disc response

The front disc response from the experimental results has been plotted in Fig. 6.26a. There are two clear resonances in this speed range, with one much larger than the other. The smaller peak at around 26 Hz is the BW mode, which is excited only very slightly by the unbalance. The second, more dominant, peak at around 28 Hz is the FW mode, which is excited much more by the unbalance. The disc orbits at each resonance are plotted for the largest unbalance mass in Fig. 6.27 and it can be observed that the orbit is approximately circular, which agrees with the predicted mode shapes in Fig. 6.21.

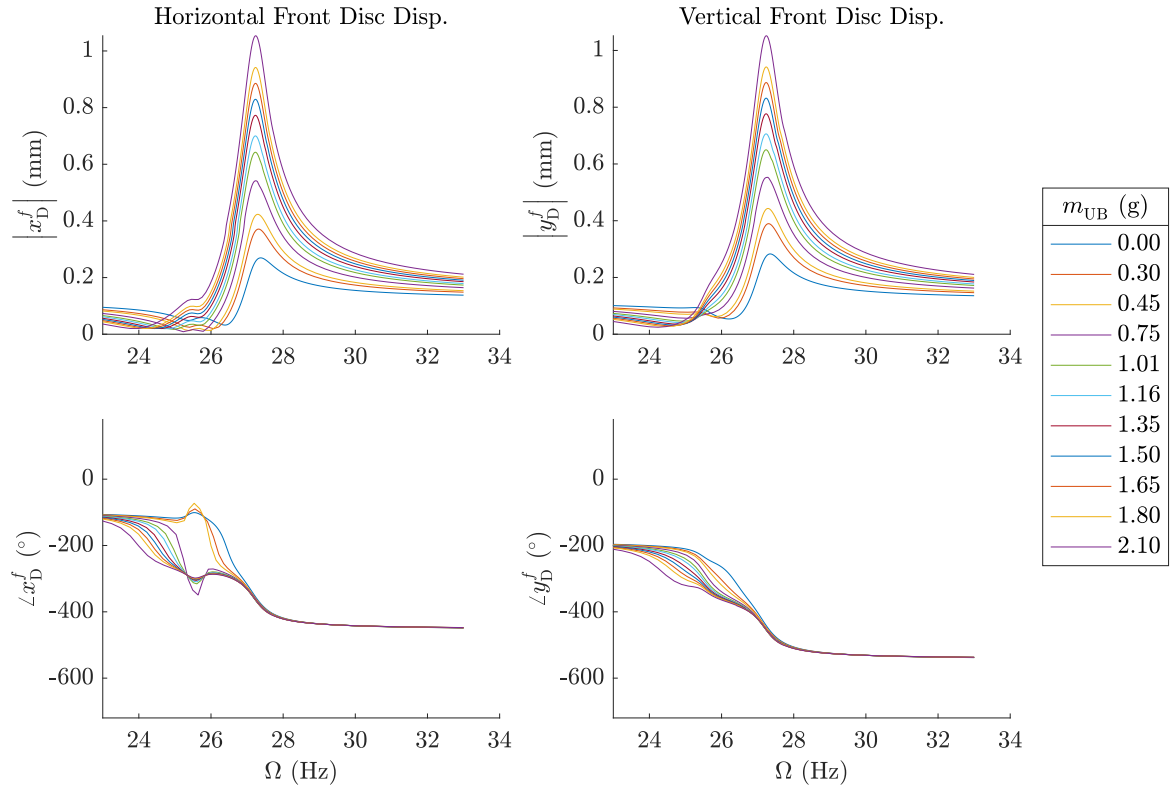
Returning to the frequency response, the phase of the response varies quite strangely, with sharp jumps at 26 Hz. This is due to the interaction of the shaft runout and applied unbalance, and has been observed in other studies [197]. The resonance frequency appears to vary with amplitude, with the resonant peaks slightly shifting to the left or right. This indicates that some non-linearity is present in the system.

The simulated disc response is plotted in Fig. 6.26b for the same unbalance levels considered in the experiments. The response was computed using the non-linear ROLADYN model, coupled with the HBM approach outlined in Section 6.3. The identified shaft runout and residual unbalance in the rotor were also included. The model displays qualitatively similar behaviour to the experimental results, particularly around the higher frequency FW mode. The maximum amplitude is predicted accurately, with around 1 mm for the maximum unbalance mass. The same phase change of around 180° between 27 Hz and 29 Hz is present in both the experimental data and simulations. It was found that the response remains stable throughout both resonances. This is expected, since the system is only lightly non-linear and is also quite heavily damped, which tends to help maintain stability.

The response at the lower BW mode is captured poorly by the model, and is much more pronounced in the experimental data. The anti-resonance in the horizontal response at around 26.5 Hz moves with unbalance level in the simulated response, and is present for all

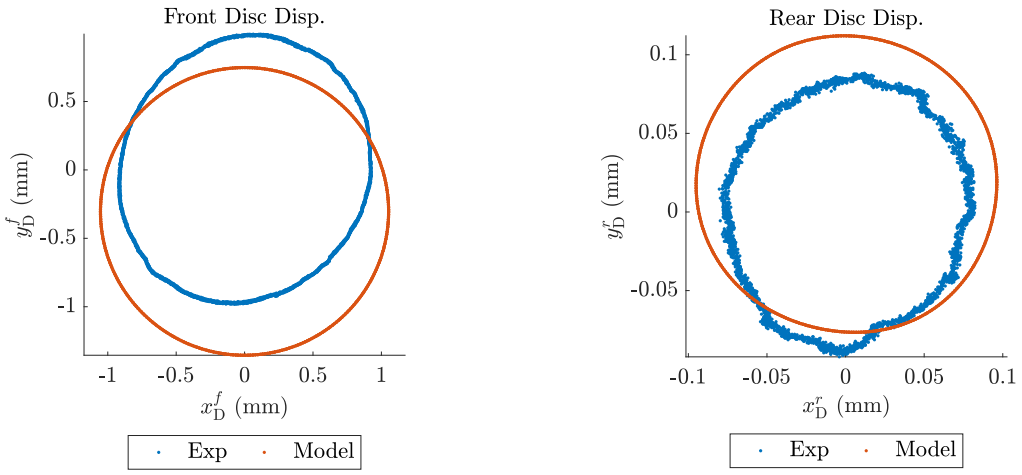


(a) Experiment



(b) Model

Figure 6.26: Frequency response of the front disc due to front disc unbalance



(a) Front disc (b) Rear disc

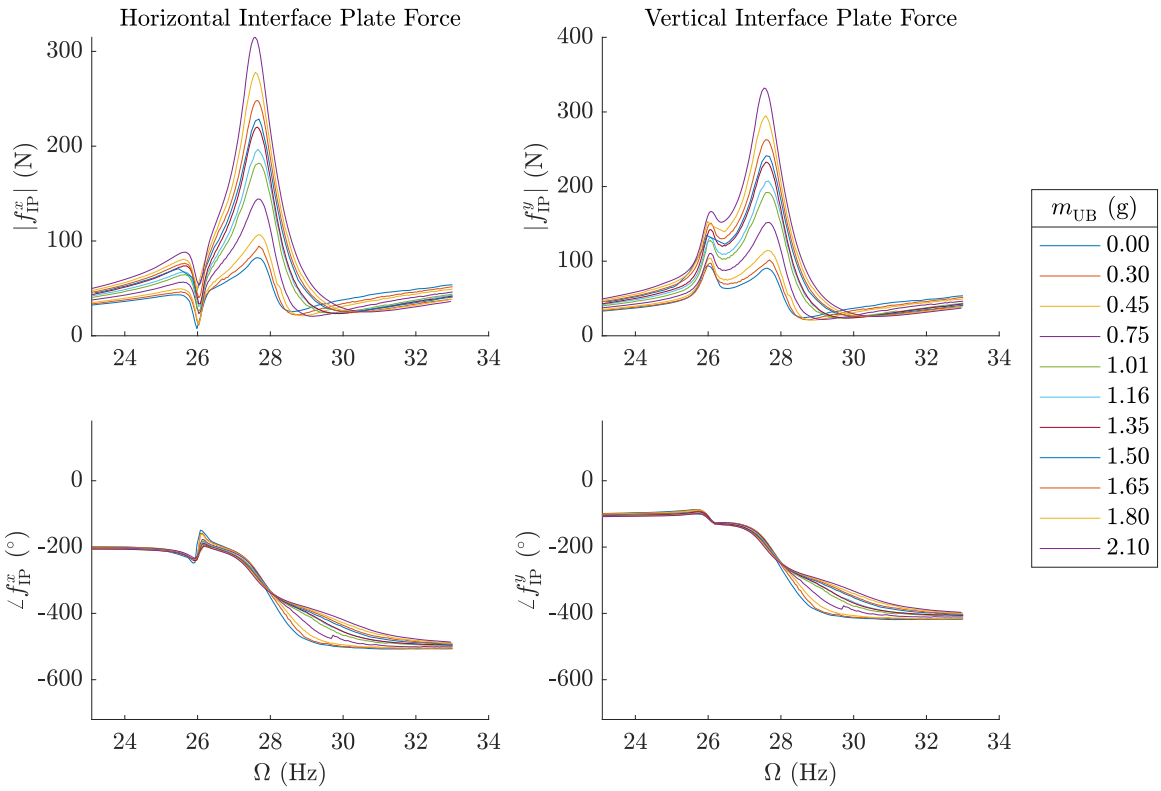
Figure 6.27: Disc orbits at resonance with a 2.1 g front disc unbalance

unbalance levels, whilst this anti-resonance becomes less significant at higher unbalance levels in the experimental data. In addition, the phase response is very different in the simulated data around the BW mode. All of these discrepancies between the model and experiments can likely be attributed to two main areas; the response in this region was found to be very sensitive to the shaft runout and residual unbalance, which could only be estimated in an approximate way from the data. In addition, the asymmetry from both the front bearing and its supporting structure has a large influence on the ellipticity of the BW and FW modes, which in turn influences how much they are excited by an unbalance. The fixed bearing and its support and were the two most complex components to model, some discrepancies between the model and experiments are expected. However, neither of these phenomena were the focus of this study, and since the primary resonance was predicted well by the model, the correlation was deemed to be good.

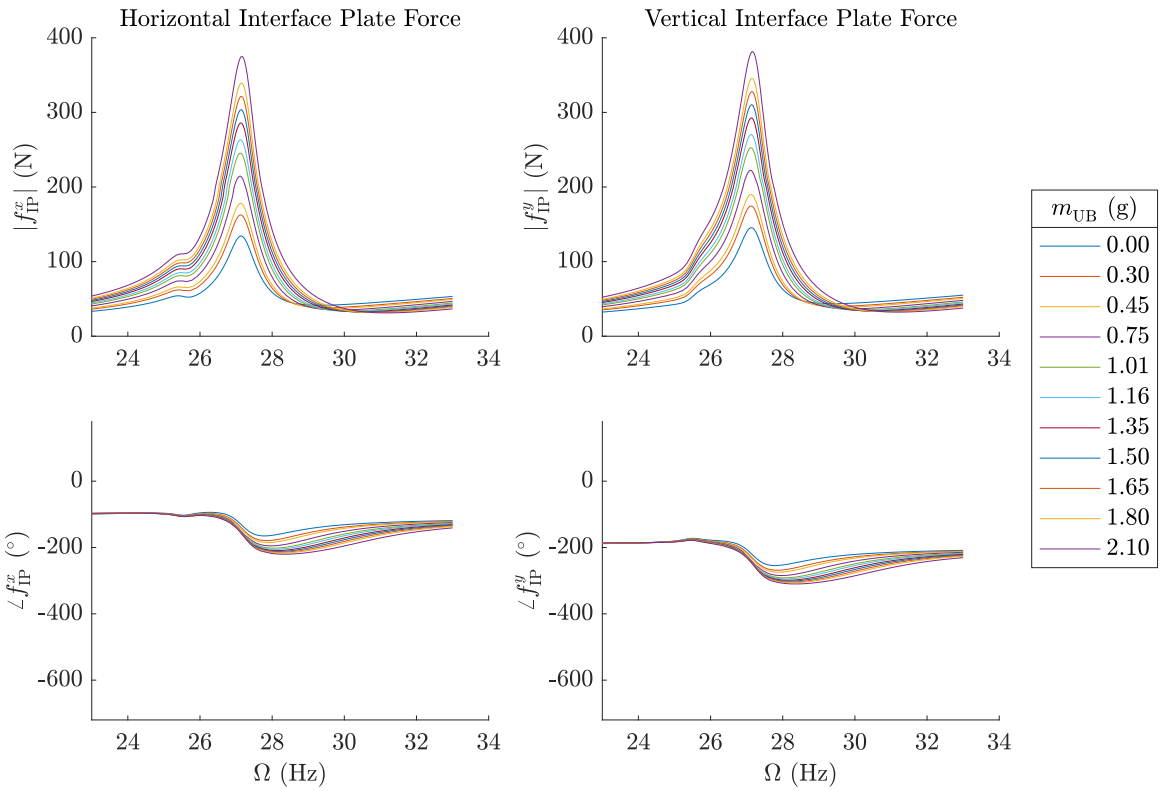
6.5.4.4 Bearing transmissibility

In order to assess the transmissibility through the fixed bearing, the frequency response of the interface plate force (measured by the PEAs) has been plotted in Fig. 6.28. The response looks very similar to the disc response in Fig. 6.26, with the same large resonance corresponding to the FW mode. In addition, the BW mode can be observed in the experimental data in Fig. 6.28a, but is much less prominent in the simulated response in Fig. 6.28b.

The simulations generally predict the magnitude of the force transmitted through the bearing to the interface plate around the primary resonance well. The numerical results overestimate the magnitude at resonance by around 20 %, but this was deemed to be quite an acceptable level of accuracy, given the difficulty in modelling the bearing support and



(a) Experiment



(b) Model

Figure 6.28: Frequency response of the reacted interface plate force due to front disc unbalance

the damping in the system. The phase evolution is very different in the model, when compared to the experimental data. Both display a 180° phase change over the resonance; however, after the resonance, the phase returns towards 0° in the numerical results, whilst it continues to decrease in the experimental data. This difference in behaviour is quite unexpected, but most likely indicates some deficiency in the support model. Investigating this phenomena further was deemed beyond the scope of this project. Nevertheless, since the behaviour around the resonance was captured well by the model, these results demonstrate that the quasi-static bearing model can accurately predict the forces transmitted through the bearing.

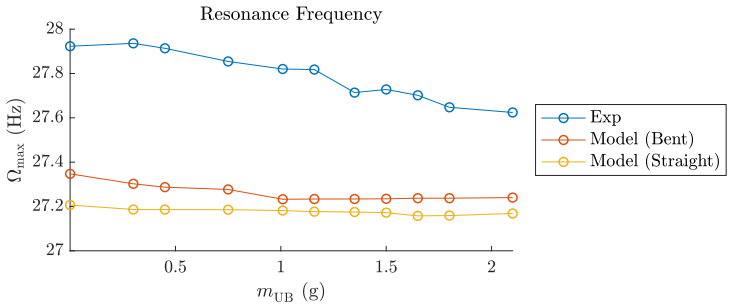
6.5.4.5 Backbone curve

The focus then moved onto non-linear behaviour, which was assessed by considering how the response at resonance varies with the applied unbalance. The resonance frequency, peak disc response, and peak transmitted force has been plotted as a function of the unbalance mass in Fig. 6.29, with results from both the experiments and numerical model. For the simulated results, the backbone curves were computed for two different cases:

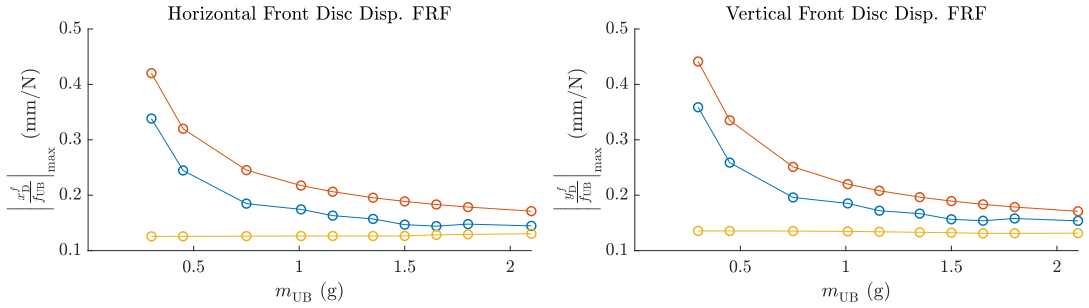
- *Straight rotor:* The rotor was assumed to be straight and perfectly balanced, so the only excitation source was the applied unbalance.
- *Bent rotor:* The identified shaft runout and residual unbalance was incorporated into the model, which synchronously excites the rotor in addition to the applied unbalance.

The results from the two different cases can be compared, in order to separate the influence of the shaft runout from the influence of the fixed bearing.

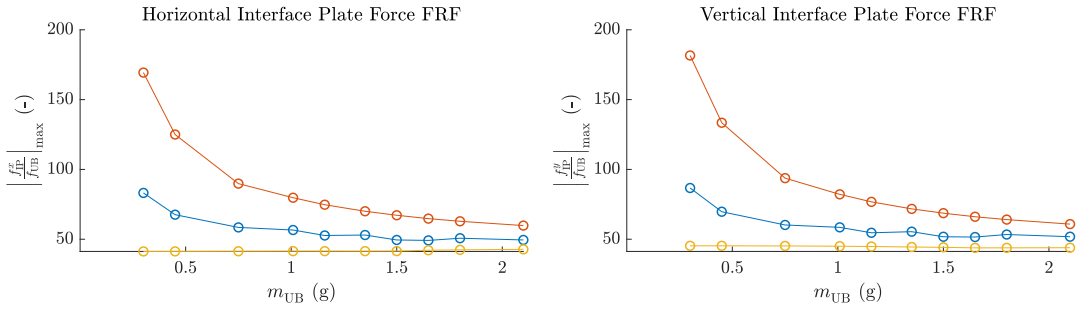
Resonance frequency The resonance frequency is plotted as a function of the applied unbalance mass in Fig. 6.29a. The results from the model show a complex non-monotonic variation with excitation amplitude, no matter whether the rotor runout and residual unbalance is included (shown in orange) or excluded (shown in yellow). For the case of a straight rotor, the resonance frequency initially drops due to the effect of clearance, before increasing very slightly for $m_{\mathrm{UB}} > 1.2\,\mathrm{g}$ due to Hertzian contact stiffening. Once the runout is included, the frequency at very low unbalance levels is increased. This is because the internal bearing clearance is taken up by the excitation from the shaft runout and residual unbalance, which stiffens the bearing. However, at very high unbalance levels, the resonance frequency from the bent and straight rotor converge, since the applied unbalance dominates over the shaft runout and residual unbalance in this regime.



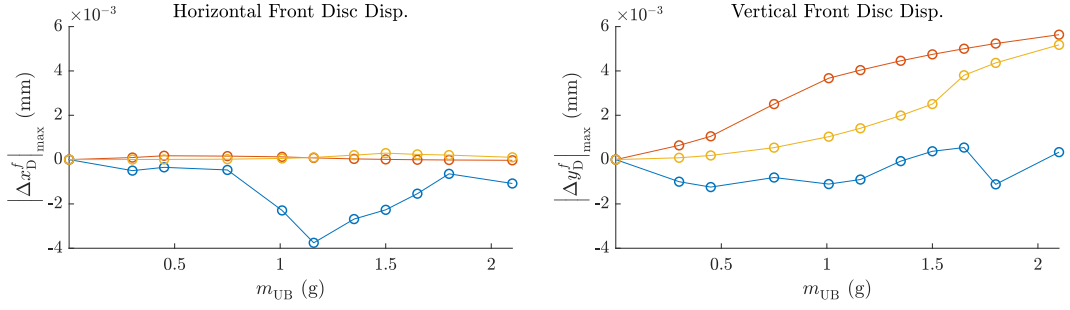
(a) Resonance frequency



(b) Amplitude of front disc displacement



(c) Amplitude of interface plate force



(d) Centre of front disc orbit

Figure 6.29: Backbone curve for different floating bearing models

The experimental results, on the other hand, show a significant monotonic reduction in the resonance frequency as the applied unbalance is increased. For low unbalance levels, there is some agreement with the simulations with the bent rotor. However, no set of bearing parameters were able to capture the softening effect at high unbalance levels. Although this could indicate a deficiency of the bearing model, the bearing model was already validated using results from BELOS. Therefore, it seems much more likely that there are other un-modelled sources of non-linearity on the rig which are more significant than the bearing non-linearity in this regime. The most obvious candidate is the fixed bearing support, since this contains many joints leaving a lot of potential for frictional non-linearities. Another potential source of non-linearity are the TranTorque adapters connecting the discs to the shaft, but the overall damping contribution from the rotor was found to be small from the hammer tests. It also seems unlikely that this non-linearity can be attributed to the floating bearing, since this would introduce a softening effect which would eventually saturate, as with the fixed bearing. Given that this effect was not believed to be associated with the bearings, and the scope of this project was to investigate the vibration transmission through the bearing, this was not investigated further. However, it does highlight the relatively small impact of bearing non-linearities in a realistic rotating machine.

Disc response The synchronous frequency response function was estimated by dividing the maximum disc response by the excitation force from the applied unbalance (excluding the additional unmeasured excitation from the shaft runout and residual unbalance). This is plotted in Fig. 6.29b as a function of the unbalance level. The experimental results show a drop in the peak response as the unbalance mass is increased. This effect can be attributed to the runout and residual unbalance of the rotor, since this drop in the peak response is only captured by the model with the bent rotor. When the applied unbalance is small, the response of the rotor is increased significantly by the shaft runout and residual unbalance. Therefore, the FRF magnitude is much higher than predicted by a perfectly straight rotor in this region. However, at larger unbalance levels, the excitation from the applied unbalance dominates, so the FRF is very similar for a straight or bent rotor.

Bearing transmissibility The maximum force reacted by the interface plate was divided by the excitation force from the applied unbalance to yield the transmissibility ratio plotted in Fig. 6.29c. As was found with the disc response, the peak transmissibility was found to reduce as the unbalance level was increased. Again, this can be attributed to the influence of the shaft runout and residual unbalance, since the transmissibility is insensitive to unbalance level for the case of the straight rotor.

The model with the bent rotor appears to substantially over-predict the transmitted force at lower unbalances, but is much more accurate at higher unbalance levels. This suggests that the model has not accurately captured the influence of the shaft runout and residual unbalance, which would lead to a larger discrepancy at low unbalance levels. The peak transmissibility remains constant for the case of a straight rotor (in yellow), indicating that although the bearing non-linearity leads to changes in the resonance frequency, it has a negligible effect on the vibration transmission.

Centre of disc orbit The average horizontal and vertical displacement of the front disc at resonance is also shown in Fig. 6.29d. It can be observed that in the simulated response, the rotor moves vertically at resonance, as the excitation level is increased. A similar phenomenon was observed for the Jeffcott rotor study in Section 4.4.3, where the rotor moved toward the central position at resonance for high excitation levels. This is because the effective bearing stiffness increases as the unbalance load increased, due to Hertzian contact stiffening as shown in Fig. 6.25, so that the sag due to the vertical preload from self-weight reduces.

In the experimental results, there is some evidence that the disc moves upward for $m_{\mathrm{UB}} > 1\,\mathrm{g}$ which would agree with the predictions from the model. However, the experimental results show a downward motion for lower unbalance levels, which is not predicted by the model. In addition, there is evidence that the disc moves horizontally at resonance in the experimental data, which is not predicted by the model because the rig is assumed symmetrical in the vertical plane. The experimental results suggest that there is some source of asymmetry in the system, which is most likely from the bearing support structure; even though a torque wrench was used to tighten all of the bolts, some small discrepancies between the bolts will remain. This provides further evidence that the non-linear behaviour observed at larger unbalance levels may in fact be attributable to the support structure.

6.5.4.6 Summary

The non-linear unbalance response of the ARES rig has been investigated experimentally at the first pair of critical speeds for a range of unbalance levels. The unbalance response was also computed numerically using the ROLADYN model and the HBM for the same unbalance levels, whilst incorporating the identified shaft runout and residual unbalance of the rotor. The frequency response from the model was compared to the experimental data, and it was found that the response of the rotor at the primary resonance (due to the FW mode) was captured well. In addition, the model accurately predicts the force transmitted through the bearing to the interface plate.

The non-linearity of the system was assessed by analysing the sensitivity of the response at resonance to the unbalance level. It was found that the resonance frequency varied only very slightly indicating that the system was only lightly non-linear. This agrees with the analysis of the bearing stiffness using the quasi-static bearing model, where it was demonstrated that the non-linearity of the fixed bearing is significantly reduced by the compliance from the support structure.

It was then assessed how much of the observed non-linearity could be attributed to the fixed bearing. From the simulations with the ROLADYN model, an initial softening characteristic due to clearance was expected, followed by a small stiffening characteristic at higher unbalance levels, due to the Hertzian contacts. However, in the experimental results, a strong softening non-linearity was observed over all unbalance levels. It was suggested that, while the softening effect at low unbalance levels may be due to the bearing, the softening effect at high unbalance levels likely originates from other frictional non-linearities on the rig, which are more significant than the bearing non-linearities.

6.6 Summary

In this chapter, the ARES setup was optimised in order to maximise the influence of the fixed bearing as explained in Section 6.2, thereby accentuating its non-linearity. The remaining unknown damping parameters were identified from hammer testing, and the ROLADYN was shown to accurately predict the natural frequencies of first two pairs of modes to within 2 %. The Campbell diagram was computed numerically from the ROLADYN model, and it was found that the modes diverged by around 5 Hz at a speed of 50 Hz due to gyroscopic loads. These results were validated using asynchronous PEA excitation, which allowed the bifurcation of the first two pairs of modes to be observed experimentally. In this way, the linear dynamics of the model were fully validated in both a non-rotating and rotating setting.

The attention then moved onto the forced response of the rig, with a particular focus on the influence of the fixed bearing. It was demonstrated using the quasi-static bearing model that variable compliance is negligible for the fixed bearing on ARES. This is primarily due to the larger number of elements within the bearing, but also due to the compliance of the support structure which is in series with the bearing. These predictions were confirmed experimentally by examining the spectrum of the rig response during a ramp-up, where no content at the BPF was observed. This result indicates that variable compliance can likely be neglected as an excitation source in many applications, unless the rotor is very rigidly supported or has very few elements.

The rig was then excited by various levels of unbalance on the front disc. Both the response of the front disc and the force transmitted through the bearings to the interface

plate were analysed. It was found that there was a primary resonance corresponding to the FW mode, and that the model predicted the response in this region very well, including the peak transmitted force. However, the BW mode was also quite prominent in the experimental results, but this was not predicted by the model. This discrepancy was attributed to inaccuracies in the bearing support model or identified shaft runout and unbalance.

The influence of the bearing non-linearities was then considered, and it was found that the rig displays a small but consistent softening characteristic, whereby the resonance frequency reduces as the unbalance level is increased. Once the identified runout and residual shaft unbalance were incorporated into the model, it was found that the model could capture this behaviour at lower unbalance levels. However, the model was unable to capture the softening non-linearity at larger excitation levels, so it was concluded that there are other sources of non-linearity such as friction at the joints which are more significant in this regime. This suggests that in industrial rotating machines, it may be sufficient to model the bearings as linear elements, to predict the vibration transmission between the rotors.

The results demonstrated that the ROLADYN model of the ARES rig, incorporating the quasi-static bearing model, was able to accurately predict the response of the rotor, as well as the force transmitted through the bearing. In addition, the non-linear bearing model was partially validated, since it was able to capture some of the observed non-linear behaviour. However, there appear to be other sources of non-linearity on ARES which are much more significant.

Chapter 7

Conclusions

7.1 Summary of the thesis

The motivation behind this thesis was to investigate the non-linear transmission of vibrations through rolling-element bearings, with a view to developing an improved understanding of the "cross-shaft coupling" phenomenon in aero-engines. The three main objectives were as follows:

1. *Develop a simplified REB model for rotordynamic applications and any associated numerical methods.*
2. *Provide physics-based explanations for the influence of REB non-linearities in rotating machines.*
3. *Experimentally validate the REB modelling approach using a rotordynamic test rig.*

The first objective was to provide the necessary tools to predict the vibration transmission through rolling-element bearings in rotating machinery. The second objective was to provide a better insight into the problem, and the significance of the different mechanisms at play within the bearing, which is useful for diagnosing problems which may arise within industrial rotating machines. The final objective was to develop confidence in the modelling approach, by validating the predictions using a realistic rotating test rig. The work carried out to achieve these objectives will now be summarised.

7.1.1 Modelling of rolling-element bearings for rotordynamic applications

In order to ensure that the response of a rotor-bearing system is accurately predicted, as well as the vibration transmission across the bearing, it is necessary to develop a

sufficiently detailed bearing model. In Section 3.2, a quasi-static bearing model was introduced based upon the existing literature. This was a physics-based model incorporating the influence of the internal clearance and non-linear Hertzian contacts. This model could predict both the radial and tilt-stiffness of the bearing.

The effect of dynamic loads on the elements, due to the rolling and spin motion of the elements, was incorporated into the model using the approach from Harris [45]. This requires the unknown deflections of the elements to be solved for numerically, in order to satisfy radial and axial equilibrium of the elements. On the other hand, it was demonstrated how a simplified approach can be used [46] at low speeds, when the dynamic loads can be neglected. Although both approaches are well-established, the physical significance of the two models, as well as their equivalence at low speeds, has never been highlighted before.

The model was also able to capture the time-varying nature of the bearing stiffness due to variable compliance, which has often been ignored in previous studies, whilst remaining fast to evaluate. However, it was shown how these fluctuations can be explicitly smoothed out using a Sjovall-integral formulation, where the discrete bearing elements are replaced with a continuous domain. This yields an accurate estimate of the average bearing stiffness. Although the application of the Sjovall-integral formulation has been used previously for static analyses, this is the first time it has been used for rotordynamic purposes.

In the Jeffcott rotor study in Chapter 4, the modular nature of the model was highlighted. It was shown how the same model can be reduced to a 2DOF model, for the case where there is only planar motion. In addition, since the model is physics-based, it is simple to augment with additional features; for example, ring compliance was incorporated into the model in Section 4.1.3.1. This model is therefore applicable to a wide variety of rotating machines.

7.1.2 Efficient simulation of rotor-bearing systems using HBM

Due to the time-varying nature of the rolling-element bearing model presented in Section 3.2, efficient numerical techniques were required to be able to predict the periodic response of the complete rotor-bearing system. This is because the variable compliance of the bearing introduces self-excitation from the bearing at the BPF, which is not commensurate with the synchronous unbalance excitation in the general case, and the response becomes quasi-periodic. For this reason, existing studies either ignore the effect, or resort to expensive time-integration to compute the response.

In this thesis, it was demonstrated in Section 4.3 that the Generalised Harmonic Balance Method can be applied in a novel way to predict the non-linear periodic response of

such rotor-bearing systems, whilst incorporating the variable compliance of the bearing. This involves the introduction of a multi-dimensional time domain, where one time axis corresponds to rotation of the rotor, and another relates to rotation of the bearing cage. This approach was able to predict the presence of sub-resonances due to the self-excitation from the rolling-element bearing. At the same time, the GHBM is significantly more computationally efficient than time-integration.

In other systems, the variable compliance is negligible. For example, the fixed bearing on ARES was found to have negligible variable compliance, due to its large number of elements, and the effect was further attenuated by the support compliance in series with the bearing. It was demonstrated in Chapter 6 that the response then becomes periodic, so that conventional HBM can be applied using the rotor speed as the single base frequency.

The range of numerical techniques developed in this thesis will allow the forced response of rotating machines to be analysed more accurately than was previously possible, by incorporating fully non-linear models of each bearing. This will be a valuable tool for future studies into cross-shaft coupling phenomena.

7.1.3 Parametric study of a rotor-bearing system

In order to develop a deep understanding of the influence of REBs on rotor-bearing systems, an in-depth numerical study was performed into the non-linear unbalance response of a Jeffcott rotor in Chapter 4. The bearing was modelled using the high-fidelity quasi-static bearing model from Section 3.2. The rotor parameters were chosen so that the system remained deterministic, displaying periodic or quasi-periodic responses, which is the regime most relevant to real industrial machines. This contrasts with much of the existing literature which focus on the highly non-linear regime where response is often chaotic.

The system was found to have distinct horizontal and vertical resonances due to the asymmetry introduced by the rolling-element bearing, as shown in Section 4.4. The response was found to be highly nonlinear, with both softening and stiffening behaviour present, and the vibration transmission through the bearing was found to increase with the amplitude of excitation. For the first time, these effects were explained by studying the non-linear bearing stiffness. The periodic response was found to loose stability around the resonance peak for certain excitation levels, which is governed by the bearing clearance. Super-harmonic self-excitation from the VC effect was observed; this was found to lead to sub-resonances where the BPF coincided with the frequency of the horizontal and vertical modes. This effect could only be captured with the time-varying bearing model.

A systematic parameter study was then carried out in Section 4.5, allowing, for the first time, the significance of four key physical mechanisms to be quantified on the same system. In addition, the influence of the parameters on the bearing stiffness was investigated, which helped to interpret the changes in the forced response. It was shown that bearing clearance has by far the largest influence on the dynamic response of the rotor, leading to strong nonlinear effects and controlling the stability of the system. It was also found to amplify the self-excitation due to the VC effect. Only the addition of a soft support compliance around the bearing was found to limit this nonlinear behaviour by linearising the system; when the stator was around a fifth of the bearing stiffness, the effect of the bearing non-linearity was negligible. Ring compliance and centrifugal loading had only a small impact on the nonlinear dynamic response of the rotor, suggesting that they may generally be neglected, although they may become of relevance for heavily unbalanced machines and high speed applications respectively. A much improved understanding of the different physical mechanisms within the bearing was developed, and in particular the interaction between the softening effect from bearing clearance and the stiffening effect to the Hertzian contacts. This will aid diagnosis of future vibrations in other rotating machines.

7.1.4 Validation of non-linear bearing model using a static bearing test rig

In Section 5.2, a bearing test rig known as the BEaring LOading System (BELOS) was presented, which was novel in its simplicity. This was a purpose-built test rig, designed specifically for measuring the load-displacement relation of a bearing in a lab environment, without complex machinery. The bearing was statically loaded using weights via a pulley system, and the relative bearing displacement was measured using laser displacement sensors.

From the experimental data, it was shown that the bearing stiffness is heavily non-linear, with a strong stiffening characteristic due to the Hertzian contacts. Critically, unlike existing test rigs found in the literature, it was possible to apply bi-directional horizontal loads to the bearing, which meant that the deadband at low loads due to clearance could be measured. To the author's knowledge, this is the first time the internal clearance of a bearing has been measured in this way.

The results from BELOS were used to parameterise the quasi-static bearing model from Section 3.2. The unknown Hertzian contact stiffness coefficient and radial clearance were identified by tuning the model parameters to match the experimental results in a least-squares sense. The agreement of the updated model with the experimental data was found to be very good, thereby further validating the quasi-static bearing model. It can

now be used to analyse cross-shaft coupling phenomena with more confidence.

7.1.5 Investigations into non-linear vibration transmission on a rotor-bearing test rig

The ARES rotordynamic rig was introduced in Chapter 5, which is an existing test facility at Imperial College. Well-correlated models of each of the subsystems of ARES were developed with extensive component-level testing. The test bearing from ARES was parameterised using BELOS, as explained previously. The bearing support structure turned out to have a particularly large influence on the vibration transmission through the bearing, and therefore a low-order lumped-mass model was developed based on the results from hammer tests. However, since the support structure contains many joints, there was some inherent variability during assembly, which made parameter identification difficult. To mitigate this, the unknown parameters were identified by tuning the model to minimise the error with the experimental results in a least-squares sense. A similar approach was applied to parameterise a 1D FE model of the rotor. This approach was found to be a robust method for parameterising models of jointed structures, and may be a useful tool in the development of low-order rotor and stator models for future investigations into cross-shaft coupling.

The complete model of the ARES rig was then used to investigate the influence of the bearing non-linearities on the forced response and vibration transmission over the course of Chapter 6. After optimising the rig setup to maximise the influence of the non-linearity from the fixed bearing, the rig was assembled and the remaining unknown damping parameters were identified from further hammer tests. The Campbell diagram was measured experimentally using asynchronous base excitation, which allowed the bifurcation of the first two pairs of modes due to gyroscopic effects to be observed experimentally. The numerical model was found to predict the natural frequencies with only an error of around 2 %. It was found that the support structure had a particular large influence on the second pair of modes, whereas the first pair of modes were rotor-dominated. This work resulted in a fully-validated, low-order model, capable of accurately predicting the rotor response and vibration transmission in the linear regime.

Once the linear dynamics of the numerical model had been completely validated, the forced response was investigated. It was demonstrated using the quasi-static bearing model that variable compliance is negligible for the fixed bearing in ARES. This was confirmed experimentally by examining the spectrum of response of the rig, where no content at the BPF was observed. This justifies the existing practice in industry of neglecting the variable compliance of bearings, particularly when the bearing has many elements or the compliance in series with the bearing is high as was the case on ARES.

However, previous results from the Jeffcott rotor study in Chapter 4 demonstrated that this is not true for all bearings and the designer must take extra care when deciding if it is significant or not. As was demonstrated in Section 6.5, this can be predicted by analysing the sensitivity of the bearing stiffness to cage angle, and does not necessarily require a simulation of the complete rig.

The rig was then excited by various levels of unbalance. It was found that the vibration transmission through the bearing was predicted accurately by the model, to an accuracy of around 20 %. The non-linear behaviour was then considered, and it was found that the rig displayed a consistent softening characteristic, whereby the resonance frequency reduced as the unbalance level was increased. Although the non-linearity was small, this is one of the first times that such shifts in resonance frequency have been observed experimentally in rotating machinery. Once the runout and residual shaft unbalance were identified from the experimental data and incorporated into the model, it was found that the model could capture this behaviour at lower unbalance levels. This provided some evidence that the non-linearity in this regime was due to the fixed bearing, and therefore validated the predictions from the numerical model. However, it was suggested that non-linearity at higher unbalance levels could be attributed to the supporting structure, due to the many joints. This highlights that it may be more important to consider the non-linearity from the joints in the rotor or stator rather than the bearings themselves, when attempting to predict the cross-shaft coupling. Therefore, this suggests that the current practice of modelling bearings with linear elements may often be sufficiently accurate for predicting the vibration transmission between rotors.

7.2 Main contributions

The original contributions made during this thesis have been summarised below:

- The well-established quasi-periodic approach for modelling bearings was used to develop a high-fidelity yet lightweight model of a ball-bearing in Section 3.2. This is able to capture the influence of internal clearance, Hertzian contacts and dynamic loading on the elements. In Section 4.1.2, it was shown how this model can be further simplified to study planar systems. This model was later validated experimentally using BELOS in Section 5.2, so can therefore be used to accurately predict the non-linear bearing stiffness in rotating machines.

- A systematic parameter study was performed on a Jeffcott rotor supported by a rolling-element bearing using this bearing model, as presented in Section 4.5. For the first time, the relative significance of the different physical mechanisms within

the bearing was quantified on the same system. This has been published as part of a journal paper [182].

- A novel application of the Generalised Harmonic Balance method was presented in Section 4.3, for efficient simulation of rotor-bearing systems whilst incorporating the time-varying nature of the bearing stiffness. This is capable of capturing the quasi-periodic nature of the response as well as self-excitation from the bearing. This has also been published as part of a journal paper [182].

- The BEaring LOading test rig (BELOS) was designed and built, in order to experimentally measure the bearing stiffness in a lab setting without specialised machinery. In Section 5.2, it was shown to be possible to identify the Hertzian contact stiffness and internal clearance from only the load-displacement relation. This work has been published in a conference paper [189].

- A high-fidelity model of the complete ARES test rig was developed over the course of Chapter 5. This was used to investigate the vibration transmission and influence of the rolling-element bearing, but will also be an invaluable tool for studies into other rotordynamic phenomena at Imperial College in the future.

- In Chapter 6, the effect of bearing non-linearities on the forced response, as well the force transmitted through the bearing, was observed in an experimental setting for the first time using the ARES test rig. The predictions from the numerical model were found to agree well with the experimental data. This work will be incorporated into a journal paper.

- The Generalised Harmonic Balance method presented in Section 3.3, which was used to simulate the forced response of the systems studied in this thesis, was implemented within a MATLAB toolbox known as HarmLAB. This was written in a generic way, so that it is capable of simulating any system governed by a 1st or 2nd ODE. Unlike existing solvers, this is able to predict both periodic and quasi-periodic responses. This has been released as an open-source toolbox [180], so can be used as a basis for future research.

7.3 Future work

There are many areas for extension of the work presented in this thesis. In addition, there were some gaps in the literature which were not chosen as the focus of this work, but could be investigated in the future.

7.3.1 Flexible support configuration on ARES

A low-order model of the bearing support structure was developed and parameterised in Section 5.4. This model was able to capture the dynamics in both the rigid configuration, where the bearing housing was rigidly fixed to the interface plate; and the flexible configuration with compliant support rods between the bearing housing and interface plate. Unfortunately, the experimental test programme on ARES was interrupted by the COVID-19 pandemic, during which there was no access to the lab. Therefore, the response of the rig could only be investigated with the rigid bearing configuration. It was expected that the influence of the bearing would be attenuated by the introduction of the support rod compliance in the flexible configuration, so the rigid configuration was prioritised.

It was found from the Jeffcott rotor study in Section 4.5 that stator compliance linearises the system, and reduces the influence of the bearing non-linearities on the vibration transmission. Testing with the flexible configuration on ARES would allow this result to be validated in an experimental setting. It may also be possible to confirm that the source of the non-linearity observed in Section 6.5.4 with the rigid configuration was indeed the support structure.

7.3.2 Investigate response to base excitation using ARES

In this thesis, only the transmission of synchronous vibrations was investigated, in order to provide better insight into the problem. However, in a rotating machine with multiple rotors, there will be excitations at different frequencies from each rotor. Therefore, it is important to consider the transmission of *asynchronous* vibrations through the bearings.

This could be investigated using ARES by exciting the interface plate with the PEAs with large voltages. The assumption that the interface displacement is linearly proportional to the applied PEA voltage may break down, due to some interaction between the rotor and stator dynamics as the rig passes through resonance. Therefore, it may be necessary to control the interface plate displacement using closed-loop control. Alternatively, different types of excitation could be considered, such as using electromagnetic shakers, which would instead apply a constant forcing.

7.3.3 Bearing clearance study using ARES and BELOS

It was established in the Jeffcott rotor study that the internal clearance is the most significant source of non-linearity in the bearing. In this project, only a single clearance level was considered, since it was expected that the bearing was loose enough to display

a significant non-linear effect. However, the support compliance was much larger than expected, so this turned out not to be the case. However, it would be of interest to vary the clearance of the fixed bearing on ARES, and to investigate the sensitivity of the dynamic response to bearing clearance. No such parameter study has ever been attempted before.

The clearance of the fixed bearing on ARES can be varied by tightening the adapter sleeve by different amounts. The BELOS test rig could be used to measure the load-displacement relationship for each adapter sleeve tightening angle, in order to map the relation between adaptor sleeve angle and radial bearing clearance. Dynamic tests could then be carried out for each clearance level on ARES. It may be advantageous to directly measure the displacement across the bearing using additional sensors.

It would be expected that the resonance frequency at low unbalance levels should be sensitive to the clearance level. In addition, increased clearance should both amplify the self-excitation due to the variable compliance of the bearing, and lead to changes in the vibration transmission through the bearing. Such an experimental study would allow the results from the Jeffcott rotor parameter study in Section 4.5.1 to be confirmed experimentally.

7.3.4 Development of an advanced bearing damping test rig

It was found from the literature review that the understanding of damping from rolling-element bearings is particularly poor. Although the focus of this thesis was on the stiffness non-linearities in REBs which are generally more significant, the damping will also influence the transmissibility of the bearing. Many existing studies have either been purely computational, or have only been able to investigate the sensitivity to a limited range of parameters such as rotor speed or radial preload.

It could be beneficial to design a new advanced bearing test rig, which allows a wide variety of parameters related to bearing damping to be controlled. In particular, it should be possible to vary the fit of the bearing housing, since it is known that this joint is one of the largest sources of energy dissipation. If the bearing is excited harmonically, it may also be possible to use this rig to measure the non-linear bearing stiffness at the same time, thereby incorporating the functionality of BELOS.

7.3.5 Modelling of jointed structures supporting the rotor

It was established in Chapter 6 that the influence of the bearing non-linearity on ARES was small, and that the bearing transmissibility could be predicted to a sufficient level of

accuracy using a linear model. However, there was evidence that there were other significant sources of non-linearity on the rig, which it was proposed could be attributed to the joints in the bearing support structure. It is essential that an improved understanding of such systems is developed, in order to accurately predict the vibration transmission between rotors which are supported by similar flexible structures. Unlike rolling-element bearings, joints can introduce both a softening linearity due to micro-slip, as well as significant damping due to frictional losses, and therefore play a large role in the maximum transmitted force at resonances. This also means that their behaviour is quite unpredictable, so that stochastic approaches may be necessary.

Appendix A

HarmLAB: derivation of analytical derivatives

The Generalised HBM was introduced in Section 3.3 for the case of two fundamental frequencies. It was stated that is possible to write the equation enforcing Harmonic Balance in the following algebraic form:

$$\boldsymbol{r}(\boldsymbol{z},\boldsymbol{\omega}) = \boldsymbol{L}(\boldsymbol{\omega})\boldsymbol{z} + \boldsymbol{h}\left(\boldsymbol{\omega},\boldsymbol{z}\right) + \boldsymbol{g}\left(\boldsymbol{\omega}\right) = \boldsymbol{0}$$

where $\boldsymbol{z}$ is a vector of phasors and the term $\boldsymbol{h}\left(\boldsymbol{\omega},\boldsymbol{z}\right)$ contains the contribution from the non-linearities. It was demonstrated in Section 3.3.4 how this can be computed an Alternating Frequency-Time approach. It was also shown how the frequency response can be computed using HBM using continuation, which requires computation of the derivatives of the residual vector $\boldsymbol{r}$. In order to avoid numerical differentiation which would otherwise become computationally expensive for large numbers of harmonics, it is useful to derive analytical expressions for the required derivative terms. The approach implemented in HarmLAB will now be presented.

A.1 Alternating Frequency-Time

The AFT approach presented in Section 3.3.4 was only expressed in terms of the phasors $\boldsymbol{X}_{k_1,k_2}$. In order to eventually be able to compute analytical derivatives the residual $\boldsymbol{r}$, it is necessary to first re-express the AFT approach in terms of the vector $\boldsymbol{z}$:

$$\boldsymbol{z} \xrightarrow{\boldsymbol{Q}} \boldsymbol{x}(t_1,t_2) \rightarrow \boldsymbol{f}_{nl}(\boldsymbol{x}(t_1,t_2),\dot{\boldsymbol{x}}(t_1,t_2),) \xrightarrow{\boldsymbol{P}} \boldsymbol{h}\left(\boldsymbol{\omega},\boldsymbol{z}\right)$$

This allows the non-linear term $\boldsymbol{h}$ to be computed more efficiently, and will ultimately simplify the required analytical derivatives.

A.1.1 Converting from frequency to hyper-time domain

The first stage is to convert the vector $\boldsymbol{z}$ into the hyper-time domain to yield $\boldsymbol{x}(t_1, t_2)$, which can be achieved by introducing the harmonic matrix $\boldsymbol{Q}$ [174]:

$$\begin{aligned}\boldsymbol{Q}(t_1,t_2) = [1 \quad & \cos(\omega_1 t_1) \quad -\sin(\omega_1 t_1) \quad \cdots \quad \cos(\omega_2 t_2) \quad -\sin(\omega_2 t_2) \\ & \cdots \quad \cos(M_1^H \omega_1 t_1 + M_2^H \omega_2 t_2) \quad -\sin(M_1^H \omega_1 t_1 + M_2^H \omega_2 t_2)]\end{aligned} \tag{A.1}$$

so that the equation for the displacements $\boldsymbol{x}$ in Eq. (3.103) can be re-expressed as [174]:

$$\boldsymbol{x}(t_1,t_2) = \left(\boldsymbol{Q}(t_1,t_2) \otimes \boldsymbol{I}_{N_{dof}}\right) \boldsymbol{z} = \boldsymbol{\Gamma}\boldsymbol{z} \tag{A.2}$$

where $\boldsymbol{\Gamma} = \boldsymbol{Q}(t_1,t_2) \otimes \boldsymbol{I}_{N_{dof}}$ is the matrix which maps the vector $\boldsymbol{z}$ to displacements $\boldsymbol{x}$. To compute the velocity vector $\dot{\boldsymbol{x}}$, the following operator denoted by $\boldsymbol{\nabla}_i$ can be introduced, where the subscript i denotes whether the differentiation is w.r.t t_1 or t_2:

$$\boldsymbol{\nabla}_i = \begin{bmatrix} 0 & & & & & \\ & \boldsymbol{\nabla}^i_{1,0} & & & & \\ & & \ddots & & & \\ & & & \boldsymbol{\nabla}^i_{0,1} & & \\ & & & & \ddots & \\ & & & & & \boldsymbol{\nabla}^i_N \end{bmatrix} \tag{A.3}$$

where each submatrix $\boldsymbol{\nabla}^i_{k_1,k_2}$ is given by:

$$\boldsymbol{\nabla}^i_{k_1,k_2} = \begin{bmatrix} 0 & -k_i \\ k_i & 0 \end{bmatrix}$$

which can be seen to swap the sin and cos components, which corresponds to differentiation. The matrix $\boldsymbol{\nabla}^i$ can then be used to differentiate $\boldsymbol{Q}(t_1,t_2)$ by pre-multiplying:

$$\dot{\boldsymbol{Q}}(t_1,t_2) = \boldsymbol{Q}(t_1,t_2)\left(\omega_1\boldsymbol{\nabla}^1 + \omega_2\boldsymbol{\nabla}^2\right) \tag{A.4}$$

This then allows the velocity $\dot{\boldsymbol{x}}$ to be expressed in terms of $\boldsymbol{z}$:

$$\begin{aligned}\dot{\boldsymbol{x}}(t_1,t_2) &= \left(\dot{\boldsymbol{Q}}(t_1,t_2)\otimes \boldsymbol{I}_{N_{dof}}\right)\boldsymbol{z}\\ &= \left(\left(\boldsymbol{Q}(t_1,t_2)\left(\omega_1\boldsymbol{\nabla}_1+\omega_2\boldsymbol{\nabla}_2\right)\right)\otimes \boldsymbol{I}_{N_{dof}}\right)\boldsymbol{z}\\ &= \left(\omega_1\boldsymbol{\Gamma}^1+\omega_2\boldsymbol{\Gamma}^2\right)\boldsymbol{z}\end{aligned} \tag{A.5}$$

where $\boldsymbol{\Gamma}^i = \left(\boldsymbol{Q}(t_1,t_2)\boldsymbol{\nabla}^i\right)\otimes \boldsymbol{I}_{N_{dof}}$. Now that expression for both $\boldsymbol{x}$ and its derivative $\dot{\boldsymbol{x}}$ have been derived, the response of the non-linear components can now be computed in the hyper-time domain.

A.1.2 Converting from hyper-time to frequency domain

The final stage of the AFT process it to convert the non-linear forces $\boldsymbol{f}$ from the hyper-time domain, into the frequency domain to yield the non-linear vector $\boldsymbol{h}(\boldsymbol{z},\boldsymbol{\omega})$. This can be achieved by introducing another harmonic matrix $\boldsymbol{P}(t_1,t_2)$:

$$\boldsymbol{P}(t_1,t_2) = \begin{bmatrix} 1 \\ 2\cos\omega_1 t_1 \\ -2\sin\omega_1 t_1 \\ \vdots \\ 2\cos\omega_2 t_2 \\ -2\sin\omega_2 t_2 \\ \vdots \\ 2\cos M_1^H\omega t_1 + M_2^H\omega t_2 \\ -2\sin M_1^H\omega t_1 + M_2^H\omega t_2 \end{bmatrix} \tag{A.6}$$

which can then be used to re-express Eq. (3.111) in vector form:

$$\begin{aligned}\boldsymbol{h}\left(\boldsymbol{\omega},\boldsymbol{z}\right) &= \frac{1}{T_1T_2}\int_0^{T_2}\int_0^{T_1}\left(\boldsymbol{P}(t_1,t_2)\otimes \boldsymbol{I}_{N_{dof}}\right)\boldsymbol{f}\left(\boldsymbol{x},\dot{\boldsymbol{x}}\right)dt_1dt_2\\ &= \frac{1}{T_1T_2}\int_0^{T_2}\int_0^{T_1}\boldsymbol{\Phi}\boldsymbol{f}\left(\boldsymbol{x},\dot{\boldsymbol{x}}\right)dt_1dt_2\end{aligned} \tag{A.7}$$

where $\boldsymbol{\Phi} = \left(\boldsymbol{P}(t_1,t_2)\otimes \boldsymbol{I}_{N_{dof}}\right)$ is the matrix mapping $\boldsymbol{f}$ to $\boldsymbol{h}$. This completes the derivation of the AFT process in terms of the vector $\boldsymbol{z}$.

A.2 Analytical Jacobians

Now that it has been shown how to compute the non-linear term $\boldsymbol{h}$ term directly from the vector $\boldsymbol{z}$, it is possible to derive expressions of the analytical derivatives of the harmonic balance relation Eq. (3.108). The derivatives w.r.t both the vector $\boldsymbol{z}$ and base frequencies $\boldsymbol{\omega}$ will now be presented.

A.2.1 Jacobian w.r.t the vector z

Differentiating Eq. (3.108) w.r.t $\boldsymbol{z}$ gives:

$$\frac{\partial \boldsymbol{r}}{\partial \boldsymbol{z}} = \boldsymbol{L}(\boldsymbol{\omega}) + \frac{\partial \boldsymbol{h}(\boldsymbol{\omega}, \boldsymbol{z})}{\partial \boldsymbol{z}} \tag{A.8}$$

The term involving the contribution from the non-linearities $\frac{\partial \boldsymbol{h}(\boldsymbol{\omega}, \boldsymbol{z})}{\partial \boldsymbol{z}}$ can be found by differentiating Eq. (A.7):

$$\begin{aligned}\frac{\partial \boldsymbol{h}(\boldsymbol{\omega}, \boldsymbol{z})}{\partial \boldsymbol{z}} &= \frac{1}{T_1 T_2} \int_0^{T_2} \int_0^{T_1} \boldsymbol{\Phi} \left(\frac{\partial \boldsymbol{f}}{\partial \boldsymbol{x}} \frac{\partial \boldsymbol{x}}{\partial \boldsymbol{z}} + \frac{\partial \boldsymbol{f}}{\partial \dot{\boldsymbol{x}}} \frac{\partial \dot{\boldsymbol{x}}}{\partial \boldsymbol{z}} \right) dt_1 dt_2 \\ &= \frac{1}{T_1 T_2} \int_0^{T_2} \int_0^{T_1} \boldsymbol{\Phi} \left(\frac{\partial \boldsymbol{f}}{\partial \boldsymbol{x}} \boldsymbol{\Gamma} + \frac{\partial \boldsymbol{f}}{\partial \dot{\boldsymbol{x}}} \left(\omega_1 \boldsymbol{\Gamma}^1 + \omega_2 \boldsymbol{\Gamma}^2 \right) \right) dt_1 dt_2 \end{aligned} \tag{A.9}$$

where the term $\frac{\partial \dot{\boldsymbol{x}}}{\partial \boldsymbol{z}}$ has been found from Eq. (A.5) and Γ^i is defined in Eq. (A.5). It can be observed that there are two components to the Jacobian; one due to the dependence of the non-linear force on displacement $\boldsymbol{x}$, and another due to the dependence on velocity $\boldsymbol{x}$.

A.2.2 Derivative w.r.t the base frequencies ω

Since the continuation algorithm uses the derivative of Eq. (3.108) w.r.t the vector of base frequencies $\boldsymbol{\omega}$, it will also be useful to derive analytical representations for this term. Differentiating Eq. (3.108) w.r.t a single base frequency ω_i yields:

$$\frac{\partial \boldsymbol{r}}{\partial \omega_i} = \boldsymbol{L}^i(\boldsymbol{\omega}) \boldsymbol{z} + \frac{\partial \boldsymbol{h}(\boldsymbol{\omega}, \boldsymbol{z})}{\partial \omega_i} \tag{A.10}$$

where the matrix $\boldsymbol{L}^i(\boldsymbol{\omega}) = \frac{\partial}{\partial \omega_i} \boldsymbol{L}(\boldsymbol{\omega})$ can be found by simply differentiating Eq. (3.110):

$$\boldsymbol{L}^i(\boldsymbol{\omega}) = \begin{bmatrix} \mathbf{0} & \mathbf{0} & \dots & \dots & \mathbf{0} \\ \mathbf{0} & \boldsymbol{L}_1^i & \dots & \dots & \mathbf{0} \\ \vdots & \vdots & \boldsymbol{L}_2^i & \dots & \vdots \\ \vdots & \vdots & \vdots & \ddots & \vdots \\ \mathbf{0} & \dots & \dots & \dots & \boldsymbol{L}_N^i \end{bmatrix} \tag{A.11}$$

where $\boldsymbol{L}_k^i$ is given by:

$$\boldsymbol{L}_k^i = \begin{bmatrix} -2\omega_{k_1,k_2} k_i \boldsymbol{M} & -k_i \boldsymbol{C} \\ k_i \boldsymbol{C} & -2\omega_{k_1,k_2} k_i \boldsymbol{M} \end{bmatrix}$$

The term $\frac{\partial \boldsymbol{h}(\boldsymbol{\omega},\boldsymbol{z})}{\partial \omega^i}$ from the non-linearities can be found by differentiating Eq. (3.111):

$$\frac{\partial \boldsymbol{h}(\boldsymbol{\omega_i}, \boldsymbol{z})}{\partial \omega_i} = \frac{1}{T_1 T_2} \int_0^{T_2} \int_0^{T_1} \boldsymbol{\Phi} \left(\frac{\partial \boldsymbol{f}}{\partial \omega_i} + \frac{\partial \boldsymbol{f}}{\partial \dot{\boldsymbol{x}}} \frac{\partial \dot{\boldsymbol{x}}}{\partial \omega_i} \right) dt \tag{A.12}$$

$$= \frac{1}{T_1 T_2} \int_0^{T_2} \int_0^{T_1} \boldsymbol{\Phi} \left(\frac{\partial \boldsymbol{f}}{\partial \omega_i} + \frac{\partial \boldsymbol{f}}{\partial \dot{\boldsymbol{x}}} \boldsymbol{\Gamma}^i \right) \boldsymbol{z} dt \tag{A.13}$$

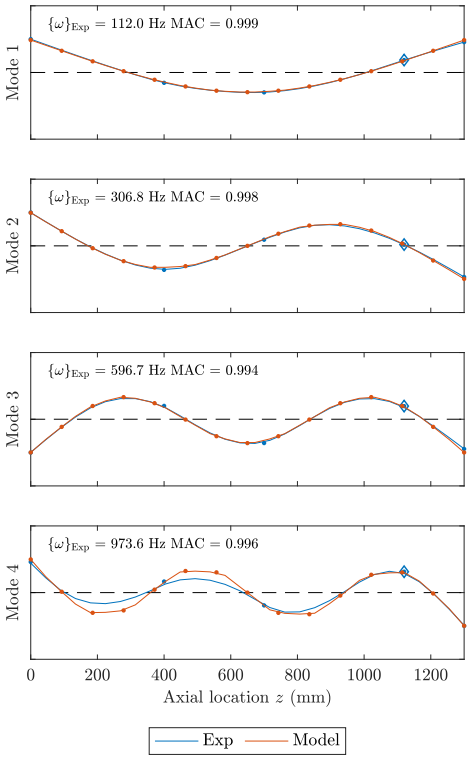
where the term $\frac{\partial \dot{\boldsymbol{x}}}{\partial \omega_i}$ has been found from Eq. (A.5). It can be observed that there are again two components to the frequency derivative; one due to the direct dependence of the non-linear forces on excitation frequency ω_i, and another due to the dependence on velocity $\dot{\boldsymbol{x}}$.

Appendix B

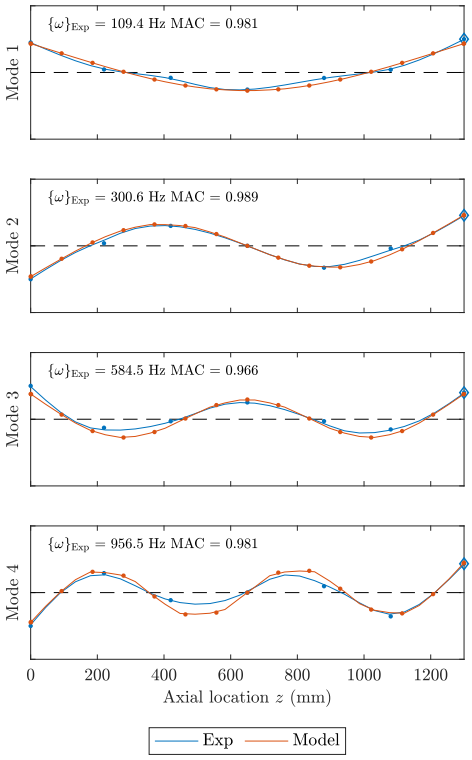
ARES hammer tests

B.1 Rotor

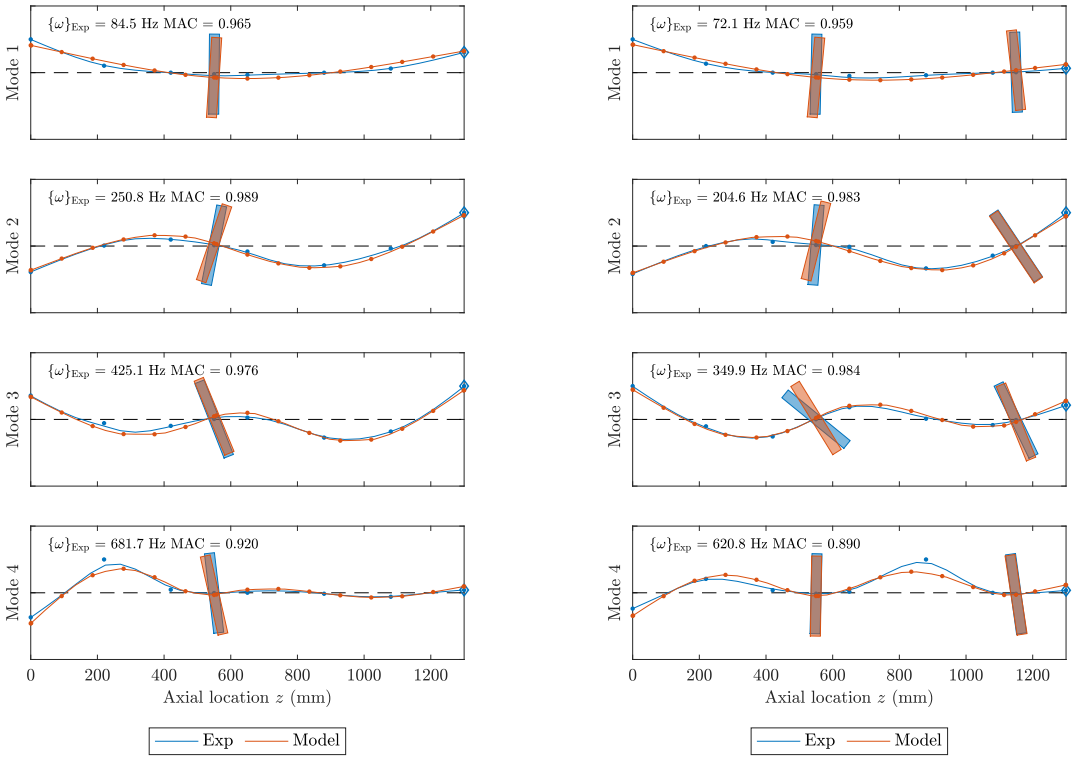
In Section 5.3, the mode shapes of the rotor were only plotted for the configuration with two discs for brevity. The mode shapes for all four of the configurations considered are shown below. It can be observed that the model correlates with the experimental results very well for all rotor configurations.



(a) Shaft only - plain



(b) Shaft only - instrumented



(c) Rear disc (d) Two discs

Figure B.1: Comparison of the experimental and numerical mode shapes of the ARES rotor for different numbers of discs

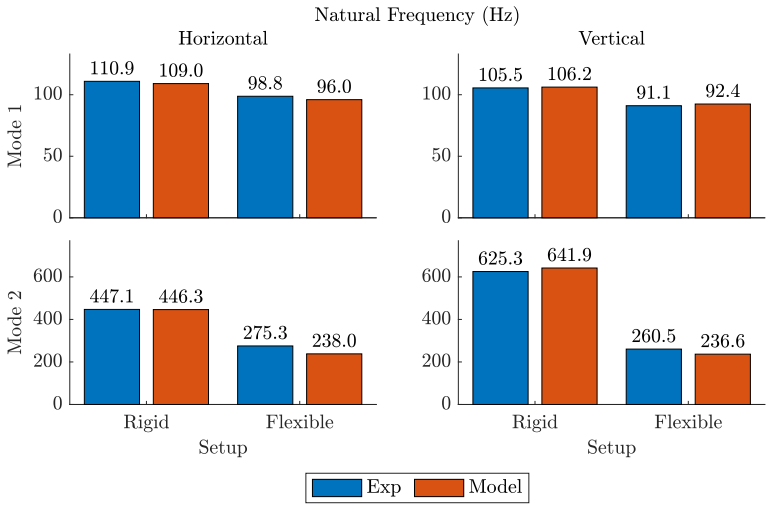
B.2 Bearing support structure

In Section 5.4, only the first order modes were presented in all configurations for brevity. However, in some of configurations with the bearing housing fitted, some second order modes were also visible in the FRFs, which were used in the parameter identification process. The full set of identified modes will now be presented.

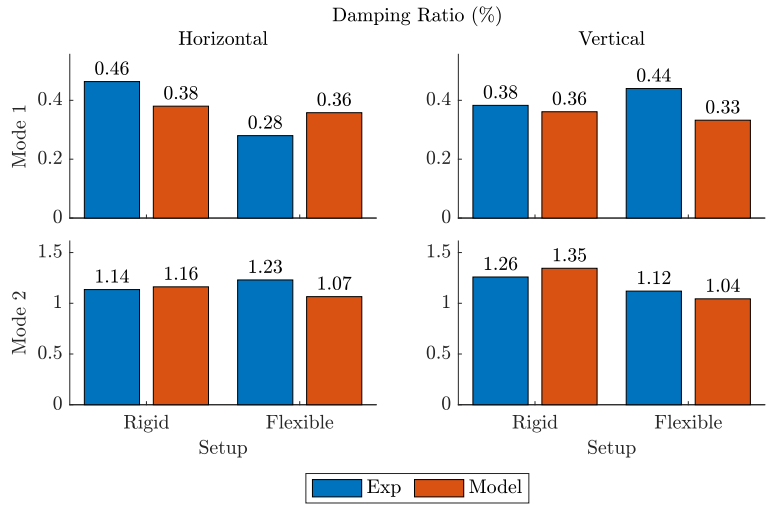
B.2.0.1 Free case with PEAs disconnected

In the free case, without PEAs fitted, two pair of modes were identified in both the rigid and flexible bearing configurations.

Rigid configuration The extra inertia from the bearing housing leads to significant coupling with the L-shape in the second pair of modes, as shown in Fig. 5.39. The L-shape displays significant motion, and deflects in a similar pattern to its own mode shown in Fig. 5.35. The frequencies are only very slightly lower than the modes of the L-shape itself, suggesting that this is an L-shape dominated mode. This has the additional consequence that the horizontal mode has a lower frequency than the vertical mode, due



(a) Natural frequencies



(b) Damping ratios

Figure B.2: Modal properties of the bearing supports (PEAs disconnected)

to the increased torsional inertia of the L-shape. The damping level of these modes is also very close that of the L-shape's own modes.

The second modes do not correlate quite as well as the first order modes, with the vertical mode being over-predicted by 17 Hz. However, since this pair of modes is dominated by the L-shape, it would seem likely this this is highlighting the limitations of the simplified 1DOF L-shape model. However, the much larger damping in the second pair of modes is captured well by the model.

Flexible configuration Once compliance between the bearing housing and interface plate is added from the support rods, the second pair of modes no longer display any significant L-shape motion, as shown in Fig. B.4. Instead, the bearing housing and

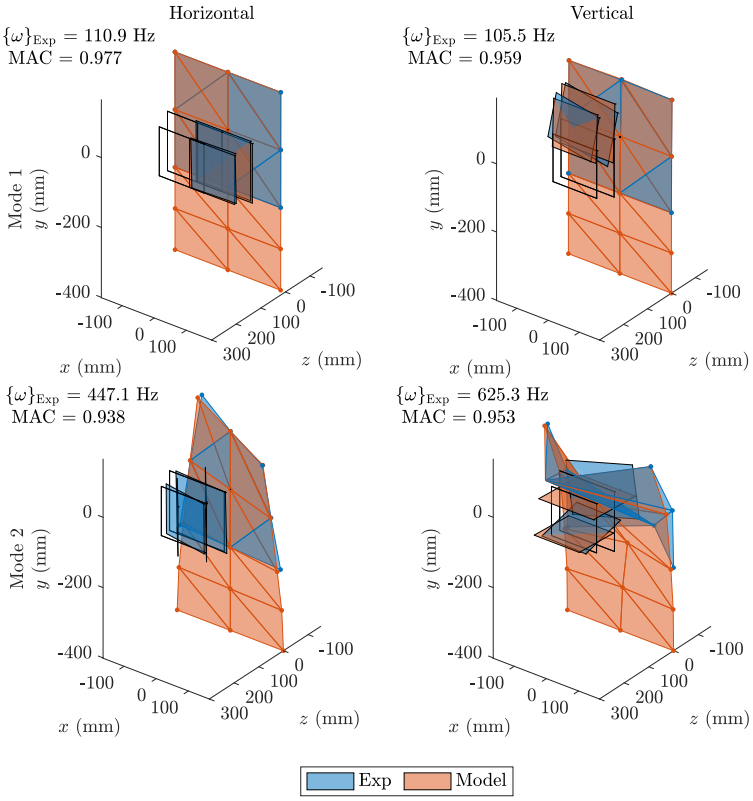


Figure B.3: Mode shapes of the rigid bearing configuration (PEAs disconnected)

interface plate move out of with each other. The frequency of these mode is significantly lower than the second pair of modes with the rigid bearing housing, since both the interface plate and bearing still display significant motion. The separation between the frequencies is significantly under-predicted by the model, was again attributed to some error during assembly.

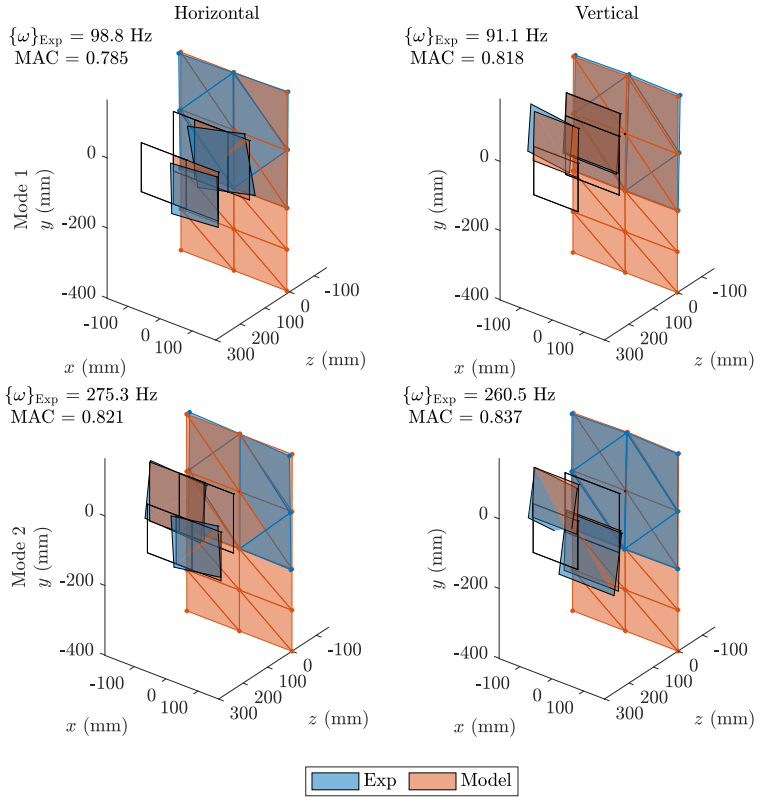
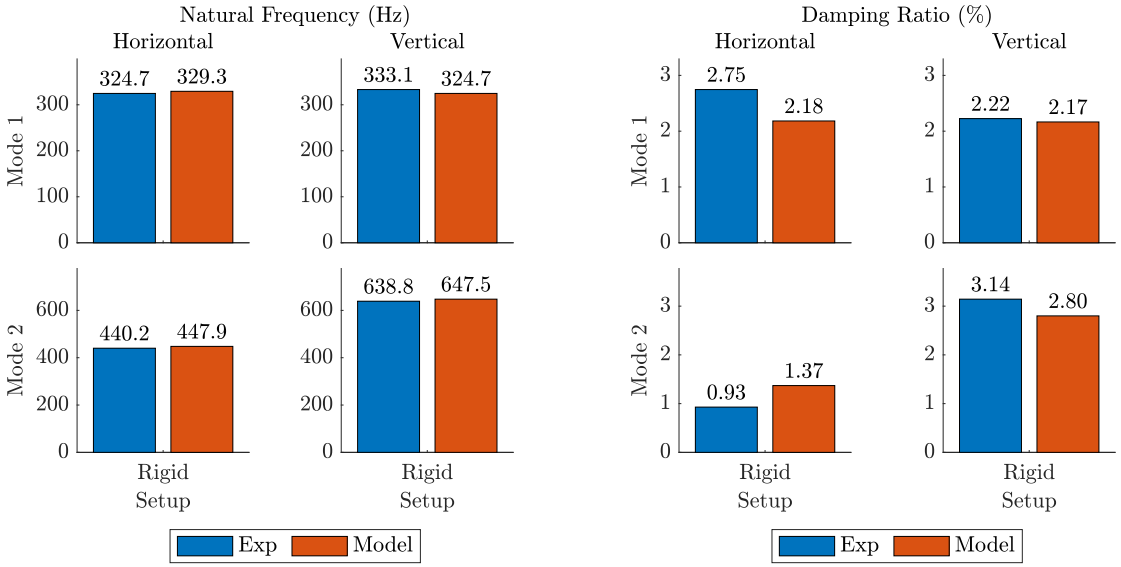


Figure B.4: Mode shapes of the flexible bearing configuration (PEAs disconnected)

B.2.0.2 Fixed case with PEAs connected

Once the PEAs were attached, it was possible to identify a second pair of modes in the rigid bearing configuration, as shown in Fig. B.5. These results will now be discussed in more detail. Note that no second pair of modes was observed for the flexible configuration once the PEAs were fitted.

Rigid configuration The second pair of modes display significant coupling with the L-shape. Since this set of modes displayed little in-plane motion of the interface plate even in the "free" configuration, the addition of the PEAs has little influence, and therefore the frequencies remain nearly unchanged. The damping does however increase significantly (approximately doubling) from the "free" case, which is captured by the model. However, damping ratios of each mode is slightly under- and over-predicted. This suggests that the simple tilt damper within the PEA model may not be sufficient, and it may no longer be valid to assume that the damping from the PEA is symmetric. However, this mode is even further out of the running range of the rig, so this level of agreement was deemed sufficient.



(a) Natural frequencies (b) Damping ratios

Figure B.5: Modal properties of the bearing supports (PEAs connected)

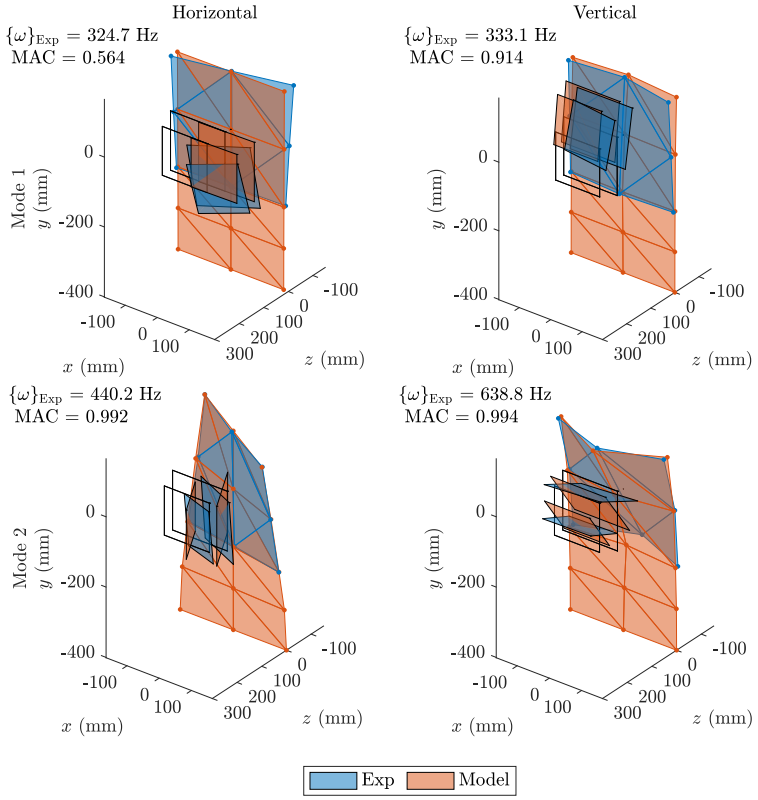
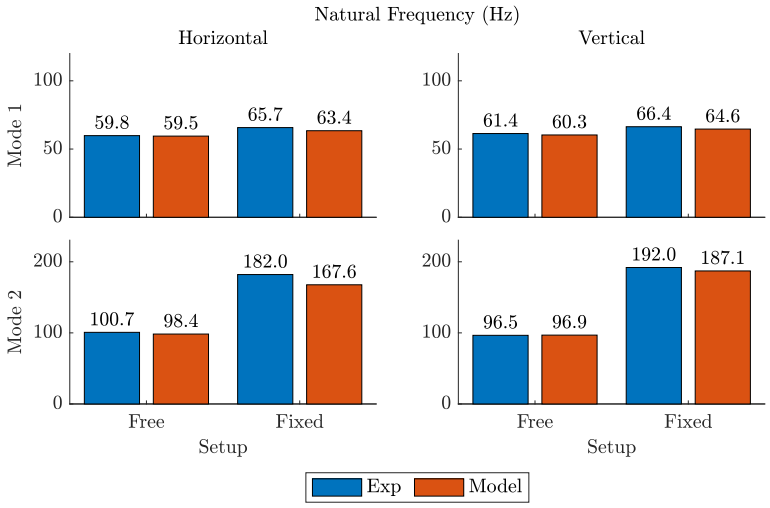


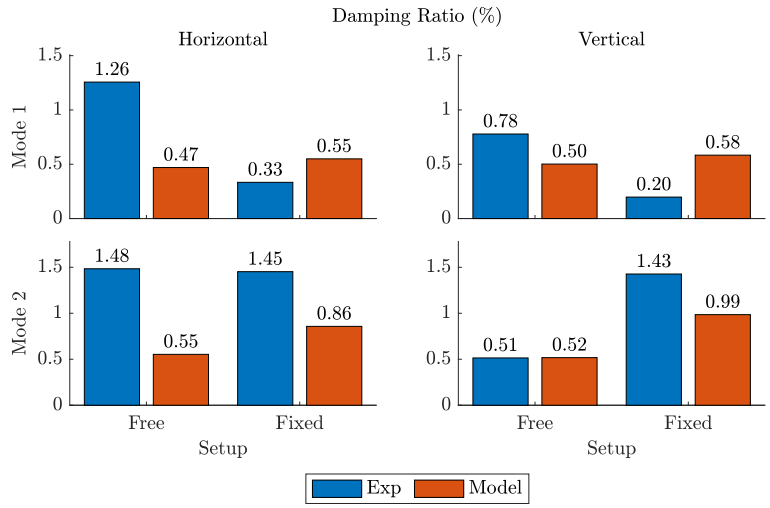
Figure B.6: Mode shapes of the rigid bearing configuration (PEAs connected)

B.3 Complete rig

As explained in Section 6.4, the rig was gradually assembled into the final configuration, with hammer tests carried out at each stage. Only the results from the final stage of assembly, where the discs were fitted, were plotted in Section 6.4. The results from the earlier stages of assembly will be presented here.



(a) Natural frequencies



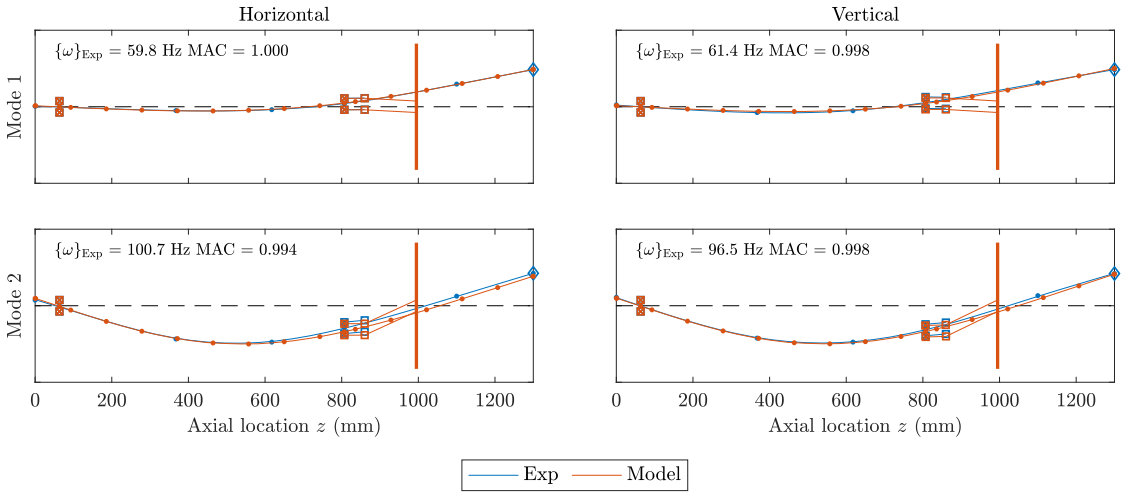
(b) Damping ratios

Figure B.7: Comparison of the experimental and numerical modal properties of the ARES rig with and without the PEAs connected

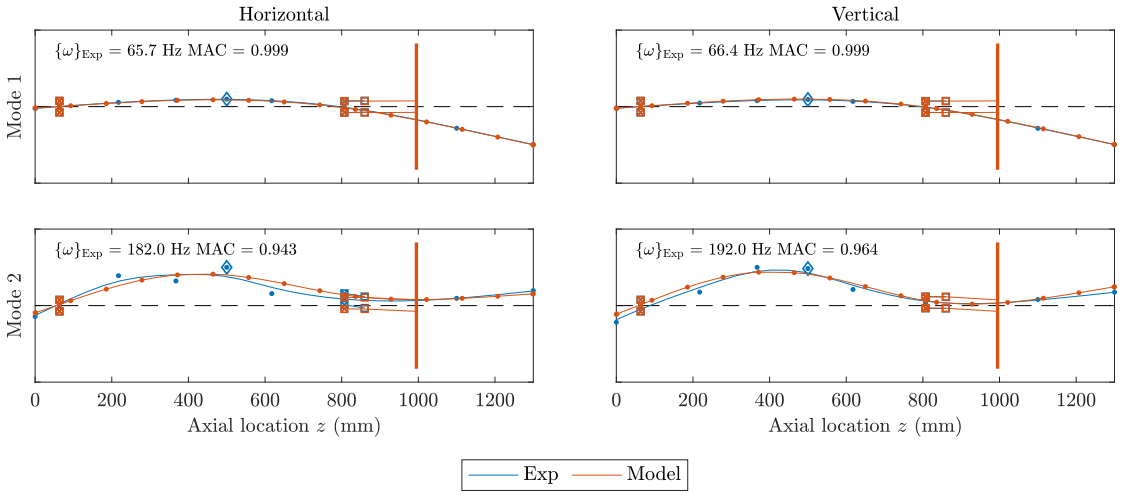
B.3.1 Installation of PEAs

Hammer tests were first carried out with only the shaft fitted without any discs. The PEAs were not fitted to the bearing housing, in order to amplify the effect of the bearing

support structure. The PEAs were then fitted, and the hammer test was repeated. The modes for both configurations are shown in Figs. B.7 and B.8.



(a) Free (PEAs disconnected)

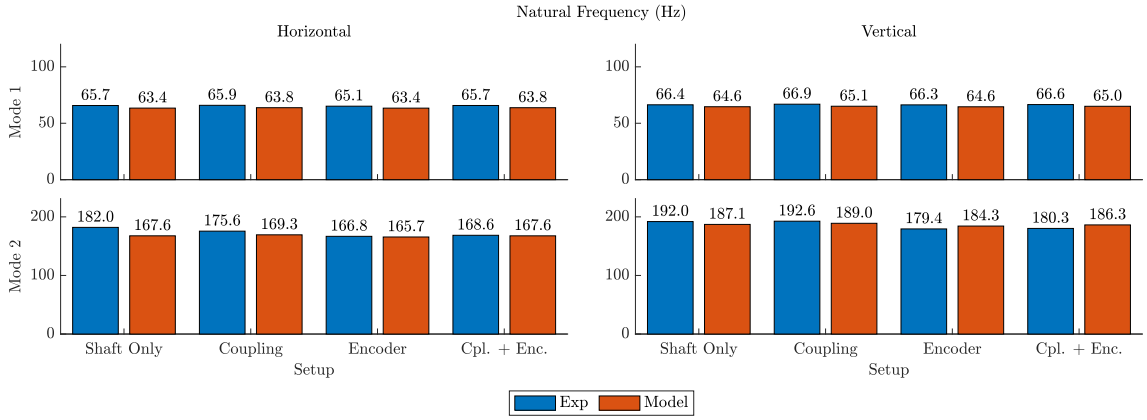


(b) Fixed (PEAs connected)

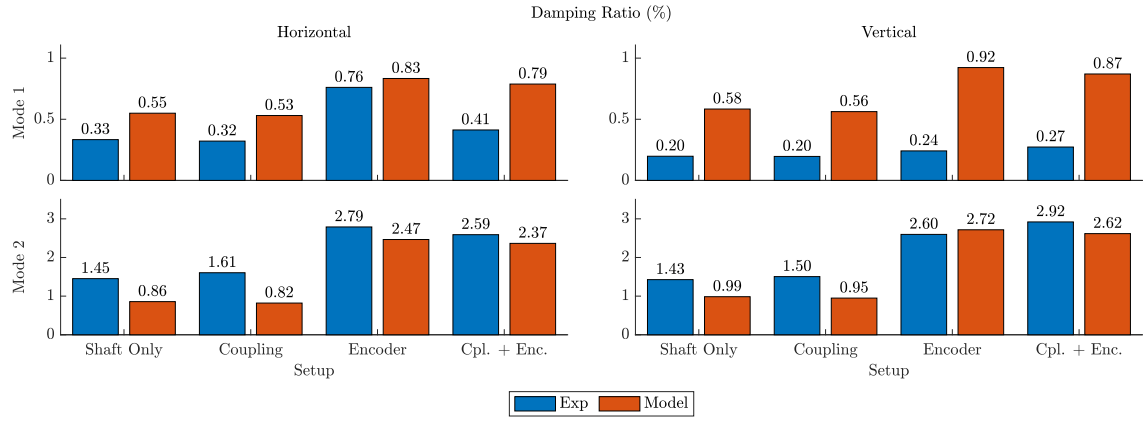
Figure B.8: Comparison of the experimental and numerical mode shapes of the ARES rig with and without the PEAs connected

B.3.2 Ancillary components

The ancillary components were added next, which were expected to have only a small influence on the structure. The natural frequencies and damping ratios are plotted in Fig. B.9. It can be observed that the effect of the ancillaries on the frequencies was minimal, but that damping ratio increased once the encoder was fitted. The mode shapes have not been plotted since the impact of the ancillaries was found to be minimal.



(a) Natural frequencies

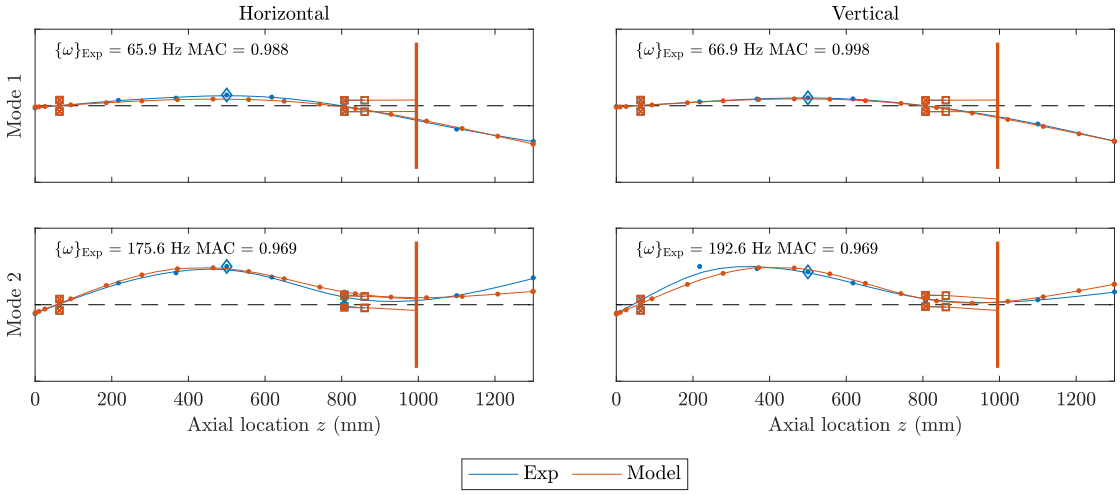


(b) Damping ratios

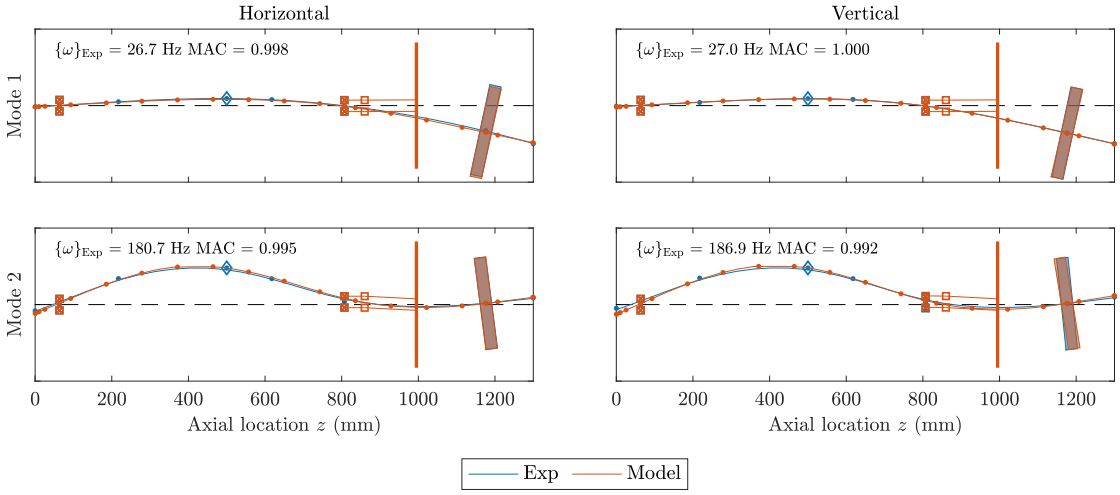
Figure B.9: Comparison of the experimental and numerical modal properties of the ARES rig with different ancillary components connected

B.3.3 Discs

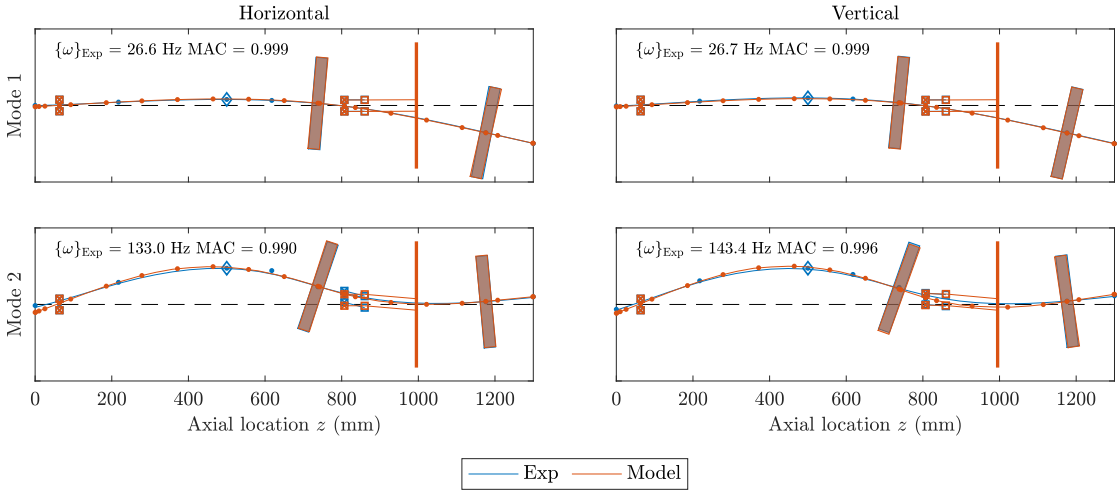
The last stage of assembly was to fit the discs. In Section 6.4, the mode shapes were only plotted for the final configuration with 2 discs. The full set of mode shapes are plotted in Fig. B.10.



(a) Shaft only



(b) Shaft + Front Disc



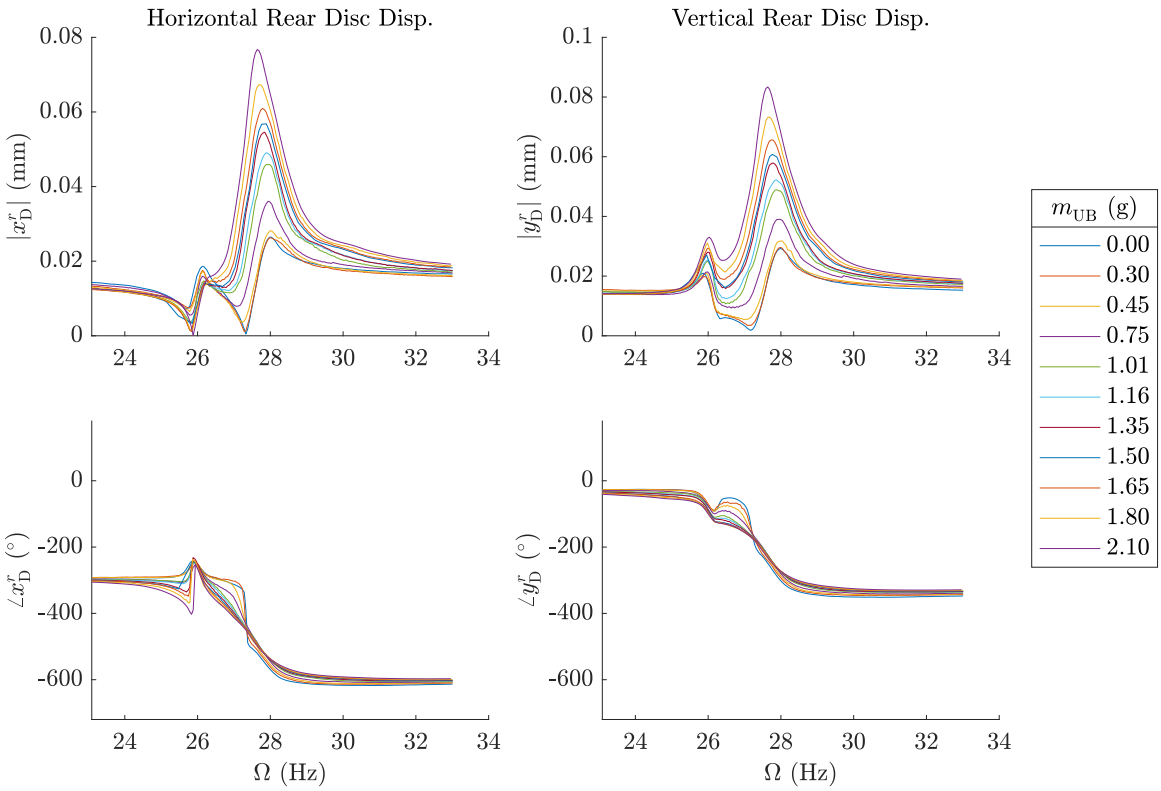
(c) Shaft + Two Discs

Figure B.10: Comparison of the experimental and numerical modal properties of the ARES rig with different numbers of discs

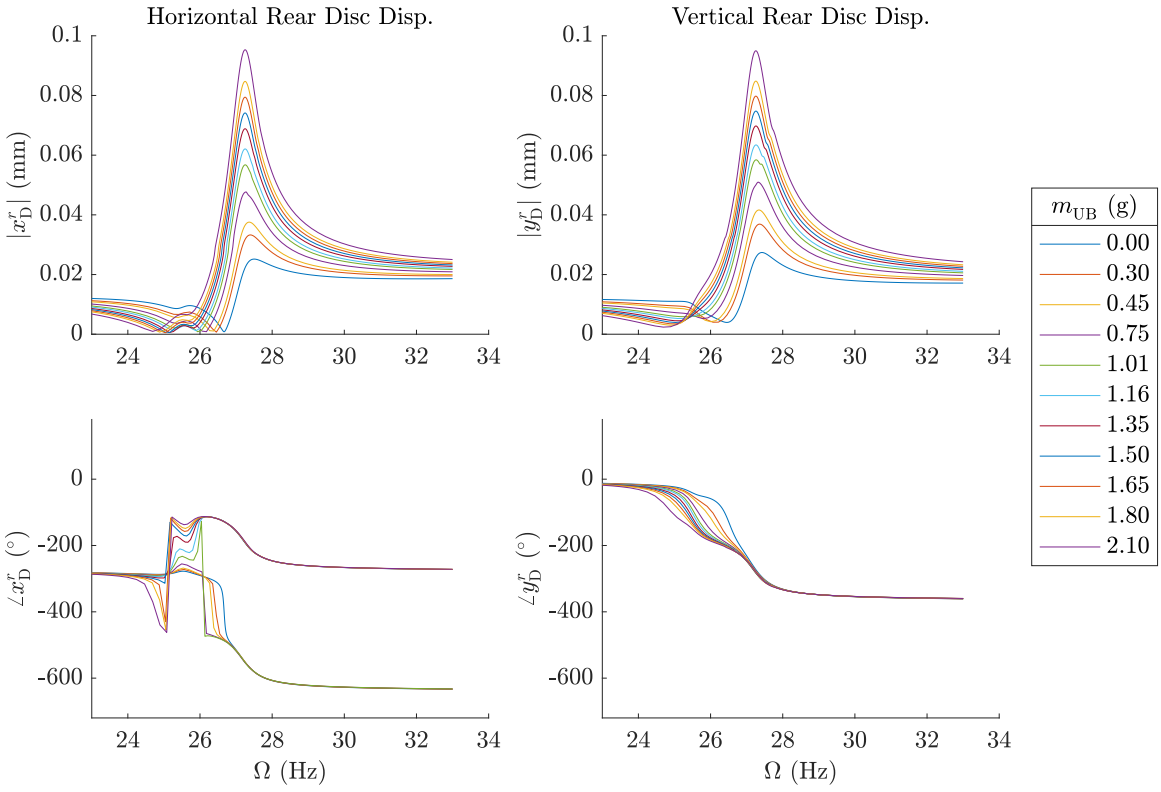
Appendix C

ARES unbalance responses

In Section 6.5.4, only the unbalance response of the front disc and interface plate forces were plotted. However, the response of the rear disc, bearing housing and interface were also measured. These results will now be presented.

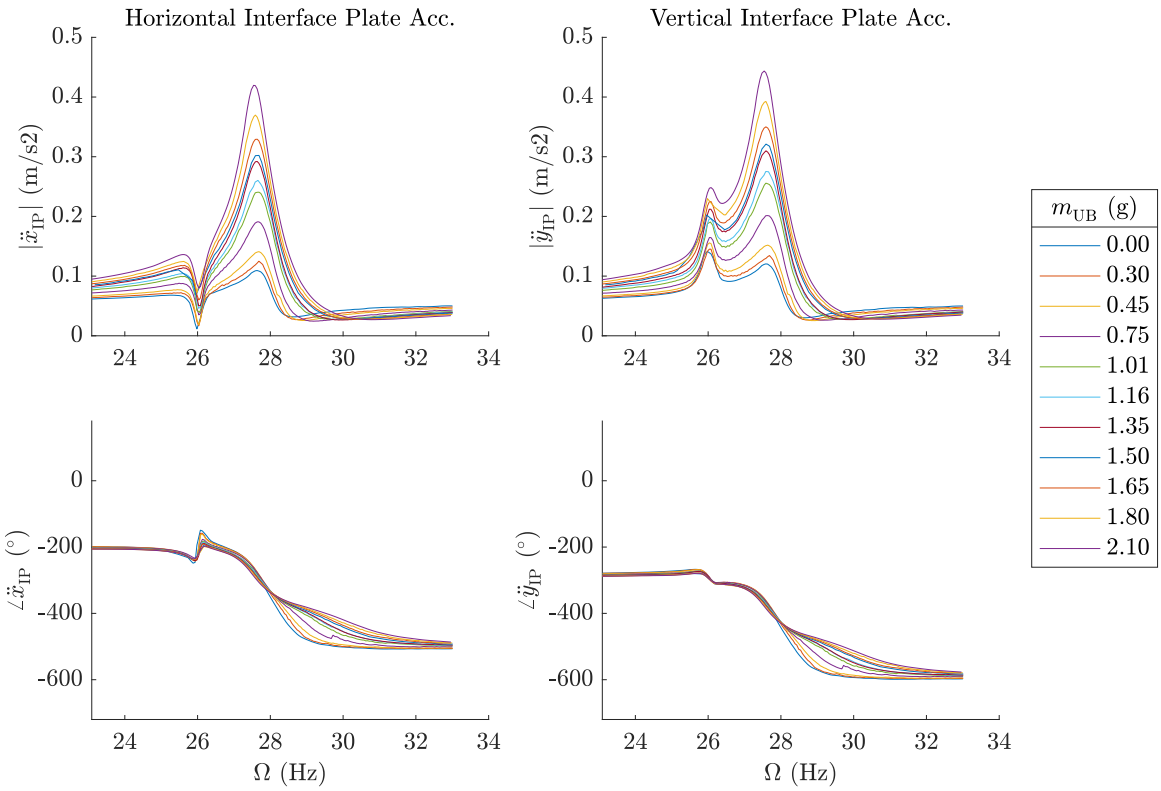


(a) Experiment

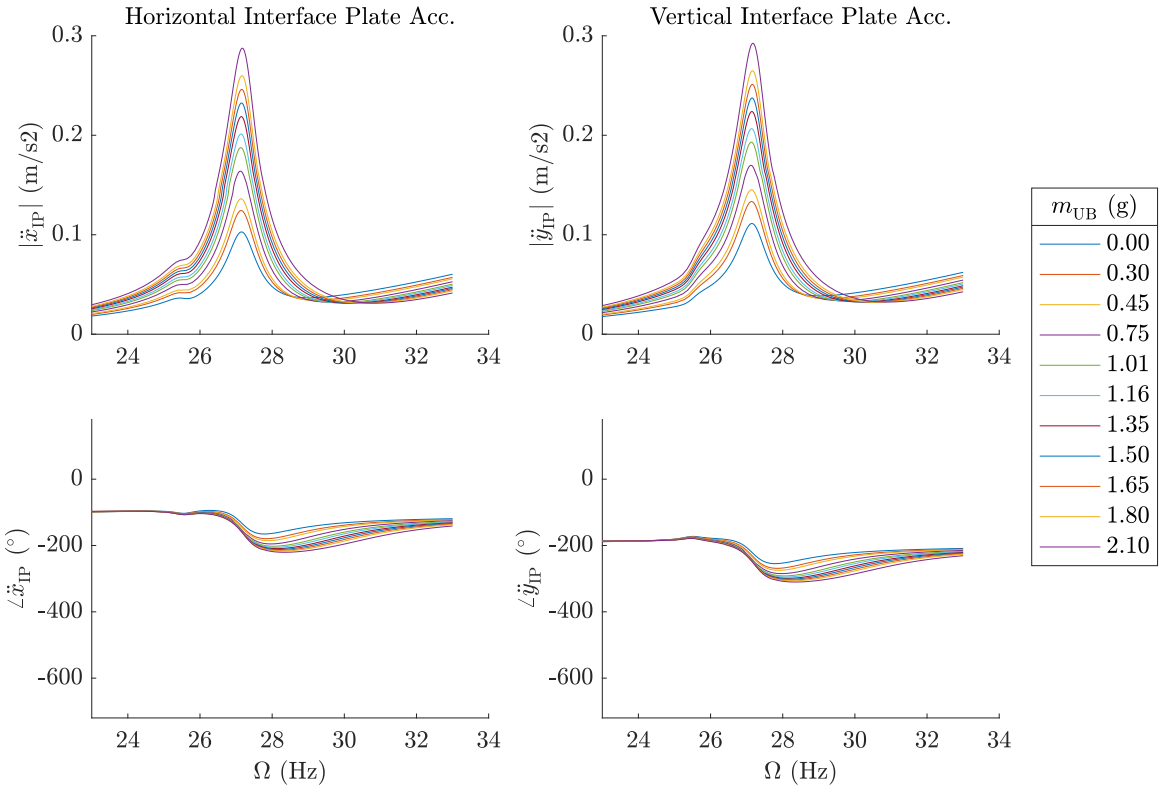


(b) Model

Figure C.1: Frequency response of the rear disc due to front disc unbalance

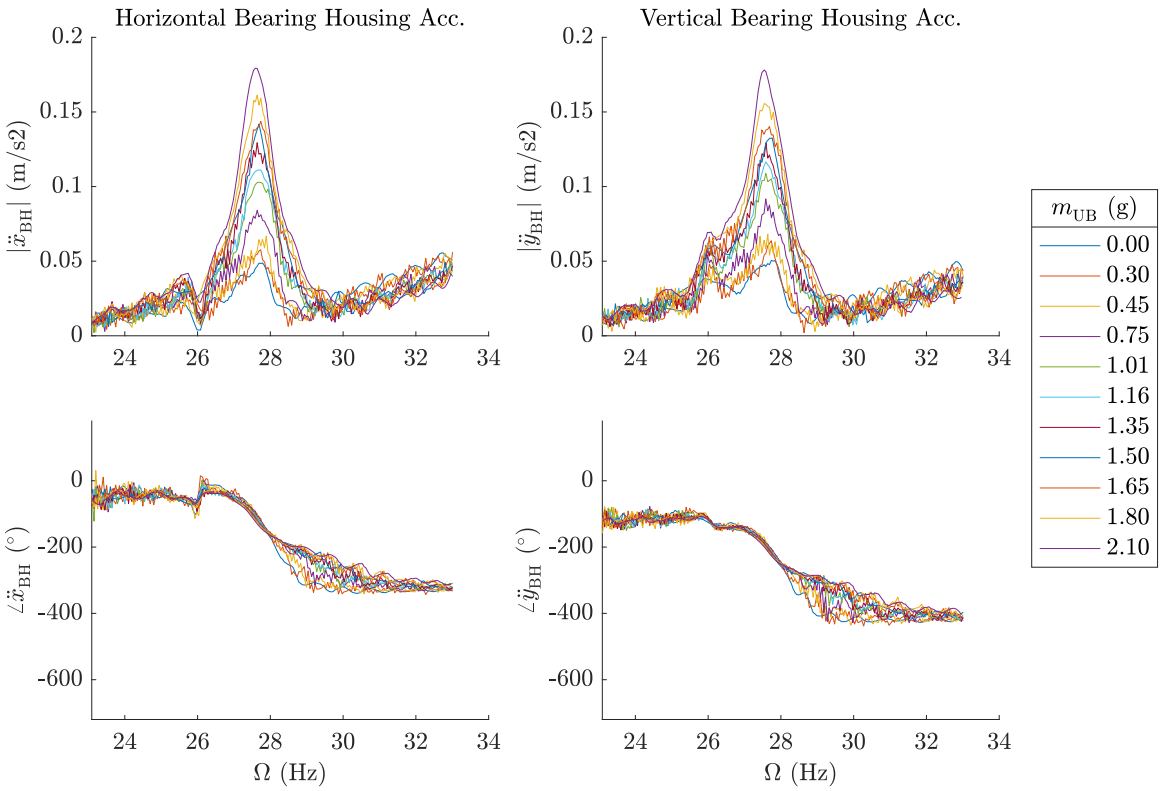


(a) Experiment

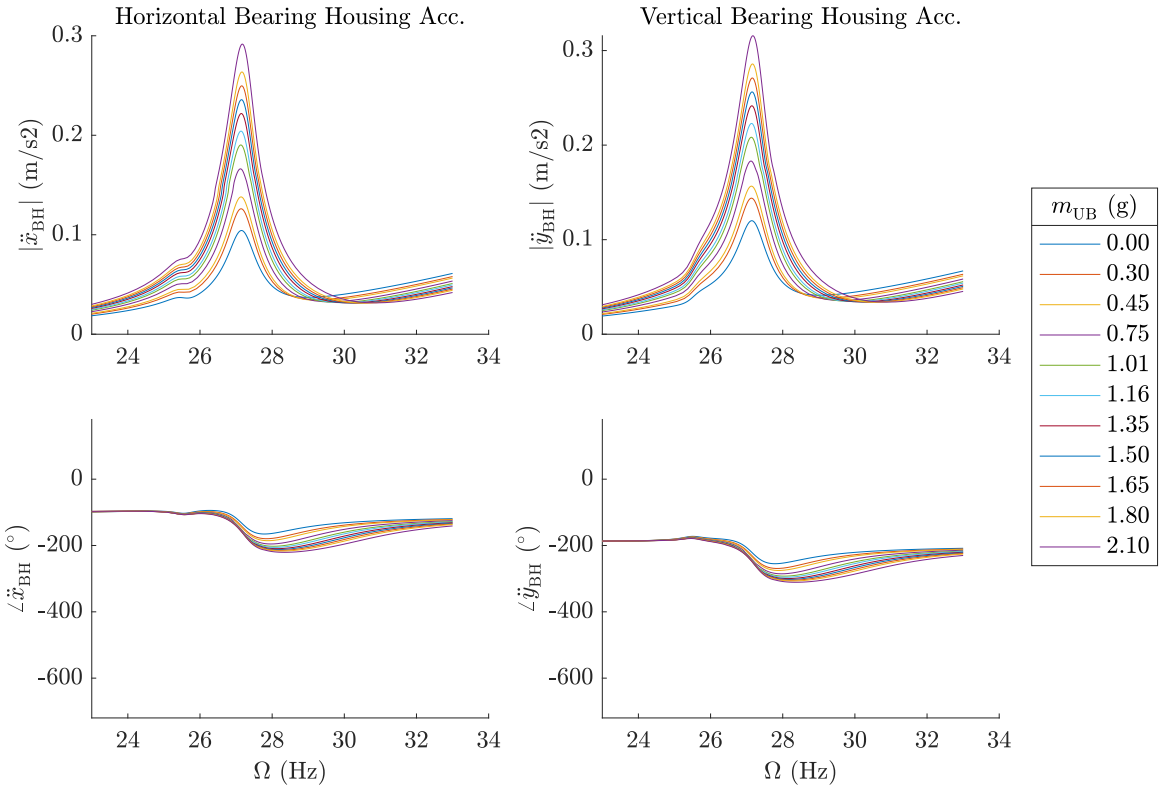


(b) Model

Figure C.2: Frequency response of the interface plate due to front disc unbalance



(a) Experiment



(b) Model

Figure C.3: Frequency response of the bearing housing due to front disc unbalance

Appendix D

ARES support model

In Section 5.4, an equivalent model of the bearing support structure on ARES was presented. The equations of motion will be derived here, as well as some other useful results.

D.1 Equations of motion

The equations of motion for this system can be derived by first finding expressions for the kinetic and potential energies. These are given by:

$$T = \frac{1}{2}\left(I_{\mathrm{L}}^{x} + I_{\mathrm{IP}} + I_{\mathrm{BH}}\right)\dot{\theta}_{\mathrm{L}}^{2} + \frac{1}{2}m_{\mathrm{IP}}\dot{x}_{\mathrm{IP}}^{2} + \frac{1}{2}m_{\mathrm{BH}}\dot{x}_{\mathrm{BH}}^{2} \tag{D.1}$$

$$\begin{aligned} V = {} & \frac{1}{2}k_{\mathrm{L}}^{x}\theta_{\mathrm{L}}^{2} + \frac{1}{2}k_{\mathrm{IP}}\left(x_{\mathrm{IP}} - \theta_{\mathrm{L}}l_{\mathrm{IP}}\right)^{2} + \frac{1}{2}k_{\mathrm{BH}}\left(x_{\mathrm{BH}} - x_{\mathrm{IP}} - \theta_{\mathrm{L}}l_{\mathrm{BH}}\right)^{2} \\ & + \frac{1}{2}k_{\mathrm{PEA}}^{\delta}x_{\mathrm{IP}}^{2} + \frac{1}{2}k_{\mathrm{PEA}}^{\theta}\theta_{\mathrm{L}}^{2} \end{aligned} \tag{D.2}$$

Denoting the displacement vector of the bearing support structure as:

$$\boldsymbol{x}_{s} = \begin{bmatrix} \theta_{\mathrm{L}} & x_{\mathrm{IP}} & x_{\mathrm{BH}} \end{bmatrix}^{T} \tag{D.3}$$

and finding the Hessian of the kinetic energy T yields the following mass matrix $\boldsymbol{M}_{s}$:

$$\boldsymbol{M}_{s} = \begin{bmatrix} I_{\mathrm{L}}^{x} + I_{\mathrm{IP}} + I_{\mathrm{BH}} & 0 & 0 \\ 0 & m_{\mathrm{IP}} & 0 \\ 0 & 0 & m_{\mathrm{BH}} \end{bmatrix} \tag{D.4}$$

while the Hessian of the potential energy V yields the stiffness matrix $\boldsymbol{K}_{s}$:

$$\boldsymbol{K}_s = \begin{bmatrix} k_{\mathrm{L}}^x + k_{\mathrm{PEA}}^\theta + k_1 & k_2 & k_3 \\ k_2 & k_{\mathrm{IP}} + k_{\mathrm{BH}} + k_{\mathrm{PEA}}^\delta & -k_{\mathrm{BH}} \\ k_3 & -k_{\mathrm{BH}} & k_{\mathrm{BH}} \end{bmatrix} \tag{D.5}$$

where the following stiffness terms are given by:

$$\begin{aligned} k_1 &= k_{\mathrm{IP}} l_{\mathrm{IP}}^2 + k_{\mathrm{BH}} l_{\mathrm{BH}}^2 \\ k_2 &= -k_{\mathrm{IP}} l_{\mathrm{IP}} + k_{\mathrm{BH}} l_{\mathrm{BH}} \\ k_3 &= -k_{\mathrm{BH}} l_{\mathrm{BH}} \end{aligned}$$

The damping in the support structure was assumed to arise from the L-shape and support rods. The damping matrix $\boldsymbol{C}_c$ can therefore be found by simply replacing the stiffness terms in Eq. (D.5) with their damping counterpart.

The PEAs exert an piezo-electric force on the interface plate denoted by f_{PEA}^x. Similarly, the rolling-element bearing exerts a force on the bearing housing denoted by f_{B}^x. These can be written in vector form as:

$$\boldsymbol{f}_s = \begin{bmatrix} 0 & f_{\mathrm{PEA}}^x & f_{\mathrm{B}}^x \end{bmatrix}^T \tag{D.6}$$

These expressions can be assembled to yield the equation of motion for the support structure:

$$\boldsymbol{M}_s \ddot{\boldsymbol{x}}_s + \boldsymbol{C}_s \dot{\boldsymbol{x}}_s + \boldsymbol{K}_s \boldsymbol{x}_s = \boldsymbol{f}_s \tag{D.7}$$

The modes, natural frequencies and damping ratios of the system can now be found using eigenvalue analysis.

D.2 Interface plate stiffness

In order to derive the expression for the effective stiffness at the interface plate, the inertial and damping terms from Eq. (D.7) can be removed, and the terms in the stiffness matrix involving x_{BH} can be eliminated, since the bearing housing was not fitted for the stiffness tests. This yields the following equilibrium problem:

$$\begin{bmatrix} k_{\mathrm{L}}^x + k_{\mathrm{PEA}}^\theta + k_{\mathrm{IP}} l_{\mathrm{IP}}^2 & -k_{\mathrm{IP}} l_{\mathrm{IP}} \\ -k_{\mathrm{IP}} l_{\mathrm{IP}} & k_{\mathrm{IP}} + k_{\mathrm{PEA}}^\delta \end{bmatrix} \begin{bmatrix} \theta_{\mathrm{L}} \\ x_{\mathrm{IP}} \end{bmatrix} = \begin{bmatrix} 0 \\ f_{\mathrm{PEA}}^x \end{bmatrix} \tag{D.8}$$

The reduced stiffness matrix on the LHS can then be inverted to solve for the interface plate deflection x_{IP} as a function of the applied load f^x_{PEA}:

$$x_{\mathrm{IP}} = \frac{k^x_{\mathrm{L}} + k^\theta_{\mathrm{PEA}} + k_{\mathrm{IP}} l^2_{\mathrm{IP}}}{\left(k^x_{\mathrm{L}} + k^\theta_{\mathrm{PEA}} + k_{\mathrm{IP}} l^2_{\mathrm{IP}}\right)\left(k_{\mathrm{IP}} + k^\delta_{\mathrm{PEA}}\right) - k^2_{\mathrm{IP}} l^4_{\mathrm{IP}}} f^x_{\mathrm{PEA}}$$

The load measured by the force gauge is not simply f^x_{PEA}, as this is only the piezo-electric excitation force exerted by the PEAs. There is also another load on the force gauge due to the mechanical stiffness of the PEA. Therefore the net load measured by the force gauges f^x_{IP} is slightly smaller than the piezo-electric PEA load f^x_{PEA}:

$$f^x_{\mathrm{IP}} = f^x_{\mathrm{PEA}} - k^\delta_{\mathrm{PEA}} x_{\mathrm{IP}}$$

which can then be substituted into the above equation to yield as expression relating the interface displacement and force gauge load:

$$\left[\left(k^x_{\mathrm{L}} + k^\theta_{\mathrm{PEA}} + k_{\mathrm{IP}} l^2_{\mathrm{IP}}\right)\left(k_{\mathrm{IP}} + k^\delta_{\mathrm{PEA}}\right) - k^2_{\mathrm{IP}} l^4_{\mathrm{IP}}\right] x_{\mathrm{IP}} = \left(k^x_{\mathrm{L}} + k^\theta_{\mathrm{PEA}} + k_{\mathrm{IP}} l^2_{\mathrm{IP}}\right)\left(f^x_{\mathrm{IP}} + k^\delta_{\mathrm{PEA}} x_{\mathrm{IP}}\right)$$

where it can be observed that the PEA radial stiffness k^δ_{PEA} will cancel out, thereby eliminating k^δ_{PEA}. Therefore the radial PEA stiffness has no influence on the measured stiffness. This expression can then be simplified and rearranged to yield the effective interface plate stiffness k^{test}_{IP}:

$$k^{test}_{\mathrm{IP}} \triangleq \frac{f^x_{\mathrm{IP}}}{x_{\mathrm{IP}}} = \left(\frac{1}{k_{\mathrm{IP}}} + \frac{l^2_{\mathrm{IP}}}{k^x_{\mathrm{L}} + k^\theta_{\mathrm{PEA}}}\right)^{-1} \tag{D.9}$$

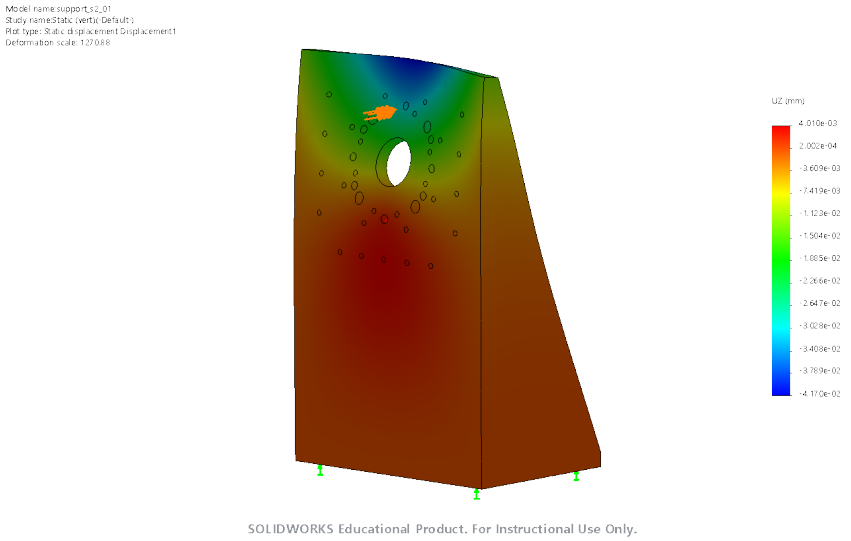
D.3 FE Analysis of L-shape

In order to be able to visualise the full L-shape displacement field from the reduced order support model, a static analysis was performed using Solidworks 2018. The L-shape was fixed at four points on the base, which correspond to the locations of the bolts fixing it to the test bed. Axial loads were then applied at the tapped holes for the support rods, in order to replicate the moment applied by the interface plate on the L-shape. Two load cases were considered:

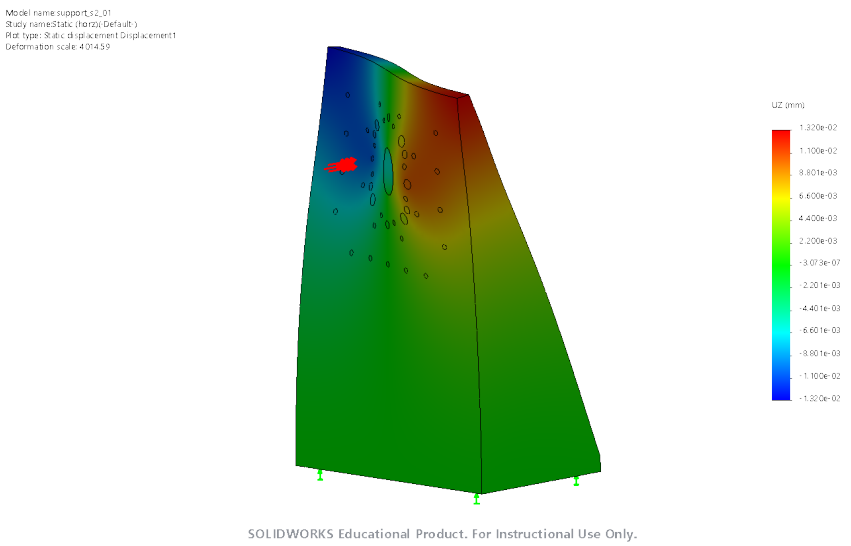
- Moment about the x-axis, with opposite loads on the bottom and top holes for the support rods. This is shown in Fig. D.1a.

- Moment about the y-axis, with opposite loads on the left and right holes for the support rods. This is shown in Fig. D.1b.

The results deflection shapes are depicted in Fig. D.1. The deflection perpendicular to the front face of the support was extracted from the FEA results. The equivalent L-shape rotation was identified from the deflections of the four support holes. Each displacement field was normalised so that the equivalent L-shape rotation was unity.



(a) Moment about x-axis



(b) Moment about y-axis

Figure D.1: Static response of the L-shape due to moments from the interface plate support rods

Appendix E

BELOS Technical drawings

A special test rig known as BELOS was designed and built in order to measure the non-linear stiffness of the fixed bearing from ARES. Although an existing pulley system was used to load the bearing, a custom bearing housing and loading shaft were designed. The drawings of these components are presented here.

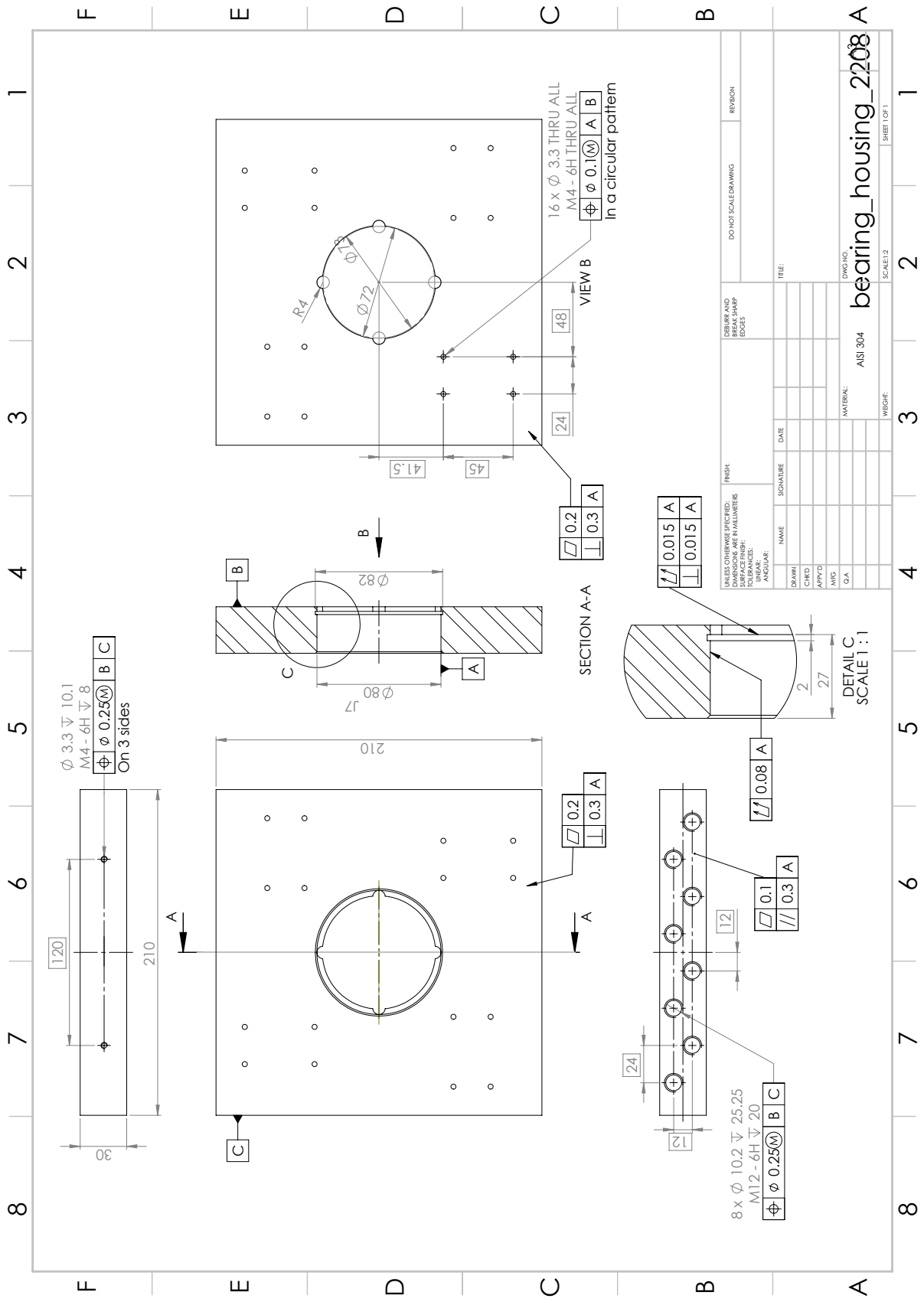


Figure E.1: Bearing housing

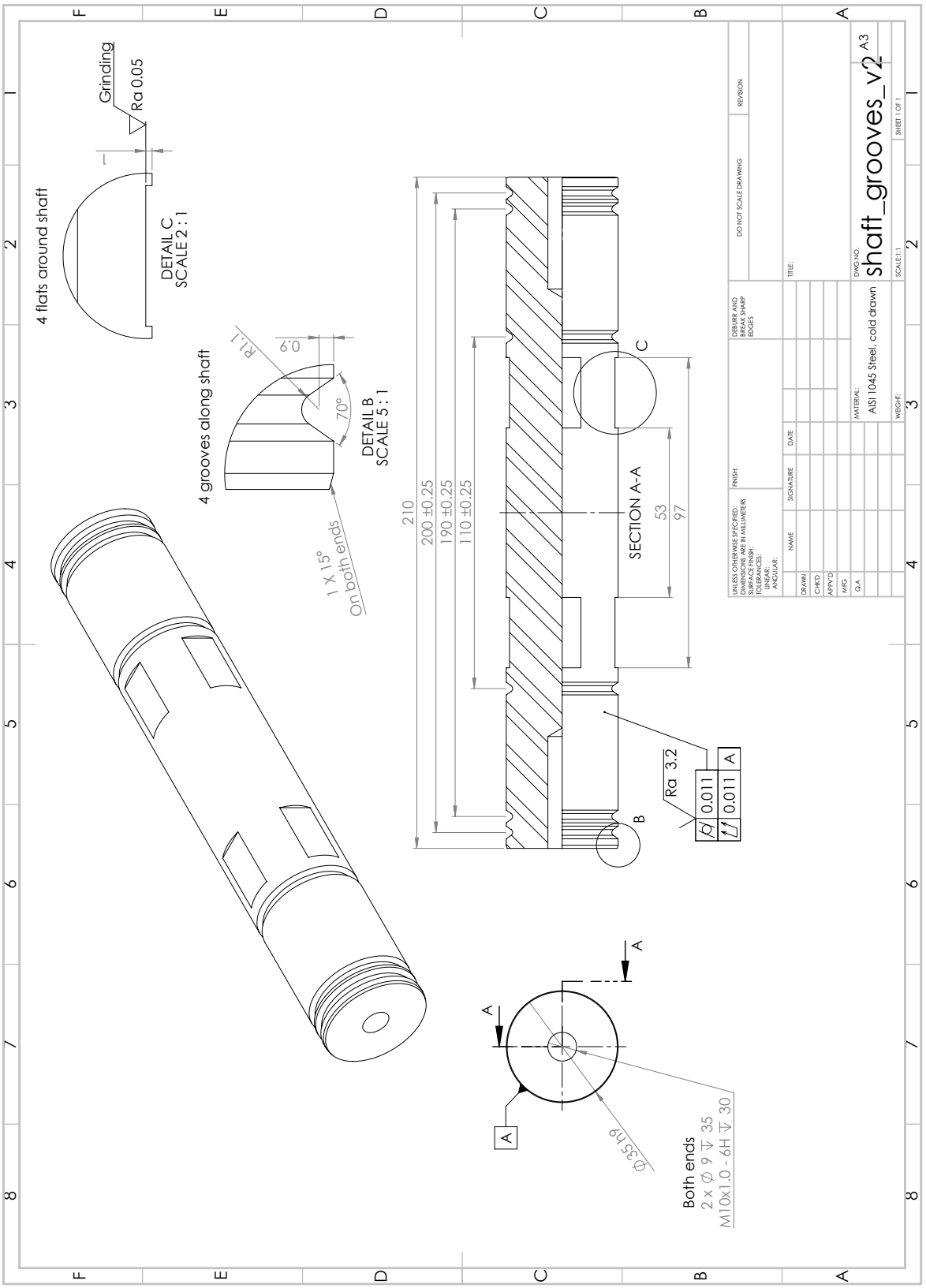


Figure E.2: Solid loading shaft

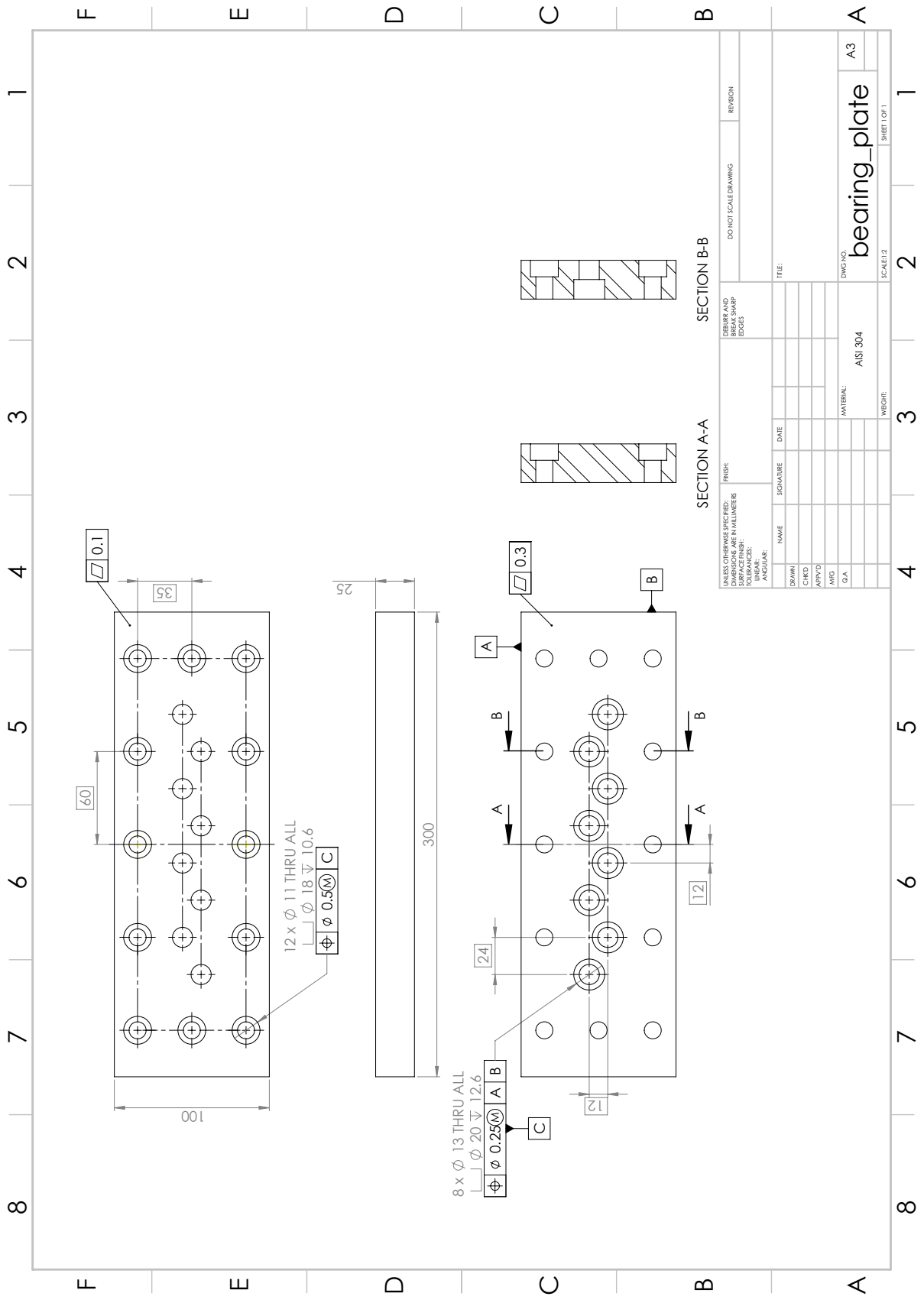


Figure E.3: Base plate for mounting to test bed

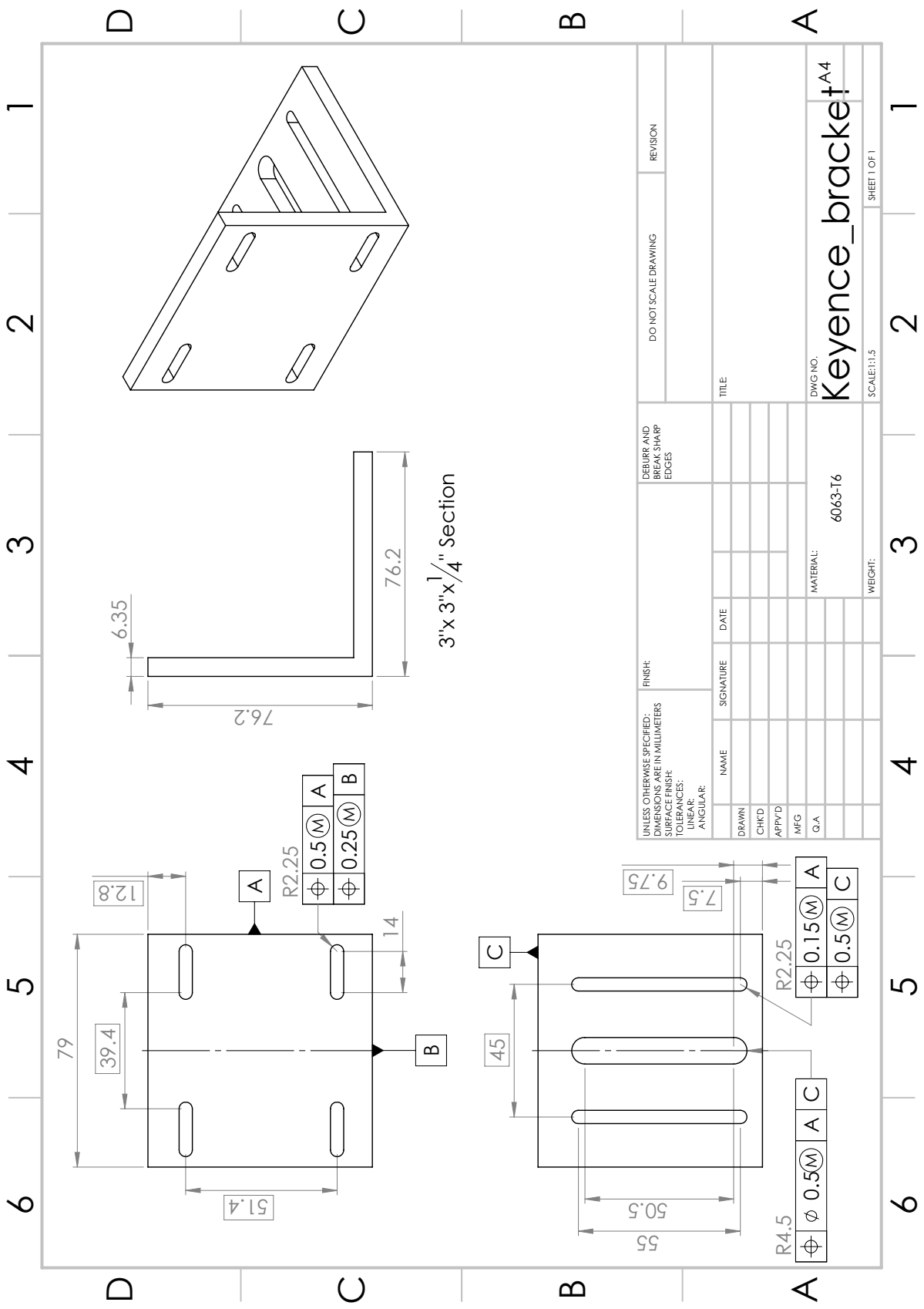


Figure E.4: Bracket for Keyence laser displacement sensors

References

[1] Rolls-Royce Ltd., *The Jet Engine*. Wiley, 5th ed., 2015.

[2] M. I. Friswell, J. E. T. Penny, S. D. Garvey, and A. W. Lees, *Dynamics of Rotating Machines*. Cambridge University Press, 1st ed., 2010.

[3] H. Jeffcott, "The lateral vibration of loaded shafts in the neighbourhood of a whirling speed - The effect of want of balance," *The London, Edinburgh, and Dublin Philosophical Magazine and Journal of Science*, vol. 37, pp. 304–314, mar 1919.

[4] A. Muszynska, *Rotordynamics*. Boca Raton, FL: CRC Press, 1st ed., 2005.

[5] E. Krämer, *Dynamics of Rotors and Foundations*. Berlin: Springer-Verlag, 1st ed., 1993.

[6] J. H. Ginsberg, *Mechanical and structural vibrations : theory and applications*. Wiley, 1st ed., 2001.

[7] M. Guskov, J.-J. Sinou, F. Thouverez, and O. S. Naraikin, "Experimental and Numerical Investigations of a Dual-Shaft Test Rig with Intershaft Bearing," *International Journal of Rotating Machinery*, vol. 2007, pp. 1–12, 2007.

[8] H.-W. D. Chiang, C.-N. Hsu, W. Jeng, S.-H. Tu, and W.-C. Li, "Turbomachinery Dual Rotor-Bearing System Analysis," in *ASME Turbo Expo 2002: Power for Land, Sea, and Air; Volume 4: Turbo Expo 2002, Parts A and B*, (Amsterdam), pp. 803–810, ASME, 2002.

[9] H.-W. D. Chiang, C.-N. Hsu, and S.-H. Tu, "Rotor-Bearing Analysis for Turbomachinery Single- and Dual-Rotor Systems," *Journal of Propulsion and Power*, vol. 20, pp. 1096–1104, nov 2004.

[10] Z.-x. Fei, S.-g. Tong, and C. Wei, "Investigation of the dynamic characteristics of a dual rotor system and its start-up simulation based on finite element method," *Journal of Zhejiang University SCIENCE A*, vol. 14, pp. 268–280, apr 2013.

[11] J. Sopanen and A. Mikkola, "Dynamic model of a deep-groove ball bearing including localized and distributed defects. Part 2: implementation and results," *Proceedings of the Institution of Mechanical Engineers, Part K: Journal of Multi-body Dynamics*, vol. 217, pp. 213–223, jan 2003.

[12] V. Parmar, V. Saran, and S. Harsha, "Nonlinear vibration response analysis of a double-row self-aligning ball bearing due to surface imperfections," *Proceedings of the Institution of Mechanical Engineers, Part K: Journal of Multi-body Dynamics*, p. 146441932092491, may 2020.

[13] J.-J. Sinou, C. Villa, and F. Thouverez, "Experimental and Numerical Investigations of a Flexible Rotor on Flexible Bearing Supports," *International Journal of Rotating Machinery*, vol. 2005, no. 3, pp. 179–189, 2005.

[14] C.-H. Yang and S.-C. Huang, "The influence of disk's flexibility on coupling vibration of shaft–disk–blades systems," *Journal of Sound and Vibration*, vol. 301, pp. 1–17, mar 2007.

[15] S. C. Huang and K. B. Ho, "Coupled shaft-torsion and blade-bending vibrations of a rotating shaft-disk-blade unit," *Journal of Engineering for Gas Turbines and Power*, vol. 118, pp. 100–106, jan 1996.

[16] J. S. Rao and R. Sreenivas, "Dynamics of a Three Level Rotor System Using Solid Elements," in *Proceedings of ASME Turbo Expo 2003; Volume 4: Turbo Expo 2003;*, (Atlanta, GA), pp. 601–606, ASME, 2003.

[17] V. Ruffini, C. W. Schwingshackl, and J. S. Green, "Prediction Capabilities of Coriolis and Gyroscopic Effects in Current Finite Element Software," in *IFToMM International Conference on Rotor Dynamics* (P. Pennacchi, ed.), (Milan), pp. 1853–1862, Springer, 2015.

[18] Z. Lu, S. Zhong, H. Chen, Y. Chen, J. Han, and C. Wang, "Modeling and Dynamic Characteristics Analysis of Blade-Disk Dual-Rotor System," *Complexity*, vol. 2020, pp. 1–13, jan 2020.

[19] T. A. Harris and M. N. Kotzalas, *Rolling Bearing Analysis: Essential Concepts of Bearing Technology*. Boca Raton, FL: CRC Press, 5th ed., 2006.

[20] J. S. Rao, *Rotor Dynamics*. New Delhi: Wiley Eastern Ltd., 2nd ed., 1991.

[21] K. D. Gupta, K. D. Gupta, and K. Athre, "Unbalance Response of a Dual Rotor System: Theory and Experiment," *Journal of Vibration and Acoustics*, vol. 115, no. 4, p. 427, 1993.

[22] A. Liew, N. S. Feng, and E. J. Hahn, "On Using the Transfer Matrix Formulation for Transient Analysis of Nonlinear Rotor Bearing Systems," *International Journal of Rotating Machinery*, vol. 10, no. 6, pp. 425–431, 2004.

[23] R. L. Ruhl and J. F. Booker, "A Finite Element Model for Distributed Parameter Turborotor Systems," *Journal of Engineering for Industry*, vol. 94, p. 126, feb 1972.

[24] H. D. Nelson and J. M. McVaugh, "The Dynamics of Rotor-Bearing Systems Using Finite Elements," *Journal of Engineering for Industry*, vol. 98, p. 593, may 1976.

[25] D. J. Inman, *Engineering Vibration.* Harlow, UK: Pearson Education Limited, 4th ed., 2014.

[26] M. B. Wagner, A. Younan, P. Allaire, and R. Cogill, "Model reduction methods for rotor dynamic analysis: A survey and review," *International Journal of Rotating Machinery*, vol. 2010, 2010.

[27] M. C. C. Bampton and R. R. Craig Jnr, "Coupling of Substructures for Dynamic Analyses," *AIAA Journal*, vol. 6, pp. 1313–1319, jul 1968.

[28] S. N. Hou and Others, "Review of modal synthesis techniques and a new approach," *Shock and vibration bulletin*, vol. 40, no. 4, pp. 25–39, 1969.

[29] R. Craig and C.-J. Chang, "A Review of Substructure Coupling Methods for Dynamic Analysis," in *Advances in engineering science*, vol. 2, pp. 1633–1635, 1976.

[30] D. Herting, "A general purpose, multi-stage, component modal synthesis method," *Finite Elements in Analysis and Design*, vol. 1, pp. 153–164, aug 1985.

[31] W. Wang and J. Kirkhope, "Component mode synthesis for multi-shaft rotors With flexible inter-shaft bearings," *Journal of Sound and Vibration*, vol. 173, pp. 537–555, jun 1994.

[32] R. H. MacNeal, "A Hybrid Method of Component Mode Synthesis," *Computers & Structures*, vol. 1, pp. 581–601, dec 1971.

[33] R. M. Hintz, "Analytical Methods in Component Modal Synthesis," *AIAA Journal*, vol. 13, pp. 1007–1016, aug 1975.

[34] C. Bucher, "A modal synthesis method employing physical coordinates, free component modes, and residual flexibilities," *Computers & Structures*, vol. 22, pp. 559–564, jan 1986.

[35] R. R. Craig and Z. Ni, "Component mode synthesis for model order reduction of nonclassicallydamped systems," *Journal of Guidance, Control, and Dynamics*, vol. 12, no. 4, pp. 577–584, 1989.

[36] H. Schmidt, D. Kriebel, and J. Mehner, "Reduced Order Component & System Level Modelling for Fluid-Solid Interactions in Complex MEMS Devices," *Proceedings*, vol. 2, no. 13, p. 937, 2019.

[37] D. A. Glasgow and H. D. Nelson, "Stability Analysis of Rotor-Bearing Systems Using Component Mode Synthesis," *Journal of Mechanical Design*, vol. 102, p. 352, apr 1980.

[38] D. F. Li and E. J. Gunter, "Study of the Modal Truncation Error in the Component Mode Analysis of a Dual-Rotor System.," *American Society of Mechanical Engineers (Paper)*, no. 81 -GT-144, 1981.

[39] W. Wang and J. Kirkhope, "Complex component mode synthesis for damped systems," *Journal of Sound and Vibration*, vol. 181, pp. 781–800, apr 1995.

[40] Silberwolf, "Deep-groove ball bearing, with seals on both sides [translated from german]." `https://commons.wikimedia.org/wiki/File:Radial-deep-groove-ball-bearing_din625-t1_2rs_120.png`. [Online; Accessed: 2020-08-19].

[41] Silberwolf, "Cylindrical roller bearing, with flanges on both sides [translated from german]." `https://commons.wikimedia.org/wiki/File:Cylindrical-roller-bearing_din5412-t1_type-n_120.png`. [Online; Accessed: 2020-08-19].

[42] A. SKF, "Single Row Angular Contact Ball Bearings." `https://www.skf.com/uk/products/rolling-bearings/ball-bearings/angular-contact-ball-bearings/single-row-angular-contact-ball-bearings/designs-and-variants`. [Online; Accessed: 2020-09-11].

[43] A. SKF, "Double Row Angular Contact Ball Bearings." `https://www.skf.com/uk/products/rolling-bearings/ball-bearings/angular-contact-ball-bearings/double-row-angular-contact-ball-bearings/designs-and-variants`. [Online; Accessed: 2020-09-11].

[44] A. B. Jones, "A General Theory for Elastically Constrained Ball and Radial Roller Bearings Under Arbitrary Load and Speed Conditions," *Journal of Basic Engineering*, vol. 82, no. 2, p. 309, 1960.

[45] T. A. Harris and M. N. Kotzalas, *Rolling bearing analysis: Advanced concepts of bearing technology*. Boca Raton, FL: CRC Press, 5th ed., 2006.

[46] T. Lim and R. Singh, "Vibration Transmission Through Rolling Element Bearings. Part I: Bearing Stiffness Formulation," *Journal of Sound and Vibration*, vol. 139, no. 2, pp. 179–199, 1990.

[47] T. Lim and R. Singh, "Vibration Transmission Through Rolling Element Bearings. Part II: System Studies," *Journal of Sound and Vibration*, vol. 139, no. 2, pp. 201–225, 1990.

[48] J. M. de Mul, J. M. Vree, and D. A. Maas, "Equilibrium and Associated Load Distribution in Ball and Roller Bearings Loaded in Five Degrees of Freedom While Neglecting Friction—Part I: General Theory and Application to Ball Bearings," *Journal of Tribology*, vol. 111, p. 142, jan 1989.

[49] L. Houpert, "A Uniform Analytical Approach for Ball and Roller Bearings Calculations," *Journal of Tribology*, vol. 119, no. 4, p. 851, 1997.

[50] P. Guay and A. Frikha, "Ball Bearing Stiffness: A New Approach Offering Analytical Expressions," in *European Space Mechanisms and Tribology Symposium*, (Bilbao), pp. 23–25, 2015.

[51] S. Jain and H. Hunt, "A Dynamic Model to Predict the Occurrence of Skidding in Wind-Turbine Bearings," *Journal of Physics: Conference Series*, vol. 305, p. 012027, jul 2011.

[52] H. Sjovall, "The Load Distribution within Ball and Roller Bearings under Given External Radial and Axial Load," *Tekniks Tidskrift Mek.*, no. 9, 1933.

[53] L. Houpert, "An Engineering Approach to Hertzian Contact Elasticity—Part I," *Journal of Tribology*, vol. 123, no. 3, p. 582, 2001.

[54] L. Houpert, "An Engineering Approach to Non-Hertzian Contact Elasticity—Part II," *Journal of Tribology*, vol. 123, no. 3, p. 589, 2001.

[55] M. Leontiev, V. Ivannikov, and S. Degtyarev, "Radial roller bearings with flexible rings : application to rotor dynamics and extension to multibody simulations," in *International Symposium on Transport Phenomena and Dynamics of Rotating Machinery*, (Maui, HI), pp. 1–9, 2017.

[56] F. F. Ehrich, "High Order Subharmonic Response of High Speed Rotors in Bearing Clearance," *Journal of Vibration Acoustics Stress and Reliability in Design*, vol. 110, no. 1, p. 9, 1988.

[57] F. Ehrich, "Observations of Subcritical Superharmonic and Chaotic Response in Rotordynamics," *Journal of Vibration and Acoustics*, vol. 114, p. 93, jan 1992.

[58] D. W. Childs, "Fractional-Frequency Rotor Motion Due to Nonsymmetric Clearance Effects," *Journal of Engineering for Power*, vol. 104, no. 3, p. 533, 1982.

[59] Y. B. Kim and S. T. Noah, "Bifurcation analysis for a modified Jeffcott rotor with bearing clearances," *Nonlinear Dynamics*, vol. 1, pp. 221–241, may 1990.

[60] M. F. While, "Rolling Element Bearing Vibration Transfer Characteristics: Effect of Stiffness," *Journal of Applied Mechanics*, vol. 46, no. 3, p. 677, 1979.

[61] T. Royston and I. Basdogan, "Vibration Transmission Through Self-Aligning (Spherical) Rolling Element Bearings: Theory and Experiment," *Journal of Sound and Vibration*, vol. 215, pp. 997–1014, sep 1998.

[62] S. Saito, "Calculation of Nonlinear Unbalance Response of Horizontal Jeffcott Rotors Supported by Ball Bearings With Radial Clearances," *Journal of Vibration Acoustics Stress and Reliability in Design*, vol. 107, no. 4, pp. 416–420, 1985.

[63] A. Kahraman and R. Singh, "Non-linear Dynamics of a Geared Rotor-bearing System with Multiple Clearances," *Journal of Sound and Vibration*, vol. 144, no. 3, pp. 469–506, 1991.

[64] M. Tiwari, K. Gupta, and O. Prakash, "Effect of Radial Internal Clearance of a Ball Bearing on the Dynamics of a Balanced Horizontal Rotor," *Journal of Sound and Vibration*, vol. 238, no. 5, pp. 723–756, 2000.

[65] C. Bai, H. Zhang, and Q. Xu, "Effects of axial preload of ball bearing on the nonlinear dynamic characteristics of a rotor-bearing system," *Nonlinear Dynamics*, vol. 53, pp. 173–190, aug 2008.

[66] F. F. Ehrich, "Some Observations of Chaotic Vibration Phenomena in High-Speed Rotordynamics," *Journal of Vibration and Acoustics*, vol. 113, p. 50, jan 1991.

[67] A. Leblanc and D. Nelias, "Analysis of Ball Bearings with 2, 3 or 4 Contact Points," *Tribology Transactions*, vol. 51, pp. 372–380, may 2008.

[68] D. Noel, M. Ritou, B. Furet, and S. Le Loch, "Complete Analytical Expression of the Stiffness Matrix of Angular Contact Ball Bearings," *Journal of Tribology*, vol. 135, p. 041101, jun 2013.

[69] C. Lei, Z. Rui, J. Liu, R. Feng, and J. Zhao, "A New Method for Computing Contact Angle of High Speed Ball Bearing," in *2010 Third International Joint Conference on Computational Science and Optimization*, pp. 331–334, IEEE, 2010.

[70] E. Kurvinen, J. Sopanen, and A. Mikkola, "Ball bearing model performance on various sized rotors with and without centrifugal and gyroscopic forces," *Mechanism and Machine Theory*, vol. 90, pp. 240–260, aug 2015.

[71] B. Fang, J. Zhang, K. Yan, J. Hong, and M. Yu Wang, "A comprehensive study on the speed-varying stiffness of ball bearing under different load conditions," *Mechanism and Machine Theory*, 2019.

[72] A. Liew, N. S. Feng, and E. J. Hahn, "Transient Rotordynamic Modeling of Rolling Element Bearing Systems," in *ASME Turbo Expo 2001: Power for Land, Sea, and Air; Volume 4* (ASME, ed.), (New Orleans, LA), p. V004T03A021, ASME editor, jun 2001.

[73] W.-z. Wang, S.-g. Zhang, Z.-q. Zhao, and S.-y. Ai, "Effect of the Inhomogeneity in Races on the Dynamic Behavior of Rolling Bearing," *Journal of Vibration and Acoustics*, vol. 137, p. 061015, oct 2015.

[74] H. Wang, Q. Han, and D. Zhou, "Nonlinear dynamic modeling of rotor system supported by angular contact ball bearings," *Mechanical Systems and Signal Processing*, vol. 85, pp. 16–40, feb 2017.

[75] S. Upadhyay, S. Harsha, and S. Jain, "Analysis of Nonlinear Phenomena in High Speed Ball Bearings due to Radial Clearance and Unbalanced Rotor Effects," *Journal of Vibration and Control*, vol. 16, pp. 65–88, jan 2010.

[76] G. Sun, N. Kaushik, A. B. Palazzolo, A. J. Provenza, C. Lawrence, and K. Carney, "An Efficient Algorithm for Blade Loss Simulations Using a High Fidelity Ball Bearing and Damper Model," in *Volume 5: 19th Biennial Conference on Mechanical Vibration and Noise, Parts A, B, and C*, vol. 2003, pp. 1011–1020, ASME, 2003.

[77] A. B. Jones and T. A. Harris, "Analysis of a Rolling-Element Idler Gear Bearing Having a Deformable Outer-Race Structure," *Journal of Basic Engineering*, vol. 85, p. 273, jun 1963.

[78] G. Cavallaro, D. Nelias, and F. Bon, "Analysis of High-Speed Intershaft Cylindrical Roller Bearing with Flexible Rings," *Tribology Transactions*, vol. 48, pp. 154–164, apr 2005.

[79] Y. Mao, L. Wang, and C. Zhang, "Influence of ring deformation on the dynamic characteristics of a roller bearing in clearance fit with housing," *International Journal of Mechanical Sciences*, vol. 138-139, pp. 122–130, feb 2018.

[80] J. Wensing, *On the dynamics of ball bearings*. PhD thesis, University of Twente, dec 1998.

[81] R. R. Davis and C. Vallance, "Incorporating General Race and Housing Flexibility and Deadband in Rolling Element Bearing Analysis," tech. rep., NASA, Lewis Research Centre, 1988.

[82] A. Leblanc, D. Nelias, and C. Defaye, "Nonlinear dynamic analysis of cylindrical roller bearing with flexible rings," *Journal of Sound and Vibration*, vol. 325, pp. 145–160, aug 2009.

[83] P. K. Gupta and B. Paul, *Advanced Dynamics of Rolling Elements*. New York, NY: Springer New York, 1st ed., 1984.

[84] B. Mevel and J. Guyader, "Experiments on routes to chaos in ball bearings," *Journal of Sound and Vibration*, vol. 318, pp. 549–564, dec 2008.

[85] C. Sunnersjö, "Varying Compliance Vibrations of Rolling Bearings," *Journal of Sound and Vibration*, vol. 58, no. 3, pp. 363–373, 1978.

[86] M. Tiwari, K. Gupta, and O. Prakash, "Dynamic Response Of An Unbalanced Rotor Supported On Ball Bearings," *Journal of Sound and Vibration*, vol. 238, pp. 757–779, dec 2000.

[87] B. Mevel and J. L. Guyader, "Routes to Chaos in Ball Bearings," *Journal of Sound and Vibration*, vol. 162, pp. 471–487, apr 1993.

[88] S. Fukata, E. H. Gad, T. Kondou, T. Ayabe, and H. Tamura, "On the Radial Vibration of Ball Bearings," *Bulletin of JSME*, vol. 28, no. 239, pp. 899–904, 1985.

[89] X. Hernot, M. Sartor, and J. Guillot, "Calculation of the Stiffness Matrix of Angular Contact Ball Bearings by Using the Analytical Approach," *Journal of Mechanical Design*, vol. 122, no. 1, p. 83, 2000.

[90] F. M. El-Saeidy, "Time-varying total stiffness matrix of a rigid machine spindle-angular contact ball bearings assembly: Theory and analytical/experimental verification," *Shock and Vibration*, vol. 18, no. 5, pp. 641–670, 2011.

[91] H. Rahnejat and R. Gohar, "The Vibrations of Radial Ball Bearings," *Proceedings of the Institution of Mechanical Engineers, Part C: Journal of Mechanical Engineering Science*, vol. 199, pp. 181–193, jul 1985.

[92] N. Aktürk, M. Uneeb, and R. Gohar, "The Effects of Number of Balls and Preload on Vibrations Associated With Ball Bearings," *Journal of Tribology*, vol. 119, p. 747, oct 1997.

[93] R. Tomović, "A Simplified Mathematical Model for the Analysis of Varying Compliance Vibrations of a Rolling Bearing," *Applied Sciences*, vol. 10, p. 670, jan 2020.

[94] H.-V. Liew and T. C. Lim, "Analysis of time-varying rolling element bearing characteristics," *Journal of Sound and Vibration*, vol. 283, pp. 1163–1179, may 2005.

[95] T. L. H. Walford and B. J. Stone, "The Measurement of the Radial Stiffness of Rolling Element Bearings under Oscillating Conditions," *Journal of Mechanical Engineering Science*, vol. 22, pp. 175–181, aug 1980.

[96] B. Stone, "The State of the Art in the Measurement of the Stiffness and Damping of Rolling Element Bearings," *CIRP Annals*, vol. 31, pp. 529–538, jan 1982.

[97] Y. Mitsuya, H. Sawai, M. Shimizu, and Y. Aono, "Damping in Vibration Transfer through Deep-Groove Ball Bearings," *Transactions of the Japan Society of Mechanical Engineers Series C*, vol. 58, no. 556, pp. 3714–3721, 1992.

[98] P. Dietl, J. Wensing, and G. C. van Nijen, "Rolling bearing damping for dynamic analysis of multi-body systems—experimental and theoretical results," *Proceedings of the Institution of Mechanical Engineers, Part K: Journal of Multi-body Dynamics*, vol. 214, pp. 33–43, mar 2000.

[99] J. Sopanen and A. Mikkola, "Dynamic model of a deep-groove ball bearing including localized and distributed defects. Part 1: theory," *Proceedings of the Institution of Mechanical Engineers, Part K: Journal of Multi-body Dynamics*, vol. 217, pp. 201–211, jan 2003.

[100] D. P. Fleming and J. V. Poplawski, "Unbalance Response Prediction for Rotors on Ball Bearings Using Speed- and Load-Dependent Nonlinear Bearing Stiffness," *International Journal of Rotating Machinery*, vol. 2005, no. 1, pp. 53–59, 2005.

[101] S. Harsha, "Nonlinear dynamic analysis of a high-speed rotor supported by rolling element bearings," *Journal of Sound and Vibration*, vol. 290, pp. 65–100, feb 2006.

[102] J.-J. Sinou, "Non-linear dynamics and contacts of an unbalanced flexible rotor supported on ball bearings," *Mechanism and Machine Theory*, vol. 44, pp. 1713–1732, sep 2009.

[103] B. J. Hamrock and D. Dowson, "Isothermal Elastohydrodynamic Lubrication of Point Contacts: Part 1—Theoretical Formulation," *Journal of Lubrication Technology*, vol. 98, p. 223, apr 1976.

[104] Y. Wijnant, J. Wensing, and G. Nijen, "The Influence Of Lubrication On The Dynamic Behaviour Of Ball Bearings," *Journal of Sound and Vibration*, vol. 222, pp. 579–596, may 1999.

[105] F. Nonato and K. L. Cavalca, "An approach for including the stiffness and damping of elastohydrodynamic point contacts in deep groove ball bearing equilibrium models," *Journal of Sound and Vibration*, vol. 333, pp. 6960–6978, dec 2014.

[106] P. Patra, V. H. Saran, and S. Harsha, "Non-linear dynamic response analysis of cylindrical roller bearings due to rotational speed," *Proceedings of the Institution of Mechanical Engineers, Part K: Journal of Multi-body Dynamics*, p. 146441931876267, mar 2018.

[107] R. Aini, H. Rahnejat, and R. Gohar, "Vibration Modeling of Rotating Spindles Supported by Lubricated Bearings," *Journal of Tribology*, vol. 124, p. 158, jan 2002.

[108] N. A. Hoshikawa Tsuha and K. L. Cavalca, "Stiffness and damping of elastohydrodynamic line contact applied to cylindrical roller bearing dynamic model," *Journal of Sound and Vibration*, p. 115444, may 2020.

[109] P. K. Gupta, "Dynamics of Rolling-Element Bearings—Part II: Cylindrical Roller Bearing Results," *Journal of Lubrication Technology*, vol. 101, no. 3, p. 305, 1979.

[110] P. K. Gupta, "Dynamics of Rolling-Element Bearings—Part IV: Ball Bearing Results," *Journal of Lubrication Technology*, vol. 101, no. 3, p. 319, 1979.

[111] J. W. Kannel and S. S. Bupara, "A Simplified Model of Cage Motion in Angular Contact Bearings Operating in the EHD Lubrication Regime," *Journal of Lubrication Technology*, vol. 100, no. 3, p. 395, 1978.

[112] P. Sun, W. Chen, Y. Shen, and D. Wang, "Calculation method for comprehensive damping of ball bearings based on multigrid method," *Industrial Lubrication and Tribology*, vol. ahead-of-p, apr 2020.

[113] W. Jacobs, R. Boonen, P. Sas, and D. Moens, "The influence of the lubricant film on the stiffness and damping characteristics of a deep groove ball bearing," *Mechanical Systems and Signal Processing*, vol. 42, no. 1, pp. 335–350, 2014.

[114] T. L. H. Walford and B. J. Stone, "The Sources of Damping in Rolling Element Bearings under Oscillating Conditions," *Proceedings of the Institution of Mechanical Engineers, Part C: Journal of Mechanical Engineering Science*, vol. 197, pp. 225–232, oct 1983.

[115] R. Zeillinger, H. Springer, and H. Köttritsch, "Experimental Determination of Damping in Rolling Bearing Joints," in *Volume 5: Manufacturing Materials and Metallurgy; Ceramics; Structures and Dynamics; Controls, Diagnostics and Instrumentation; Education; General*, p. V005T14A016, ASME, jun 1994.

[116] J. Kraus, J. J. Blech, and S. G. Braun, "In Situ Determination of Rolling Bearing Stiffness and Damping by Modal Analysis," *Journal of Vibration Acoustics Stress and Reliability in Design*, vol. 109, p. 235, jul 1987.

[117] R. J. W. Knaapen, *Experimental determination of rolling element bearing stiffness*. Master's, Eindhoven University of Technology, 1999.

[118] A. Gunduz, J. T. Dreyer, and R. Singh, "Effect of bearing preloads on the modal characteristics of a shaft-bearing assembly: Experiments on double row angular contact ball bearings," *Mechanical Systems and Signal Processing*, vol. 31, pp. 176–195, aug 2012.

[119] H. Luo, J. Fu, C. Yu, G. Liu, W. Wang, and P. Wang, "Numerical simulation and experimental testing of dynamic stiffness of angular contact ball bearing," *Advances in Mechanical Engineering*, vol. 10, p. 168781401879897, sep 2018.

[120] S. Lacroix, D. Nélias, and A. Leblanc, "Experimental Study of Four-Point Contact Ball Bearing with Deformable Rings," *Tribology Transactions*, vol. 58, pp. 963–970, nov 2015.

[121] J. M. de Mul, J. M. Vree, and D. A. Maas, "Equilibrium and Associated Load Distribution in Ball and Roller Bearings Loaded in Five Degrees of Freedom While Neglecting Friction—Part II: Application to Roller Bearings and Experimental Verification," *Journal of Tribology*, vol. 111, p. 149, jan 1989.

[122] Y. Jin, Z. Lu, R. Yang, L. Hou, and Y. Chen, "A new nonlinear force model to replace the Hertzian contact model in a rigid-rotor ball bearing system," *Applied Mechanics and Mechanics*, vol. 39, no. 3, pp. 365–378, 2018.

[123] J.-J. Sinou, D. Demailly, C. Villa, F. Thouverez, M. Massenzio, and F. Laurant, "Rotordynamics Analysis: Experimental and Numerical Investigations," in *Volume 5: 19th Biennial Conference on Mechanical Vibration and Noise, Parts A, B, and C*, vol. 2003, pp. 2633–2640, ASME, jan 2003.

[124] J.-J. Sinou and F. Thouverez, "Experimental Study of a Flexible Rotor and Its Dependency on the Rolling-Bearing Temperature," *International Journal of Rotating Machinery*, vol. 2006, pp. 1–8, mar 2006.

[125] J.-J. Sinou, C. Villa, F. Thouverez, and M. Massenzio, "Experimental analysis of the dynamical response of a flexible rotor including the effects of external damping," *Journal of Engineering and Applied Sciences*, vol. 1, no. 4, pp. 483–490, 2006.

[126] G. Chen, "Vibration modelling and verifications for whole aero-engine," *Journal of Sound and Vibration*, vol. 349, pp. 163–176, aug 2015.

[127] A. A. Khan and N. S. Vyas, "Application of Volterra and Wiener Theories for Nonlinear Parameter Estimation in a Rotor-Bearing System," *Nonlinear Dynamics*, vol. 24, no. 3, pp. 285–304, 2001.

[128] C. Bai, H. Zhang, and Q. Xu, "Experimental and Numerical Studies on Nonlinear Dynamic Behavior of Rotor System Supported by Ball Bearings," *Journal of Engineering for Gas Turbines and Power*, vol. 132, p. 082502, aug 2010.

[129] C. Bai, H. Zhang, and Q. Xu, "Subharmonic resonance of a symmetric ball bearing–rotor system," *International Journal of Non-Linear Mechanics*, vol. 50, pp. 1–10, apr 2013.

[130] Y. Jin, R. Yang, L. Hou, Y. Chen, and Z. Zhang, "Experiments and Numerical Results for Varying Compliance Contact Resonance in a Rigid Rotor–Ball Bearing System," *Journal of Tribology*, vol. 139, p. 041103, apr 2017.

[131] R. Yang, L. Hou, Y. Jin, Y. Chen, and Z. Zhang, "The Varying Compliance Resonance in a Ball Bearing Rotor System Affected by Different Ball Numbers and Rotor Eccentricities," *Journal of Tribology*, vol. 140, p. 051101, mar 2018.

[132] G. Chen and M. Qu, "Modeling and analysis of fit clearance between rolling bearing outer ring and housing," *Journal of Sound and Vibration*, vol. 438, pp. 419–440, jan 2019.

[133] S. Edwards, A. W. Lees, and M. I. Friswell, "Experimental Identification of Excitation and Support Parameters of a Flexible Rotor-Bearings-Foundation System from a Single Run-Down," *Journal of Sound and Vibration*, vol. 232, pp. 963–992, may 2000.

[134] R. Tiwari, A. Lees, and M. Friswell, "Identification of Speed-Dependent Bearing Parameters," *Journal of Sound and Vibration*, vol. 254, pp. 967–986, jul 2002.

[135] P. Čermelj and M. Boltežar, "An indirect approach to investigating the dynamics of a structure containing ball bearings," *Journal of Sound and Vibration*, vol. 276, pp. 401–417, sep 2004.

[136] M. Chouksey, J. Dutt, and S. Modak, "Model updating of rotors supported on ball bearings and its application in response prediction and balancing," *Measurement*, vol. 46, pp. 4261–4273, dec 2013.

[137] R. Tiwari and N. Vyas, "Estimation of Non-Linear Stiffness Parameters of Rolling Element Bearings from Random Response of Rotor-Bearing Systems," *Journal of Sound and Vibration*, vol. 187, pp. 229–239, oct 1995.

[138] R. Tiwari and N. Vyas, "Parameter Estimation in Imbalanced Non-Linear Rotor-Bearing Systems from Random Response," *Journal of Sound and Vibration*, vol. 208, pp. 1–14, nov 1997.

[139] R. Tiwari and N. Vyas, "Non-Linear Bearing Stiffness Parameter Extraction from Random Response in Flexible Rotor-Bearing Systems," *Journal of Sound and Vibration*, vol. 203, pp. 389–408, jun 1997.

[140] A. Chatterjee and N. S. Vyas, "Nonlinear Parameter Estimation in Rotor-Bearing System Using Volterra Series and Method of Harmonic Probing," *Journal of Vibration and Acoustics*, vol. 125, p. 299, jul 2003.

[141] N. S. Feng and E. J. Hahn, "Rolling Element Bearing Non-Linearity Effects," in *Volume 4: Manufacturing Materials and Metallurgy; Ceramics; Structures and Dynamics; Controls, Diagnostics and Instrumentation; Education*, p. V004T03A034, ASME, may 2000.

[142] Y. Zhuo, X. Zhou, and C. Yang, "Dynamic analysis of double-row self-aligning ball bearings due to applied loads, internal clearance, surface waviness and number of balls," *Journal of Sound and Vibration*, vol. 333, pp. 6170–6189, nov 2014.

[143] S. P. Harsha, K. Sandeep, and R. Prakash, "Effects of Preload and Number of Balls on Nonlinear Dynamic Behavior of Ball Bearing System," *International Journal of Nonlinear Sciences and Numerical Simulation*, vol. 4, pp. 265–278, jan 2003.

[144] S. Harsha, K. Sandeep, and R. Prakash, "The effect of speed of balanced rotor on nonlinear vibrations associated with ball bearings," *International Journal of Mechanical Sciences*, vol. 45, pp. 725–740, apr 2003.

[145] X. Chen and M. Liao, "Steady-State Characteristics of a Dual-Rotor System With Intershaft Bearing Subjected to Mass Unbalance and Base Motions," in *Proceedings of the ASME Turbo Expo 2018: Turbomachinery Technical Conference and Exposition. Volume 7A: Structures and Dynamics.*, ASME International, jun 2018.

[146] C. Nataraj and H. D. Nelson, "Periodic Solutions in Rotor Dynamic Systems With Nonlinear Supports: A General Approach," *Journal of Vibration Acoustics Stress and Reliability in Design*, vol. 111, p. 187, apr 1989.

[147] E. J. Hahn and P. Y. P. Chen, "Harmonic Balance Analysis of General Squeeze Film Damped Multidegree-of-Freedom Rotor Bearing Systems," *Journal of Tribology*, vol. 116, p. 499, jul 1994.

[148] P. Bonello, M. J. Brennan, and R. Holmes, "A Study of the Nonlinear Interaction Between an Eccentric Squeeze Film Damper and an Unbalanced Flexible Rotor," *Journal of Engineering for Gas Turbines and Power*, vol. 126, no. 4, p. 855, 2004.

[149] M. Settipalli, R. Chandran, V. Ganji, and T. Brockett, "Imbalance response of non-linear rotor-SFD dynamic systems with structure modelled as frfs using harmonic balance method," in *ASME 2017 Gas Turbine India Conference, GTINDIA 2017*, (Bangalore, India), p. V002T05A024, 2017.

[150] C. Villa, J.-J. Sinou, and F. Thouverez, "Stability and vibration analysis of a complex flexible rotor bearing system," *Communications in Nonlinear Science and Numerical Simulation*, vol. 13, no. 4, pp. 804–821, 2008.

[151] M. Guskov and F. Thouverez, "Harmonic Balance-Based Approach for Quasi-Periodic Motions and Stability Analysis," *Journal of Vibration and Acoustics*, vol. 134, no. 3, p. 031003, 2012.

[152] Y.-B. Kim and S. Noah, "Quasi-Periodic Response and Stability Analysis for a Non-Linear Jeffcott Rotor," *Journal of Sound and Vibration*, vol. 190, pp. 239–253, feb 1996.

[153] Y. Kim and S.-K. Choi, "A Multiple Harmonic Balance Method for the Internal Resonant Vibration of a Non-Linear Jeffcott Rotor," *Journal of Sound and Vibration*, vol. 208, pp. 745–761, dec 1997.

[154] M. Guskov, J.-J. Sinou, and F. Thouverez, "Multi-dimensional harmonic balance applied to rotor dynamics," *Mechanics Research Communications*, vol. 35, no. 8, pp. 537–545, 2008.

[155] J. Didier, J.-J. Sinou, and B. Faverjon, "Multi-Dimensional Harmonic Balance With Uncertainties Applied to Rotor Dynamics," *Journal of Vibration and Acoustics*, vol. 134, p. 061003, sep 2012.

[156] L. Hou, Y. Chen, Y. Fu, H. Chen, Z. Lu, and Z. Liu, "Application of the HB-AFT method to the primary resonance analysis of a dual-rotor system," *Nonlinear Dynamics*, vol. 88, pp. 2531–2551, 2017.

[157] A. Kahraman, H. Nevzatozguven, D. R. Houser, and J. J. Zakrajsek, "Dynamic analysis of geared rotors by finite elements," *Journal of Mechanical Design, Transactions of the ASME*, vol. 114, pp. 507–514, sep 1992.

[158] A. S. Lee, J. W. Ha, and D. H. Choi, "Coupled lateral and torsional vibration characteristics of a speed increasing geared rotor-bearing system," *Journal of Sound and Vibration*, vol. 263, pp. 725–742, jun 2003.

[159] A. Labuschagne, N. F. van Rensburg, and A. J. van der Merwe, "Comparison of linear beam theories," *Mathematical and Computer Modelling*, vol. 49, no. 1-2, pp. 20–30, 2009.

[160] W. Weaver, S. P. Timoshenko, and D. H. Young, *Vibration Problems in Engineering*. A Wiley-Interscience publication, Wiley, 1990.

[161] G. R. Cowper, "The shear coefficient in timoshenko's beam theory," *Journal of Applied Mechanics, Transactions ASME*, vol. 33, no. 2, pp. 335–340, 1964.

[162] M. D. Olson and G. M. Lindberg, "Annular and circular sector finite elements for plate bending," *International Journal of Mechanical Sciences*, vol. 12, pp. 17–33, jan 1970.

[163] G. Nigh and M. Olson, "Finite element analysis of rotating disks," *Journal of Sound and Vibration*, vol. 77, pp. 61–78, jul 1981.

[164] A. A. S. Shahab and J. Thomas, "Coupling effects of disc flexibility on the dynamic behaviour of multi disc-shaft systems," *Journal of Sound and Vibration*, vol. 114, pp. 435–452, may 1987.

[165] S. B. Chun and C. W. Lee, "Vibration analysis of shaft-bladed disk system by using substructure synthesis and assumed modes method," *Journal of Sound and Vibration*, vol. 189, pp. 587–608, feb 1996.

[166] J. Chung, J. W. Heo, and C. S. Han, "Natural frequencies of a flexible spinning disk misaligned with the axis of rotation," feb 2003.

[167] J. W. Heo, J. Chung, and K. Choi, "Dynamic time responses of a flexible spinning disk misaligned with the axis of rotation," *Journal of Sound and Vibration*, vol. 262, pp. 25–44, apr 2003.

[168] J. D'Errico, "Consistently sorted eigenvalue and eigenvector sequences." `http://uk.mathworks.com/matlabcentral/fileexchange/22885-eigenshuffle`. [Online; Accessed: 2017-09-19].

[169] A. Haslam, "Roladyn." `https://github.com/alxhslm/ROLADYN`, 2019.

[170] S. Singh, C. Q. Howard, and C. H. Hansen, "An extensive review of vibration modelling of rolling element bearings with localised and extended defects," *Journal of Sound and Vibration*, vol. 357, pp. 300–330, 2015.

[171] Y. Qin, C. Li, X. Wu, Y. Wang, and H. Chen, "Multiple-degree-of-freedom dynamic model of rolling bearing with a localized surface defect," *Mechanism and Machine Theory*, vol. 154, p. 104047, 2020.

[172] P. K. Gupta, "Dynamics of Rolling-Element Bearings—Part III: Ball Bearing Analysis," *Journal of Lubrication Technology*, vol. 101, no. 3, p. 312, 1979.

[173] C. R. Meeks and K. O. Ng, "The dynamics of ball separators in ball bearings- part i: Analysis," *ASLE Transactions*, vol. 28, no. 3, pp. 277–287, 1985.

[174] T. Detroux, L. Renson, L. Masset, and G. Kerschen, "The harmonic balance method for bifurcation analysis of large-scale nonlinear mechanical systems," *Computer Methods in Applied Mechanics and Engineering*, vol. 296, pp. 18–38, 2015.

[175] T. M. Cameron and J. H. Griffin, "An Alternating Frequency/Time Domain Method for Calculating the Steady-State Response of Nonlinear Dynamic Systems," *Journal of Applied Mechanics*, vol. 56, p. 149, mar 1989.

[176] Y. Kim, S. Noah, and Y. Choi, "Periodic response of multi-disk rotors with bearing clearances," *Journal of Sound and Vibration*, vol. 144, pp. 381–395, feb 1991.

[177] A. H. Nayfeh and B. Balachandran, *Applied nonlinear dynamics : analytical, computational, and experimental methods*. Wiley, 1995.

[178] P. Sundararajan and S. T. Noah, "Dynamics of Forced Nonlinear Systems Using Shooting/Arc-Length Continuation Method—Application to Rotor Systems," *Journal of Vibration and Acoustics*, vol. 119, p. 9, jan 1997.

[179] A. Dhooge, W. Govaerts, and Y. A. Kuznetsov, "MATCONT: A MATLAB package for numerical bifurcation analysis of ODEs," *ACM Transactions on Mathematical Software*, vol. 29, pp. 141–164, jun 2003.

[180] A. Haslam, "Harmlab." `https://github.com/alxhslm/HarmLAB`, 2018.

[181] A. Wächter and L. T. Biegler, "On the implementation of an interior-point filter line-search algorithm for large-scale nonlinear programming," *Mathematical Programming*, vol. 106, pp. 25–57, mar 2006.

[182] A. H. Haslam, C. W. Schwingshackl, and A. I. Rix, "A parametric study of an unbalanced Jeffcott rotor supported by a rolling-element bearing," *Nonlinear Dynamics*, vol. 99, no. 4, pp. 2571–2604, 2020.

[183] D. Petersen, C. Howard, and Z. Prime, "Varying stiffness and load distributions in defective ball bearings: Analytical formulation and application to defect size estimation," *Journal of Sound and Vibration*, 2015.

[184] C. Schwingshackl, L. Muscutt, M. Szydlowsky, A. Haslam, G. Tuzzi, V. Ruffini, M. Price, A. Rix, and J. Green, "Asynchronous Rotor Excitation System (ARES) – A new rotor dynamic test facility at Imperial College London," in *12th International Conference on Vibrations in Rotating Machinery*, (Liverpool), 2020.

[185] A. SKF, "1208 EKTN9 Self-Aligning Ball Bearing." `https://www.skf.com/uk/products/rolling-bearings/ball-bearings/self-aligning-ball-bearings/productid-1208EKTN9`. [Online; Accessed: 2019-08-22].

[186] AB SKF, "2208 EKTN9 Self-Aligning Ball Bearing." `https://www.skf.com/uk/products/rolling-bearings/ball-bearings/self-aligning-ball-bearings/productid-2208EKTN9`. [Online; Accessed: 2019-08-22].

[187] R+W, "Bkh metal bellows coupling with split hub." `https://www.rw-couplings.com/products/precision-couplings/metal-bellows-couplings/bkh/`. [Online; Accessed: 2020-08-19].

[188] E. P. Company, "Thru-bore series encoder model 776." `http://encoder.com/products/incremental-encoders/incremental-thru-bore-motor-mount-encoders/model-776/`. [Online; Accessed: 2020-08-19].

[189] A. Haslam, C. Schwingshackl, L. Muscutt, A. Rix, and M. Price, "Experimental investigation of non-linear stiffness behaviour of a rolling-element bearing," in *12th International Conference on Vibrations in Rotating Machinery*, (Liverpool), 2020.

[190] J. Gere, *Mechanics of Materials*. Mechanics of Materials, Cengage Learning, 6th ed., 2003.

[191] D. Ewins, *Modal Testing: Theory, Practice and Applications*. Hertfordshire, UK: Research Studies Press Ltd., 2nd editio ed., 2000.

[192] A. Brandt, *Noise and Vibration Analysis: Signal Analysis and Experimental Procedures*. Chichester, UK: Wiley, 1st ed., 2011.

[193] A. Haslam, "Modelab." `https://github.com/alxhslm/ModeLAB`, 2019.

[194] M. Pastor, M. Binda, and T. Harčarik, "Modal Assurance Criterion," *Procedia Engineering*, vol. 48, pp. 543–548, 2012.

[195] M. Goldfarb and N. Celanovic, "Modeling piezoelectric stack actuators for control of micromanipulation," *IEEE Control Systems*, vol. 17, pp. 69–79, jun 1997.

[196] J. M. Tessarzik, R. H. Badgley, and W. J. Anderson, "Flexible rotor balancing by the exact point-speed influence coefficient method," *Journal of Manufacturing Science and Engineering, Transactions of the ASME*, vol. 94, no. 1, pp. 148–158, 1972.

[197] J. C. Nicholas, E. J. Gunter, and P. E. Allaire, "Effect of Residual Shaft Bow on Unbalance Response and Balancing of a Single Mass Flexible Rotor—Part I: Unbalance Response," *Journal of Engineering for Power*, vol. 98, pp. 171–181, apr 1976.